Università degli Studi di Milano-Bicocca
Facoltà di Scienze Matematiche Fisiche e Naturali

Corso di Dottorato di Ricerca in Fisica e Astronomia
XXIV° Ciclo

Thin protein film plasma removal: application to biological decontamination

Fumagalli Francesco

Milano, 24.01.2012

Internal supervisor: Prof. Claudia Riccardi

External supervisor: Dott. Francois Rossi

Abstract

Surgical instruments are intended to come into direct contact with the patients' tissue and therefore need to be sterilized and decontaminated in order to prevent infections, inflammations and transmission of diseases. In the last years low-pressure plasma discharges have been successfully applied to remove various biomolecules from surfaces. However, the knowledge of the physical-chemical interaction mechanisms between plasma and biomolecules is still rather poor, which is a major limiting factor for the optimization of this type of plasma treatment. In this work an original contribution to the field is presented, either in terms of process development, of physical mechanisms investigation and process diagnostic protocols assessment. Experimental results were obtained with a low pressure double coil planar inductively coupled plasma reactor.

Plasma interactions with low bio-contamination levels (less than 5 $\mu g/mm^2$) typical of biological residuals present after standard hospital sterilization protocols were studied. Removal mechanisms of biological thin films during plasma treatment with oxygen and water vapor containing discharge mixtures were characterized in-situ by means of quartz crystal microbalance (QCM), time resolved mass spectrometry and optical emission spectrometry. A novel QCM measurement technique was developed in this work as a quasi-online diagnostic tool in pulsed plasma operation. After plasma treatment, surfaces analysis techniques (XPS and AFM and profilometry) have been used to investigate ex-situ chemical and morphological changes at the surface of the protein films.

Moreover mass removal rates as measured by QCM were found to depend on treatment time, showing a self limiting etching kinetics. Removal rates dynamics has been characterized in different plasma conditions by a set of descriptive parameters and correlated with plasma induced chemical composition changes and morphological modification of the protein film.

The interaction mechanism between plasma and protein films have been studied in-situ. In the last years several authors presented experimental investigations devoted to isolate potential agents effective in plasma decontamination (UV, radicals, ions, heat)

and to identify possible synergic mechanisms between them, but in most cases particle fluxes have been produced outside plasma environments (beam experiments) or the effect on biofilm was studied by physically decoupling the effects of single mechanisms (UV screen, afterglows). In this work experiments were designed to quantitatively measure the fluxes of different potentially sterilizing species in the plasma phase (ions, radicals, UV and heat) and their interaction effects with a model protein biofilm. Particle fluxes have been calculated using data from Langmuir probe, mass spectrometry, optical emission actinometry and infrared pyrometry measurements. Different experiments have been performed using plasma internal parameters (e.g. fluxes) as independent variables for the decontamination treatments, modifying one flux component at time while keeping the others constant the influence of synergetic effects between decontamination agents have been measured.

Furthermore the control of the DC bias applied on the sample holder allows changing the energy of the ions (moderate voltages from 10 to 150 V were applied) interacting with the surface.

Within the confidence limits of the statistical method implemented for validation, ion assisted chemical etching operating in an ion limited regime proved to be the mechanism which describes more accurately the etching rates for our biological substrates

Contents

1. Introduction

Developments in the medical field produced, in the last years, several new healing strategies; along with the introduction of novel technologies new tasks and technical challenges arise in order to accomplish their full implementation in the medical practice. An important example is the class of new materials synthesized especially for medical purposes or for surgical tools components and the processing needed before their utilization. These materials are undergoing a steady development for improving mechanical properties and, in the case of implants, tissue interface properties; at the same time new materials have new demands, compared to conventional materials, associated to the surface decontamination processes.

Special materials such as composite metals, ceramics and plastics assembly require cold and gentle decontamination mechanisms and are incompatible with common sterilization techniques, mainly because of the chemical and thermal stress imposed to the polymer-based components of the treated materials. Moreover other disadvantages are associated with traditional sterilization techniques. A γ-radiation sterilization device requires large and costly installations and radioactive source like cobalt 60 are needed. Distributors for cobalt are mainly based in Canada and Russia and the availability of such material is affected also by the international political situation. Sterilization using ethylene oxide (EO) requires long treatment times and the processing gas mixture is very toxic and highly explosive thus imposing special requirements on the infrastructure and users. As a last drawback, outgassing of EO based sterilization chambers may takes days.

A new sterilization process which is cold, dry, non-toxic and fast is required. Additionally, new requirements (which are beyond the capabilities of the actual decontamination methods) have to be fulfilled, i.e. the deactivation of harmful viruses and infectious proteins like prions.

In principle low pressure plasma discharges have the potential to fulfill all these requirements and hey have been proposed in the last years as an alternative technology for medical materials sterilization and decontamination. However, both the efficiency and physical mechanisms of plasma –biomaterials interaction processes have to be investigated in order to achieve a better understanding of the

sterilization/decontamination processes and a reliable implementation of the new technology. Additionally, the effect of plasma particle fluxes on treated materials must be characterized.

The aim of the experiments described in this PhD dissertation is the characterization of the plasma processes used for decontamination of materials and the investigation of the basic physical mechanism involved in the interaction between biological materials and plasma discharges.

1.1 Organization of the Dissertation

Basic information about state-of the-art of actually employed decontamination methods, fore-front research activity and the contribution of this PhD. dissertation are given in the first chapter *Introduction*.

An historical overview of the evolution of inductively plasma sources as well as a summary of the basic physical principles governing the operation of this class of plasma reactors is given in chapter 2: *Reactor and diagnostics*. This chapter includes and overview and a brief description of the standard diagnostics tools employed in this work, both for plasma diagnostics and surface analysis.

Results and discussion of this research work are presented and discussed through chapters from 3 to 6.

Chapter 3: *Plasma discharges characterization* describes investigations on plasma parameters relevant for decontamination processes for oxygen containing discharges (paragraph 3.1) together with basic findings on decontamination capabilities of such plasmas, water vapor discharges are also investigated (paragraph 3.2) as an low-cost environmental-friendly alternative for surfaces decontamination. Finally plasma process byproducts analysis by means of time resolved mass and optical spectrometry (paragraph 3.2) are characterized.

Chapter 4: *Quartz crystal microbalance in-situ diagnostic* describes the development of a new approach for protein mass loss measurements (paragraph 4.1), in-situ diagnosis and good time resolution of this experimental strategy allows a deeper and novel investigation on biomaterials etching kinetics, (paragraph 4.2).

Chapter 5: 5 *Plasma biomaterials interaction*, presents a series of quantitative measurements of plasma fluxes performed by means of RF compensated Langmuir

probe and threshold ionization mass spectrometry (paragraph 5.1). Using the results of the former paragraph the second part of chapter 5 describes investigations of a series of possible plasma biomaterials interaction mechanisms tested against protein removal measurements using a statistical approach (paragraph 5.2).

Chapter 6: *Biological measurements,* summarizes a series of experiments aimed to the definition of a fast and easily applicable protocol for surface contamination qualitative quantification using fluorescent molecules labeling (paragraph 6.1). An immunological staining experiment for the determination of residual biological functionality of plasma treated proteins is also described in the second part of this chapter (paragraph 6.2)

1.2 Cooperation

Joint Research Centre – Institute of Health and Consumer Protection – Nanobiotechnology Laboratory

The Institute for Health and Consumer Protection (IHCP) is one of the seven scientific institutes of the Joint Research Centre (JRC) of the European Commission. The mission of the JRC-IHCP is to protect the interests and health of the consumer in the framework of EU legislation on chemicals, food, and consumer products by providing scientific and technical support, including risk-benefit assessment and analysis of traceability. IHCP activities are supporting EU policies in the following areas: genetically modified organisms, health and environment, consumer products and nutrition, alternatives to animal testing and nanotechnology.

The main activity of the NanoBiotechnology Laboratory deals with Bio interface Engineering, Nanotoxicology and molecular detection applied in the field of life science. The group develops and characterizes different processes based on electro chemistry, self assembled monolayers and plasma technologies for surface modification and patterning of materials at the nanometer scale. In parallel, detection and characterization techniques allow the precise study of the mechanisms of interaction of surfaces and biological entities such as proteins or cells.

Major topics of IHCP research are the following:

- Development of Bio-functional surfaces: surface functionalisation and controlled immobilisation of proteins for biomaterials and biosensors.
- Surface patterning by soft lithography, UV and E- beam lithography and colloidal techniques for applications in the field of cell based biosensors and protein chips.
- Biomaterials interfaces: plasma treatment of polymers and alloys for improvement of biocompatibility of implants
- Development of Microsystems for cell toxicology studies
- Nanotoxicology and interaction of cells with nanostructures and nanomaterials.

BIODECON Project

The Decontamination of Biological Systems using Plasma Discharges (BIODECON) project investigates cold plasma discharges as a novel method for decontaminating surfaces. The partners hope to pioneer a highly effective decontamination procedure that avoids the damage to the decontaminated thermolabile substrates associated with existing techniques. Contamination with microorganisms and toxins is one of the biggest hygiene problems facing medical personnel. The Decontamination of Biological Systems using Plasma Discharges (BIODECON) project explores the feasibility of developing new decontamination procedures using plasma discharges. BIODECON is being coordinated by the Center of Plasma Science and Technology at the Ruhr-Universit¨at Bochum. Other partners are the Joint Research Center (JRC) in Ispra, Italy, the French SME ACXYS in Saint-Martin le Vinoux, France, and the French Atomic Energy Commission contributes their facilities for secure research into prion proteins. Specialist expertise in the application of plasma discharges to biological samples is provided by the Fraunhofer Institute for Process Engineering and Packaging (IVV) in Freising near Munich, Germany. The partnership brings together an ideal trans-disciplinary mix of expertise in plasma physics, microbiology and commercial production. The project has been funded by Europen Commission - Framework Plan 6.

1.3 Definitions

The colloquial meaning of sterile is the absence of augmentable microorganisms like bacteria and moulds. In every day life, this ideal case is not guaranteed. Among other things, this ideal case can not be verified. According to Wallhauser [1]:

> Sterile means the absence of biological units which are augmentable like microorganism or are able to pass genetic information e.g. like viruses, prions or infectious nucleic acids.

The term decontamination refers to a more radical elimination process which has to be able to prevent the health risk associated with the presence of material of biological origin on a surface, from this point of view the definition of contamination enlarges to include not only microorganisms but also biomolecules or portions of them. According to Segen [2]:

> Decontaminated means that blood borne or other pathogens on a surface or item are removed, destroyed or inactivated to the point where they are no longer capable of transmitting infectious particles, and the surface or item is rendered safe for handling, use, or disposal.

1.4 State of the art for medical devices sterilization and decontamination

Medical devices such as tools and implants are sterilized to eliminate living organisms including bacteria, yeasts, mould and viruses [3]. Many sterilization/decontamination techniques are available today and these include the traditional methods of autoclaving, ethylene oxide (EtO) and gamma irradiation and the more recently introduced systems involving low-temperature gas plasma and vapor phase sterility. Despite the availability of a wide range of techniques, it is generally agreed that no single process is capable of sterilizing or decontaminate all medical devices without adverse effects. All processes have their own inherent advantages and disadvantages

and many adverse effects relate to incompatibilities between polymers used in biomedical applications and sterilization process parameters.

Decontamination processes act on biological material in a chemical or physical way. Generally, each process results in a change in the structure or function of the organic macromolecules, leading to physical destruction or to inability to perform biological activity. The macromolecules of biomedical polymers can be attacked by the same mechanisms, and different forms of sterilization may result in hydrolysis, oxidation, softening, melting, chain scission and depolymerisation. Research has shown that sterilization can modify the bulk and surface properties and alter the physiochemical stability of biomedical polymers [4,5,6,7]. Sterilization may also result in the formation of degradation products, which may present a toxicological risk [8].

When selecting a method, an analysis of the compatibility of each device, particularly the chemical composition of the materials, with the process parameters of the sterilization method and the chemicals used, is necessary.

In the following the most widely used methods of sterilization will be briefly described for medical devices and some of their effects on biomedical polymers.

Heat. Steam sterilisation or autoclaving is a relatively simple process that exposes the device to saturated steam at 121ºC for a minimum of 20 minutes at a pressure of 121kPa [9]. The deactivation of prions proteins requires a higher temperature (around 134◦ C) and additional treatment time. The process is usually carried out in a pressure vessel designed to withstand the elevated temperature and pressure and kills micro-organisms by destroying metabolic and structural components essential to their replication. It is the method of choice for sterilisation of heat-resistant surgical equipment and intravenous fluid as it is an efficient, reliable, rapid, relatively simple process that does not result in toxic residues. The high temperature, humidity and pressure used during the steam sterilisation process can lead to hydrolysis, softening or degradation of many biomedical polymers [5] such Ultra High Molecular Weight Poly Ethylene (UHMWPE) and polymers with low glass transition temperature in general. Several workers [10,11] have reported that autoclaving is unsuitable for the sterilisation of many biomedical polymers due to unacceptable changes in mechanical properties and surface degradation. A further issue is the potential formation of degradation products [10] during autoclave sterilisation of these materials.

γ-Radiation. A dry sterilization process at room temperature is the treatment using γ-rays from a Cobalt 60 source in the wavelength range from 0.001 nm to 0.01 nm. Either gamma rays from a cobalt-60 (60Co) isotope source or machine generated accelerated electrons can be used. Gamma irradiation is the most popular form of radiation sterilisation and is used when materials are sensitive to the high temperature of autoclaving but compatible with ionizing radiation. Exposure is achieved when the materials to be sterilized are moved around an exposed 60Co source for a defined period of time and the sterilization result depends on the radiation dose and not on treatment time. The most commonly validated dose used to sterilize medical devices is 25kGy.[9] It is a simple, rapid and efficacious method of sterilisation. However, high capital costs are a major disadvantage.

The penetration depth of γ-radiation for polyvinyl chloride (PVC) like materials is above 10 centimeters and it is therefore possible to treat devices in a package. Sterilisation of biomedical polymers using gamma irradiation is also known to result in physical changes in some biomaterials, including embrittlement, discolouration,[12,13,14] odor generation, stiffening, [15,16] softening, an increase or decrease in melt temperature [17] and decreases in molecular weight [9,11,16,18,19,20,21]. For example glass, PVC and polystyrene (PS) cannot be treated more than once since after one treatment they start to discolor.

Hydrogen Peroxide. A common sterilization process exploits hydrogen peroxide (H_2O_2) and heat. The material is first immersed in or sprayed with H_2O_2 and then, to enhance the efficiciency, the immersion bath is heated up to 80 °C. In this case the treatment time is less than 10 s. A problem with this process is that the treated materials must be free of adipose films on the surface before sterilizing with H2O2. Another problem is the residual H_2O_2 on the surface and in the material. The U.S. Food and Drug Admistration (FDA) require less than 0.5 ppm of H_2O_2 left on the materials. The process of using hydrogen peroxide and a surrounding plasma for sterilization is patented by Johnson & Johnson and is called SterradR. The hydrogen peroxide dissociates in the sterilization device and the oxidation capability of hydrogen and oxygen as OH and O deactivates organisms. At a relatively low temperature around 50◦ C the treatment time lasts for 70 minutes.

This process is capable of treating heat sensitive materials but is also known to change for example the surface characteristics of UHMWPE.

Ethylene Oxide. Ethylene Oxide (EtO) sterilization is used routinely to sterilize materials that cannot withstand the high temperatures of autoclaving. The EtO sterilisation procedure involves drawing a vacuum in the sterilisation vessel, after which EtO is injected at a concentration of 600–1,200mg/litre. The sterilizer is maintained at the desired conditions of 30–50°C and 40% to 90% humidity for the duration of sterilisation, usually between two to eight hours. The critical parameters of the cycle are temperature, pressure, humidity, EtO concentration and gas dwell time. Following the sterilisation cycle, the chamber is then evacuated several times to remove residual EtO. Further aeration is usually required after removal from the chamber, with aeration time ranging from two hours to two weeks, depending on the device and packaging. [3] EtO is the most widely used industrial sterilant for medical devices today. Its primary advantages are the low processing temperature and the wide range of compatible materials. Its bactericidal, sporicidal and viricidal effects result from alkylation of sulfhydryl, amino, carboxyl, phenolic and hydroxyl groups in nucleic acids, causing cell injury or death. The main disadvantage of EtO relates to the toxicity and suspected carcinogenicity of the gas and residuals in the product and manufacturing environment. A long aeration process is also required to remove EtO and its by-products from sterilized materials and this can affect inventory requirements.

1.5 Definition of the research task

The role of the research activities described in this dissertation is investigating cold plasma discharges as a novel method for decontaminating surfaces. The goal is to pioneer a highly effective decontamination procedure that avoids the damage of the decontaminated thermo labile substrates associated with existing techniques. This work is especially relevant for the inactivation of the infectious proteins known as "prions" (PrP) [22].

Contamination with biomolecules and toxins is one of the biggest hygienic problems facing medical personnel [23,24,25]. Some of the most difficult contaminations to deal

with, such as the "prion" protein that are the transmissible agents of neurodegenerative diseases (like the Creutzfeld-Jakob disease in humans, more commonly known as "mad cow" disease [26,27]), are resistant to heat and other traditional disinfecting procedures [28,29,30,31,32,33,34,35,36,37]. In some cases the treatment needed to deal with these contaminants can cause major damage to the solid materials, such us surgical instruments or the living tissues that are being treated. The unique advantage of plasma discharges is that they are relatively harmless to sensitive substrate materials. Effects of interaction between plasma and bio-materials are studied in order to increase knowledge about processes of biomolecules destruction.

1.6 Plasma decontamination research overview

Research performed in recent years in the field of plasma sterilization uses plasmas ranging widely different operating pressures (from high vacuum to atmospherics pressure), electromagnetic power coupling mechanism to ignite the discharge (inductive or microwave in vacuum, dielectric barrier or plasma jet at atmospheric pressure) or position of the treated object with respect to the plasma (ionization or recombination plasma region). Many research groups focus on non-thermal plasmas in order to achieve low processing gas temperature and maintain the integrity of thermo labile materials. Special care is taken in order to limit the operating gas mixture to non-toxic gaseous components (argon, oxygen, nitrogen, hydrogen, helium are among the most widely used). The main task in several published works is first to prove and then to increase the efficiency (e.g. reduce the treatment time) of a specific plasma treatment setup. Moreover methods to control the material characteristic's plasma induced modifications has been investigated in more recent times. Lately interest appears also concerning the understanding of the basic physical mechanism governing the interaction between plasma fluxes and microorganisms or biomolecules.

Hereafter a short synthesis of relevant peer reviewed publications in the field of plasma sterilization/decontamination is presented. Atmospheric and low pressure plasma reactors are treated separately.

1.6.1 Atmospheric Pressure Discharges.

At atmospheric pressure dielectric barrier discharge (DBD) [38,39,40,41], resistive barrier discharge (RBD) [42, 43, 44], cascaded dielectric barrier discharge (CDBD) [45] or corona plasma discharge (CPD) [46, 47] have been applied to plasma sterilization/ decontamination processes. In this class of discharges the samples are in direct contact with the plasma ionization region. Other discharge geometries investigated for sterilization purposes are the plasma jet [48] or the plasma plume [49] which have a compact setup and are intended for living tissue plasma treatment. For bacterial 6-Log reduction treatments, depending on the discharge (gas mixture, power and setup) and the type of microorganism and substrate, treatment time varies from seconds to minutes. [46,49] The mechanisms responsible for microorganism death and biomaterial removal at atmospheric pressure are still discussed in literature. In atmospheric discharges with oxygen it seems that reactive oxidative species like atomic oxygen and ozone play a significant role. In the presence of hydrogen and oxygen the hydroxyl-radical OH also reacts with biological surfaces. The role of UV photons in atmospheric plasma is controversially discussed [52] as opposed to low pressure processes, where radiation with a wavelength below 300nm is known to play an important role [50,51].

1.6.2 Low Pressure Discharges.

In low pressure plasma sterilization/decontamination processes a distinction has to be done between direct (ionization plasma region) and remote treatment (recombination plasma region) of samples.

For the case of remote exposure to a flowing afterglow from microwave plasma many results are presented by Moisan *et al.* [52, 53, 54, 55] and Rossi *et al.* [52]. It is shown that UV radiation plays a key role in the deactivation of spores whereas adding oxygen to the plasma enhances the physical erosion of living spores. Substrate temperature also shows a direct influence on the erosion by oxygen radicals.

Rossi *et al.* [56] show the sterilization feasibility in a low pressure inductively coupled plasma (ICP) reactor with direct samples exposure in the ionization region. Moreau *et al.* [53] give a two- (in the case of a pure argon discharge) and three- (argon with added oxygen discharge) step kinetics for the reduction of *B. atrophaeus* spores. Kylian et al. [57] investigate the sterilization agents of *Geob. stearothermophilus* in a low

pressure ICP discharge with an O_2:N_2 mixture they claim the role of oxygen atoms by erosion as the main sterilization agent in the case of a multilayer structure.

Efficacy of low pressure ICP and MW reactor has bee investigated by Kylian et al. on Bovine Serum Albumine (BSA) protein model contamination, proving the key role of oxygen containing discharge in order to achieve high biomaterials etching rates [58]. Kylian et al. also investigated the selectivity of plasma removal comparing plasma efficacy on different model contaminations ranging from amino-acid homopolymers (Lysine, Arginine, Cisteine) and model proteins (BSA, Ubiquitine, Lisozyme). They found plasma interaction, in terms of etching rates, doesn't change while changing the contaminant material treated. [59]

1.6.3 Basic interactions mechanisms.

The role of chemical sputtering, as a driving biomaterial erosion mechanism, independently of the discharge setup, is the focus of Opretzka *et al*. [60] and Keudell et al [61]. They show how only the simultaneous interactions of chemically reactive radicals and ions leads to biomaterial significant modifications while single fluxes (ions or radicals only) are incapable to induce significant changes in the treated substrates.

References

[1] Wallhauser K H [in German] 1995 *Practice of Sterilization, Disinfection and Preservation*, Thieme Verlag, Stuttgart.

[2] Segen J C 2006 *Concise Dictionary of Modern Medicine,* McGraw-Hill, New York.

[3] Anderson J M, Bevacqua B, Cranin A N, Graham L M, Hoffman A S, Klein M, Kowalski J B, Morrissey R F, Obstbaum S A, Ratner B D, Schoen F J, Sirakian A and Whittlesey D 1996 *Implants and Devices, in Biomaterials Science* (Eds. Ratner B D, Hoffman A S, Schoen F J and Lemons J E), Academic Press, London.

[4] Lerouge S, Guignot C, Tabrizian M, Ferrier D, Yagoubi N and Yahia L 2000 *J. Biomed. Mater. Res.*, **52**(4) pp. 774–82.

[5] Nair P D 1995 *J. Biomater. Appl.*, **10**(2) pp. 121–35.

[6] Mazzu A L and Smith C P 1984 *J. Biomed. Mater. Res.*, **18**(8), pp. 961–8.

[7] Shintani H and Nakamura A 1989 *J. Anal. Toxicol.*, **13**(6), pp. 354–7.

[8] Lelah M D and Cooper S L 1986, *Polyurethanes in Medicine*, CRC Press, Boca Raton, Florida.

[9] Booth A F 1999 *Sterilization of medical devices*, Buffalo Grove, Illinois, Interpharm Press.

[10] Terheyden H, Lee U, Ludwig K, Kreusch T and Hedderich J 2000 *Br. J. Oral Maxillofac. Surg.*, **38**(4), pp. 299–304.

[11] Zhang Y Z, Bjursten L M, Freij-Larsson C, Kober M and Wesslen B, 1996 *Biomaterials*, **17**(23), pp. 2265–72.

[12] Sturdevant M, 1991 *Plastics Engineering*, **47**(1), pp. 27–32.

[13] Hermanson N J and Steffen J F 1993, *Antec. 93 Conference Proceedings*.

[14] Abraham G A, Frontini P M and Cuadrado T R 1997 *J Appl Polym Sci*, **65**(6), pp. 1193–1203

[15] Deng M and Shalaby S W 1995 *J Appl Polym Sci*, **58**(11), pp. 2111–2119.

[16] Moisan M, Barbeau J, Crevier M C, Jacques Pelletier J, Philip N and Saoudi B 2002 *Pure Appl. Chem.,* **74**, pp. 349-358.

[17] Bong P, Park J, D.H. Lee D H, and Park J C 2003 *Phys. of Plasmas*, **10**, pp. 4539-44.

[18] Hooper K A, Cox J D and Kohn J 1997 *Journal of Applied Polymer Science*, **63**(11) pp. 1499–1510.

[19] Ries M D, Weaver K, Rose R M, Gunther J, Sauer W and Beals N 1996 *Clinical Orthopaedics and Related Research*, **333**, pp. 87–95.

[20] Goldman M, Gronsky R and Pruitt L 1998 *Journal of Materials Science – Materials in Medicine*, **9**(4), pp. 207–212.

[21] Hirata N, Matsumoto K I, Inishita T, Takenaka Y, Suma Y and Shintani H 1995 *Radiation Physics and Chemistry*, **46**(3), pp. 377–381.

[22] Darbord J C 1999 *Biomed. Pharmacother*., **53**, pp. 34-38.

[23] Baxter R L, Baxter H C, Campbell G A, Grant K, Jones A, Richardson P and Wittacker G 2006 *Journal of Hospital infection*, **63**(4), p. 439-44.

[24] Pratt R J, Yellow C and Loveday H P 2001 *Journal of Hospital Infection,* **47**, pp.S3-S82.

[25] Williams D 2003 *Medical Devices Technology*, **14**, pp. 8-11.

[26] Brown P and Abee C R 2005 *ILAR journal*, **46**, pp. 44-52.

[27] Aguzzi A 2006 *Journal of neurochemistry*, **97**, p. 1726-39.

[28] Lemmer K, Miele M, Pauli G and Beekes M 2004 *Journal of general Virology*, **85**, pp. 3805-16.

[29] Brown P, Prece M and Brandel J P 2000 Neurology, **55**, pp. 1075-81

[30] Dean M 2002 *Lancet*, **360**(9344), p. 1485.

[31] Sehulster L M 2004 *Infect. Control. Hosp. Epidemiology*, **25**, pp. 276-279.

[32] Taylor D M 2006 *Journal of Hospital infection*, **43**, pp. S69-S76.

[33] Taylor D M 2004 *Contrib. Microbiol.*, **11**, pp.136-145.

[34] Zobeley E, Flechsig E and Cozzio A 2001 *Mol. Med.*, **5**, pp. 240-243.

[35] Flechsig E, Hegyi I and Enari M, *Mol. Med.*, **7**, pp. 679-684.

[36] Yang Z X, Stitz L and Heeg P 2004 *Infect. Control. Hosp. Epidemiology*, **25**, p. 280-283, (2004).

[37] Baxter H C, Campbell G A and Whittacker A G 2005 *Journal of general virology*, **86**, pp. 2393-99.

[38] Laroussi M, Sayler G S, Glascock B B, McCurdy B, Pearce M E, Bright N G, and Malott C M 1999 *IEEE Transactions on Plasma Science*, **27**, pp. 34–35.

[39] Laroussi M, Alexeff I and Kang W L 2000 *IEEE Transactions on Plasma Science*, **28** pp. 184–188.

[40] Laroussi M 2002 *IEEE Transactions on Plasma Science,* **30**, pp. 1409–15.

[41] Boudam M K, Moisan M, Saoudi B, Popovici C, Gherardi N and Massines F 2006 *Journal of Physics D: Applied Physics*, **39**, pp. 3494–3507.

[42] Thiyagarajan M, Alexeff I, Parameswaran S and Beebe S. 2005 *IEEE Transactions on Plasma Science*, **33**, pp. 322–23.

[43] Laroussi M, Richardson J P and Dobbs F C 2002 *Applied Physics Letters*, **81**, pp. 772–74.

[44] Laroussi M, Alexeff I, Richardson J P and Dyer F F 2002 *IEEE Transactions on Plasma Science*, **30**, pp. 158–159.

[45] Heise M, Neff W, Franken O, Muranyi P and Wunderlich P 2004 *Plasmas and Polymers*, **9**, pp. 23–33.

[46] Birmingham J G 2004 *IEEE Transactions on Plasma Science* **32** pp. 1526–31.

[47] Menashi W P 1968 U.S. Patent 3 383 163.

[48] Herrmann H W, Henins I, Park J, Selwyn G S 1999 *Phys. Plasmas*, **6**, pp. 2284–89.

[49] Laroussi M, Lu X. 2005 *Applied Physics Letters*, **87**, pp. 1139021-3.

[50] Lerouge S, Fozza A, Wertheimer M R, Marchland R, Yahia L. 2000 *Plasmas and Polymers*, **5**, pp. 31-46.

[51] Rossi F, De Mitri R, Bobin S and Eloy R 2005 *Plasma sterilisation: mechanisms overview and influence of discharge parameters* (Eds. D'Agostino R, Favia P, Oehr C, Wertheimer) Wiley, Ch. 24.

[52] Moreau S, Moisan M, Tabrizian M, Barbeau J and Pelletier J. 2000 *Journal of Applied Physics*, **88**, pp. 1166–74.

[53] Moisan M, Barbeau J, Moreau S, Pelletier J, Tabrizian M and Yahia Y 2001 *Int. J. of Pharmaceutics,* **226**, pp. 1–21.

[54] Moisan M, Barbeau J, Crevier M C, Pelletier J, Philip N and Saoudi B 2002 *Pure Applied Chemistry,* **74**, pp. 349–58.

[55] Philip N, Saoudi B, Crevier M C, Moisan M, Barbeau J and Pelletier J 2002 *IEEE Trans. on Plasma Science,* **30**, pp. 1429-36.

[56] Rossi F, Kylian O and Hasiwa M 2006 *Plasma Processes and Polymers*, **3**, pp. 431–42.

[57] Kylian O, Sasaki T and Rossi F 2006 *Eur. Phys. J. Appl. Phys*., **34**, pp. 139–42.

[58] Kylian O, Rauscher H, Gilliland D, Bretagnol F and Rossi F 2008 *J. Phys. D: Appl. Phys.,* **41**, 095201-9.

[59] Kylian O, Rauscher H, Denis B, Ceriotti L, Rossi F 2009 *Plasma Process. Polym.,* **6**, pp. 848–854

[60] Opretzka J, Benedikt J, Awakowicz P, Wunderlich J and Keudell A. 2007 *Journal of Physics D: Applied Physics*, **40**, pp. 2826–30.

[61] Keudell A, Awakowicz P, Benedikt J, Raballand V, Yanguas-Gil A, Opretzka J, Floetgen C, Reuter R, Byelykh L, Halfmann H, Stapelmann K, Denis B, Wunderlich J, Muranyi P, Rossi F, Kylian O, Hasiwa M, Ruiz A, Rauscher H, Sirghi L, Comoy E, Dehen C, Challier L and Deslys J P 2010 *Plasma Processes and Polymers*, **7**, pp. 327–352.

2 Reactor and Diagnostics

2.1 Brief history of inductively coupled plasma reactors

The first inductively coupled plasma (ICP) was produced in 1884 by J.H. Hittorf by discharging a Leyden jar through a coil surrounding a glass chamber [1,2]. At the end of the 19th century, the development of alternating current (AC) sources allowed the stationary generation of ICP discharges.

The electrodeless mechanism that sustains ICP generation was disputed until 1929 when McKinnen showed that these discharges were usually capacitively sustained by power coupling between the low- and high-voltage ends of the coil. He believed that only at high applied powers and erroneously at high gas pressures the plasma was inductively coupled to the coil [3]. Mainly due to higher power costs, capacitively coupled plasmas (CCPs) and microwaves were used in place of ICPs for electrodeless discharge technology.

As an initial application in 1961, T.B. Reed proposed an ICP [4,5,6] for atomic emission spectroscopy (AES). In AES, inorganic materials are dissociated using a gaseous discharge. The plasma emissions determine qualitatively the elemental composition of the sample. Direct current plasma (DCP) discharges were used before 1964, when Greenfield S. et. al. [7] and then Wendt R.H. and Fassel V.A. [8] performed AES using an ICP. The new ICP-AES method was more accurate than the DCP-AES, because impurities from sputtering the walls and electrodes were reduced. ICP-AES has been available commercially since the middle of 1970s [9], and was the most expensive AES technique at the time.

In 1973, the IBM Corporation experimented ICPs for semiconductor manufacturing. Early studies were performed on ICP-assisted silicon oxidation for the thin-film transistor's (TFT) fabrication on glass for flat panel displays [10,11]. They were looking for a low temperature alternative to direct thermal oxidation. A 1 MHz oxygen ICP at about 4 Pa produced similar quality materials then thermal oxidation. This study also contained the very important innovation of using an additional electrode with the ICP source. The

silicon substrate was placed on the electrode, and the energy of coming ions was controlled by DC biasing.

Widespread use of ICPs in industry began at the end of the 1980s after the successful study and commercialization of the helicon discharge [12]. However, this discharge was later developed independently from other ICPs. Because of the unusually high ionization efficiency, the plasma densities achieved in the helicon discharge were almost one order of magnitude higher then in other discharges for comparable gas pressures and input powers. The view that ICPs are inefficient had completely changed. However, normal ICPs operate by capacitive coupling at lower powers and then shift to an inductive coupling mechanism at a threshold transition power. At this threshold, the total power coupling in the plasma has minimum efficiency. To operate a normal ICP efficiently, it needs to be operated at a power lever much higher than the threshold. ICP reactors are therefore only efficient for high-density plasma sources.

Today the ICP discharges are widely used for lighting and technological processes, because of their high charged particle density and their low power losses in the sheath. The inductive power coupling mechanism does not generate a large voltage across the RF sheath, and therefore reduces the interaction of the ions with chamber walls. This reduces chemical reactions on the wall surface, sputtering, and etching in comparison to a CCP. Several contemporary applications of ICPs are presented below.

In 1990s, the DCP-AES was totally replaced by high-density ICP-AES. Increased power costs were compensated by shorter measurement times. This caused a major change in the techniques, methodology, and apparatus used for AES. Today ICP-AES is widely used for the elemental analysis of metallic aerosols and powders, dusts, and fly ashes.

A high-density ICP was also used as an ion source for analytical mass spectrometry (ICP-MS) [13,14]. In ICP-MS, the test sample is typically converted to an aerosol, injected into the plasma and measured by a coupled mass spectrometer.

In 1993, D.P. Myers and G.M. Hieftje combined an ICP with time-of-flight mass spectrometry (ICP-TOF-MS). The TOF-MS acquires data at least two orders of magnitude faster than a quadrupole. The application of ICP-TOF-MS for elemental analysis is reviewed in [15]. Commercial ICP-TOF-MS instruments have been available since 1998.

The plasma-assisted thin-film deposition, etching, surface cleaning, oxidation, and hardening play a crucial role in the multibillion-dollar semiconductor industry. The requirements of this industry continue to spawn a large variety of different ICP source designs. For example, the efficiency of ICPs generated by the internal and external antennas was investigated by several research groups [16,17]. In 1995, an ICP source with a neutral magnetic loop inside the plasma cell was developed [18]. The presence of magnetic field gradients inside the vacuum chamber increases the power coupling efficiency at low pressures. The etching rate of the neutral loop discharge (NLD) was several times higher than a conventional ICP for otherwise identical conditions. A number of particular improvements for ICP sources can also be found in the literature, and ICP generation is now available for powers as low as several Watts and at gas pressures below 0.1 Pa.

Up until 1990, almost all ICPs had a cylindrical, barrel-like geometry with the antenna wrapped around the diameter. This monopoly ended with the introduction of planar antennas [19]. These new discharges had reduced plasma losses, better power coupling, and were more uniform for flat surfaces. Since silicon wafers are flat, planar ICPs were immediately applied in the microelectronics industry.

It is interesting that early research in using ICPs for spectral chemistry did not vary the geometry from the original 1884 design. Designers varied the cell dimension, the gas composition, the power, and the pressure; but it was always a cylindrical coil surrounding the reactor vessel. For ICP lamps, cylindrical antennas placed within re-entrant cavities have been used since 1936 [20]. Most innovations in ICP design have been for materials processing. It seems as though this is the most flexible, complicated, and progressive application for ICPs, and an area where many technological requirements still need to be satisfied.

2.2 ICPs fundamentals

Since the discovery of RF discharges, a broad variety of experimental data and theoretical facts about this phenomenon have been collected. Today this allows a detailed interpretation of the physical processes occurring in RF plasmas. Of course, all of this material cannot be reviewed in the framework of this dissertation. In this paragraph, the

underlying physical principles of ICP plasma sources operated at low pressures, p < 100 Pa are briefly considered.

Radio frequency gas discharge plasmas are produced when the electromagnetic energy released in a certain discharge volume is sufficient to ionize the gas and maintain the density of charged particles. RF discharges are excited by applying an oscillating electromagnetic field across a discharge gap. Under regulations set up by the International Telecommunication Agreements (ITA) and the Industrial, Scientific and Medical use (ISM), the standard frequency that should be used in commercial RF generators is f_{RF} = 13.56 MHz and its higher harmonics. Systems using non ITA/ISM frequencies must be fully shielded to emissions to ensure that they will not interfere with communications equipment. However, also nonstandard frequencies below this limiting frequency are used [21].

In a qualitative sense, we can define two operating regimes for RF discharges which are distinguished by the ratio between the exciting-field frequency ω and the electron ω_e and the ion ω_i plasma frequencies:

$$\omega_e = \sqrt{\frac{n_e e^2}{m_e \varepsilon_0}} \quad , \quad \omega_i = \sqrt{\frac{n_i e^2}{M_i \varepsilon_0}} \qquad [2.1]$$

In a "low-frequency regime", where $\omega << \omega_i << \omega_e$, the motion of all charged particles is governed by electromagnetic-field oscillations. In a "high-frequency regime", where $\omega_i << \omega << \omega_e$, the spatial positions of ions vary only slightly in time.

Breakdown of a neutral gas is an avalanche-like process. The gas always contains a small quantity of free electrons produced by cosmic rays. These primary electrons are accelerated by the applied electric field to high energies and collide with neutrals and walls of the chamber producing more charged particles. This gives rise to an avalanche, resulting in the gas breakdown. The final state of the produced plasma and its parameters are determined by a balance between the input and loss power and a particle balance.

The processes outlined above is based on energy transfer from electrons accelerated in an RF E-field to the background gas, and is an illustration of the dominant role of electron-neutral collisions in a plasma. Therefore, it is named collisional or Ohmic heating. The

electron elastic collision frequency, υ_m, is proportional to the gas density and, at a constant gas temperature, to the gas pressure:

$$\upsilon_m \propto N \propto p \qquad [2.2]$$

Figure 2.1 shows the dependence of the ratio υ_m /p on the electron energy ε_e for hydrogen and argon. In particular, the value of υ_m /p for hydrogen is constant over a wide range of electron energies:

$$\upsilon_m = \alpha \cdot p \text{, where } \alpha = 4.5 \cdot 10^7 \text{ Pa}^{-1}\text{s}^{-1} \qquad [2.3]$$

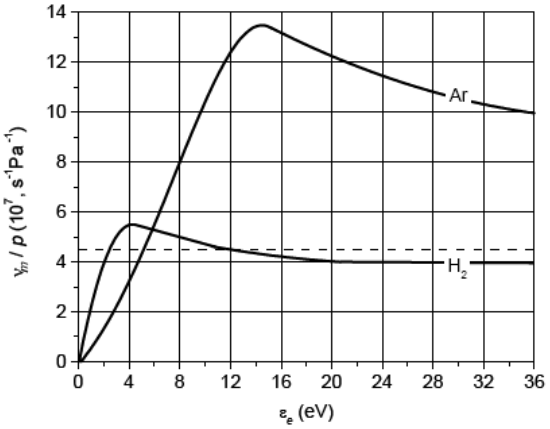

Fig.2.1. Collision frequency versus electron energy for hydrogen and argon gases [22].

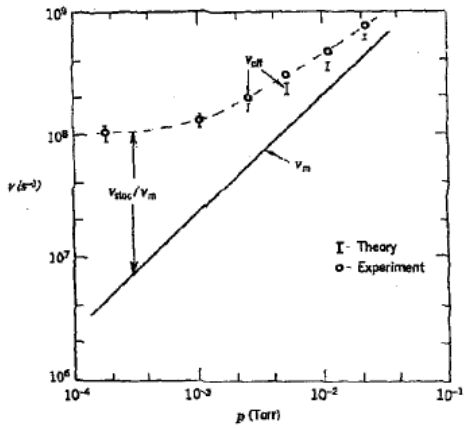

Fig.2.2. Experimental determination of the effective collision frequency in the RF discharge at f_{RF} = 40,8 MHz in mercury [23].

In RF discharges collisionless or stochastic heating is an additional heating mechanism. In order account for stochastic heating, the effective electron collision frequency, v_{eff}, is used instead of the elastic-collision frequency, v_m. Figure 2.2 shows measurements of v_{eff} in an RF discharge at a frequency of f_{RF} = 40.8 MHz in mercury [23], and demonstrates that the stochastic heating is more efficient at low gas pressures.

Theoretical descriptions of the stochastic heating are still been disputed. Two models are encountered in the literature. One model is based on Fermi acceleration, where electrons

gain additional energy due to their reflections from the moving edge of the sheath [24]. The alternative model is based on the effect of repetitive compression and rarefaction of the electron cloud at the sheath edge [25,26,27,28]. The stochastic heating in this case is attributed to pressure variations.

A strategy for RF discharge maintainance is by inductive coupling [29]. An ICP is used for technologies where a low-temperature, dense and uniform plasma is needed. A typical diagram and the equivalent electric circuit of the ICP source are presented in figure 2.3 [30,31].

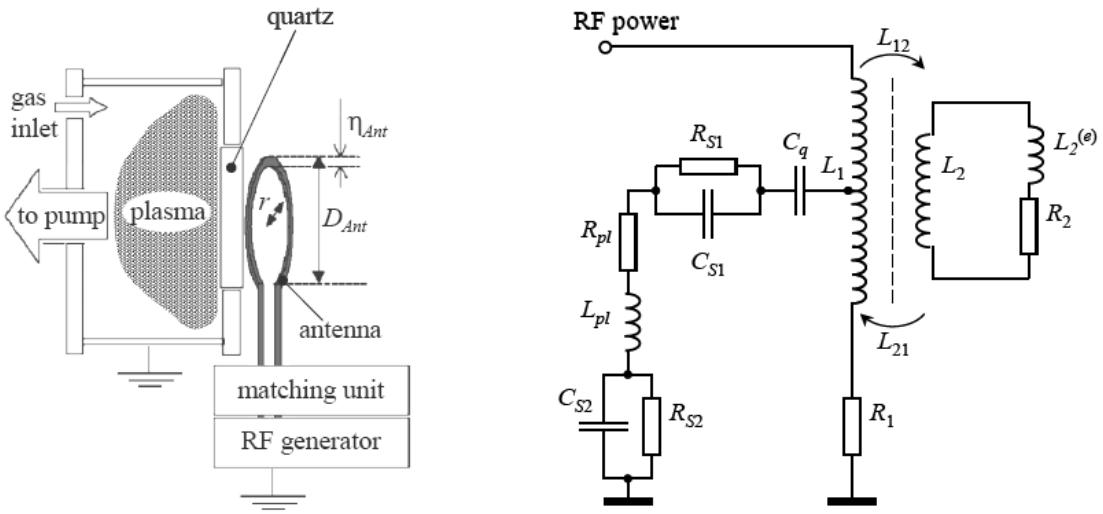

Fig.2.3. Diagram of the ICP cell and the equivalent electric circuit of an antenna-plasma transformer. R_1 and L_1 are the antenna resistance and induction. R_2, L_2 and $L_2^{(e)}$ are the plasma resistance, geometrical plasma inductance and inductance due to inertia of electrons. L_{12} and L_{21} are the interactive inductions between antenna and plasma.

An inductively coupled discharge is a plasma created applying an oscillating, radiofrequency potential to an inductive coil. The oscillating current in the coil generates an RF magnetic flux penetrating the plasma region. Time-varying magnetic flux density induces a solenoidal RF electric field according to Maxwell-Faraday law. Power is coupled to the plasma and the discharge is sustained through the acceleration of free electrons in the induced RF electric field.

Different configurations of reactors are possible:

- Cylindrical geometry in which a spiral antenna is rolled up around a cylindrical quartz glass vacuum tube. Historically this was the first ICP configuration.
- Plane geometry in wich a planar antenna is placed above a flat dielectric window of the vacuum chamber. This configuration is actually widely used in the industry of microelectronics [32,33,34,35].

Some technical solutions of ICP exists with the antenna placed inside the vacuum chamber immersed into the plasma exist. In this case the coil is floating with the plasma potential and it is connected to the tuning circuit by means of two capacities at antenna's ends.

All the possible different geometric configurations of ICP discharges work with respect to the same basic principles, in the following the plane configuration with axial symmetry will be taken as example.

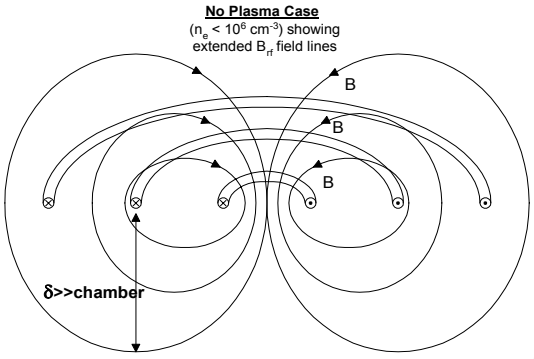

Fig. 2.4) Magnetic field streamlines without plasma in the discharge gap.

Accordingly to the definition given before the RF oscillating current into the antenna induces an electromagnetic field inside the discharge region with components $H_r(r,z)$, $H_Z(r,z)$ and $E_\theta(r,z)$. Here is considered a cylindrical reference system with the z axis perpendicular to the antenna plane, passing through its center and directed from discharge region towards the coil.

If vacuum is considered to fill the discharge gap the fields streamlines can be considered, as a rough approximation (picture 2.4), circular around antenna wirings and symmetrical

with respect to antenna axis, the electric field is azimuthal and parallel to the antenna plane.

More detailed calculations proves that the actual radial and height dependencies of magnetic streamlines are described analytically by an infinite sum of terms containing first type Bessel functions of the zeroth and first order. Leading term approximation of this result describes fields proportional to a single Bessel $J_i(\lambda_1 r)$ with i=0 for magnetic filed and i=1 for electric field argument and λ_1 being the first root of the function itself [36].

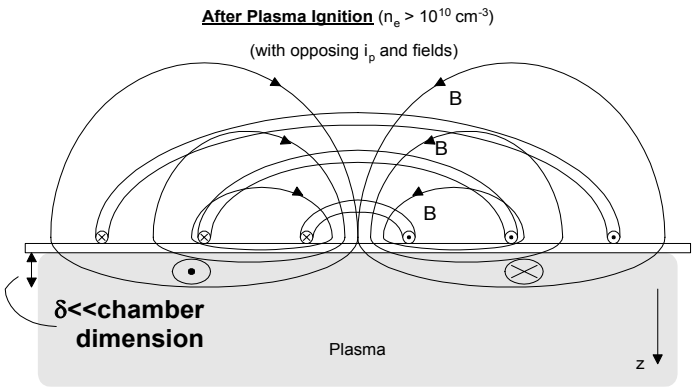

Fig. 2.5) Shielded magnetic and electric fields streamlines with plasma on.

Free electrons in the discharge create an oscillating current parallel to the antenna winding and are thus accelerated on a mean length depending on the gas pressure. It follows that the ions are created by inelastic collisions between these electrons and the gas molecules or atoms. As it was theoretically predicted [37] and then experimentally verified [38], the induced electric field is shielded by dielectric plasma effect and its value decreases exponentially with the distance from the dielectric window (picture 2.5).

The characteristic length for this damping can be derived solving the Maxwell equations system for this configuration and choosing normal modes solution. The damping factor corresponds to the inverse of the imaginary component of the wave number of the normal mode and can be written as the so called “skin depth”:

$$\delta_{SkD} = \left(\frac{2}{\mu_0 \sigma_{pl} \omega_{RF}} \right) \propto \sqrt{\frac{1}{n_e} \frac{\upsilon_m}{\omega_{RF}}} \qquad [2.4]$$

where in the second form principal scaling are given explicitly in terms of basic plasma properties, the screening is more efficient when many particles built up an appropriate volume charge density, the second multiplicative term accounts for collisions effect. In the approximation of collisionless plasma ($\nu_m < \omega_{RF}$) only the imaginary part of the plasma conductivity is important and an approximate equation can be written as:

$$\delta_{SkD} \cong \frac{c}{\omega_{pe}} \qquad [2.5]$$

In the collisional case this depth is multiplied by the real part of the plasma conductivity taking in account that the effective collisional momentum transfer frequency is composed by the sum of three collision frequency, electron-neutrals, electron ions and stochastic:

$$\upsilon_{eff} = \upsilon_{en} + \upsilon_{ei} + \upsilon_{st} \qquad [2.6]$$

the letter is given by the interaction of electrons traversing the sheath with the averaged electric field, this actually collisionless electron heating mechanism is important only at low pressures (p < 10mTorr) [39].

2.3 Biodecon-ICP reactor

Biodecon-ICP (Figure 2.6) is a reactor designed for basic studies on plasma processing, it is laboratory scale and it allows plasma monitoring by several different diagnostics.

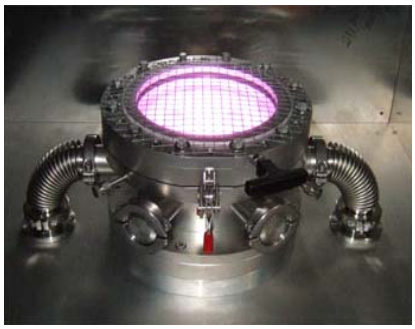

Fig. 2.6) Biodecon reactor

Specifically biodecon-ICP is a double coil planar plasma reactor, fully computer controlled, that allows plasma discharges to be ignited with powers up to 600 W allowing pulsed power delivery operation with frequencies ranging from 1 Hz to several tenth of kHz, the working pressure range from 1 to 30 Pa and gas flows from 1 to 50 sccm with different gases mixtures

comprising Argon, Nitrogen, Oxygen, Hydrogen and water vapor. The reaction chamber (5 L volume) is evacuated by a mechanical pump backed by a turbomolecular (Varian milliTorr L50) pumping system down to a minimum pre-vacuum pressure of $1 \cdot 10^{-3}$ Pa. The vacuum chamber is fed by a gas inlet system composed of MKS flow controllers. The scheme of the plasma reactor components is depicted in figure 2.7, the components marked in red are computer controlled.

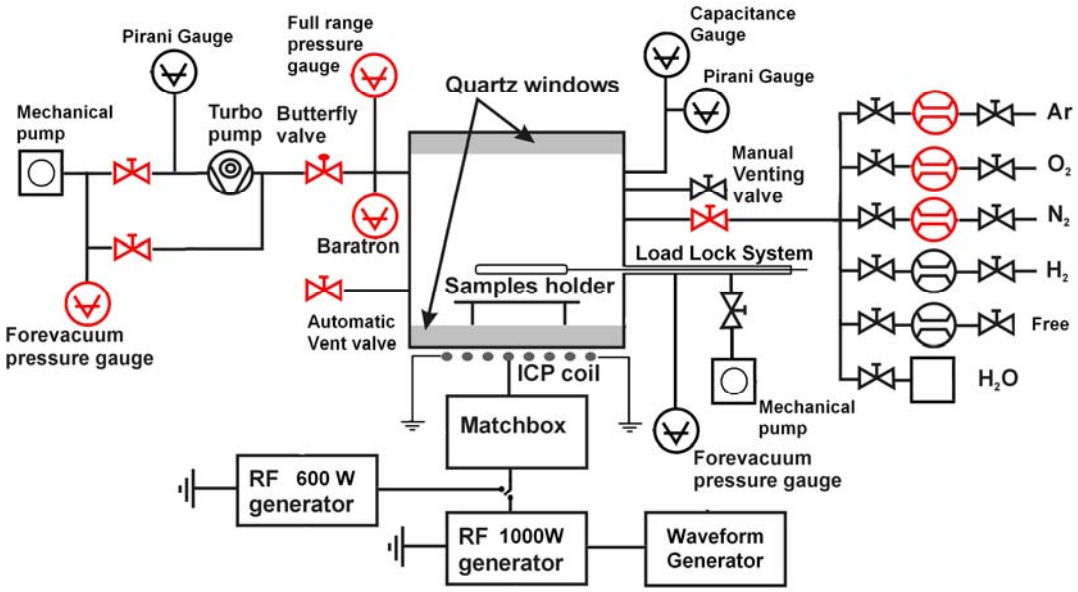

Fig. 2.7) Schematics of Biodecon-ICP reactor equipment.

The picture shows the actual configuration of the reactor, with respect to the former (2008) configuration, during this PhD work the following modifications have been implemented:

- ✓ New AE matching box, enables automatic match operations with almost all the gas mixtures in use.
- ✓ New power stage with 1000W RF power at 13.56 MHz, the new generator can be piloted by an external waveform generator with a TTL logic signal, trigger signals can be used to synchronize plasma diagnostics for time resolved measurements.
- ✓ Pressure controllers enable to monitor the base pressure
- ✓ New hydrogen gas line, MFC 100 sccm
- ✓ New kripton gas line, MFC 100 sccm

- ✓ Water vapor dry vacuum tank, actual flow is controlled Liquiflow MKS controller.
- ✓ New principal pumping system (both turbo pump and rotary pump were changed)
- ✓ A load-lock system for quick samples insertion without braking the vacuum has been installed (independent pumping system and pressure control)

2.4 Direct discharge ignition into H-mode.

In order to assure repeatability and uniformity of plasma treatment is important to obtain direct ignition of the plasma discharge in the inductive mode at the selected combination of treatment parameters (power, pressure, gas flow and gas mixture). This is particularly important when the discharge is operated in pulse mode. Due to the narrowness of the stable operative matching box electrical point for direct plasma ignition without reflection of power, the automatic RF generator feature cannot be used and the tuning must be found manually.

As explained in paragraph 2.2 in an inductive discharge, the RF power is coupled to the plasma by an electromagnetic interaction with the current flowing into the coil. The inductive electric field is non-propagating and penetrates into the plasma over a distance of the plasma skin depth δ. When the RF generator is switched on and the antenna is excited through a matching circuit the voltage across the exciting coil can be as high as several kilovolts, so that a capacitive current can also be driven into the discharge through the dielectric window, providing a second power deposition mechanism. While both power coupling mechanism normally coexist in an inductive discharge, it is now widely recognized that they represent two distinct modes of the discharge operation.

As the excitation RF power (or antenna current) is increased from zero in electrodeless plasmas, the gas first breaks down into a capacitively coupled plasma or E-mode. This is characterized by low electron density ($10^{10} – 10^{12}$ cm^{-3}) and a faint glow localized near the coil. Above a certain threshold current, the discharge switches abruptly to an H-mode where inductive power deposition dominates. In this mode the plasma density is high ($10^{10} – 10^{12}$ cm^{-3}) resulting in a much brighter glow. By looking at the plasma brightness

by means of optical emission spectroscopy techniques it is thus, in general, possible to determine whether the plasma is operating in E- or H-mode.

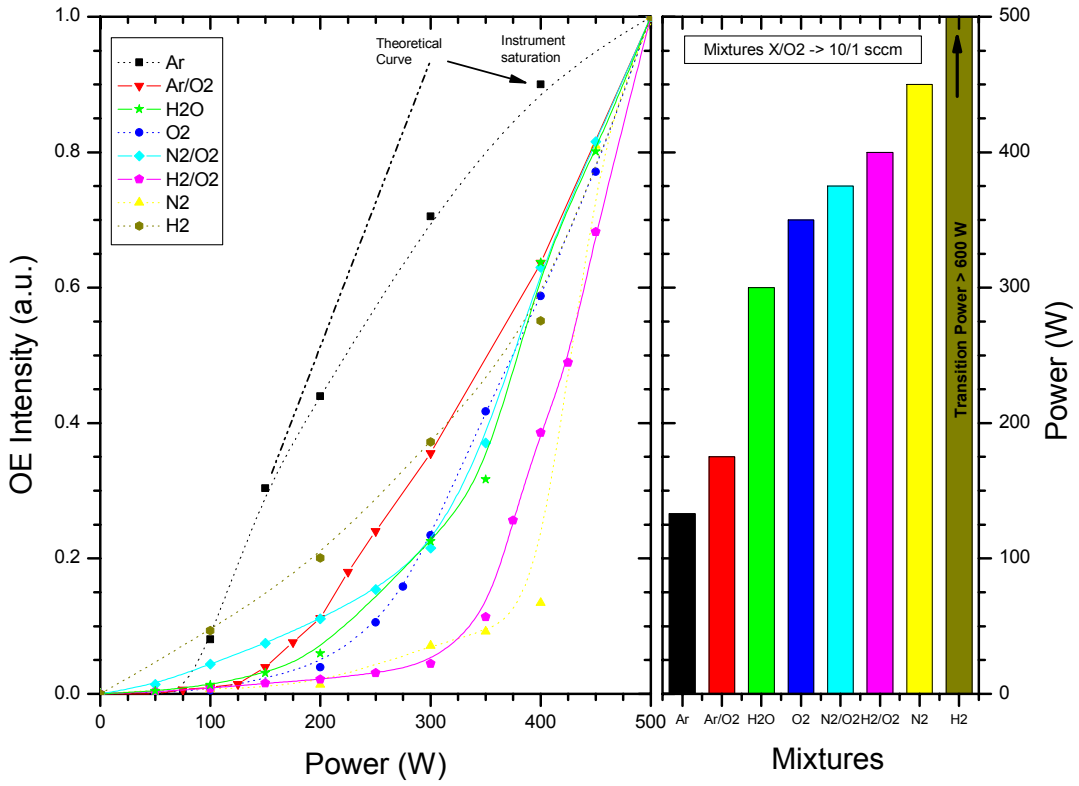

Fig.2.8 Left panel. Optical emission intensities of selected atomic emission lines as a function for delivered RF power for different gas mixtures. Right panel. Extrapolated E to H transition power for different gas mixture composition.

In figure 2.8 is shown the optical emission intensity as a function of the delivered RF power from different ICP discharges operated with various gases (Ar, O_2, N_2, H_2, water vapor and some oxygen containing gas mixtures). With increasing power the intensity of the plasma optical emission increases with a clear jump in the first derivative at certain power values depending on the gas composition, this discontinuity is identified with the transition of the discharges between E and H modes. Since different emission lines exhibit different relative changes in the emission intensity, indicating a complex change in the electron density, energy distribution function and degree of dissociation between

modes, for this measure was chosen to acquire the full spectral emission intensity at wavelengths from 200 to 800 nm.

It has been observed that argon and argon containing mixtures exhibit a substantially lower power threshold for the mode transition the other molecular gases containing mixtures. Low power E-mode operation of an ICP discharge has to be avoided, in our application, in order to enhance plasma treatment efficiency.

2.5 In-situ diagnostics

For discharge and plasma process characterization the reactor was coupled with the following diagnostic systems (not shown in the picture 2.7):

In this section, the diagnostics used to study RF plasmas are described: Langmuir probe diagnostic (Subsection 2.5.1), optical emission spectroscopy (Subsection 2.5.2), ion mass and energy analyzers (Subsection 2.5.3), quartz crystal microbalance (Subsection 2.5.4) and infrared pyrometry Subsection 2.5.3).

2.5.1 RF compensated langmuir probe

In order to monitor plasma ion density a movable RF compensated Langmuir probe (SmartProbe, Scientific Systems LTD) was used. Data acquisition was performed at the centre of the discharge chamber and at a vertical distance of 5,5 cm from the quartz glass facing the inductive antenna. This is the same position of the samples inserted in the reactor via the QCM diagnostic flange. Because of the presence of negative ions the analysis of the acquired I/V characteristics was performed with a MatLab^{TM} routine in the framework of the ABR radial motion theory (thin sheath case), modified by the presence of negative ions. [40]

An advantage of Langmuir probe is the simplicity of the measurements, and ability to measure the key plasma characteristics. Probe diagnostics are used extensively in plasma studies, and considered a classical experimental method. The information about the

plasma potential, density, and electron temperature that are obtained by this technique are commonly used as a reference for other types of plasma diagnostics [41,42,43].

In this study, the analysis method invented by Druyvesteyn in 1930 was used [22,44,45,46,47,48,49]. This method calculates the electron energy distribution function (EEDF) from the second derivative of the I-V characteristic of the probe.

The Druyvesteyn method is applicable for I-V characteristics measured in a static sheath. However, an RF sheath has a constant component and a time-varying component that oscillates. When measurements are performed in an IPC discharge, the RF component of the sheath potential should be compensated because the Druyvesteyn theory is unable to account for the oscillations [50,51].

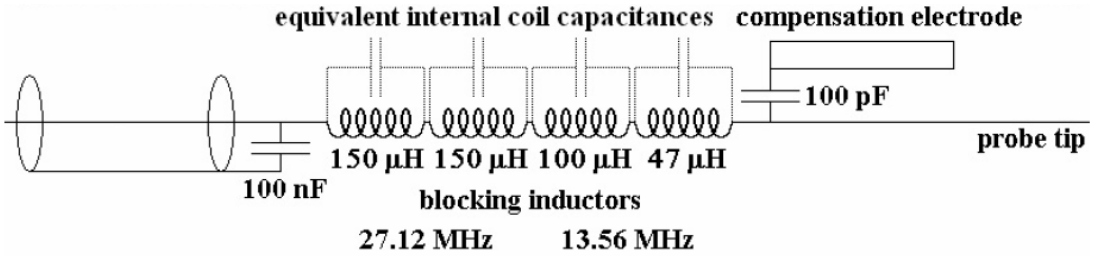

Fig.2.9. Langmuir probe with passive compensation of the RF component of sheath potential**.**

An example of RF compensation is shown in figure 2.9. In comparison to a standard Langmuir probe, a probe with passive RF compensation has an additional electrode. This electrode is large, and connected with a probe tip through a capacitor. Therefore, the electrode potential will be near the RF floating potential. The probe tip is connected to the power supply through an electrical filter to suppress the RF frequency. During measurement, the probe tip is DC biased through the electrical filter and RF biased by the additional electrode. The probe tip's RF biasing is effective due to the high impedance of the filter. The RF component of the voltage drop across the probe's sheath is suppressed by the RF biasing signal [52,53]. In active compensation, the RF component of the sheath potential is suppressed in a similar fashion, except that the RF biasing signal is generated by the probe power supply. The wave form of the biasing signal can either be independently synthesized or be an amplification the signal from small additional

electrode. For proper compensation, it is critical that the phase of the probe power supply and the RF floating potential of the plasma be synchronized [54].

2.5.2 Optical Emission Spectroscopy

In low-temperature plasmas, light emission is a relaxation of excited states of background species. Since atomic excitation is predominantly obtained by electron impact, the spectral emissions contain information about the portion of electron population with enough energy to cause transition [55] and about the density of the beckground species that are excited from their round or metastables states.

The optical emission spectroscopy measurements described in this dissertation were obtained by means of an Avantes AVS-PC 2000 monochromator, equipped with a 2048-elemnt linear CCD array. The emitting light of the plasma was collected through a silica optical window for analyzing. The lattice parameter is 1200 grooves per millimeter and the spectral range is between 200 and 880 nm, recorded in three channels.

The relative ground state oxygen and hydrogen atoms as well as hydroxyl molecules density was estimated by optical emission actinometry. For costant Ar flow rate and no lines overlapping argon $2p_1 \rightarrow 1s_2$ transition at 750.4 nm was chosen for actinometric measurements. [56] Otherwise Argon spectral line at 750.4 nm, was not used because total argon flow was changed during the experiments, Kr line at 826.3 nm (E_{th}=12,2 eV) emission intensity from the Paschen $2p_2$ level was used to normalize emission intensities of O 844 nm, H 656 nm and OH 309 nm. The dominant mechanism for excitation of the Kr $2p_2$ level is a one step electronic excitation from the ground state and, in addition its energy threshold for this process is (~12 eV), near the respective excitations of O (~11 eV), H (~12 eV) and OH A-X (~10eV).

2.5.3 Mass spectrometer/Residual Gas Analyzer

The neutral atoms composition of plasma discharge during the processing of samples was determined by means of mass spectroscopy measurements (PSM probe, Hiden Analytical Ltd.) operated in residual gas analyzer mode. The instrument was placed on the upper

diagnostics flange. The 50 μm entrance orifice of the mass spectrometer was at distance of 100 mm from the bottom quartz window.

This device is generally used to measure either the ion energy distribution with ions mass being a constant or to measure the ion mass spectra for a constant kinetic energy. The PSM construction scheme includes an ion-optical system, an ion energy filter, and a quadrupole mass analyzer (QMA).

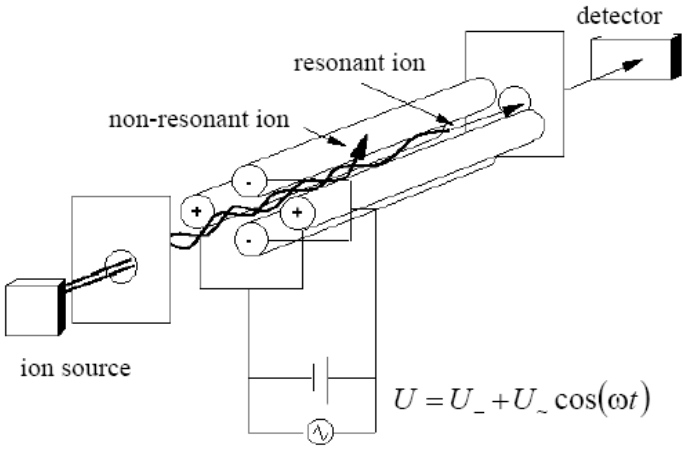

Fig.2.10. Schematic of the quadrupole mass analyzer.

The ion-optical system of the PSM is mounted in the front section of the device. It consists of a small entrance orifice and a system of electrostatic lenses. The entrance orifice is electrically isolated and can be biased positively, biased negatively, or floated. If the bias voltage is lower than the plasma potential, positive ions are extracted from the plasma and enter to the PSM. A system of electrostatic lenses directs these ions into the entrance of the energy filter, and is designed to transmit 100% of ions traveling within a small solid angle around of the device axis. An ionization chamber behind the entrance orifice allows neutrals to be analyzed also.

Operation of the PSM, in which ions are selected depending on the mass-to-charge ratio (M_i/Q), is shown schematically in figure 2.10. The device consists of four parallel metal rods. Two oppositely placed rods are biased positively (U), whereas the other two are biased negatively (-U). Only ions with a fixed mass-to-charge ratio will be able pass through the QMA and measured by the detector. The ion motion trajectory along the axis of the QMA is described by the Mathieu-equations [57].

2.5.4 Infrared pyrometer

Infrared pyrometers are a class of non-contact thermometers that infer temperature using a portion of the thermal radiation emitted by the object of measurement. An IR-pyrometer (Raynger MX4, Raytek) was used to measure the temperature at a spot on the sample surface (actually a small area determined by the distance-to-spot ratio, the DS ratio is the ratio of the distance to the object and the diameter of the temperature measurement area). This kind of device is particularly useful in our experimental situation where the object is surrounded by an electromagnetic field and it is contained in a vacuum chamber.
The sensor has an adjustable emissivity setting, which can be set to measure the temperature of reflective and non-reflective surfaces depending on the composition material.

2.5.5 Quartz crystal microbalance

The quartz crystal microbalance is a commonly used diagnostic in the study and monitoring of deposition and etching processes. The principle of the QCM is based on a quartz crystal resonating at a high frequency (5-30 MHz), which is exposed to a reactive environment. When a molecule adheres or leaves the exposed surface of the crystal, the oscillation frequency of the crystal deviates due to the increase/decrease in mass. A small change in mass during device operation (less than 2% of the total mass of the crystal) is accompanied by a proportional change in the resonant frequency.[58] In optimal conditions the mass density of the chemisorbed species can be calculated with great precision (~0.3 ng cm^{-2}) from the measured frequency shift. Because of its mass sensitivity, the QCM has been used to monitor the mass removal during each separate step of a pulsed plasma treatment. In this fashion insight into the etching mechanism of biofilms can be obtained. In particular, in this work, the QCM has been used to study biofilm etching during plasma-assisted decontamination treatments. A major difference compared to standard QCM apprach proved to be the exposure of the QCM to the plasma environment, in which charged particles are present. A large spike in signal, not related to

the actual plasma-biomaterials interaction process, was observed when the plasma was ignited. It remains unclear if this can be attributed to a temperature increase, an electrical interference, or a combination of both causes. When the plasma was turned off, the QCM signal recovered over a time period of ~10 s after which a correct value of the mass change could be deduced.

In the experiments described in chapter 4 protein film mass removal was monitored by a quartz crystal microbalance (QCM, Inficon). The QCM water cooled crystal holder is mounted to diagnostic flange that holds the sample upright and exposes a circular area of 0.785 cm^2 to plasma particle fluxes. All experiments were performed at a substrate temperature of 303 ± 7 K pulsing the plasma discharge and cooling the QCM crystal. The QCM crystal was monitored on line with an USB oscilloscope (Picoscope2003). The conversion factor between the measured voltage V and the mass of the protein deposit was in this study M/V = 4.36 μg/V.

2.6 Ex-situ surface analysis techniques.

In this section, plasma induced modifications of biofilms were analyzed by means of the following surface analysis techniques: X-ry photoelectron spectroscopy (Subsection 2.6.1), atomic force microscope (Subsection 2.6.2), stylus profilometry (Subsection 2.5.3), and ellipsometry (Subsection 2.6.4).

2.6.1 X-ray Photoelectron Spectroscopy

XPS measurements for protein film surface analysis have been performed with an AXIS ULTRA Spectrometer (KRATOS Analytical, UK). Instrument calibration was performed using a clean pure Au/Cu sample and pure Ag sample (99.99%). Measured values for electron binding energies (BE) were 84 ± 0,02 eV, and 932 ± 0,04 eV. The samples were irradiated with monochromatic AlKα X-rays (hν = 1486,6 eV) using X-ray spot size of 400x700 μm^2 and a take off angle of 90° with respect to the sample surface. The base

pressure of the instrument was better than $1 \cdot 10^{-7}$ Pa and the operating pressure better than 3.3×10^{-6} Pa. An electron flood gun was used to compensate for surface charging and all spectra were corrected by setting hydrocarbon C1s peak to 285.00eV. For each sample, a survey spectrum (0-1150eV), from which the surface chemical compositions without hydrogen were determined, was recorded at pass energy of 160eV. In addition one set of high-resolution spectra as also recorded on each sample.

Sample compositions were obtained from the survey spectra after linear background subtraction and using the RSF (Relative Sensitivity Factors) included in the software derived from Scofield cross-sections.

2.3.2 Atomic Force Microscope

The morphological changes of the protein deposits at the nanometer scale were determined by atomic force microscopy (AFM type Solver P47H, NT-MDT Co. operated in the tapping mode). The AFM measurements were made using silicon AFM probes (NSG11 from NTMDT) with sharp conical tips (nominal tip radius 10 nm and cone angle of 22°) and stiff cantilevers (elasticity constant of 5 $N \cdot m^{-1}$). The scanning speed was around 8 microns per second. The topography images were corrected to compensate for the tilting of the sample surfaces.

2.3.3 Stylus profilometry

Stylus profilometry is a technique that is commonly used to characterize the surface roughness of materials. The technique uses a fine cone-shaped diamond stylus, with a given load, which is drawn across a surface by a precision motion stage. Variation in surface topography cause vertical movement of the stylus that is sensed by a transducer. Although it is clearly a surface contact tool, the low stylus application force typically makes this technique non destructive for many materials. The shape of deposited BSA before and after plasma treatments was investigated by means of Alpha-step $IQ^{(R)}$ (KLA-Tencor) profilometer. In all measurements maximum lateral resolution was 0.4 μm with scan speed of 20 μm/s and sampling rate of 50 Hz. Equivalent force exerted from the stylus tip on the surface corresponded to 27,4 mg.

2.3.6 Ellipsometry

Ellipsometry can be used for non-contact optical characterization of organic layers, including proteins, down to the sub-monolayer. [59] For the acquisition of 2D maps of the ellipsometric D and J angles we employed a variable angle, multi-wavelength imaging ellipsometer (EP3, Nanofilm Surface Analysis GmbH). All measurements were performed in air at room temperature at an angle of incidence of 42º and a field of view of 2000 mm x 2000 mm. A monochromatized Xe-arc lamp was used as light source at 554.3 nm wavelength. A PCSA (Polariser – Compensator – Sample – Analyser) null-ellipsometric procedure is used to obtain 2D maps of the Δ and Ψ angles. [60]

Protein deposits volumes were determined from the ellipsometric parameters maps using standard classical electromagnetic theory in conjunction with a parallel layer model consisting of a silicon/silicon oxide/protein. The analysis of Δ and Ψ maps assumes that the total sample consists of semi-infinite parallel slabs, each a uniform material of homogeneous composition described by a single set of optical constants. The film thickness was determined using values for the substrate and film optical functions obtained by best fit of a set of three different incidence angle measurements.

References.

[1] Eckert H U 1962 *J.Appl.Phys*, **33**(9), pp. 2780-88.

[2] Mattox D M 2003 *The foundation of vacuum coating technology*, William Andrei Publishing, New York.

[3] MacKinnon K A 1929 *Phil. Mag.* **8**, pp. 605-17.

[4] Reed T B 1961 *J.Appl.Phys.*, **32**(5), pp. 821-24.

[5] Reed T B 1961 *J.Appl.Phys.*, **32**(12), pp. 2534-35.

[6] Reed T B 1962 *Int. Sci. Technol.*, **6**, pp. 42-48.

[7] Greenfield S, Jones I L and Berry C T 1964 *Analyst*, **89**, pp. 713-20.

[8] Wendt R H and Fassel V A 1965 *Anal. Chem.*, **37**, pp. 920-22.

[9] Moore G L 1989 *Introduction to ICP-AES*, Analytical Spectroscopy Library New York, **3**.

[10] Pulfrey D L, Hathorn F G M and Young L 1973 *J. Electrochem. Soc.*, **120**(11), pp. 1529-35.

[11] Pulfrey D L and Reche J J H 1974 *Solid State Electron.*, **17**(6), pp. 627-32.

[12] Boswell R W 1970 *Phys. Lett*, **33A** (7), pp. 457-458.

[13] Houk R S, Fassel V A, Flesch G D, Svec H J, Gray A L, and Taylor C E 1980 *Anal. Chem.* **52**, pp. 2283-89.

[14] Montacer A 1998 *Inductively Coupled Plasma MS*, Willey-VCH, New York.

[15] Balcerzak M 2003 *Analytical Science* **19**, pp. 979-989

[16] Lister G G and Cox M 1992 *Plasma Sources Sci. Technol.* **1**, pp. 67-73.

[17] Suzuki K, Nakamura K, Ohkubo H and Sugai H 1998 *Plasma Sources Sci. Technol.* **7**, pp. 13-20.

[18] Tsuboi H, Itoh M, Tanabe M, Hayashi T, Uchida T 1995 *Jpn. J. Appl. Phys.* **34**, pp. 2476-81.

[19] Ogle J S 1990 US patent 4948458.

[20] Bethenod J 1936 US patent 2030957.

[21] Tuszewski M and Tobin J A 1996 *J. Vac. Sci. Technol. A*, **14**(3), pp. 1096-1101.

[22] Raizer Y P 1997 *Gas Discharge Physics*, Springer-Verlag, Berlin.

[23] Popov O A and Godyak V A 1985 *J.Apll.Phys.*, **57**, pp. 53-58.

[24] Lieberman M A and Godyak V A 1995 *IEEE Trans. Plasma Sci.*, 26, pp. 955-86.

[25] Gozadinos G, Turner M M and Vender D 2001 *Phys.Rev.Lett.*, **87**(13), pp.135004(4).

[26] Gozadinos G, Vender D, Turner M M and Lieberman M A 2001 *Plasma Sources Sci. Technol.*, **10**(2), pp. 117-124.

[27] Gozadinos G, Vender D, and Turner M M 2002 *Proceeding ESCAMPIG 16/ICRP 5, Grenoble*, **1**, 239.

[28] Turner M M 1993 *Phys. Rev. Lett.* **71**(12), pp. 1844-47

[29] Hopwood J 1992 *Plasma Sources Sci. Technol.,* **1**, pp. 109-116.

[30] Godyak V A, Piejak R B and Alexandrovich B M 1999 *J. Appl. Phys.* **85**(2), pp. 703-12.

[31] Liebermann M A and Lichtenberg A J 1994 *Principles of Plasma Discharges and Materials Processing*, John Wiley & Sons, Inc., New York

[32] Coultas D K and Keller J H 1989 European Patent Application N. EP0379828A2.

[33] Coultas D K and Keller J H 1994 US Patent Application N. 5304279.

[34] Davis M H, Proudfoot G, and Bayliss K H 1989 UK Patent Application N. GB2231197A.

[35] Ogle J S 1990 US Patent N. 4948458.

[36] El-Fayoumi I M and Jones I R 1998 *Plasma Sources Sci. Technol.*, **7**, pp. 162-78.

[37] Thomson J J 1927 *Phil. Mag. Ser.***, 4**(25)**,** pp. 1128-60.

[38] Hopwood J 1992 *Plasma Sources Sci. Technol.* **1**(2)**,** 109-116.

[39] Lee S H and Kim G H 2006 *Journal of Korean Physical Society*, **49**, pp. S726-31.

[40] Riccardi C, Barni R, and Fontanesi M 2001 *J. Appl. Phys.,* **90**(8), pp. 3735-42.

[41] Bowden M D, Kogano M, Suetome Y, Hori T, Uchino K and Muraoka K 1999 *J. Vac. Sci. Technol. A*, **17**(2), pp. 493-99.

[42] Fuller N C M, Malyshev M V, Donnelly V M and Herman I P 2000 Plasma *Sources Sci. Technol.,* **9**, pp. 116-27.

[43] Yoon H J, Chung T H and Seo D C 1999 *Jpn. J. Appl. Phys.,* **38**, pp. 6890-95.

[44] Behringer K and Fantz U 1994 *J. Phys. D: Appl. Phys*., **27**, pp. 2128-35.

[45] Kimura T and Ohe K 1997 *Jpn. J. Appl. Phys.,* **36**, pp. 1274-81.

[46] Kim J S, Rao M V V S, Cappelli M A, Sharma S P and Meyyappan M 2001 *Plasma Sources Sci. Technol.,* **10**, pp. 191-204.

[47] Kortshagen U, Pukropski I and Zethoff M 1994 *J. Appl. Phys.,* **76**(4), pp. 2048-57.

[48] Awakowicz P, Schwefel R, Werder M and Kasper W, *Diamond and Related Materials,* **6**, pp. 1816-23.

[49] Scheubert P, Fantz U, Awakowicz P and Paulin H, *J. Appl. Phys.,* **90**(2), pp. 587-98.

[50] Cohen R H and Rognlien T D 1996 *Plasma Sources Sci. Technol*., **5**, 442-52.

[51] Gagné R R J and Cantin A 1972 *J. Appl. Phys.* **43**(6), 2639-46.

[52] Hopkins M B, Graham W G and Griffin T J 1987 *Rev. Sci. Instrum.* **58**(3), 475-76.

[53] Paranjpe A P, McVittie J P and Self S A 1990 *J. Appl. Phys.* **67**(11), 6718-27.

[54] Flender U, Thi B H N, Wiesemann K, Khromov N A and Kolokolov N B 1996 *Plasma Sources Sci. Technol.* **5**, pp. 61-69.

[55] Turner M M 1996 *Plasma Sources Sci. Technol.* **5**, pp. 159-65.

[56] Coburn J W and Chen M 1980 J. Appl. Phys. **51** 3134-36.

[57] Vega J C G, Cerda S C, Nava A M and Dagnino R M R 2003 *Theory and numerical analysis of the Mathieu functions*, Monterrey NL, Mexico.

[58] Benes E 1984 *J. Appl. Phys.* **56**, 608-26.

[59] Arwin H 2000 *Thin Solid Films*, **377–78** pp. 48–56.

[60] Tompkins H G, Irene E A 2005 *Handbook of ellipsometry*. Springer, Berlin.

3 Plasma discharges characterization

3.1 Oxygen containing plasma discharges efficacy

The experiments described in this section were focused on the evaluation of mechanisms responsible for the removal of BSA proteins from the surfaces exposed to plasma discharge generated by Biodecon ICP plasma source. The removal of proteins residues from surfaces in medical applications began to attract researchers attention in the last years [1,2] and the results presented in this chapter are a summary of initial know-how on decontamination by low pressure plasma discharges. The information presented form the foundation of the research work described in this dissertation. Main understandings of the author former research work are presented in the subsequent paragraph in order to lay down the necessary background information to understand the advanced aspects treated in this PhD. dissertation. Basic investigation of the most efficient plasma treatments parameters set up and interaction mechanisms in an ICP plasma is described extensively by Fumagalli [3] (master thesis) and in several papers by JRC-IHCP group both about plasma sterilization [4,5,6,7,8,9] and plasma decontamination [10,11,12,13,14,15,16,17,18,19].

Non-equilibrium discharges are effective sources of chemically active particles, charged particles, as well as UV photons, which can inactivate, erode or destroy biomolecules at relatively low temperatures desired for the treatment of polymeric materials. These processes has been demonstrated for sterilization of bacterial spores in the works of many authors.[20,21,22] Focus of the work presented in the subsequent text will be determination of the most efficient process parameters for protein contamination removal.

3.1.1 Samples preparation

The method of protein deposition employed for profilometry measurement presented in this work results in a reproducible and spatially well organized structure of BSA on

the substrate surface. This can be seen in the stylus profilometry scan shown in figure 1 and the optical microscopy image of figure 2a, where two distinctly different regions can be distinguished. At the border of the dried droplet a well defined ring is formed with a height of about 1 micrometer and a width of 80 micrometers, whereas in the central region a film with a thickness of less than 100 nm is observed. To assure that the observed pattern reflects the BSA distribution over the surface and is not caused, e.g., by accumulation of salts or airborne impurities at the border of the drying drop, additional tests have been performed using fluorescently labelled BSA (Fluorescein isothiocyanate, Sigma Aldrich), which allows direct visualization of the protein distribution.

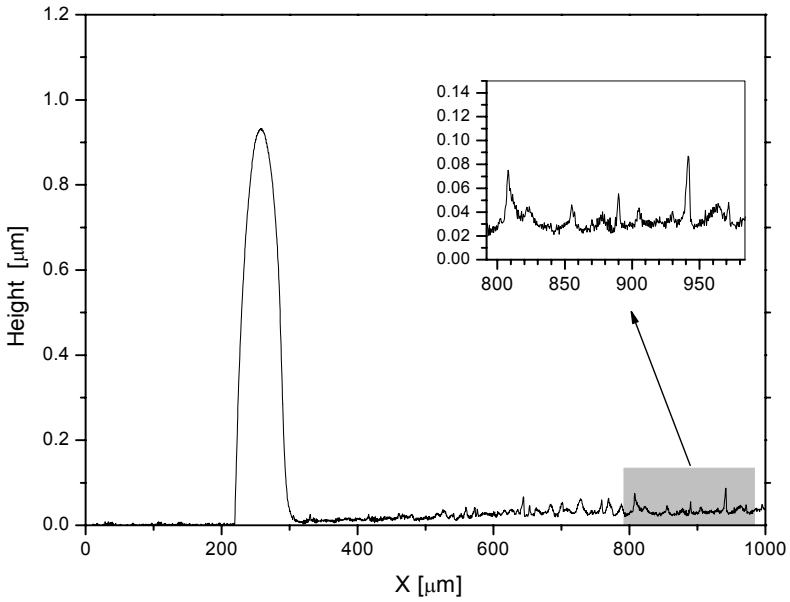

Figure 1. Profilometric scan of the untreated BSA sample. Drop volume 5 μL, spotted on silicon wafer, protein dilution in H_2O 1 mg/ml.

The images obtained by fluorescent optical microscopy (see figure 2b) showed a similar distribution as those observed by optical microscopy and profilometry measurements. Hence, the topography of the observed structure is indeed determined by the distribution of BSA.

The formation of such a “coffee-ring” structure in the deposits allows for a fast and reliable determination of the protein etching rate by measuring, by means of a

profilometer, the height decrease after plasma exposure of the ring structure. This method has been employed every time a profilometric measurement is claimed in the text.

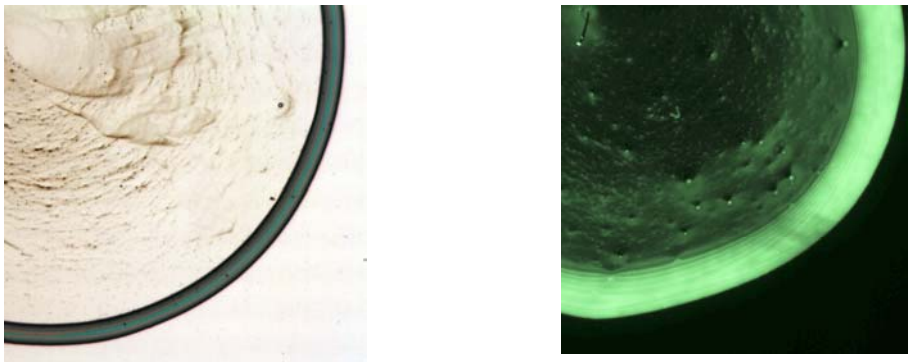

A] B]

Figure 2) Optical (A) and fluorescent (B) microscope images of deposited BSA droplets. Standard drops radius is 1 mm.

3.1.2 Binary mixtures testing

As a first step, estimation of the removal kinetics has been studied employing binary mixtures plasma discharges (argon mixed with oxygen, nitrogen and hydrogen). Samples were treated at different time steps (30 seconds each up to 2 minutes) and reduction of the height of the protein border ring was measured by means of profilometry in order to evaluate the rate of protein removal.

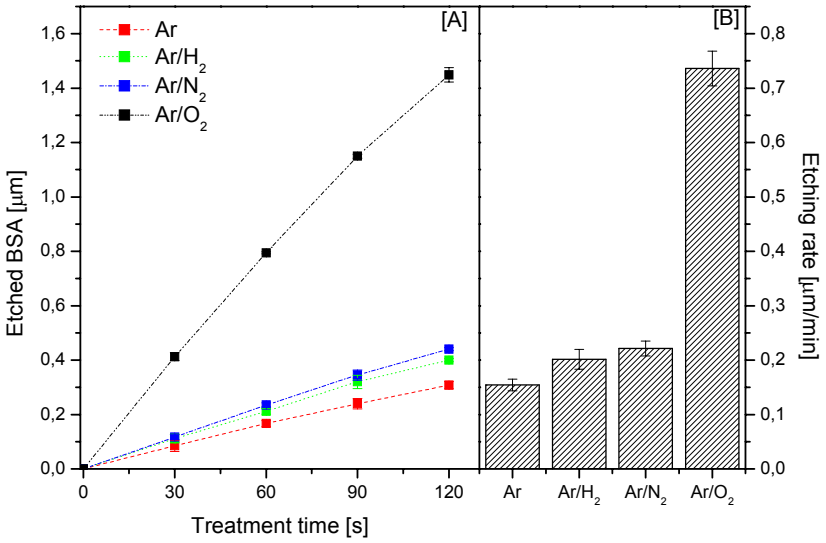

Figure 3. Profilometric measurements of BSA protein film heght decrease as a fucntion of time (a) and etch rates (b) recorded in different discharge binary mixtures. Plasma discharge parameters are: power 300W, pressure 10 Pa and total gas flow 20 sccm.

As it can be seen in figure 3 the fastest protein removal was observed employing oxygen containing discharge. Much slower decrease rate of BSA ring height was observed for pure argon, argon-nitrogen and argon-hydrogen discharges, moreover all this gas mixtures yield similar removal rates thus indicating that the different non oxygen containing plasma-phase chemistries have no important role in the interaction with the protein film. Argon-oxygen plasma instead marks a very different behavior suggesting that plasma species generated by oxygen containing plasma chemistry interacts strongly with the surface. Ar/O_2 plasma etch rate under experimental conditions indicated in figure 3 is found to be approximately 3.5 times higher then in other tested gases.

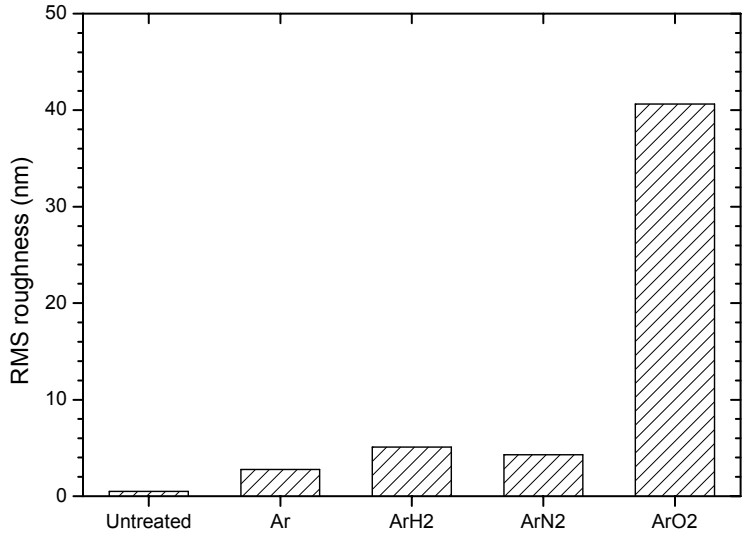

Figure 4. Surface RMS roughness measured from AFM images of protein films before and after different treatment in argon and binary mixtures discharge plasma. Plasma discharge parameters are: treatment time 1 minute, power 300W, pressure 10Pa and total gas flow 20 sccm.

Data analysis on AFM images recorded before and after plasma treatment was performed in order to obtain values for the mean roughness (average value of the small scale height variations measured peak to valley) of the protein films surfaces (see figure 4) treated with different gas mixtures plasmas. Results are also shown in picture 5 in the form of cross sectional profiles of the protein film surface for the untreated case and for 1 minute treatment in different discharges. It can be seen that only oxygen based plasma treatment are enough to induce morphological changes on initially smooth surface of BSA. Plasma treatments performed using pure argon, argon/hydrogen and argon/nitrogen discharge mixtures result only in a moderate increase of the surface roughness. These results shows, on a smaller spatial scale, the same oxygen-containing discharge efficacy behaviour seen in the profilometric measurements described in figure 3.

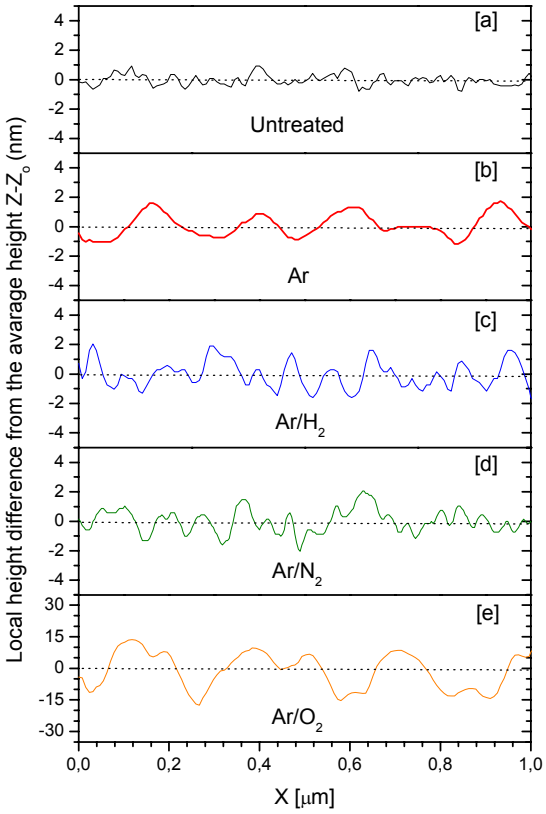

Figure 5. Surface cross sections taken from AFM images of protein films before and after different treatment in argon and binary mixtures discharge plasma. Note change of scale in the lower panel [e] showing the effect of argon-oxygen diascharge. Plasma discharge parameters are: treatment time 1 minute, power 300W, pressure 10 Pa and total gas flow 20 sccm.

3.1.3 Argon-Oxygen plasma characterization

In the gas pressure range typical of ICP applications, several Pascals, these plasmas are weakly ionised non-equilibrium discharges with charged particle densities much smaller than neutrals densities. Electrons in such plasma are not in thermo dynamical equilibrium with atoms and ions, resulting in electron temperature much higher than ions and gas temperature, usually of the order of some electronVolts. Electrons are also usually not in thermo dynamic equilibrium with their own ensemble, thus manifesting a non Maxwellian energy distribution function, so T_e here is an effective electron temperature relating to the electrons averaged energy.

Hereafter (figures 6 and 7) plasma parameters and electron energy distribution functions for argon/oxygen discharge at different mixture composition are shown. Data are derived from measured Langmuir characteristic recorded at the centre of the discharge.

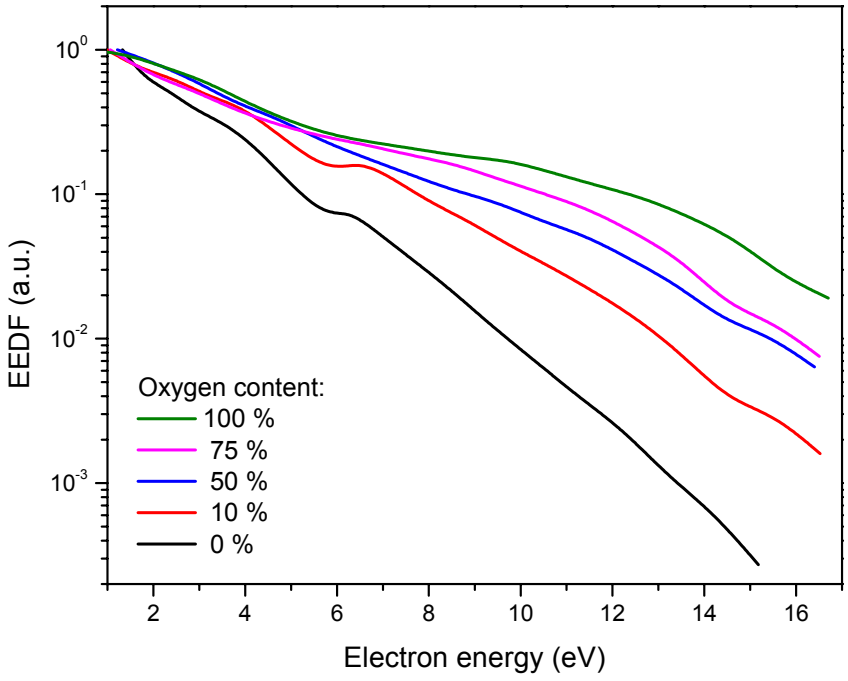

Figure 6. Electron energy distribution functions (EEDF) for different oxygen fractional flow rates in an Ar/O_2 discharge. Plasma parameters: pressure 10 Pa, RF delivered power 350W, total flow rate 20 sccm.

Figure 6 shows the electron energy probability function for Ar/O_2 plasma at 10 Pa and 350 W of delivered power for different oxygen fractional flow rates. All the data

series are normalized and the shapes of the EEDFs at all investigate mixture combinations appears to be clearly non-Maxwellian. The main difference in electron energy distributions, arising when gas mixture composition is modified, appears in the high energy region of the energy distributions. Increasing the oxygen concentration leads to an increasly populated high-energy tail (above 7 eV).

Figure 7 shows the electron temperature Te and the positive ion density n_{ion} versus the oxygen content in O_2/Ar plasma at 10 Pa (20 sccm) at 350W of absorbed power. The calculated electron temperature increase from 1.6 eV as oxygen content is increased, to a plateau around 2.55 eV in a argon-rich mixtures plasma. The onset of the Te plateau region starts when oxygen fractional flow rate has been increased above 25%. The ion density decreases with increased oxygen content. Shifting towards pure argon plasma the ion density approaches to its maximum value. The ion density increases more steeply when oxygen fractional flow rate has been decreased below 25%. By varying the Ar/O_2 ratio from pure oxygen plasma to pure argon plasma the ion density span over more than one order of magnitude ranging from $1 \cdot 10^{10}$ to $1 \cdot 10^{12}$ cm^{-3}.

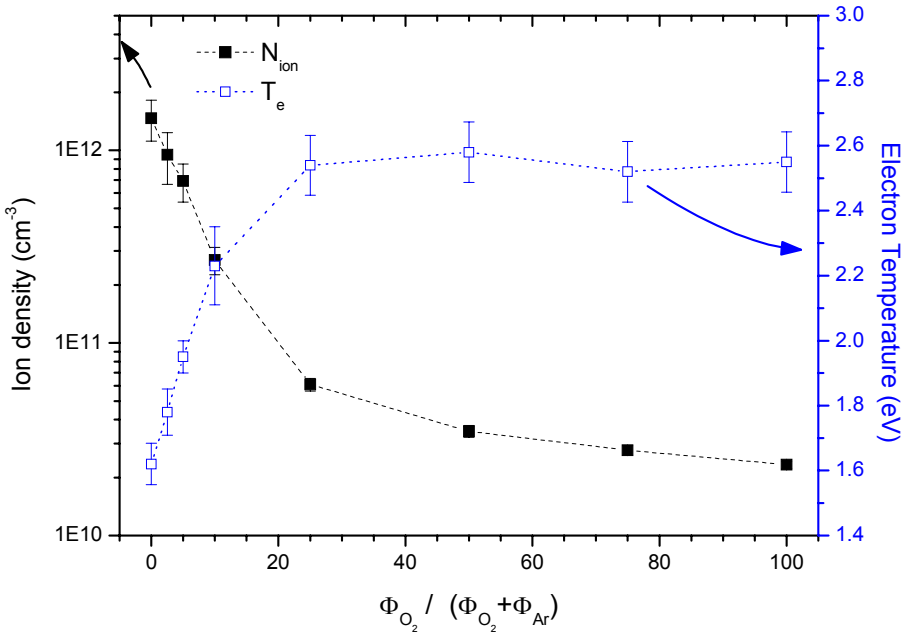

Figure 7. Positive ion density and electron temperature for different oxygen fractional flow rates in an Ar/O_2 discharge. Plasma parameters: pressure 10 Pa, RF delivered power 350W, total flow rate 20 sccm.

The effect of gas mixture variation on plasma density can be understood in terms of power and energy balance in the discharge, zero dimensional models describing energy and particle number conservation equation derivation can be found in literature [23,24,25,26,27]. According to these models plasma density is determined predominantly by power balance. For a stable H-mode discharge to exist the power absorbed by electrons P_{abs} must be identically balance the power dissipated P_{diss} in the discharge processes. If the energy lost per ionization event is considered fixed the power dissipated by the plasma electrons varies linearly with the electron density ne and a simple relationship exists between P_{abs} and n_e [28] given from the combination of particle and power balance expressed in a spatially avareged form for the steady state.

$$N_e = \frac{P_{abs}}{eu_B A_{eff} \varepsilon_{loss}} \qquad [3.1]$$

For a binary mixture formed by an atomic and a molecular species the collisional contribution to the energy loss term can be further divided into the sum of different contributions arising from collisional processes of electrons with different particle species present in the gas phase:

$$\varepsilon_{tot} = \varepsilon_e + \varepsilon_i + \varepsilon_{coll} = \varepsilon_e + \varepsilon_i + \left(\varepsilon_{coll}^{O_2} \cdot R_{O_2} + \varepsilon_{coll}^{O} \cdot R_O + \varepsilon_{coll}^{Ar} \cdot R_{Ar}\right) \qquad [3.2]$$

Where ε_e is the avarage energy of electrons escaping to the walls ($2T_e$), ε_i is the avarage energy lost per ion lost ($V_{sheath}+T_e/2$) and ε_{coll} represent the power loss due to elastic and inelastic collisions per electron-ion pair created, and includes all excitations energies such as vibrational, dissociative and electronic excitations. In the right hand side term of equation 3.2 where the collisional term allows for different neutral species, $\varepsilon_{coll}^{O_2}$ and ε_{coll}^{O} are the collisional energy electron energy loss per ionization event of oxygen molecule and atom respectively, and ε_{coll}^{Ar} is the collisional energy loss per ionization event of argon atom. The terms R_x are the ratio between a given species number density (specified by the subscript x) and the electron number density; they account for the electron collision probability with the different background gas target species.

Considering again the results shown in figure 8 the trend of plasma density measurament as a function of mixture composition can be explained. As the Ar

content in the background gas increases, the term $\left(\varepsilon_{coll}^{O_2} \cdot R_{O_2} + \varepsilon_{coll}^{O} \cdot R_O + \varepsilon_{coll}^{Ar} \cdot R_{Ar}\right)$ decreases because $\varepsilon_{coll}^{O_2}$ and ε_{coll}^{O} are several times larger than ε_{coll}^{Ar} in the average energy range of impacting electrons (1-3 eV) as it was measured by several authors [29,30]. Therefore for a fixed absorbed power N_e increases with increased Ar content and the avarage energy available per electron decreases.

3.1.4 Argon oxygen plasma protein removal efficacy

An important agent that influences the global efficiency of plasma based decontamination of surfaces from biological pathogens is their erosion and volatilization by chemically active species. Although it has been reported that some limited volatilization of biological substances can be attributed to O_2 molecules, [31] the role of the etching agent in Ar/O_2 mixtures can be related to atomic oxygen being much more reactive than O_2. Therefore, we have determined the O atom density as a function of the initial binary mixture composition by optical emission actinometry using the ratio of the Ar line at 750.4 nm (transition 2p1 → 1s2) and the O atom line at a wavelength of 844.6 nm (transition $3p^3P \rightarrow 3s^3S^0$). According to several authors [32,33] this emission line is less influenced from dissociative excitation processes contributions, compared to more intense $3p^5P \rightarrow 3s^5S^0$ transition at 777 nm, and thus is a more reliable indicator for oxygen atoms ground state density in actinometric measurements. As can be seen in figure 8, data referred to the right y-axis, the density of atomic oxygen in the plasma increases with increasing portion of O_2 in the working gas mixture, up to an oxygen content around 7.5% then has a plateau for higher concentrations.

Figure 8 also shows BSA etching rate against the discharge binary mixture composition. This data are plotted as columns and are referred to the left y-axis. Reactive molecular gases (O_2, N_2 and H_2) concentration was increased with respect to background Argon flow until a partial flow of 2 sccm is reached. Maximal efficiency is reached for oxygen contents around 5 %. A higher oxygen concentration leads to a decreasing etching rate. Hydrogen and nitrogen containing discharges show no substantial variation of the BSA etching rates when the gas mixture ratio is varied, moreover the etching rate of N_2 and H_2 containing discharges are not different form pure Argon values, confirming the results shown in figures 3-5, that indicate the poor

efficacy of non oxygen-containing plasma chemistries. Profilmetric measurements were taken over three samples for each data point, on the right and the left part of the protein ring.

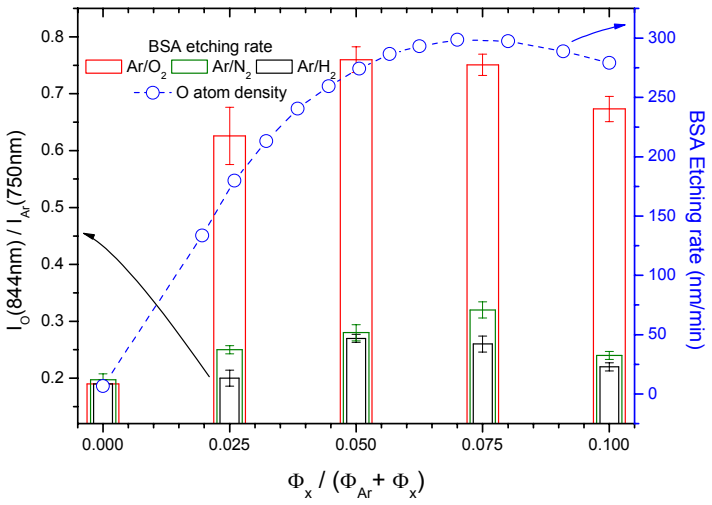

Figure 8. Right x-axis: BSA protein etching rates for different binary mixture flow rate combinations in an Argon containing discharge, as measured by profilometry. Left y-axis: oxygen atom and argon emission intensities ratio for different oxygen fractional flow rates in an Ar/O_2 discharge. Plasma parameters: pressure 10 Pa, RF delivered power 350 W, total flow rate 20 sccm.

As can be seen comparing etching rates and atoms densities plotted in figure 8, the increasing of the removal rate with oxygen addition follows similar trend the O atom density although the proportionality is not perfect. One possible explanation is the possibility of oxygen driven chemical sputtering as leading removal mechanism in the discharge [16]. The simultaneous impact of Ar positive ions, O_2 molecules and O atoms leads to an enhanced protein removal (see also chapter 5). Another hypothesis that agrees with the data in figure 9 is a simple chemical etching process due to the O atoms capability to form volatile compounds (also discussed in chapter 5).

References

[1] Whittaker A G, Graham E M, Baxter R L, Jones A C, Richardson P R, Meek G, Campbell G A, Aitken A and Baxter H C 2004 *Journal of Hospital Infection,* **56**, pp. 37-41.

[2] Baxter H C, Campbell G A, Whittaker A G, Jones A C, Aitken A, Simpson A H, Casey M, Bountiff L, Gibbard L and Baxter R L 2005, *Journal of General Virology,* **86**, pp. 2393-99.

[3] Fumagalli F. 2007 Thesis "*ICP discharge for plasma sterilization*" University of Milano Bicocca.

[4] Kylian O, Sasaki T and Rossi F 2006 *Europhysics Conference Abstract,* **30**(G), pp. 457-58

[5] Rossi F, Kylian O and Hasiwa M 2006 *Plasma processes and polymers* **3**(6-7) pp. 431-42.

[6] Kylian O Hasiwa M and Rossi F 2006 *IEEE Transactions on plasma science,* **34**(6) ,pp. 2606-10.

[7] Kylian O, Hasiwa M and Rossi F 2006 *Plasma processes and Polymers,* **3**(3), pp. 272-75.

[8] Kylian O, Sasaki T and Rossi F 2006 *European Physical Journal – Applied Physics,* **34**(2), pp. 139-42.

[9] Ceccone G, Gilliland D, Kylian O and Westermeier M 2006 *Czechoslovak Journal of Physics,* **56**(B)*,* pp. 672-77.

[10] Stapelmann K, Kylian O, Denis B and Rossi F 2005 *Journal of Physics D – Applied Physics,* **41**, 19 192005(6).

[11] Hasiwa M, Kylian O, Hartung T and Rossi F 2008 *Journal of endotoxins research*, **14**(2), pp. 89-97.

[12] Rossi F, Kylian O, Rauscher H, Gilliland D and Sirghi L *Pure and Applied Chemistry,* **80**(9), pp. 1939-51.

[13] Kylian O Rauscher H Sirghi L and Rossi F 2008 *Journal of Physics Conference Series,* **100**(6), pp. 062017(4).

[14] Kylian O, Rauscher H, Gilliland D, Bretagnol F and Rossi F *Journal of Physics D Applied Physics,* **41,** 095201(8).

[15] Kylian O, Hasiwa M, Gilliland D and Rossi F *Plasma Processes and Polymers,* **5**(1), pp. 26-32

[16] Kylian O, Benedikt J, Sirghi L, Reuter R, Rauscher H, Von Keudell A and Rossi F 2009 *Plasma Processes and Polymers,* **6**(4), pp. 255-61.

[17] Kylian O, Rauscher H, Denis B, Ceriotti L and Rossi F 2009 *Plasma Processes and Polymers,* **6**(12), pp. 848-54.

[18] Rossi F, Kylian O, Rauscher H, Hasiwa M and Gilliland D 2009 *New Journal of Physics,* **11,** 115017(33).

[19] Kyian O and Rossi F 2009 *Journal of Physics D Applied Physics,* **42**(8), pp.1-7.

[20] Moisan M, Barbeau M, Moreau S, Pelletier J, Tabrizian M, Yahia L H 2001 *International Journal of Pharmacology,* **226**(1), pp. 1-21.

[21] Moisan M, Barbeau J, Crevier M C, Pelletier J, Philip N and Saoudi B 2002 *Pure Applied Chemistry,* **74**, pp. 349–58.

[22] Lerouge S, Wertheimer M R and Yahia L H 2001 *Plasma and Polymers* **6**, pp. 175-87.

[23] Monahan D D and Turner M M 2008 *Plasma Sources Sci Technol,* **17,** 045003(10).

[24] Roberson G, Roberto M, Verboncoeur J and Verdonck P 2007 *Brazilian Journal of Physics,* **37**(2A), pp. 457-65.

[25] Lee C, Graves D B Lieberman M A and Hess D W 1994 *J Electrochem Soc,* **141**(6), pp. 1546-55.

[26] Chung T H, Yoon H J and Seo D C 1999 *Journal of Applied Physics,* **86**(7), pp. 3536-42.

[27] Lee C and Lieberman M A 1995 *J Vac Sci Technol A,* **13**(2), pp. 368-80.

[28] Cunge G, Crowley B, Vender D and Turner M M 1999 *Plasma Sources Sci. Technol.,* **8**, pp. 576-86.

[29] Thorsteinsson E G and Gudmundsson J T 2009 *Plasma Sources Sci. Technol.*, **18**, 045001(15) .

[30] Gudmundsson J T, Kimura T and Liebermann M A 1999 *Plasma Sources Sci. Technol.,* **8**, pp. 22-30.

[31] Raballand V, Benedikt J, Wunderlich J and Keudell A 2008 *J. Phys. D: Appl. Phys.,* **41**, 115207(14).

[32] Jasik J, Macko P, Martisovits V, Lukac P and Veis P 2004 *Czechoslovak Journal of Physics,* **54**(6), pp. 661-76.

[33] Katsch H M, Tewes A, Quandt E, Goehilich A, Kawetzki T and Dobele H F 2000 *Journal of Applied Physics,* **88**(11), pp. 6232-38.

3.2 Ar/H2O plasma characterization

Among the different working gas mixtures tested oxygen gas containing binary mixtures have been proven to lead, in general, to fastest etching rates in low pressure systems. Depending to the reactor design Ar/O_2 gas mixture showed best biomaterial removal efficiency in RF discharges [1,2,3,4] while plasmas ignited in the MW range showed highest efficiency with H_2/O_2 gas mixtures. [5,6]

Water vapor plasma is an interesting possibility to address the decontamination problem and this type of discharge has already been studied for several surface modification processes, in between them we cite: corrosion resistance [7], polymers activation [8,9,10] UV light source [11] and microorganisms sterilization [12]. The rich gas phase chemistry generated in such low pressure plasmas comprises reactive ions as well as O, H and OH radicals, which all have different chemical activity.

Furthermore, water vapor discharges are considerably cheaper, safer and easier to handle then high purity commercial gas mixtures of hydrogen and oxygen. On the other side, one of the limitations arising in the applications is the strong chemical reaction occurring between such plasmas and inner metal electrodes surfaces. From the very beginning the use of electrodeless discharges (either under vacuum or at atmospheric pressure) like inductive coupling, microwave or dielectric barrier discharge has to be preferred.

In the field of decontamination, large cleaning installations will be required to treat the load of contaminated objects produced daily from a hospital facility. The main characteristics of a hospital–scale reactor will be: (i) the capability to treat large volumes and multiple objects in a reasonably short time, (ii) the capability to treat thermo-labile materials without damage, (ii) a superior decontamination efficacy compared to actually implemented methods and finally (iv) low installation and maintenance costs. The first two tasks can be issued employing large-area low-pressure plasma reactor with state-of-the-art plasma sterilization and decontamination processes. At the present state of the research last two objectives present diverging requests, the most efficient discharge mixtures containing oxygen and/or hydrogen demand the installation of expensive precision gas delivery systems and severe safety protocols due to fire and explosion hazards, while a process based on water vapor may need only a simple dry vacuum evaporator tank. A water vapor plasma might

represent an interesting trade-off between low costs and efficacy as long as the decontamination efficiency of such plasmas is kept in the same order of magnitude with respect to oxygen-based gas mixtures.

3.2.1 Samples Preparation

Microspotting of protein and brain homogenate samples on silicon wafers was performed using a Scienion S3 sci-FLEXARRAYER (Scienion AG, Germany) spotter equipped with an automated piezo driven non-contact dispensing and with a three-axis micro-positioning system. A glass nozzle with a diameter of 80 μm was applied to generate drops of the 10 μg/ml solutions of bovine serum albumin (BSA) protein (from Fluka) and brain homogenate (BrH) dispersed in 5 mM TrisHCl pH 7,5. An integrated horizontal CCD camera allowed controlling drop volumes for determining the deposited protein amounts. Brain Homogenate stock was prepared according to the method described in Viganò et al. [13] and stored at -20°C. Aliquots from the stock were thawed and used for suspensions preparation right before the microspotting..
The experimental results presented are divided in three sections. First, the efficacy of a water vapor discharge on BSA and BrH contamination models is demonstrated and compared, in terms of mass loss rates, with other gas phase chemistries; second the water vapor discharge particle fluxes are characterized by means of Langmuir and OES measurements and finally some mass removal experiments results are discussed in terms of the chemical sputtering removal mechanism.

3.2.2 H_2O and Ar/H_2O plasma decontamination efficacy tests.

Figure 3.2.1 shows a typical optical emission spectrum of the inductively coupled water vapor plasma. Spectral signatures of O, H and OH radicals were observed. The characteristic low pressure atomic lines of hydrogen (H_α at 656 nm, H_β at 486 nm and H_γ at 434 nm) and oxygen ($3p^5P$-$3s^5S$ at 777 nm and $3p^3P$-$3s^5S$ at 844 nm) were the most prominent. The (0,0) A → X transition of the OH molecular band at 309 nm was observed as well. As low intensity background between 600 and 775 nm molecular nitrogen vibrational bands, due to impurities present into the vacuum chamber, can be seen at larger integration times.

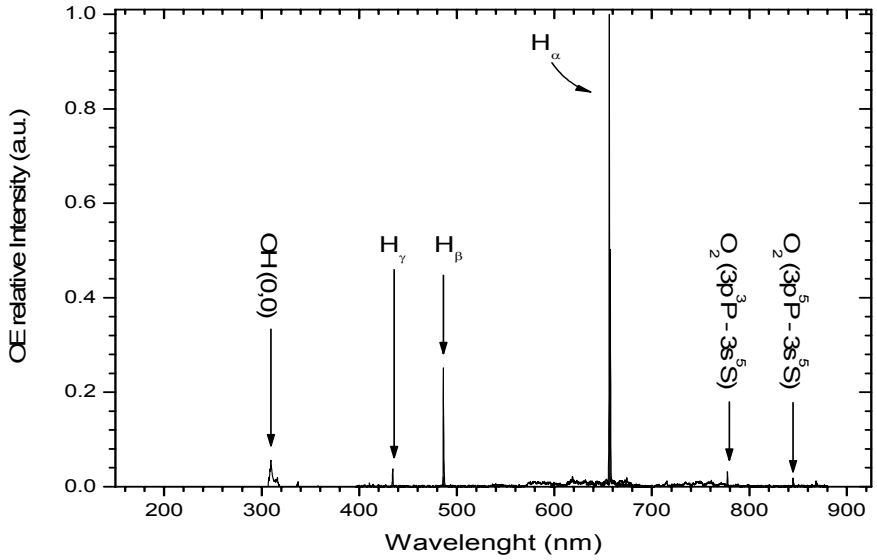

Figure 3.2.1. Typical optical emission spectrum from a water vapor discharge.

All of the radicals detected in the spectra have potential reactivity in the plasma phase with organic materials, O and H atoms together with OH molecules can be produced through different electron impact processes, the most important dissociation channels [14] for water molecules are listed in Table 1

Table 3.2.1. Dissociation channels of H_2O produced by electron impact.

Reaction	E_{th}(eV)
(1) $e + H_20 \rightarrow O(3P) + H_2(X) + e$	5.03
(2) $e + H_20 \rightarrow OH(X) + H(1s) + e$	5.10
(3) $e + H_20 \rightarrow O^*(^1D) + H_2(X) + e$	7.00
(4) $e + H_20 \rightarrow OH^*(A) + H(1s) + e$	9.15
(5) $e + H_20 \rightarrow O^*(^1S) + H_2(X) + e$	9.22
(6) $e + H_20 \rightarrow O(3P) + 2H$	9.51
(7) $e + H_20 \rightarrow O^*(3s^3S^0) + H_2(X) + e$	14.56
(8) $e + H_20 \rightarrow OH^*(A) + H^*(n=2) + e$	15.3
(9) $e + H_20 \rightarrow OH^*(A) + H^*(n=3) + e$	17.19

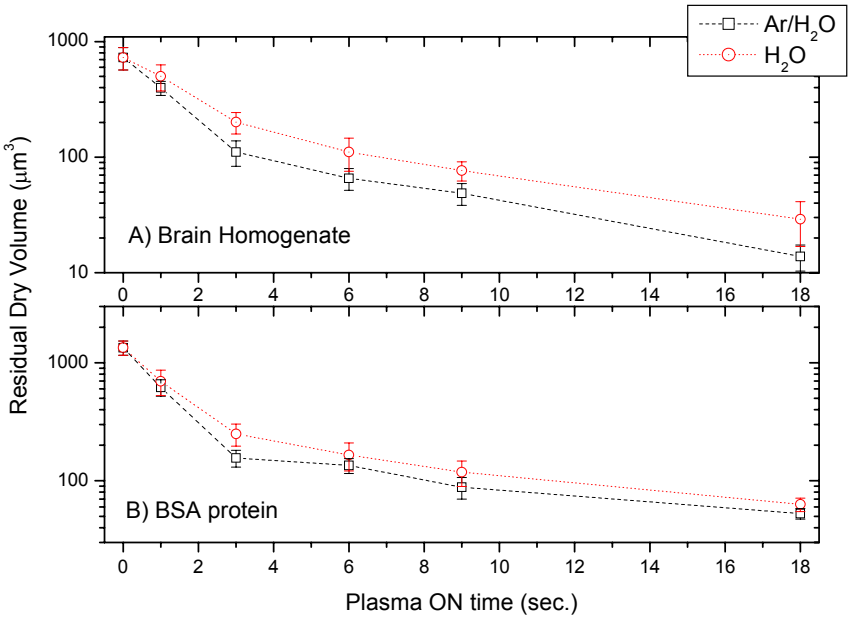

Figure 3.2.2. Residual dry volume measured by imaging ellipsometry of microspotted Brain homogenate (upper panel) and BSA protein (lower panel) after H_2O and Ar/H_2O [1:1] plasma discharge treatment. Pw = 350 W, Pr =10 Pa, Φ_{tot}=10 sccm.

To test the potential efficiency of water vapor plasma against biological residuals both BSA and brain homogenate model contamination have been treated. After the plasma treatment with H_2O and Ar/H_2O ICP discharge, pronounced modifications of both protein and brain homogenate film have been observed in the ellipsometric height-maps indicating a substantial removal degree of the protein deposit as shown in figure 3.2.2. The volume of the dry residual is reduced, in both cases, by more than one order of magnitude after 18 seconds of plasma treatment indicating substantial volatilization of the biological film induced by the plasma. The dynamics of the biological films removal shows a two-phases behavior: mass loss is faster (i.e. higher etching rates) in the first 3 seconds of treatment when the initial volume is reduced to about 10% of its initial value while for longer treatment times material removal phase appears to be much slower. This behavior for thin biological films can be interpreted as the transition from etching of the bulk biological material to a non-etchable residuals covered surface as explained in [15].

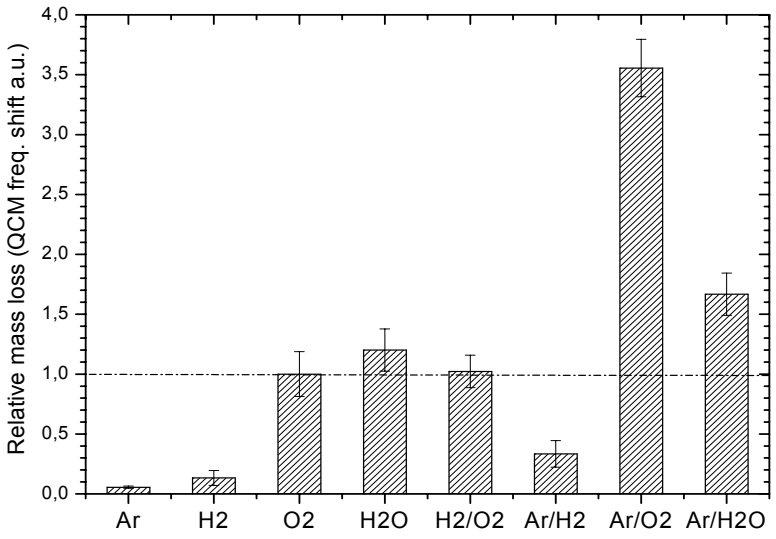

Figure 3.2.3. *In-situ* QCM measurement of different gas mixtures induced relative mass loss rates. BSA covered QCM crystals, fixed plasma parameters are P = 350 W, Pr = 10 Pa, Φ_{tot} = 22 sccm and t_{treat} = 2 sec. All binary mixtures gas flows ratio is [1:1], except H_2/O_2 mixture, which is [2:1]. Data are normalized to O_2 discharge mass loss rate.

To assess the efficiency of water vapor plasma decontamination in comparison with other gas-phase chemistries, BSA protein film mass loss induced by different discharges mixtures have been compared by means of *in-situ* QCM measurements [29] (see figure 3.2.3). In these experiments all the treatment parameters such as plasma-ON time, RF delivered power, gas pressure and gas flow were kept constant and for all the binary mixtures investigated the ratio of gas flows was 1:1 except for H_2/O_2 discharge were the ratio used was 2:1, i.e. ratio of hydrogen to oxygen in water molecule. Data have been normalized to pure oxygen discharge induced mass loss.

As can be seen, discharges sustained in pure Ar and H_2 show little effect on the biological film while discharge in pure oxygen leads to significant removal., Both pure water vapor and "synthetic" water vapor (H_2/O_2, 2:1) discharges show removal rates slightly higher than pure oxygen plasma (+ 20% for H_2O and +2% for H_2O_2).

In analogy with oxygen containing mixtures, an attempt was done to promote mass removal rates of BSA by argon gas addition. Ar/H_2 discharge removal efficacy is

augmented, but the absolute rate remains negligible compared to oxygen or water vapor discharge. Ar/H_2O discharge shows a mass removal rate enhancement of 38% as compared to pure water vapor and of +66% as compared to pure oxygen, while being about two times less efficient than the Ar/O_2 mixture.

Poor performances of the H_2 and Ar/H_2 discharges suggest that H atoms have little efficiency in the surface chemistry, while comparable removal rates between O_2, H_2O and O_2H_2 discharges may indicate that oxygen radicals are crucial for fast volatilization of biological matters. These hypotheses will be investigated more carefully in the subsequent discussion.

From an applicative point of view, these data show that pure water vapor plasma as well as Ar/H_2O plasma represent efficient alternatives for protein removal treatments.

3.2.3 Argon - Water vapor plasma characterization

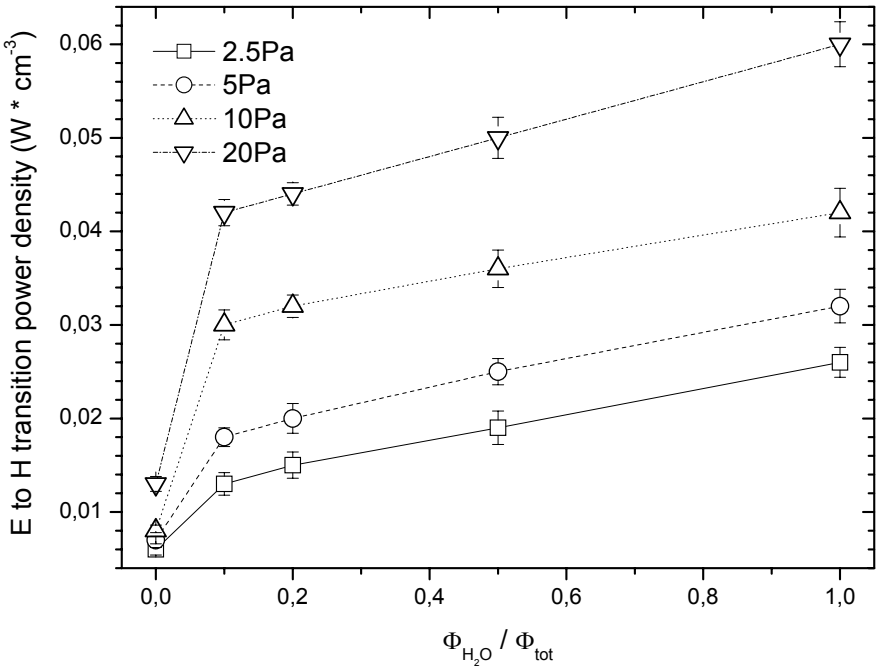

Figure 3.2.4. RF power density required for E to H mode transition as a function of the water vapor fraction contained in the gas mixture. Background gas is Argon; total gas flow was kept constant at 22 sccm.

Power and pressure dependences of the ICP mode transition are shown in figure 3.2.4. As it is reported in several papers the emission intensity rises with increasing power and suddenly change to much higher values (up to 2 orders of magnitude) when the discharge turns into H mode. The modes transition was identified by monitoring the intensity of Ha atomic line at 656 nm as function of the delivered RF power.

Transition power is observed to shift towards higher values when the pressure increases, meaning that sustainment of the inductive mode requires more power due to the decreased mean free path experienced from the capacitively generated electrons. As soon as a small amount of water vapor is introduced in the gas mixture the power required for mode transition increases abruptly. This is explained by considering the energy supplied by the electrons in order to sustain the gas phase chemistry of the water molecules which is not available anymore to sustain ionization processes. In some cases, e.g. electron attachment process, the water molecule plasma chemistry acts as an electron sink thus pushing the transition threshold to higher energies. As long as the water vapor fraction in the mixture is increased the importance of the loss processes increase determining higher transition powers required for the mode transition.

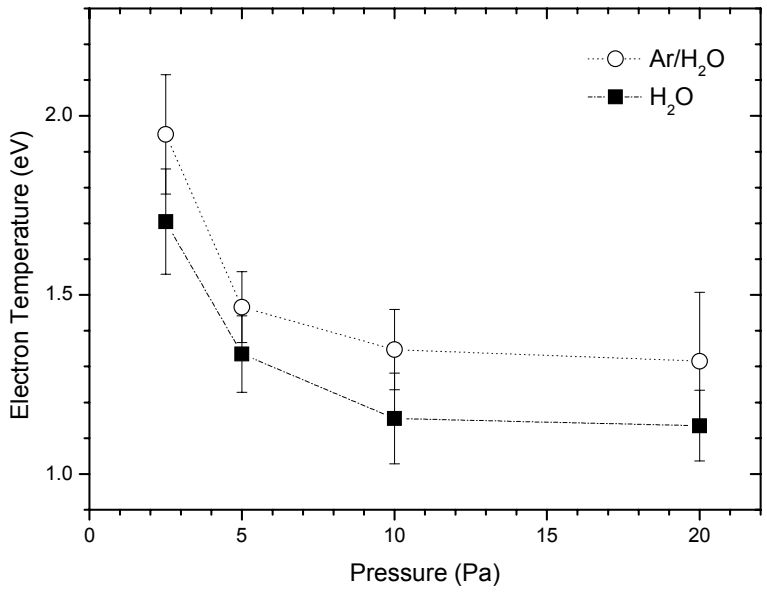

Figure 3.2.5. Electron temperature derived from Langmuir characteristics as function of operating pressure Argon/H_2O and H_2O discharge. Fixed plasma parameters are: Ar/H_2O 1:1 Φ = 10 sccm P = 0,08 W·cm^{-3}.

Hereafter (figure 3.2.5 and figure 3.2.6) plasma parameters positive ion density and electron temperature are derived from measured Langmuir characteristic recorded at the centre of the discharge. As is common for this class of discharges, the electron temperature in ICP is mainly controlled by ionization balance [16], resulting in a dependence from the working gas pressure p and a typical length size for the plasma L and practically does not depend on plasma density and discharge power. Indeed it is found that also in our discharge electron temperature decreases with increasing pressure, as is shown in figure 3.2.5.

Particles number density (figure 3.2.6) derived from Langmuir characteristic is decreasing with increasing pressure and is found linearly dependent from discharge power in the inductive H mode region. Data points corresponding to measurements on Ar/H_2O discharge at 20 Pa with less than 0,05 $W \cdot cm^{-3}$ of RF delivered power show deviations from the linear trend. In this parameter region the discharge it is observed to ignite in the E mode.

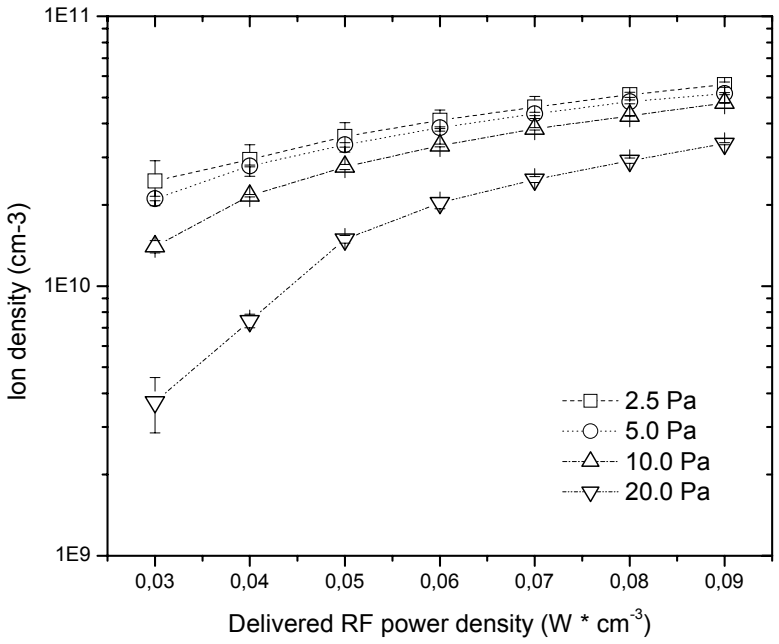

Figure 3.2.6. Positive ion density derived from Langmuir characteristics as function of operating pressure for several RF delivered power density values. Fixed plasma parameters are: Ar/H_2O 1:1 Φ = 10 sccm.

Figure 3.2.7 shows the intensity ratio between 309 nm OH band head and 826 nm kripton line, chosen as actinometer, as a function of the pressure in an Ar/H_20 discharge. All intensities are corrected for instrument spectral calibration curve. Parametric dependence from RF delivered power density is plotted. The line intensity ratio is proportional, under actinometric assumptions, to the OH molecular radical density in the plasma. For Ar/H_2O discharge parameters combinations allowing plasma ignition directly in the H-mode the concentration of OH molecules increases when both pressure or power are increased in the investigated range.

Hydroxyl radical concentrations corresponding to 0,03, 0,04 and 0,05 $W \cdot cm^{-3}$ in the discharge ignited at 20 Pa (points in the black circle in Figure 3.2.7) are lower then the corresponding power levels at 10 Pa, for this three data points OH density shows a peak value at 10 Pa. This different behavior is attributed to the fact that in this parameter region the discharge is ignited in E mode where the density of electrons available for impact dissociation reaction decreases.

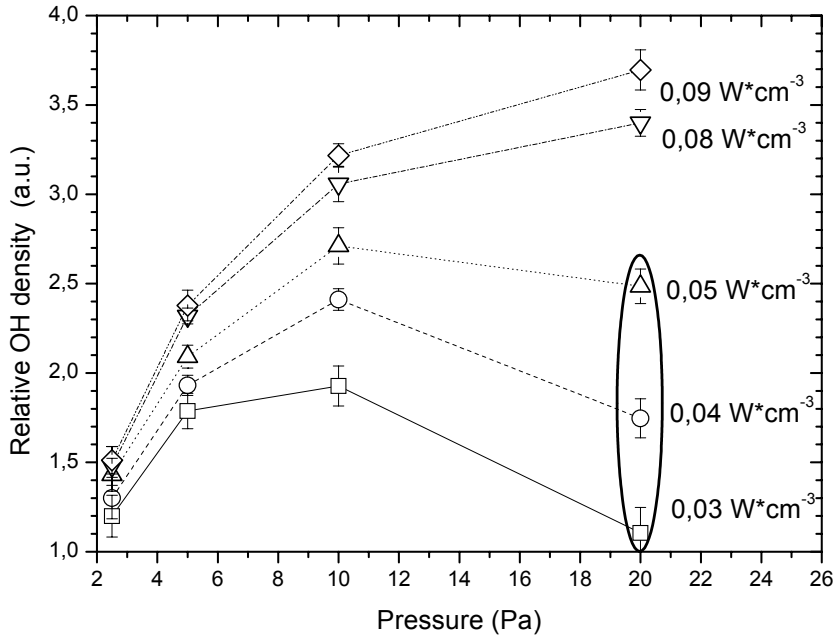

Figure 3.2.7. Relative OH molecule density as a function of the discharge pressure for several RF delivered power density values. Plasma parameters are: Ar/H_20 [1:1], Φ = 10 sccm.

Figure 3.2.8 shows the intensity ratio between 844 nm O atom line head and 826 nm kripton line, chosen as actinometer, as a function of the pressure in an Ar/H_20 discharge. All intensities are corrected for instrument spectral calibration curve. Parametric dependence from RF delivered power is plotted. The line intensity ratio is proportional, under actinometric assumptions, to the O atomic radical density in the plasma. In the pressure range investigated the concentration of O atoms initially increases and then shows a peak value at 5 Pa. For higher operating pressures all the densities decrease when increasing the pressure.

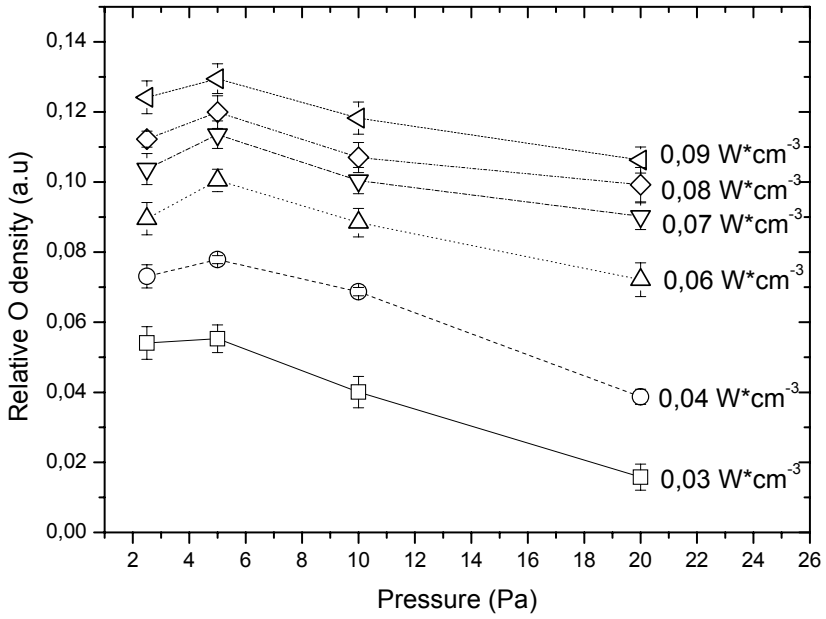

Figure 3.2.8. Relative O atom density as a function of the discharge pressure for several RF delivered power values. Plasma parameters are: Ar/H20 [1:1], Φ = 10 sccm.

The peak is explained by two competitive effects: first, the H2O molecule density increases with increasing pressure (as a reactant for the production of O according to reaction 7 in table 1 or second order electron impact dissociation reactions of OH molecule), so one would expect a monotonous increase of the emission intensity as the pressure is increased. Second, however, both the electron temperature and electron density decreases with increasing pressure. Since the emission occurs in transitions

from the excited states close to 11 eV, this factor becomes dominant at higher pressure. Delivered RF power density dependency shows that O atoms concentration increase with delivered power (proportional to the electron density) in all the parameter range investigated.

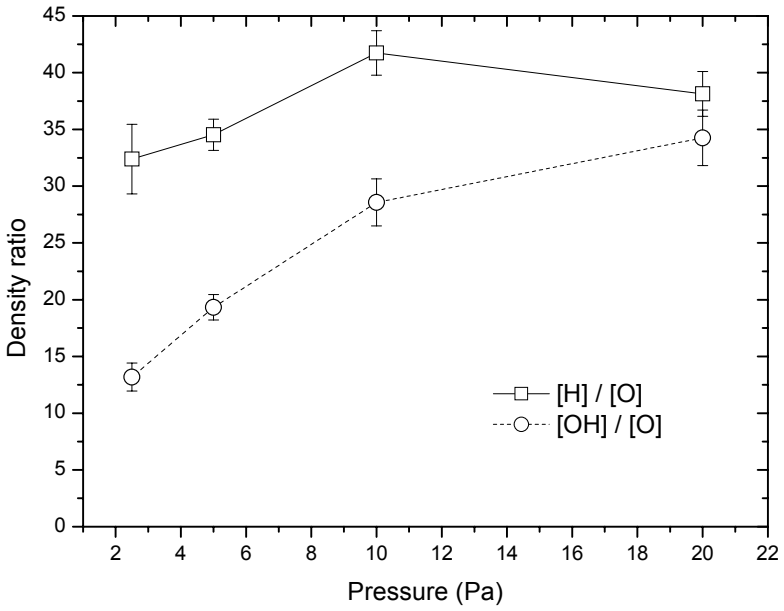

Figure 3.2.9. Hydrogen atom over oxygen atom and hydroxyl molecule over oxygen atom density ratios at 0,09 $W \cdot cm^{-3}$ as a function of pressure. Gas mixture Ar:H_2O [1:1].

Hydrogen atom over oxygen atom and hydroxyl molecule over oxygen atom density ratios as derived from actinometric measurements are shown in figure 3.2.9 as a function of discharge mixture pressure and for a fixed RF power of 0,09 $W \cdot cm^{-3}$. Intensities ratios are corrected for spectrometer relative efficiency at different wavelengths. Data show that hydrogen and hydroxyl densities are always at least one order of magnitude higher than oxygen atoms densities. Given that these species experience the same gas temperature the OH and H radical fluxes at the walls always greatly overcame the O flux in all the experimental conditions investigated.

3.2.4 Role of the radicals species in H_2O plasma biomaterials interaction

Mass loss rates for BSA protein were derived by QCM measurements data for the first 60 seconds of plasma treatments. Every etching rate value is the average of 5 independent measurements. Column bars in figure 3.2.10 show the measured pressure dependence of the mass loss rates and corresponding errors at fixed power density and discharge mixture composition (0,09 $W \cdot cm^{-3}$ and Ar:H_2O [1:1]). For better comparison, all the data are normalized to the mass loss rate measured at 20 Pa. It can be seen that as the pressure is increased, the efficacy of the plasma removal drops significantly: mass removal is more than four times slower at 20 Pa than at 2 Pa.

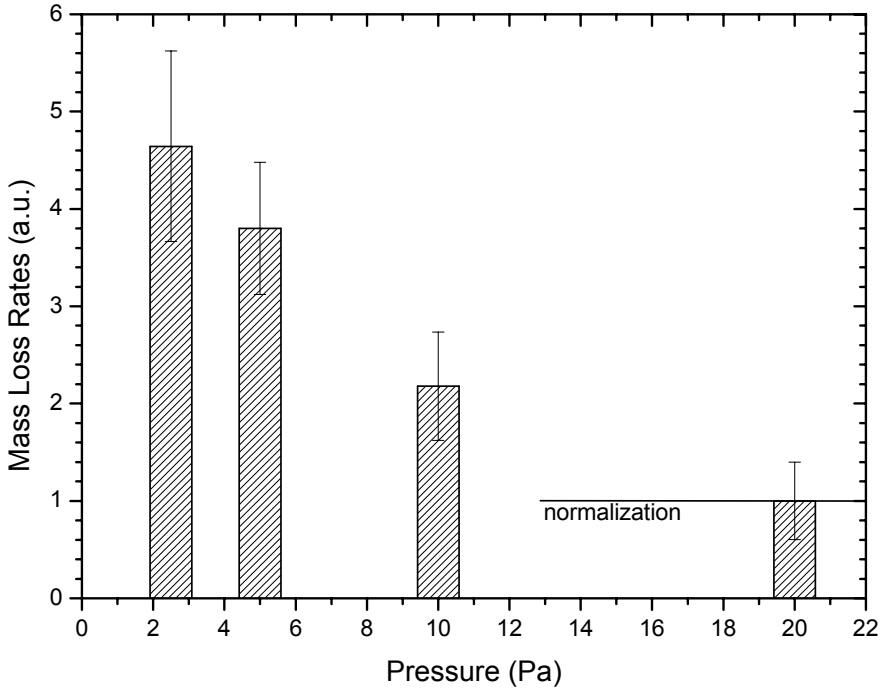

Figure 3.2.10. *In-situ* QCM measurement of water vapor plasma induced relative mass loss rates. BSA covered QCM crystals, fixed plasma parameters are Ar:H_2O = [1:1], P = 400 W, Pr = 10 Pa, Φ_{tot} = 22 sccm and t_{treat} = 60 sec. Data are normalized to the 20 Pa discharge mass loss rate.

The dependency of the measured mass loss rates shown in figure 3.2.10 is explained according to the process of chemical sputtering [17], postulating that the combined interaction of ions and chemically reactive species with the surface is important for an efficient removal of biomolecules. Chemical sputtering was already proven to be a solid framework for sterilization and biomolecules etching data interpretation. [31,18,19,20] Plasma characterization described in the previous section provides a dataset for reactive particle fluxes, which are proportional to the bulk densities of radical atoms and molecules as measured by actinometry. The ion flux is a function of the ions bulk density and the electron temperature as measured by Langmuir probe experiments.

As a rough hypothesis, it is possible to state that the mass loss rate is proportional to the product of ion flux and oxygen species flux, as already illustrated [21] for plasma etching of a hydrogenated carbon film. The model equation has the form:

$$ER = const \cdot \Gamma_{ion} \cdot \Gamma_{radical} \qquad (3.3)$$

where ER is the mass removal rate, const is a proportionality constant and Γ_{ion} and $\Gamma_{radical}$ are the ion and radical fluxes directed to the surface.

The possibility of a leading role of hydrogen atoms in the surface chemistry is ruled out by results of the experiments shown in figure 3.2.4, where hydrogen containing mixtures show little effect on biomolecules film, at a level comparable with non reactive argon discharges. The hypothesis of chemical sputtering process chemically driven by oxygen atoms adsorption on the protein surface is tested by plotting the product of ion flux and O densities (n_O*Γion) in dependence of the working pressure of the discharge. In figure 3.2.9, another model (n_{OH}*Γion) is tested as well; in this case it is assumed that the adsorbed hydroxyl radicals react on the surface to form a chemical compound that can be removed by ion bombardment, leading to biomaterial removal.

Figure 3.2.11 shows the mass removal rates calculated using values of the particle fluxes (ions and radicals) measured as described in the previous paragraphs plotted against the corresponding measured mass removal rates. The overall behavior of the measured mass loss rate (ER_m) is well reproduced by the mass removal rates calculated using the best parameter estimate obtained regressing the particle fluxes

dataset using an equation of the form $ER_m=cost*n_O*\Gamma ion$, while the values calculated using OH molecules and H atoms densities and the same equation structure cannot reproduce the trend of the measured mass loss rates. For pure hydroxyl and hydrogen chemistries the calculated datasets are heavily skewed with respect to the real measurements.

This result indicates that oxygen radicals plays a major role in water vapor plasma chemical sputtering of protein films. However, even if the mass loss values calculated using the oxygen atom density reproduce the parametric discharge pressure dependency, the magnitude of the model residuals are comparable with the magnitude of the experimental error on the mass removal rates. The possibility of secondary mechanisms involving contribution of hydroxyl molecule to the overall process cannot be absolutely ruled out.

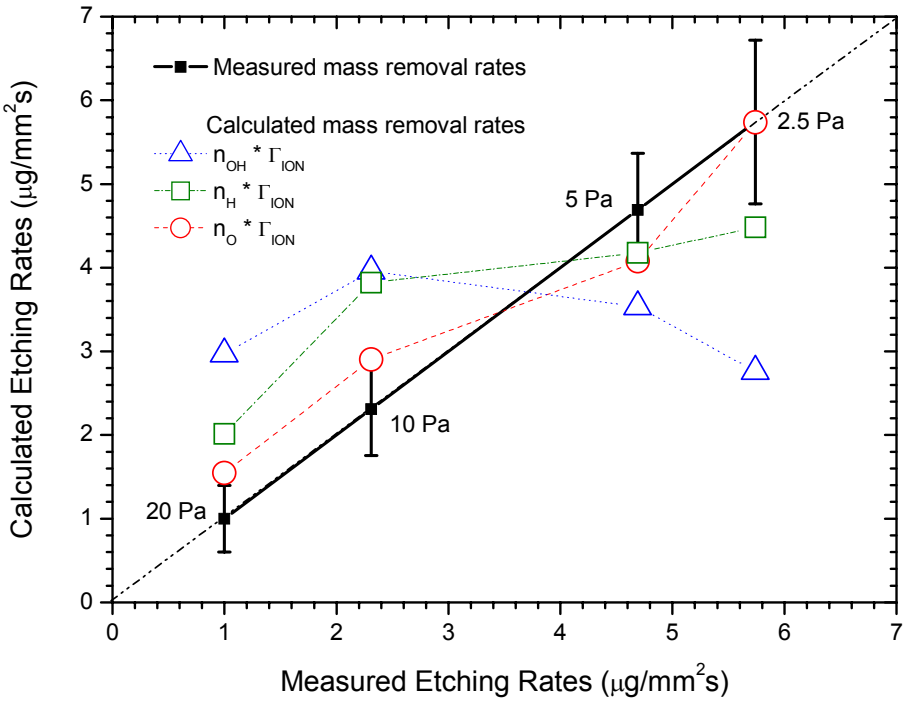

Figure 3.2.11. Measured BSA protein mass removal rates in Ar/H_2O discharge at different pressures (see figure 3.2.10 plotted against etching rates calculated using equation (1) and different radicals densities. Solid black line shows the measured mass removal rates values.

Two possible contributions to the removal mechanism can be addressed to the OH molecules itself. First emission of the excited molecular state OH A – X at 309 nm in th UV region may promote proteins removal rates by photodissociation processes on the surface. [22] Second, hydrogen abstraction processes by OH radicals has been reported [23] as being an effective reaction in surface chemistry of water vapor plasma-protein films interaction. Rate constants for H-abstraction processes from hydrocarbons by OH radicals are 3 orders of magnitude faster than the hydrogen atom driven H-abstraction and two orders of magnitude faster than oxygen atom driven H-abstraction reactions [24].

Even if the initial H abstraction event is not a direct fragmentation reaction that attacks the protein structure, the resulting radical centre formed on the biomolecule may produce in a surface site that is activated for chain scission reactions driven by oxygen atoms, thus contributing to enhance mass removal rates above the values calculated using only pure oxygen chemistry.

In conclusion the use of oxygen-based plasma discharges for biomolecules decontamination has been studied in detail in the past few years, relatively fewer results have been published concerning the removal of proteins and biological matrices from surgical instruments by means of a water vapor discharge. Recent studies [25,26] revealed, however, that the present decontamination medical protocols show little efficacy. Therefore, the possibility to eliminate biomolecular contaminations by low-pressure H_2O plasma treatment was addressed in this study.

Plasma decontamination of silicon surfaces was achieved using water vapor plasma; model contaminations created either with pure protein or with a biological matrix were effectively reduced by the interaction with the plasma on a reasonable time scale. Mass removal rates for water vapor based discharges are found to be lower then corresponding oxygen-based discharges operated in identical conditions but the absolute values are nevertheless of the same order of magnitude. This result indicates that a water vapor based mixture might be used to implement an efficient cost-effective decontamination device.

Water vapor plasma was characterized by means of optical emission spectroscopy and langmuir probe, plasma fluxes were measured in several operating parameters conditions ranging from 2 to 20 Pa and 0,03 to 0,09 W/cm^{-3}. Plasma fluxes data have been used to predict mass removal rates behavior within the framework of chemical

sputtering plasma biomaterial interaction mechanism. Comparison of different interaction schemes indicates that the leading interaction is chemically favored by oxygen atoms reactions on the surface. Anyway oxygen atoms contribution to mass removal rates cannot alone fully explain the measured data, it is postulated that hydroxyl molecules plays an auxiliary role both in terms of UV emission and H-abstraction processes.

References

[1] O. Kylian, F. Rossi *J. Phys. D: Appl. Phys*., **2009**, 42, 085207, Sterilization and decontamination of medical instruments by low-pressure plasma discharges: application of Ar/O2/N2 ternary mixture

[2] O. Kylian, H. Rauscher, D. Gilliland, F. Bretagnol, F Rossi, *J. Phys. D: Appl. Phys.* **2008**, 41, 095201, Removal of model proteins by means of low-pressure inductively coupled plasma discharge

[3] H. Rauscher, K. Stapelmann, O. Kylian, B. Denis, F. Rossi, *Vacuum* **2010**, 84, 75–78, Monitoring plasma etching of biomolecules by imaging ellipsometry

[4] Helen C. Baxter, Gaynor A. Campbell, Patricia R. Richardson, Anita C. Jones, Ian R. Whittle, Mark Casey, A. Gavin Whittaker, and Robert L. Baxter, *IEEE Trans. Plasma Sci.*, **2006**, 34, 4, 1337, Surgical Instrument Decontamination: Efficacy of Introducing an Argon:Oxygen RF Gas-Plasma Cleaning Step as Part of the Cleaning Cycle for Stainless Steel Instruments.

[5] Rossi F, Kylián O., Hasiwa M., **2006** *Plasma Process. Polym.*, 3, 431.

[6] Rossi F., Kylián O., Hasiwa M., **2007 "**Mechanisms of Sterilization and Decontamination of Surfaces by Low Pressure Plasma" *Advanced Plasma Technology*, d'Agostino, Favia, Kawai, Ikegami, Sato, Arefi-Khonsari (Editors), Wiley.

[7] T. Suzuki, T. Saburi, R. Tokunami, H. Murata, Y. Fujii, Dominant species for oxidation of stainless steel surface in water vapor plasma, *Thin Solid Films* 506– 507 (**2006**) 342 – 345

[8] Steen, M. L.; Hymas, L.; Havey, E. D.; Capps, N. E.; Castner, D. G.; Fisher, E. R. *J. Membr. Sci.* **2001**, *188*, 97-114.

[9] Steen, M. L.; Jordan, A. C.; Fisher, E. R. *J. Membr. Sci.* **2002**, *204*, 341-357.

[10] Weikart, C. M.; Yasuda, H. K. *J. Polym. Sci., Polym. Chem. Ed.* **2000**, *38*, 3028-3042.

[11] J. Oh, K. Kawamura, B. Pramanik, and A. Hatta, *IEEE Trans. Plasma Sci.* **37**, 107 _2009.

[12] Nobuya Hayashi, Shinsuke Tsutsui, Tetsushi Tomari,Weimin Guan *IEEE Trans. Plasma Sci.*, 36, 4, **2008** Sterilization of Medical Equipment Using Oxygen Radicals Produced by Water Vapor RF Plasma.

[13] Daniela Viganò . Tiziana Rubino . Angelo Vaccani . Silvia Bianchessi . Patrick Marmorato . Chiara Castiglioni . Daniela Parolaio, Molecular mechanisms involved in the asymmetric interaction between cannabinoid and opioid systems Psychopharmacology (2005) 182: 527–536

[14] Itikawa Y and Mason N 2005 Cross sections for electron collisions with water molecules *J. Phys. Chem. Ref. Data* **34** 1–22

[15] Fumagalli F Kylian O Hanus J and Rossi F, *Plasma Process. Polym.* **2011**,accepted.

[16] J. T. Gudmundsson, Plasma Sources Sci. Technol., Vol.10, p. 76-81, (**2001**).

[17]Rauscher H Kylian O Benedikt J Keudell A, and Rossi F 2010 ChemPhysChem 2010 **11** 1382 – 1389

[18] Kylian O Benedikt J Sirghi L Reuter R Rauscher R Keudell A and Rossi F *Plasma Process. Polym.* 2009 **6** 255–261

[19] J Opretzka Benedikt J Awakowicz P Wunderlich J Keudell A 2007 *J. Phys. D: Appl. Phys*. **40** 2826–2830

[20] Raballand V Benedikt J Wunderlich J and Keudell A 2008 *J. Phys. D: Appl. Phys*. 2008 **41** 115207

[21] Benedikt J Flötgen C Kussel G Raball V and Keudell A 2008 *J. Phys.: Conf. Ser.* **133** 012012

[22] Stapelmann K Kylian O Denis B, and Rossi F 2008 *J. Phys. D: Appl. Phys.* 2008 **41** 192005

[23] Stalder K R McMillen D F and Woloszko J 2005 *J. Phys. D: Appl. Phys.* **38** 1728–1738

[24] Baulch D I et al 1992 J. Phys. Chem. Ref. Data **21** 411–29

[25] R. Hervé, T. Secker, C. Keevil, *J. Hosp. Infec*. **2010**, *75*, 309;

[26] I. Lipscomb, R. Hervé, K. Harris, H. Pinchin, R. Collin and C. W. Keevil, *J. Gen. Virol.* **2007**, *88*, 2619;

3.3 Etching by-products analysis

3.3.1 Reaction byproducts during plasma treatment

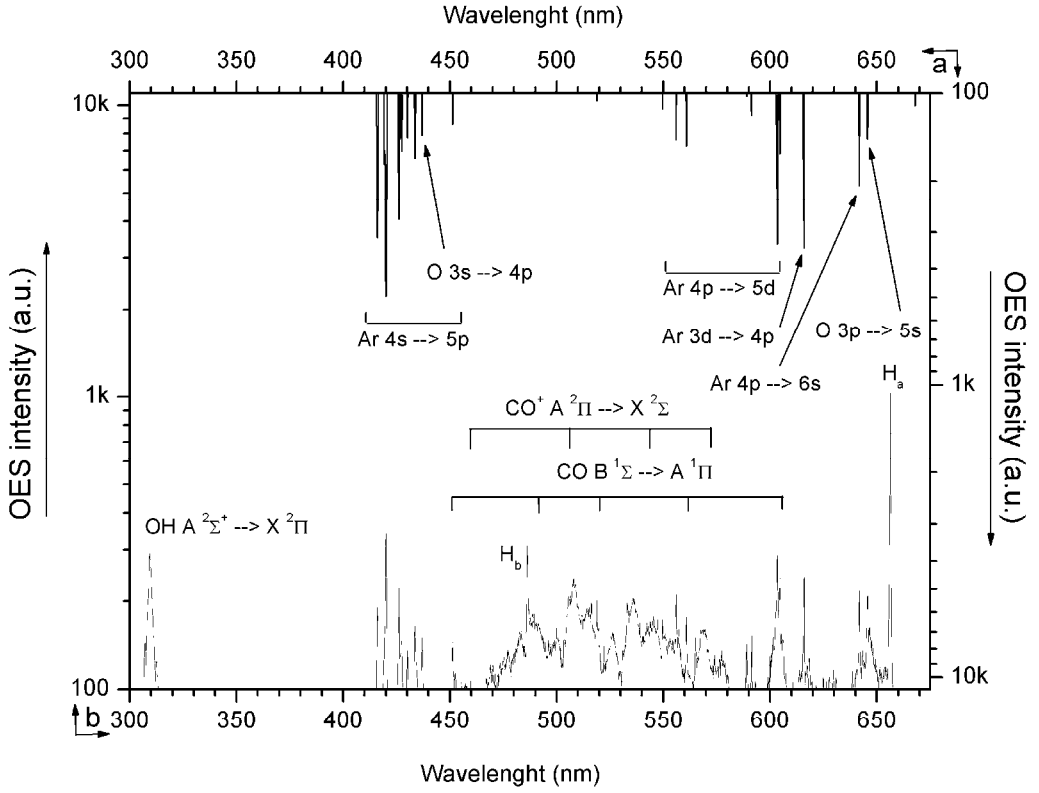

Figure 3.3.1) Optical emission spectra from Ar/O_2 plasma recorded without protein samples in the chamber (a, top and right axes) and during the first plasma pulse of BSA treatment (b, bottom and left axes). Transitions between atomic configurations and molecular bands systems are indicated. Plasma conditions are Pw = 350 W, Pr = 10 Pa, Φ_{tot} = 22sccm, O_2/Ar = 0.37.

The excitation of plasma chemical species gives also insights into the biomaterials removal plasma process. In figure 3.3.1 a portion from 300 to 675 nm of the emission spectrum of Ar/O_2 plasma is shown (data a], upper and right axes). Spectra are dominated by the emission by Argon atoms (group of transitions from $^4P \rightarrow {}^4S$) and by O transitions to metastables levels ($^5P \rightarrow {}^5S$, 777 nm; and $^3P \rightarrow {}^3S$, 844 nm) which can be

observed at higher wavelengths but are saturated at the integration time used to collect data of figure 1.

Table.3.3.1 Ar/O_2 plasma spectrum between 300 and 675 nm.

Line	Wavelength (nm)	Transition/Band
ArI	415,96	$3s^2 3p^5(^2P°_{3/2})4s$ - $3s^2 3p^5(^2P°_{3/2})5p$
ArI	419,28	$3s^2 3p^5(^2P°_{3/2})4s$ - $3s^2 3p^5(^2P°_{3/2})5p$
ArI	420,1	$3s^2 3p^5(^2P°_{3/2})4s$ - $3s^2 3p^5(^2P°_{3/2})5p$
ArI	426	$3s^2 3p^5(^2P°_{3/2})4s$ - $3s^2 3p^5(^2P°_{3/2})5p$
ArI	430,17	$3s^2 3p^5(^2P°_{3/2})4s$ - $3s^2 3p^5(^2P°_{3/2})5p$
ArI	433,45	$3s^2 3p^4(^3P)4s$ - $3s^2 3p^4(^3P)4p$
OI	436,89	$2s^2 2p^3(^4S°)3s$ - $2s^2 2p^3(^4S°)4p$
ArI	451,18	$3s^2 3p^5(^2P°_{1/2})4s$ - $3s^2 3p^5(^2P°_{3/2})5p$
ArI	555,91	$3s^2 3p^5(^2P°_{3/2})4p$ - $3s^2 3p^5(^2P°_{3/2})5d$
ArI	560,74	$3s^2 3p^5(^2P°_{3/2})4p$ - $3s^2 3p^5(^2P°_{3/2})5d$
ArI	603,33	$3s^2 3p^5(^2P°_{3/2})4p$ - $3s^2 3p^5(^2P°_{3/2})5d$
ArI	615,85	$3s^2 3p^4(^1D)3d$ - $3s^2 3p^4(^1D)4p$
ArI	641,71	$3s^2 3p^5(^2P°_{3/2})4p$ - $3s^2 3p^5(^2P°_{3/2})6s$
OI	645,53	$2s^2 2p^3(^4S°)3p$ - $2s^2 2p^3(^4S°)5s$

When a sample with protein layer is present in the vacuum chamber (data b], lower and left axes), the emission in the first seconds of the plasma pulse is remarkably different from the Ar/O_2 plasma emission without sample. Moreover, it is also shown in figure 3.3.1 that there is an intense, but evanescent group of emission lines, whose appearance can be clearly observed by naked eye as a white flash in the plasma glow. After several plasma pulses the emission becomes again identical to the normal emission of a clean Ar/O_2 discharge. The difference in emission at the beginning of the plasma treatment can be attributed to the plasma excitation of reaction byproducts released from the surface which become less intense as soon as most of the protein on the substrate is removed. From the analysis of the spectra is found that, besides argon and oxygen, the most prominent evanescent lines can be attributed to OH* (Å System, $A\ ^2\Sigma^+ \rightarrow X\ ^2\Pi$), CO* (Angstrom system, $B\ ^1\Sigma \rightarrow A\ ^1\Pi$), CO^+ * (Comet tail system, $A\ ^2\Pi \rightarrow X\ ^2\Sigma$), H*

(Balmer series), and a very low intensity line from NO* (γ system ,A $^2\Sigma^+ \rightarrow X\ ^2\Pi$) can also be distinguished from the background (not shown in figure 3.3.1). The emission lines from CO*, OH*, NO* and H* likely originate from electron-impact excitation processes of the corresponding ground state molecules and atoms. Possible excitation channels are direct excitation or ionization of CO, OH, NO molecules and H atom or dissociative excitation / ionization of the CO_2, NO_2 and H_2O molecules which are, most probably, present in the gas phase as by-products of the surface reactions between oxygen radicals from the plasma and the protein film. The cross section energy threshold for electron impact excitation and dissociative excitation for these molecules are between 15 - 25 eV [1], these electron energies are readily available in ICP plasma from the high energy tail of the electron energy distribution.

Table 3.3.2 Ar/O_2 + BSA spectrum between 300 and 675 nm.

Line	Wavelength (nm)	Transition/Band	
NO	247,8	A $^2\Sigma^+ \rightarrow$ X $^2\Pi$	(γ system, very low)
OH	309	A $^2\Sigma^+ \rightarrow$ X $^2\Pi$	(Å system)
H_β	486,18	n= 4 → 2	Balmer
H_α	656	n= 3 → 2	
CO	451,9	B $^1\Sigma$ → A $^1\Pi$	(Ångstrom series)
CO	483,5	B $^1\Sigma$ → A $^1\Pi$	
CO	519,82	B $^1\Sigma$ → A $^1\Pi$	
CO	561.0	B $^1\Sigma$ → A $^1\Pi$	
CO	607.9	B $^1\Sigma$ → A $^1\Pi$	
CO^+	427,4	A $^2\Pi$ → X $^2\Sigma$	(Comet-tail system)
CO^+	456,5	A $^2\Pi$ → X $^2\Sigma$	
CO^+	507,2	A $^2\Pi$ → X $^2\Sigma$	
CO+	549,9	A $^2\Pi$ → X $^2\Sigma$	
CO^+	569,3	A $^2\Pi$ → X $^2\Sigma$	

3.3.2 Dynamics of oxygen atoms and byproducts during the plasma pulse

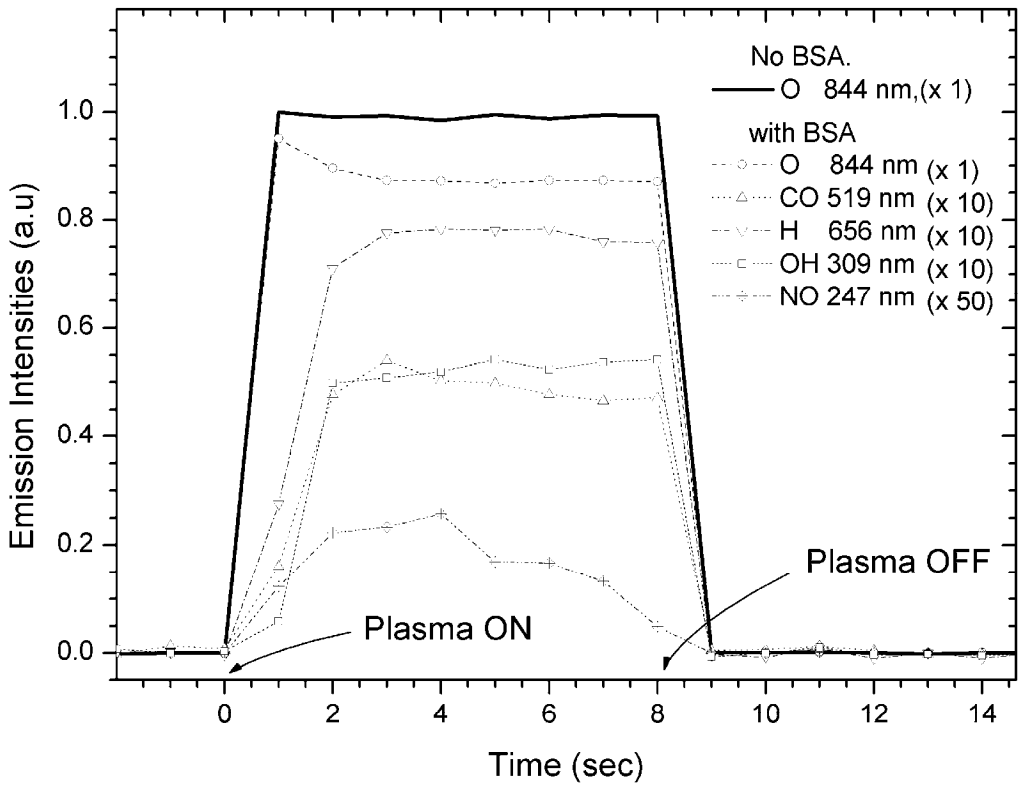

Fig. 3.3.2) Optical emission spectroscopic time resolved measurements of several plasma treatment cycles. Peak intensity of selected bands heads and emission lines is plotted against total treatment time, continuous black line refers to O* 844 nm emission from $3p^3$ P metastable state without the sample in the vacuum chamber. Dotted data series refers to spectra recorded with the sample inserted in the chamber. Plasma conditions are Pw = 350 W, Pr = 10 Pa, Φ_{tot} = 22sccm, O_2/Ar = 0.37.

Time resolved OES data, plotted in figure 3.3.2, allow investigation of the relevant time scale necessary for the surface reactions to reach steady state. Emission from selected CO*, OH*, NO* bands heads and O* and H* atomic lines was monitored by OES to qualitatively determine variations of relative densities of the corresponding excited states.

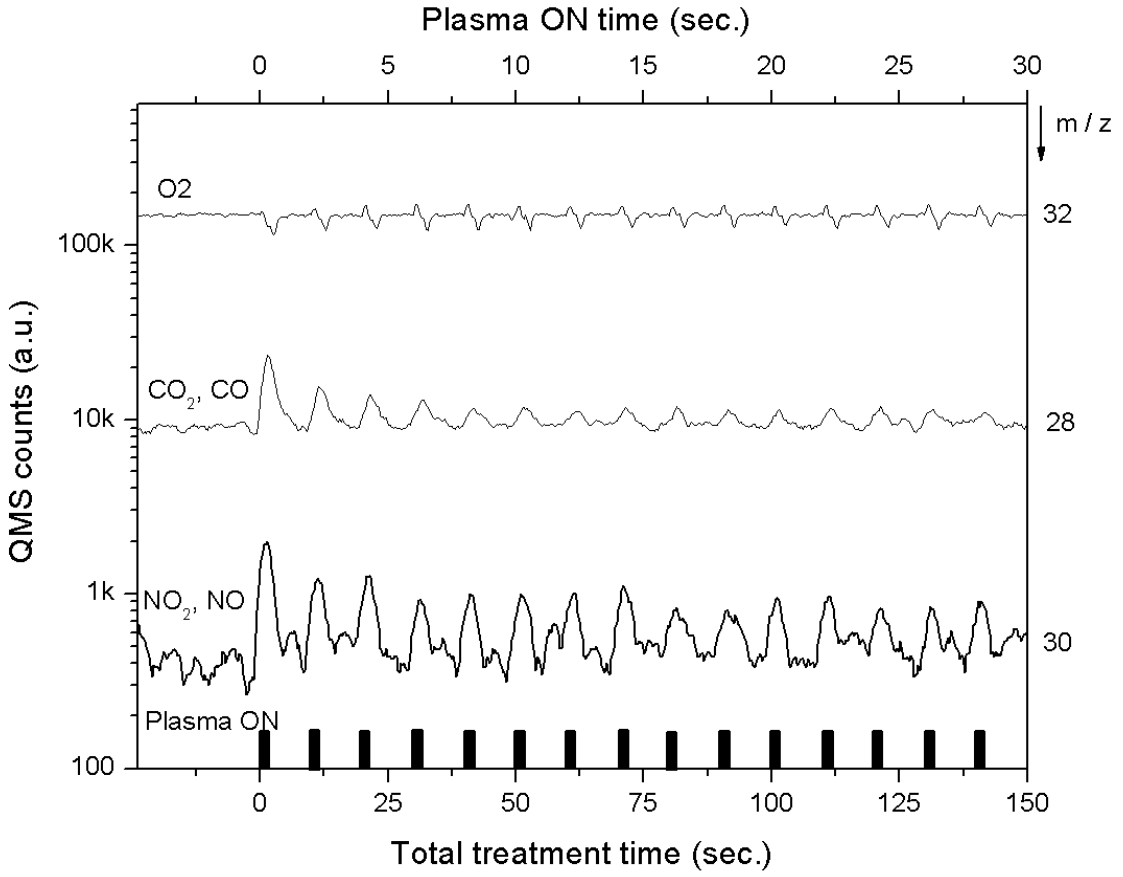

Fig. 3.3.3) Mass spectrometric time resolved measurements of several plasma treatments cycles. Parent molecules contributing to the signals at the selected m/z ratios are indicated. Bottom x-axis display total treatment at 20% DC and f = 100 mHz, top x-axis display effective plasma-ON time. . Plasma conditions are Pw = 350 W, Pr = 10 Pa, Φ_{tot} = 22sccm, O_2/Ar = 0.37.

Because of the possibility of dissociative excitation and ionization processes in the plasma phase it is possible to relate temporal evolution of these spectral peaks also as qualitative information about the parent molecules NO_2, CO_2 and H_2O. A 6 seconds plasma pulse was used in order to collect enough data points to distinguish trends in the detected emission intensities. This was necessary due to the low time resolution capability of our instrument. Transient emission after plasma switch off cannot be

resolved with this measurement resolution. In figure 3.3.2 the emission intensity from a pure Ar/O_2 plasma discharge without the protein film covered crystal inserted is shown, as reference, as a black continuous line. In the pure discharge the level of excited oxygen atoms rises within the time resolution of the spectrometer to a fixed level and remains constant for the duration of the pulse. When the protein covered crystal is present the oxygen signal rises almost to the same level of the previous case, but instead of being constant shows a slow decay and a plateau after about two seconds of plasma-on time, indicating that oxygen atoms are consumed by the surface reactions with the proteins. On the other hand dynamics for the reaction by-products CO*, OH*, NO* and H* intensities appears to be complementary, all the signals rise from the background and reach a steady state level after about two seconds, with the exception of the NO* signal which exhibits a maximum and a decay back to zero emission within the plasma pulse duration, this trends indicate that, during the plasma-protein surface chemical kinetics, steady state equilibrium is reached on a time scale of about a second, oxygen atoms are consumed in the reaction and organic oxidized compounds and water are released into the gas phase.

Figure 3.3.3 shows QMS time resolved detector counts at three mass to charge ratios, *m/z* =28, 30 and 32 for several plasma pulses after plasma ignition. At the selected duty cycle (20%) and pulse frequency (100 mHz), presented data span the firsts 30 seconds of effective plasma treatment. Because of the high energy of the electrons in the QMS ionizer at *m/z* values 28 and 30 signals arise from the contribution either of the corresponding direct ionization of CO and NO molecules either of the dissociative ionization of CO_2 and NO_2, as the most probable parent molecules.

Before the plasma ignition only the argon – oxygen gas mixture is sampled and the signals show constant values at their background levels. Data were not corrected for ions transport efficiency in the QMS (ions lens extraction, mass filter transmission and channeltron detector) but a standard calibration with test rare gases mixture results in a correction factor $\alpha(m/z)$ changing from of 1.47 at *m/z* = 28 to 1.25 at m/z = 32, too small to be appreciated on the full scale of this analysis. The background levels from channels 30 and 28 most probably arise because of impurities present on the walls of the processing vacuum chamber; in fact the oxygen signal from the gas mixture is 2-3 orders of magnitude higher. When the plasma is ignited signals at *m/z* = 28 and 30 increase

indicating the detection of CO, NO and probably CO_2 and NO_2 reaction products. The consumption of O radicals as it was detected with OES measurements has probably an influence also on the molecular oxygen mass balance but the evolution of the signal at m/z = 32 is also affected by bulk plasma dissociation of the O_2 molecule and degassing of chamber walls and these different effects cannot be distinguished.

3.3.3 Analogy with fuel combustion.

The general picture arising from the data presented in this section naturally leads to describe oxygen plasma etching of biomolecules in terms of fuel combustion concepts. Typical biomolecules mainly consist of C, N, H, and O. These are burnt in oxygen containing plasma where the final products (ash) are in principle CO_2, NO_2 and H_2O. There are also intermediary molecules that can be divided in two groups: active progress agents of the reaction process and stable non-reactive molecules. Since the triplet ground state oxygen molecules is relatively non reactive the radical chain reactions are driven by the flux of highly reactive excited singlet oxygen molecule ($a^1\Delta_g$, ε_{th}=0, 98 eV) and atomic oxygen radicals (metastable levels 3S and 5S, direct excitation and dissociative cross sections for production processes of both states have energy thresholds between 10 and 11 eV [2]).

In a plasma discharge these excited species are very easily provided at relatively high volume densities by electron impact collisions with molecular oxygen, whereas in a normal combustion process the energy required to force molecular oxygen into its spin paired singlet excited state $a^1\Delta_g$ must be provided by gas internal thermal energy, i.e. it is electron temperature rather then gas temperature that sustains the radicals production, the loop equilibrium between fuel exothermic energy release, gas heating and high kinetic energy molecular collisions is broken and a combustion-like process can be sustained even at very low (gas) temperatures. The idea of a low temperature combustion process in turn creates a problem in the surface reaction mechanism definition. Since the oxidant species diffuse at the fuel surface at low temperature, i.e. at low kinetic energy and a very small proportion of them will then have the required energy to react on the collision with the surface upper atomic layers, in this scenario the probability of a collision leading to

the formation of reaction products is very low and the fuel mass loss negligible (this scenario was confirmed by beam experiments from Kylian et al. [3]

Most common oxidation reactions for hydrocarbons are exothermic but with a certain activation energy threshold, typical bond breaking energies of interest for biomaterials are: C-C, 3.58 eV; C-H, 4.27 eV; C=O, 8.32 eV; C=C, 6.24 eV; C-N, 3.16 eV and O-H, 4.80 eV. [4] These energies are much higher then the average kinetic energy of near room temperature, around 0.025 eV. In a plasma discharge the missing energy for the bond breaking mechanism is supplied by ions (and eventually UV radiation, from 3.10 to 12.4 eV). Even without the high ion energies of capacitive coupled discharges, ions falling through the sheath potential difference of an ICP discharge gain a typical energy of 10-15 eV, well above typical bond energies, and are able to efficiently supply the activation energy for surface oxidation reactions between the oxygen atoms and molecules and the protein surface leading to formation of the reaction byproducts.

References

[1] M. A. Liebermann and A.J. Lichtenberg, Principles of plasma discharges and materials processing (Jhon Wiley & Sons Inc., New York, 1994)

[2] D Pagnon, J Amorim, J Nahorny, M Touzeau and M Vialle On the use of actinometry to measure the dissociation in 0_2 DC glow discharges: determination of the wall recombination probability J. Phys. D: Appl. Phys. 28 (1995)

[3] Kylian O Benedikt J Sirghi L Reuter R Rauscher H Von Keudell A and Rossi F 2009 Plasma Processes and Polymers 6 4 255-261

[4] R.T.Sanderson, Chemical Bonds and Bond Energy, 1976

3.4 Heat control

Heat characterization and control is of primary interest for plasma treatments of thermo-labile materials, such as polymeric materials, which are very often components of real medical tools undergoing decontamination and sterilization treatments.

Characterization of the heat generated by the plasma discharge in BIODECON reactor was performed by means of IR pyrometry. Infrared emission from plasma discharge was acquired through a high pass borosilicate window with transmittance above 95% for the near infrared spectrum.

The alignment of the laser system of the IR-detector was used in order to acquire the IR signal from a spot centred on the silicon samples mounted on the holder inside the discharge chamber; a correction of the emission coefficient for metals was used to calibrate the temperature reading of the pyrometer. The distance of the acquisition system from the sample was adjusted in order to acquire IR emission from an area around 1 cm^2 on the silicon sample.

It is important to note that the temperature measurements presented in the following of this chapter are not direct readings of the neutral gas temperature in the vacuum chamber but are related to the surface temperature of objects placed in the plasma discharge that are heated mainly because of physical impact of plasma ions and, less important mechanism at low pressures, because of heat conduction from gas phase.

The temperature raise due to exposition to plasma was monitored for periods of about 60 seconds. Based on the maximum temperature reached after 60 seconds, corresponding heating rates (in a linear approximation) were calculated to be used for estimates.

A first set of measurements (Figure 3.4.1) involved determination of heating curves, as a function of treatment time, of many different oxygen containing discharge mixtures which are of interest for plasma decontamination and sterilization.

The heating characteristics corresponding to discharge conditions of 500 W, 5 Pa and 10 sccm total gas flow shows a monotonic increase up to the final treatments times investigated; for this parameters set, no saturation of the temperature due to thermal equilibrium was observed. Considering the heating rates corresponding to different gas mixtures, we find that argon/oxygen combination presents the faster heat transfer to the

samples, up to 2.6 °C/sec while oxygen/hydrogen or oxygen/nitrogen mixtures, the heating rate ranges from 1.1 to 1.7 °C/sec.

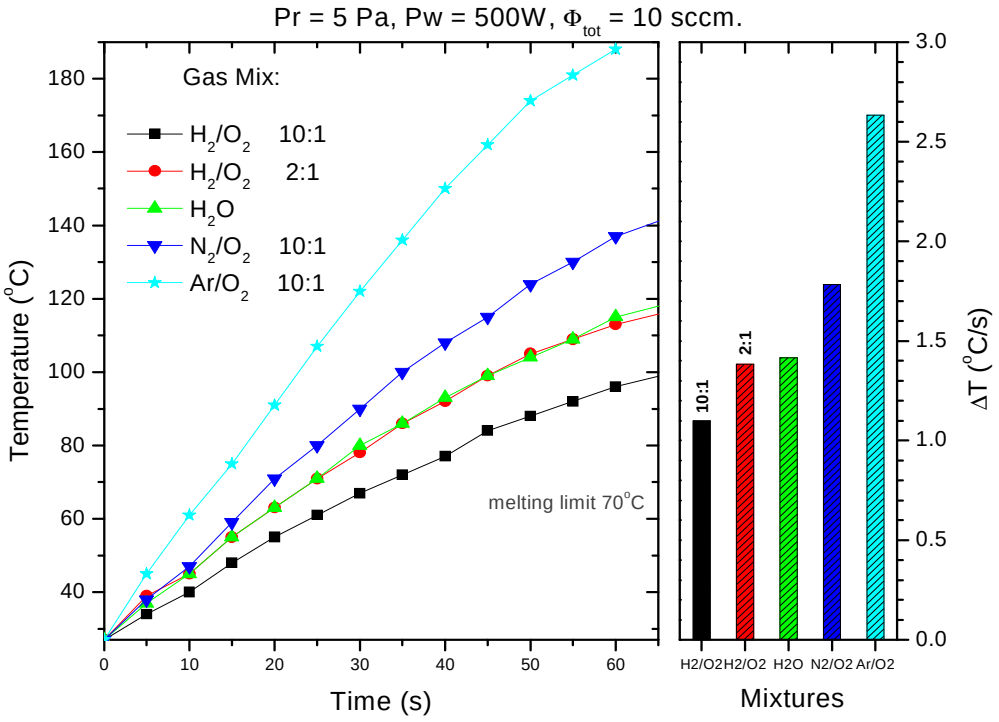

Figure 3.4.1. Measured heating curves and calculated heating rates for polystyrene substrates in different plasma chemistries.

This difference between atomic or molecular gas addition can be explained considering that, of all the electromagnetic power effectively delivered by the antenna into the vacuum chamber and absorbed by electrons, a certain fraction is dissipated by losses, a certain fraction is spent in plasma discharge self sustainment through ion-electrons pair creation by ionization events, while the rest is spent in sub-ionizing collisions like particles excitation or elastic collisions. When a molecular gas is added, some energy is consumed to excite rotational and vibrational levels of the gas molecules and this energy is not available for both gas heating and ionizations, thus damping both heating mechanisms that determine sample final temperature. This sort of loss term is not present when an atomic gas, like argon, is added to oxygen.

It is also interesting to note how water vapour plasma and the corresponding stechiometric hydrogen/oxygen mixture present the same heating behaviour despite of the differences in the volume plasma chemistry (e.g. in the relative steady-state atomic and molecular species densities).

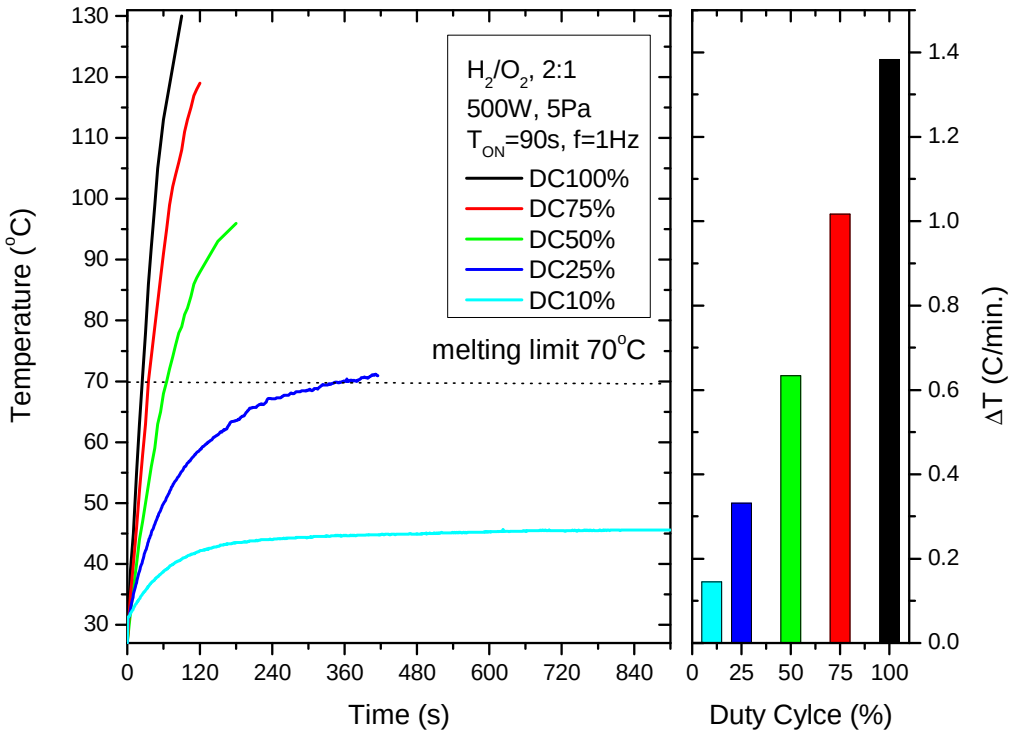

Figure 3.4.2 Measured heating curves and calculated heating rates for polystyrene substrates at different duty cycles.

From the data shown in figure 3.4.1, it appears that these parameter combinations lead to a very fast heating of the samples at levels not tolerable for polymeric materials plasma treatment (in these experiments we set a general threshold at 70 °C for irreversible structural changes of polymeric objects exposed to plasma conditions, in order to stay below typical glass-transition temperatures).

The sample temperature is a sensitive parameter for plasma sterilization and decontamination treatments and affects etch rates with the following scaling: etch rates increases with sample temperature and both sample temperature and etch rates increase with delivered RF power and operating pressure. To avoid a reduction of etching efficiency, when acting on plasma parameters like power and pressure to limit the

temperature to acceptable values, it was decided to pulse the discharge in the low frequencies range. In this way, allowing cooling times during the power OFF phase, samples temperature can be limited to low values while maintaining high etching rates; the drawback of this method is an increase of the treatment-time proportional to the inverse of the duty cycle.

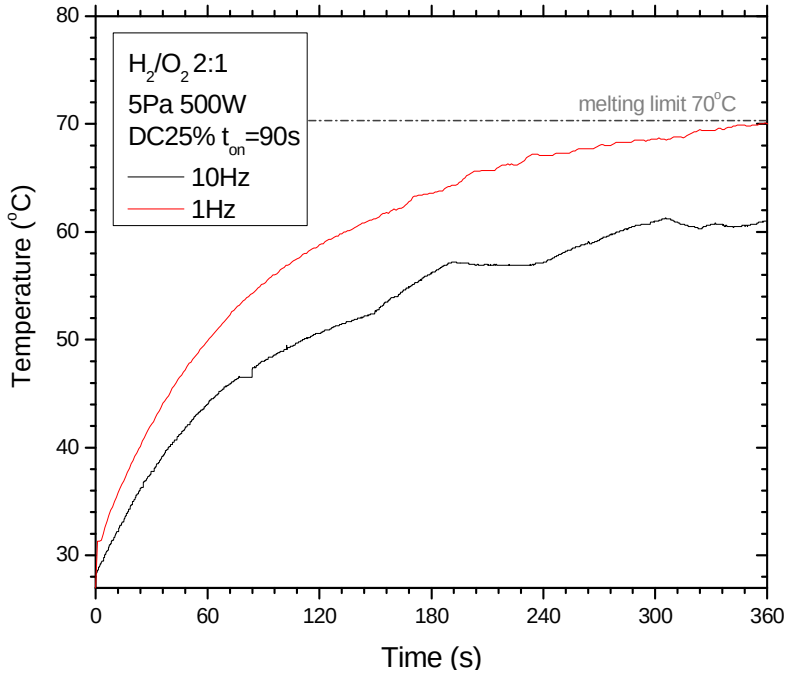

Figure 3.4.3 Measured heating curves for polystyrene substrates at different pulsing frequencies.

In figure 3.4.2 the heating characteristics as function of treatment time are reported for different values of the duty cycle, for oxygen/hydrogen gas mixture. Corresponding heating rates expressed in °C/sec and calculated within the first 60 seconds of total treatment time are shown in the right panel.

It can be seen that despite the high power, low pressure plasma conditions chosen for this experiment, pulsing the discharge with DC < 50% have a dramatic effect on sample heating curves; experiments performed at DC = 25% and DC = 10 % shown not only saturation of the heating curves with treatment time (balance of heat influx and heat losses over a pulsing cycle) but also a final temperature, after 90 seconds of effective plasma treatments, comparable or lower than the threshold temperature for thermo-labile

objects processing. Corresponding heating rates for these DC values are in the range of 0.15 to 0.30 °C/sec.

The driving frequency of the plasma pulsing as also an effect on the heating characteristic (see figure 3.4.3) and this additional parameter can be further exploited to tune the temperature values during treatments.

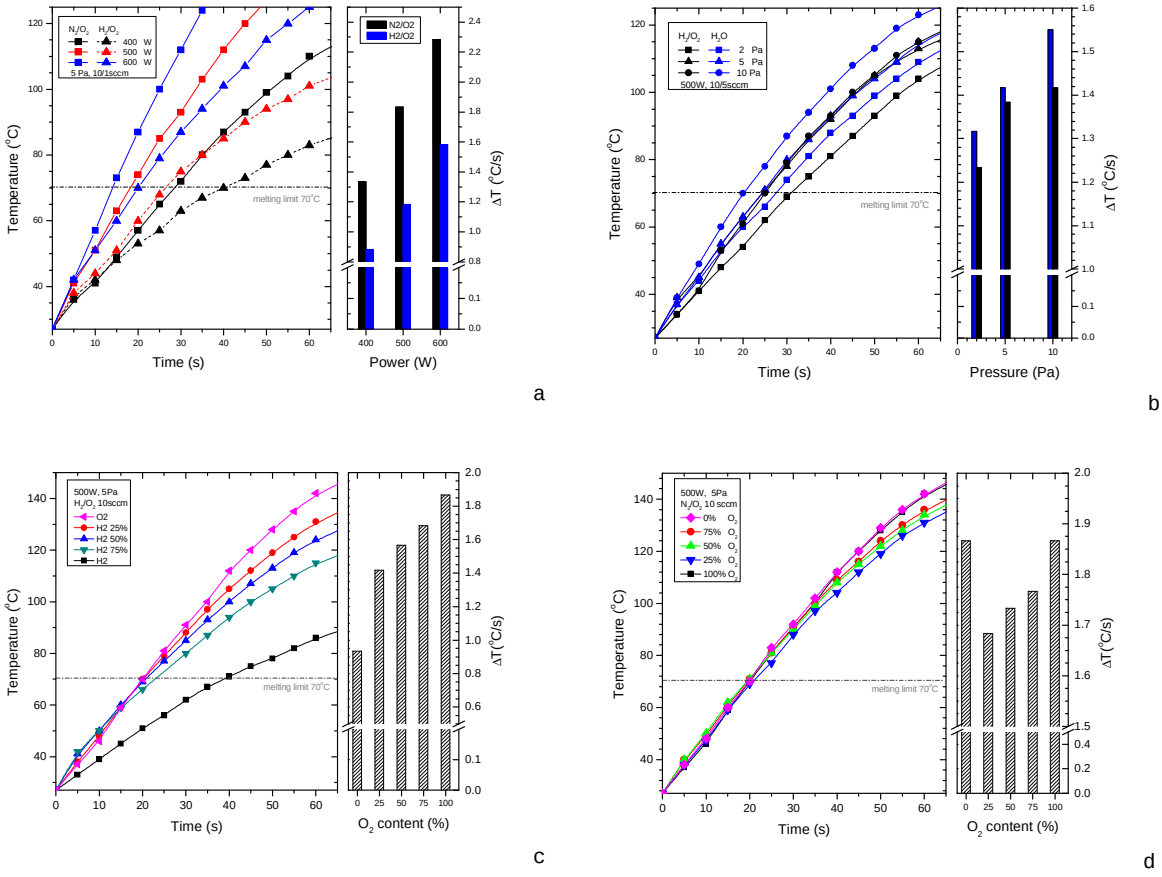

Figure 3.4.4 Measured heating curves and calculated heating rates for polystyrene substrates at different (a) delivered RF powers, (b) operating pressures (c and d) oxygen content in the discharge mixtures.

In order to have a full characterization of sample heating during plasma treatments, the complete set of external discharge parameters (power, pressure, oxygen content) was investigated in the range accessible with BIODECON reactor by means of IR pyrometry (see figure 3.4.4 a,b,c and d). In this way a complete dataset about sample temperature

was obtained in order to forecast final temperature of thermo-labile materials after a specific plasma treatments or sequence of treatments. This was important especially for polystyrene well-plates decontamination experiments presented in the next section.

Being able to predict the final temperature after plasma treatment with a given parameters set up allowed to decide a suitable sequence of treatments steps before experiments, in order to avoid substantial damage to the treated objects. A simple Excel tool calculator based on heating rates data was developed to predict samples final temperature, where two examples of the output are presented in figure 3.4.5a and 3.4.5b. This graphs show final temperature of plasma treatments as a function of treatment time for nitrogen oxygen discharge (chosen as example) at two different values of duty cycle. The others treatment parameters are the same in the two cases as well as the total effective treatments time (4 minutes). The black dots in graphs of figure 3.4.5 represent control measurements performed at the end of the plasma treatments to check the correctness of the calculation.

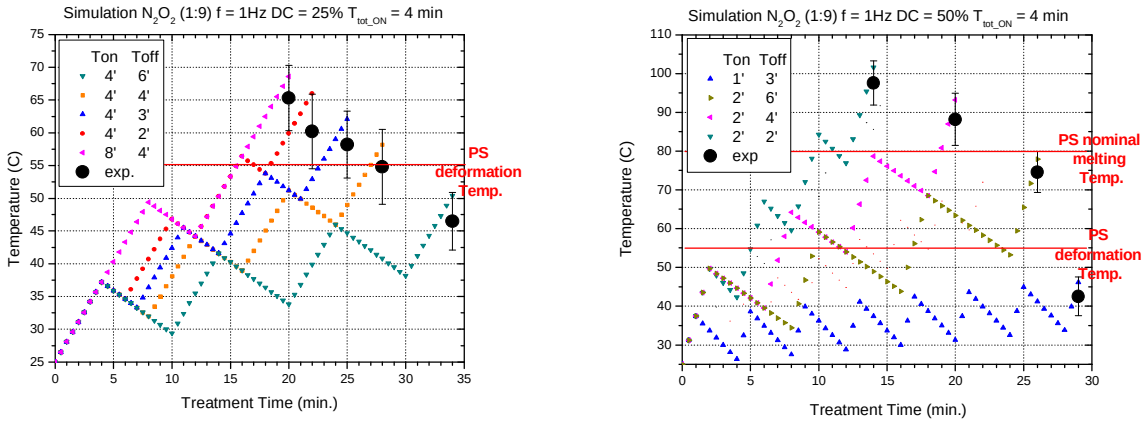

Figure 3.4.5 Calculated heating rates and measured final temperatures for polystyrene substrates at different cooling times combination for N_2O_2 discharge for different duty cycles (a) 25% DC (b) 50% DC.

In both cases it is shown how tuning of the cooling times between treatments steps at given DC and pulsing frequency conditions can be used to keep the overall temperature below the threshold for the complete duration of the plasma treatment. During experiments involving decontamination of polystyrene well plates (described later, in

chapter 6.1) it was found that extended objects exhibit irreversible structural deformations at temperatures well below the nominal glass transition temperature of the polymer. This lower temperature threshold was called deformation temperature and is most likely linked to the action of internal stress forces within different parts of the treated objects. In graph 5b it is shown how lowering the ratio between treatments and cooling times this new temperature limit can be fulfilled even if the total treatments times became much longer compared to the effective plasma ON times (effective time / total time = 0.14).

In conclusion at the actual level the measurements presented here provides a fast and efficient operational tool to perform plasma treatments at a controlled temperature.

The limit of this approach is implicit in its empirical character, these data and the Excel calculator tool are limited to polystyrene objects (or to materials with similar specific heat) and they cannot be used for extrapolation outside the parameters space investigated.

The IR diagnostic and the measurement technique described here could be used for further investigation of energy flux balance between plasma and substrate [1,2] in order to asses the relative importance of mechanisms leading to substantial sample heating within different plasma conditions of interest for decontamination/sterilization treatments. It follows the scheme for experiments:

When a solid comes in contact with plasma, energy transfer takes place. The general power balance at the substrate is given by:

$$\begin{aligned} &Q_{in} = H_S^{'} + Q_{out} \\ &PlasmaON: \quad H_S^{'} = Q_{in} - Q_{out} \\ &PlasmaOFF: \quad H_S^{'} = -Q_{out} \end{aligned} \qquad [3.4]$$

Where $H_S^{'} = mc\left(dT_S / dt\right)$ is the substrate enthalpy, Q_{in} is the total energy influx and Q_{out} summarizes the heat losses due to radiation, thermal conduction by the surrounding gas and substrate holder. The difference between the plasma ON and plasma OFF balances gives the total influx:

$$Q_{in} = mc\left[\left(\frac{dT_S}{dt}\right)_{heat} - \left(\frac{dT_S}{dt}\right)_{cool}\right]_T \qquad [3.5]$$

That can be calculated by measuring the slopes of sample temperature in experiments like the ones described in this chapter (Fig. 3.4.5).

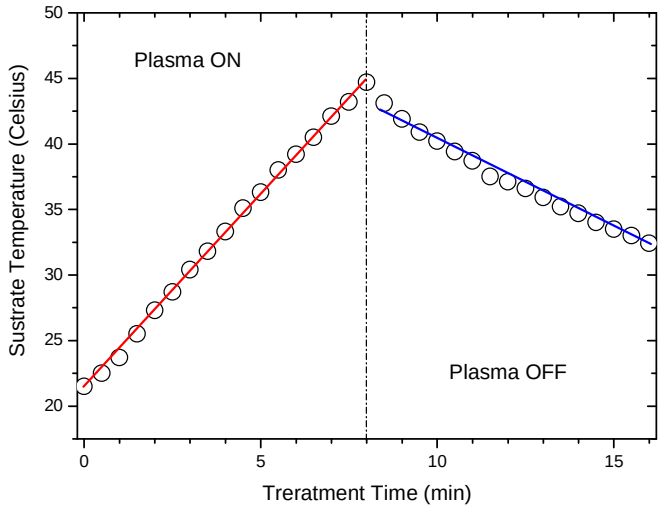

Fig. 3.4.5 Example of temperature slope measurements.

The measured total energy influx can be then linked by surface integration to the energy flux density J_{in} and this quantity can be expressed in terms of particles fluxes and plasma parameters.

J_{in} is in general the sum of different terms, different energy fluxes related to electrons, ions, neutrals and photons, but in a plasma environment usually the leading terms is the ionic bombardment and this can be expressed in terms of measurable quantities as:

$$J_{in}^{ion} = n_e \sqrt{\frac{kT_e}{m_{ion}}} \exp(-0.5) e_0 \left(V_{plasma} - V_{floating}\right) \qquad [3.6]$$

If a correlation could be established between ion bombardment and samples heating it will be possible to simplify the picture of etching mechanism in the plasma – biomaterials interaction by merging two mechanisms into a single scheme.

References

[1] Wolter M Stahl M and Kersten H 2009 *Plasma Process. Polymer.* **6** pp. S626-30.

[2] Kersten H Stoffels E Stoffels W W Otte M Csambal C Deutsch H and Hippler H 2000 *Journal of Applied Physics* **87**(8) pp. 3637-45.

4 Quartz crystal microbalance in situ diagnostic.

4.1 In-situ QCM diagnostic assessment

4.1.1 Samples preparation

The similarity of the elimination rates independently on the amino acid chemical structure of proteinaceous residues [1] (e.g., prions), allows comparing results obtained from non-pathogenic proteins as BSA to those of their pathogenic forms. Model contaminations used in this work consist of BSA protein films deposited on QCM gold coated crystals with a calibrated pipette. For cleaning, the QCM crystals were placed in an acetone bath and ultrasonicated for 5 minutes and then rinsed with milliQ water. Afterward, the crystals were kept for 30 minutes in an oxidizing bath (H_2SO_4 and H_2O_2 3:1, standard chemical grade) to remove organic traces from the surface and then rinsed again with milliQ water. Cleaned crystals were stored in an ethanol bath and dried with compressed nitrogen just before protein deposition. BSA protein was diluted at different concentrations in 2,2,2 TriFluoroEthanol (TFE, CF_3CH_2OH, from Fluka, assay > 99%), which is commonly used as a solvent in biochemistry for proteins and peptides to probe biomolecular structure,[2] and spotted on the QCM crystals. TFE was chosen also for its low boiling point (351,15 °K) that results in its fast evaporation. A low evaporation time is desidered to reduce the coffee ring effect [3] in the protein films deposited on QCM crystals.

Protein films deposited according to protocol described above results in homogenous coverege of the QCM crystals without formation of a distinguishabe coffee ring edge for all the tested solutions (profilometric measurments of the coated samples reveal no structures above the rms roughness value of the bare crystals, 300 ± 25 nm), after protein deposition the measured rms roughness value is 250 ± 25 nm.

4.1.2 In-situ QCM measuraments

Examples of the QCM signal as recorded by an oscilloscope during the plasma process are shown in figure 4.1.1 and figure 4.1.2.

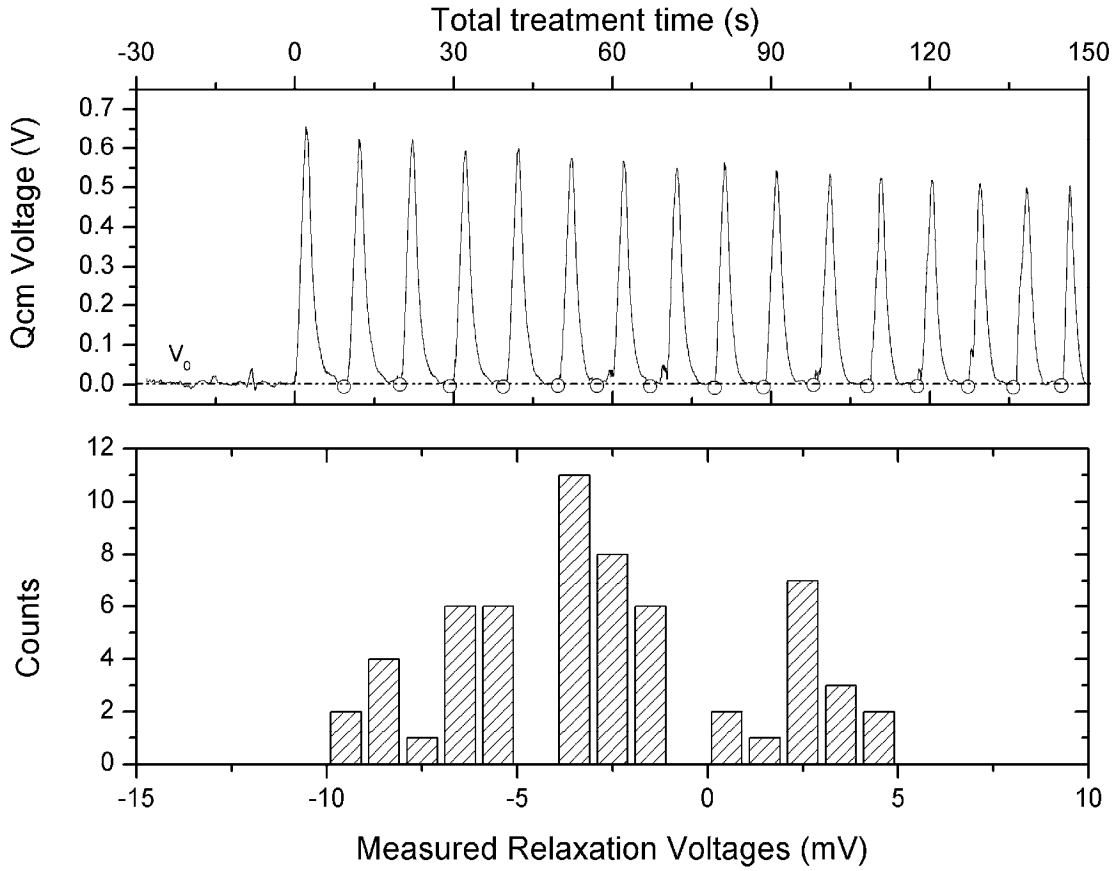

Figure 4.1.1. Top panel: apparent mass change due to plasma-crystal interaction during QCM measurements on a clean crystal exposed to several cycles of plasma treatment, O_2/Ar = 0.27, P = 350 W, p = 10 Pa, Φ_{tot} = 20 sccm, 80% DC and f = 100 mHz, the black circles indicate the measured relaxation voltages. Lower panel: distribution of the measured relaxation voltages.

The strategy for QCM measurements during the plasma discharge is derived from the work of Heil at al. [4] and consists in pulsing the plasma discharge and measuring the crystal frequency shift during the plasma-off phase after each treatment cycle. The effect of plasma discharge on a blank QCM crystal is shown in Figure 1. In the top panel the

QCM response to a series of plasma pulses is plotted: a sharp increase in the monitor output voltage signal is observed when the discharge is ignited, while during the off phase, the signal relaxes at the initial voltage offset level V_0. The black circles in figure 4.1.1a indicate the relaxation voltage measurement points after each plasma cycle. The spike during the plasma-on phase can be considered as an artifact due to AT-cut crystal response to pressure and temperature variation as well as to parasitic voltages developing during the active phase of the discharge.

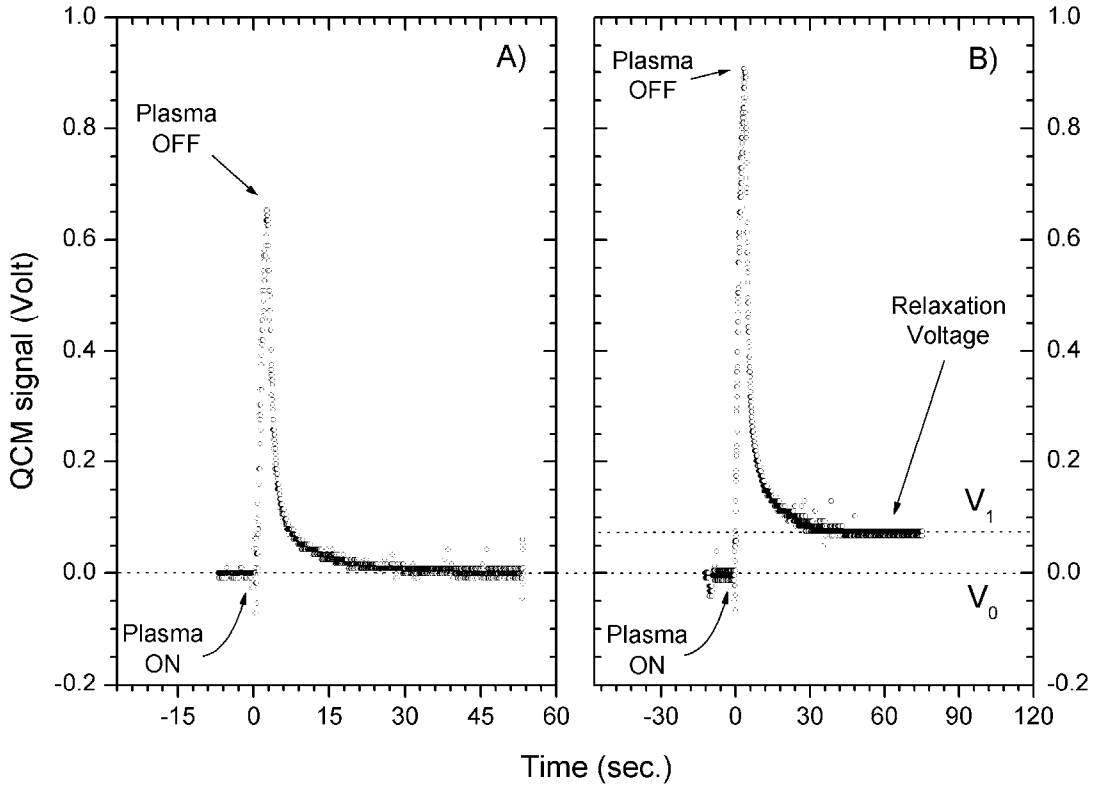

Figure 4.1.2. Single plasma pulse QCM measurements, apparent mass change due to plasma-crystal interaction A) Left panel: clean crystal exposed to Ar/O_2 plasma B) Right panel: protein coated crystal exposed to Ar/O_2 plasma

The lower panel of figure 4.1.1 shows the histogram of the final relaxation voltages measured after each plasma cycle. The statistics has been calculated using a voltage measurements dataset from a sixty plasma cycles experiment. The mean value of the recorded voltages is -2 ± 4 mV, with the lowest and highest recorded voltages of -9.7 mV

and +4.5 mV respectively. Experimental errors due to fluctuations in the offset voltage became comparable to measured etching rates only for values below 0.1 $ng \cdot s^{-1} \cdot mm^{-2}$. It can be seen that the mean of the histogram is not precisely zero. This is because of the numerical algorithm used for automatic identification of the voltage measurement points based on the identification of the minima in the smoothed QCM output signal, which results in a clean crystal voltage measurements distribution slightly unbalanced towards negative values.

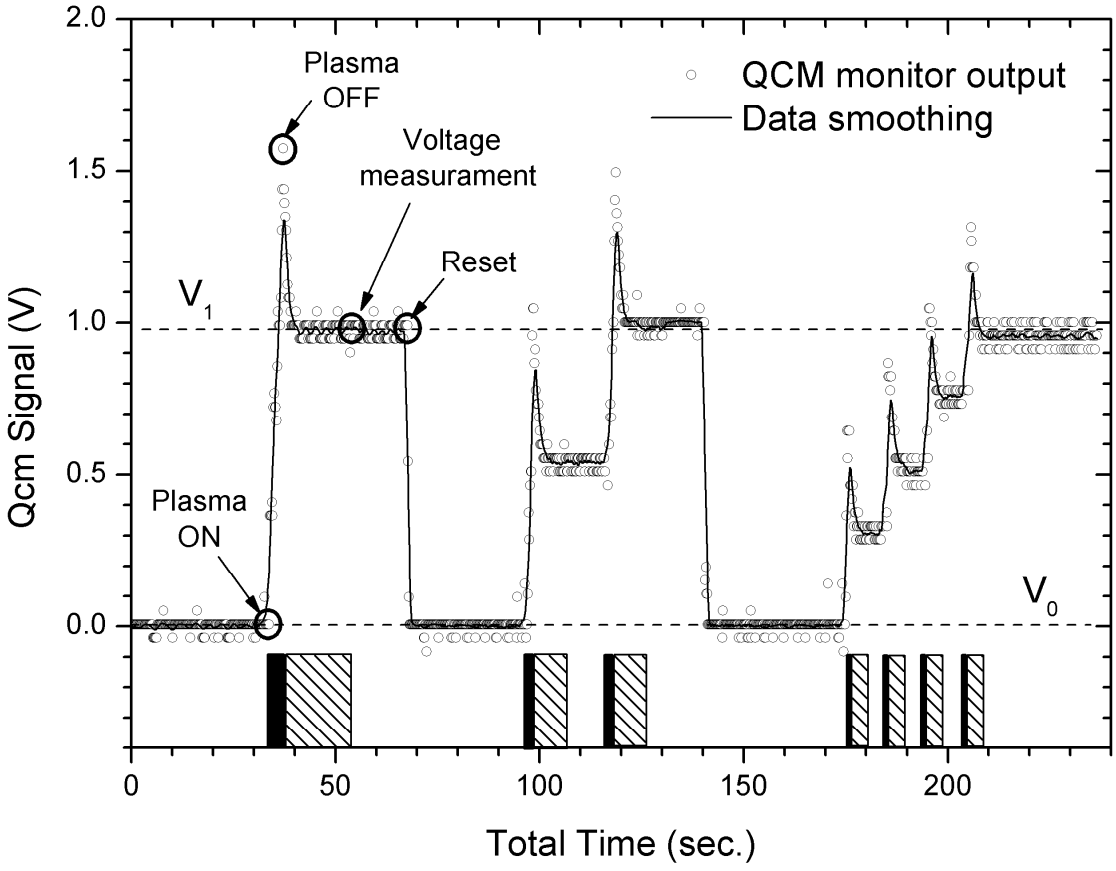

Figure 4.1.3. QCM measurements, apparent mass change due to plasma-crystal interaction for different pulsing frequencies but identical total treatment time (t_{tot} = 4 sec.). Black columns indicate the plasma ON time, shaded columns indicate the standard plasma OFF time at 20% DC used in the decontamination experiments. Plasma parameters are O_2/Ar = 0.27, P = 350 W, p = 10 Pa, Φ_{tot} = 20 sccm and BSA solution concentration = 10 $mg \cdot ml^{-1}$.

An example of single plasma pulse measurements on protein covered crystals are shown in figure 4.1.2b, a sharp increase in the monitor output voltage signal (proportional to the crystal frequency shift) is observed when the discharge is ignited, while during the off phase the signal relaxes to a new voltage level, V_1, slightly higher than the starting voltage. The same kind of peak is observed even if a clean crystal is measured. However in this case the signal relaxes at the initial voltage offset level V_0 (see figure 4.1.2a). The spike during the plasma-on phase can be considered an artifact due to AT-cut crystal response to pressure and temperature variation as well as to parasitic voltages developing during the active phase of the discharge. According to these observations, the difference between the offset voltage and the relaxation voltage is interpreted as a quantity proportional to the mass loss occurred during a plasma treatment and the difference between two consecutive relaxation voltages is interpreted as the mass loss occurred during a plasma-on cycle.

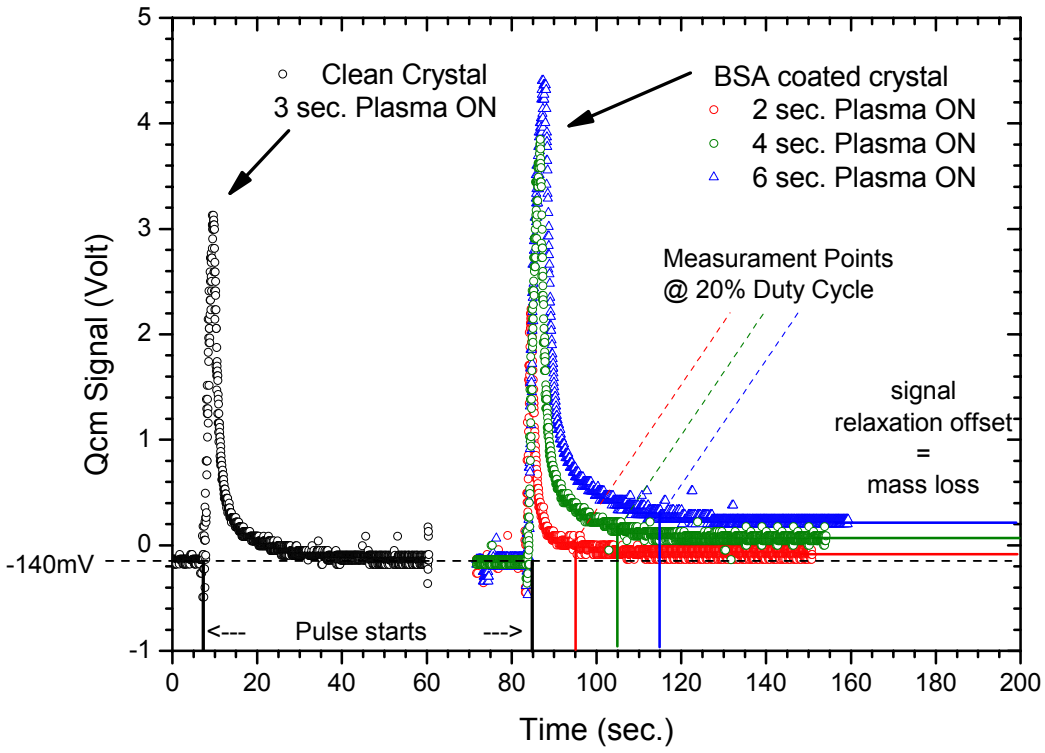

Figure 4.1.4. QCM measuraments, apparent mass change due to plasm crystal interaction for different plasma ON time. Relaxation voltages at 80% DC are indicated on curves corresponding to the BSA coated crystals.

An example of QCM measurements on protein-covered crystals is shown in figure 4.1.3. Three series of plasma pulses at different repetition frequencies are shown for a total plasma-on time of 4 seconds for each series. After each run, the frequency is changed and the QCM monitor is reset to zero voltage. When the discharge is ignited on a protein covered crystal a sharp increase in the monitor output voltage signal is again observed but now, during the off phase, the signal relaxes to a new voltage level, V_1, slightly higher than the starting voltage V_0. Moreover, it is observed that the same final relaxation voltage is reached using different treatment time steps, but keeping the total plasma on time fixed. An example of the identification of the relaxation voltage is shown in figure 4.1.4. Data show that at 20% DC the artifact signal induced by plasma ignition relax to the plateau voltage, at the end of a full cycle, therefore this minimum ratio between plasma ON and plasma OFF time must be used during experiments in order to avoid overestimation of the relaxation voltages and consequently of the deposit mass change.

5.1.3 Analysis and parameterization of the mass loss curves

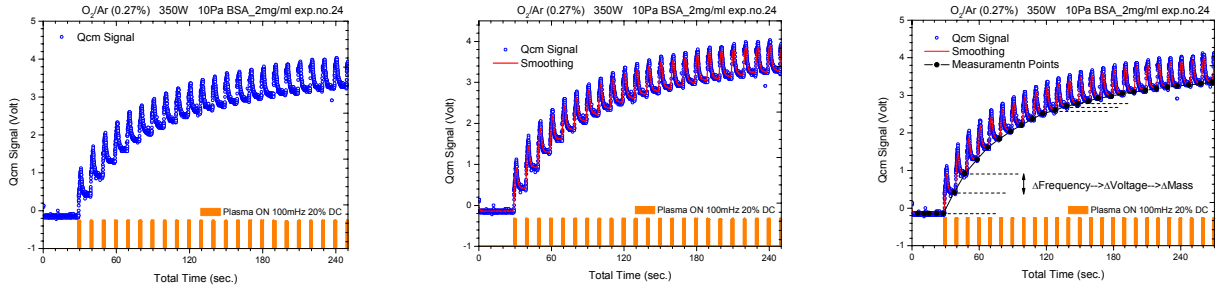

Figure 5.1.5. Data analysis for raw QCM data. a) QCM monitor output b) numerical smoothing c) identification of the relaxation points (null first derivative in the plasma OFF phase) after each plasma treatment cycle.

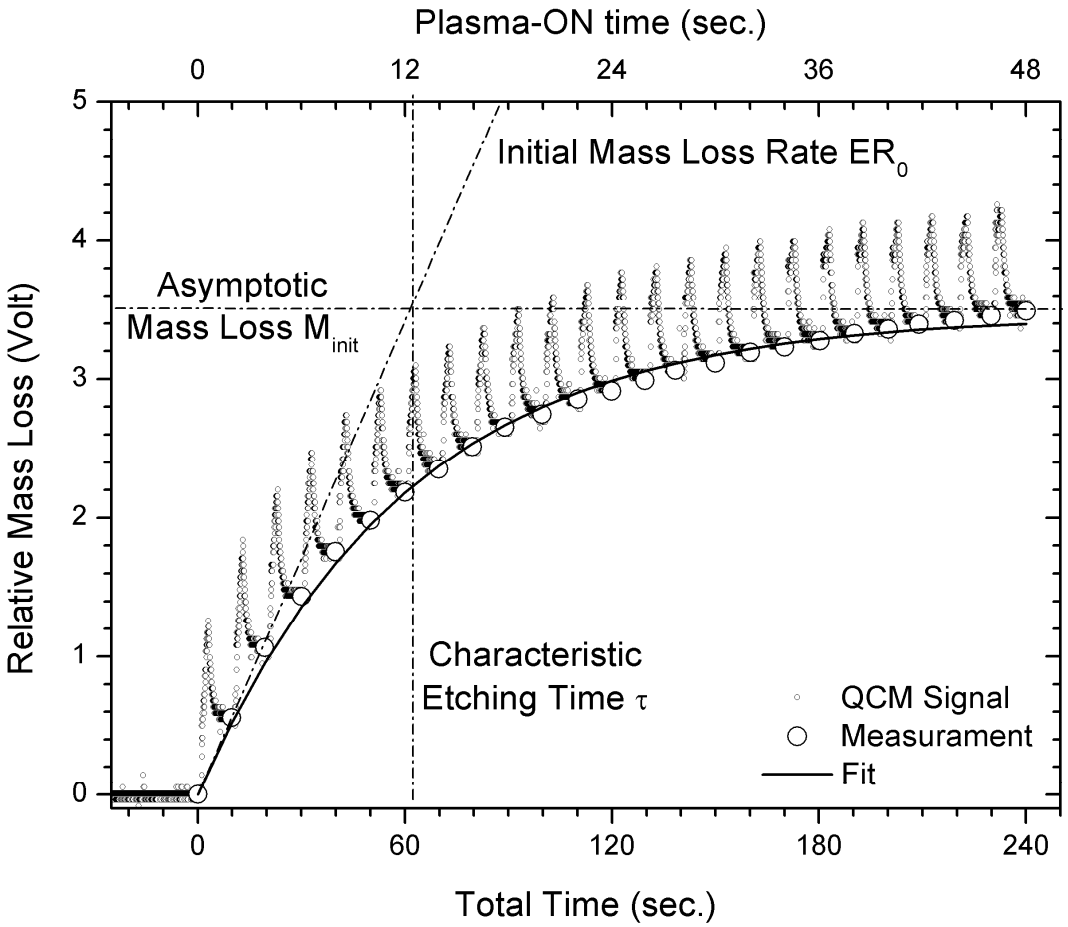

Figure 4.1.6. In situ QCM measurements during protein film removal pulsed plasma process. Plasma treatment parameters are O_2/Ar= 0.27, P = 350 W, p = 10 Pa, Φ_{tot} = 20 sccm, BSA solution concentration = 1.5 mg·ml^{-1}. Bottom x-axis display total treatment at 20% DC and f = 100 mHz, top x-axis display effective plasma-ON time.

If the analysis procedure shown in figure 4.1.3 is applied during a pulsed plasma treatment (see figure 4.1.5 and 4.1.6), mass loss curves describing the evolution of the material removal from the surface exposed to plasma are obtained by measuring the QCM voltage signal at consecutive relaxation points. The open circles in figure 4.1.6 identify the measurement points after signal relaxation.

The mass loss curves can be described by an exponential function of the form:

$$M_{loss} = M_{init} \cdot (1 - e^{-\frac{t}{\tau}}) \qquad [4.1]$$

In the above equation, M_{init}, is the mass initially deposited on the crystal, t is the effective plasma treatment time, and τ is the characteristic etching time. In this work, the end point is defined as the moment when the etch rate, i.e. the voltage difference between the measurement points of two successive plasma cycles, doesn't change anymore or drops below the sensitivity of the monitoring oscilloscope. The self-limiting nature of the process is described by the term $(1 - e^{-t/\tau})$, which may be related to two factors: the raising concentration of non-volatile compounds on the film surface and the reduction of the effective interaction area due to substrate exposure, as shown later in the text. In the example of figure 4.1.6, the values of M_{init} and τ, as determined from least square fit of the data, are respectively 0.19 $\mu g \cdot mm^{-2}$ and 12.07 s.

The time dependent protein mass removal rate *ER(t)* can be expressed by the time derivative of Equation (4.1):

$$ER(t) = \frac{dM_{loss}}{dt} = \left(\frac{M_{init}}{\tau}\right) \cdot e^{-\frac{t}{\tau}} = ER_0 \cdot e^{-\frac{t}{\tau}} \qquad [4.2]$$

The constant multiplicative term (M_{init}/τ), or ER_0, represents the initial mass removal rate, and is plotted in figure 4.1.6 as the slope of the *ER(t)* curve at $t = 0$ s. This specific functional form was chosen as an empirical model for the following two reasons: (i) it is the simplest model that both fits the data (see Figure 3) and exhibits the proper asymptotic behavior (finite etching rate at $t = 0$ and zero etching rate at $t = \infty$); (ii) under the assumption that the etching rate *ER(t)* is limited by the number of non-etchable sites on the surface θ, and proportional to the number of etchable sites on the surface $1-\theta$, the non-etchable film formation can be compared to a simple model which assumes a constant exposure rate for non-etchable compounds:

$$\frac{d\theta}{dt} = k \cdot (1 - \theta) \qquad [4.3]$$

where $k \sim \tau^{-1}$ is the rate constant. This leads to an integrated expression for the etching rate of the form:

$$ER(t) \propto 1 - \theta = \exp(-k \cdot t) \qquad [4.4]$$

Additional blocking mechanisms (e.g. substrate exposure) under similar hypothesis might contribute to the lowering of the etching rate by introducing additional time constants. Time dependent mass removal rates for protein films have already been reported in plasma decontamination experiments, when low levels of biological contamination were present. [5] Equations (4.1) and (4.2) in their simple forms are a parameterization of the experimental data and serve to determine the principal features of the mass loss curves time dependency, allowing thus a direct and quantitative comparison between the different experimental conditions.

5.1.4 Thermal effects on the QCM signal

If the temperature of the quartz crystal is constant during the plasma treatment, then the detected change of mass per time is accurate. If the temperature fluctuates, real mass changes versus time are measured concurrent with the apparent mass changes caused by the temperature dependence of the quartz crystal. Consequently, the temperature dependent apparent mass changes must be characterized and minimized to allow the QCM to provide an accurate monitoring of surface reactions and biomaterials etching.
In quartz crystal resonators, the change of frequency (f) responds to a change in temperature (T - T_o) according to [6,7]

$$\Delta f = (f - f_0) = a_1 f_0 (T - T_0) + a_2 f_0 (T - T_0)^2 + a_3 f_0 (T - T_0)^3 + \ldots \qquad [4.5]$$

where f_0 is the frequency at T_0, T_0 is any reference temperature, and a_1, a_2, and a_3 are empirically determined constants related to the crystal orientation.[8] For the AT-type quartz resonators employed in the following experiments, equation 4.1.5 is cubic and dominated by the a_1 and a_3 values.[9] Consequently, the first derivative (df/dT) provides a frequency-temperature dependence that is essentially quadratic with respect to temperature. The local minimum is centered near room temperature and is typically negative in value. This produces two "crossover" temperatures that display zero frequency-temperature dependence. Typical AT-type resonators have relatively small frequency-temperature dependence over a large temperature range between -45 and 90

°C. For an angle of crystal cut near 35° 20”, the error is ≤ ±1 ppm/°C. [8] At temperatures greater than 90 °C, the frequency-temperature dependence is positive and dramatically increases with increasing temperature.

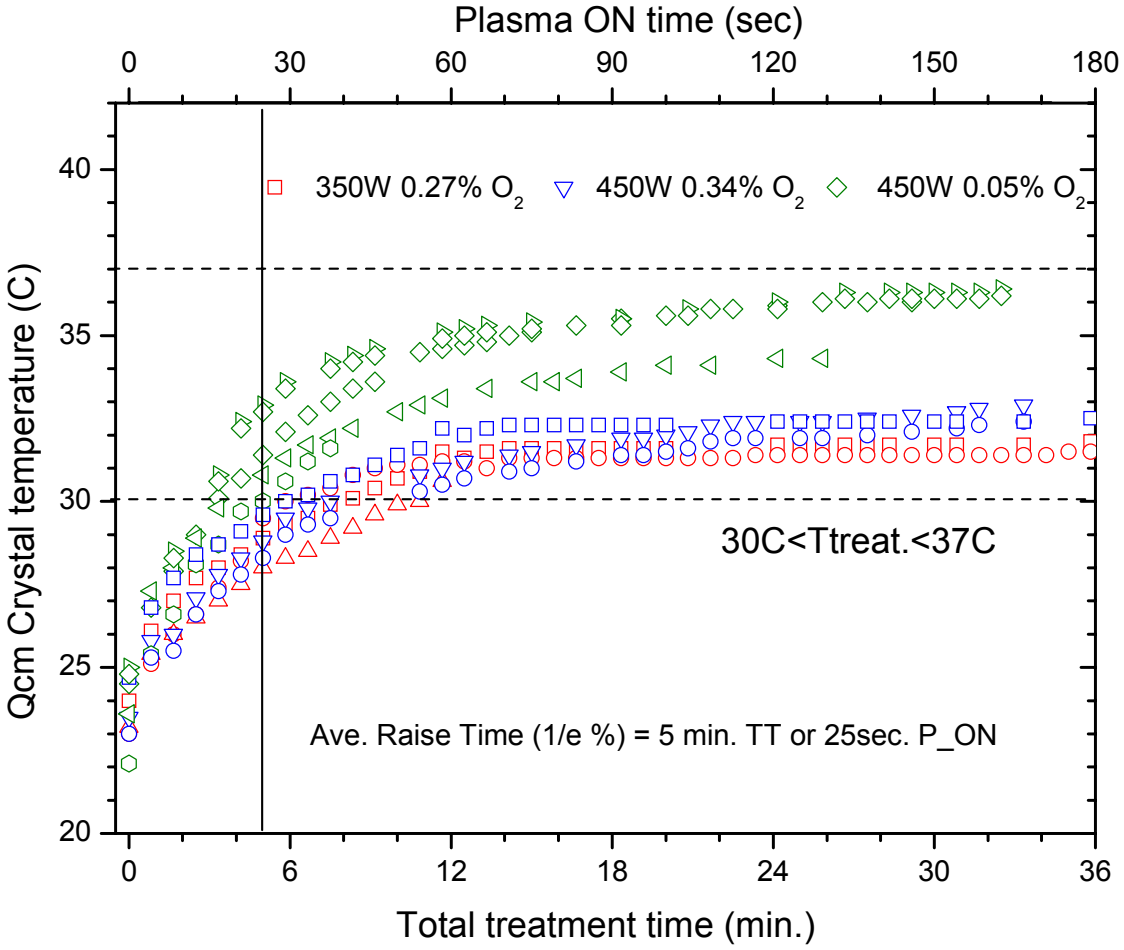

Figure 4.1.7. QCM crystal temperature profiles during different plasma processes. Pulsing frequency is 100 mHz at 20% DC.

QCM crystal temperature was monitored during plasma pulses by means of an IR pyrometer. Figure 4.1.7 shows QCM crystal temperature profiles evolution for three different plasma parameter combinations, at different RF delivered power and different oxygen gas content in the gas discharge mixture. Several experimental runs in identical plasma conditions are indicated in figure 4.1.7 by the same data point color but different shape. These temperature profiles are measured on clean crystals by pulsing the discharge at 100 mHz with 20% DC. The QCM crystal holder is kept thermally floating and the

cooling circuit is switched off in order to record consistent df/dT values when plasma induced temperature variations determine apparent mass changes.

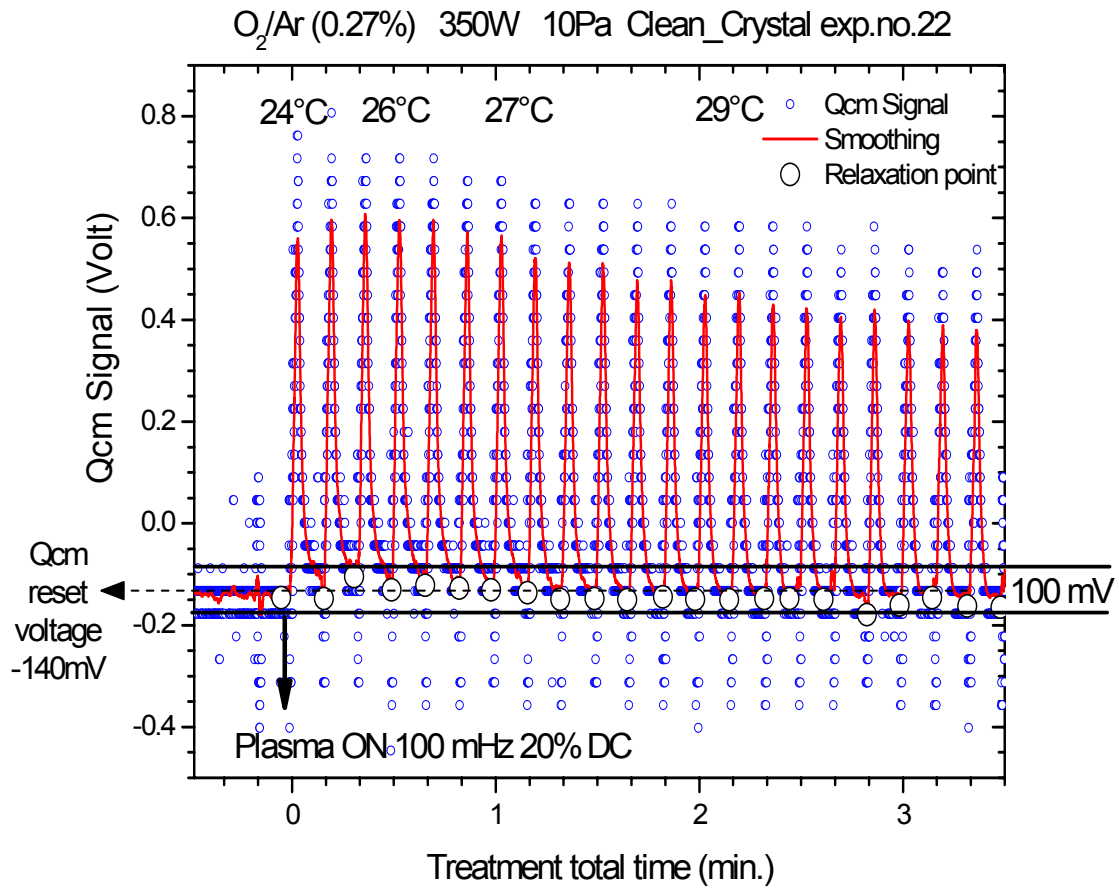

Figure 4.1.8. QCM crystal frequency shift and corresponding time-averaged crystal temperatures in typical etching experiments conditions.

It is evident form the data shown in figure 4.1.7 that even in absence of forced cooling the average temperature of the crystal (averaged over a full plasma pulse cycle) is not exceeding boundaries the stability region for our AT quartz. In order to establish the influence of the average temperature drift on the frequency shift measurements the temperature of the QCM crystal was measured simultaneously with the clean crystal frequency shift during a plasma process operated in typical etching experiments conditions, results are shown in figure 4.1.8.

The black circles in figure 4.1.8 mark the relaxation points at which the frequency shift measurements are recorded. The instantaneous effect of the temperature variation (spikes

in the QCM output signal) is more pronounced at the initial stages of the treatment where temperature variation with time is higher (between 1 and 2 °C/min. depending on the experimental conditions). Anyway the temperature variation averaged over each cycle (see figure 4.1.7) is not affecting the response of the measurement technique. The relaxation points lie always close to the QCM monitor reset voltage and within the voltage measure precision, dominated by the signal discretization introduced by the oscilloscope, indicating no average frequency shift and thus no net mass loss or gain.

4.1.5 Test calibration for the frequency shift

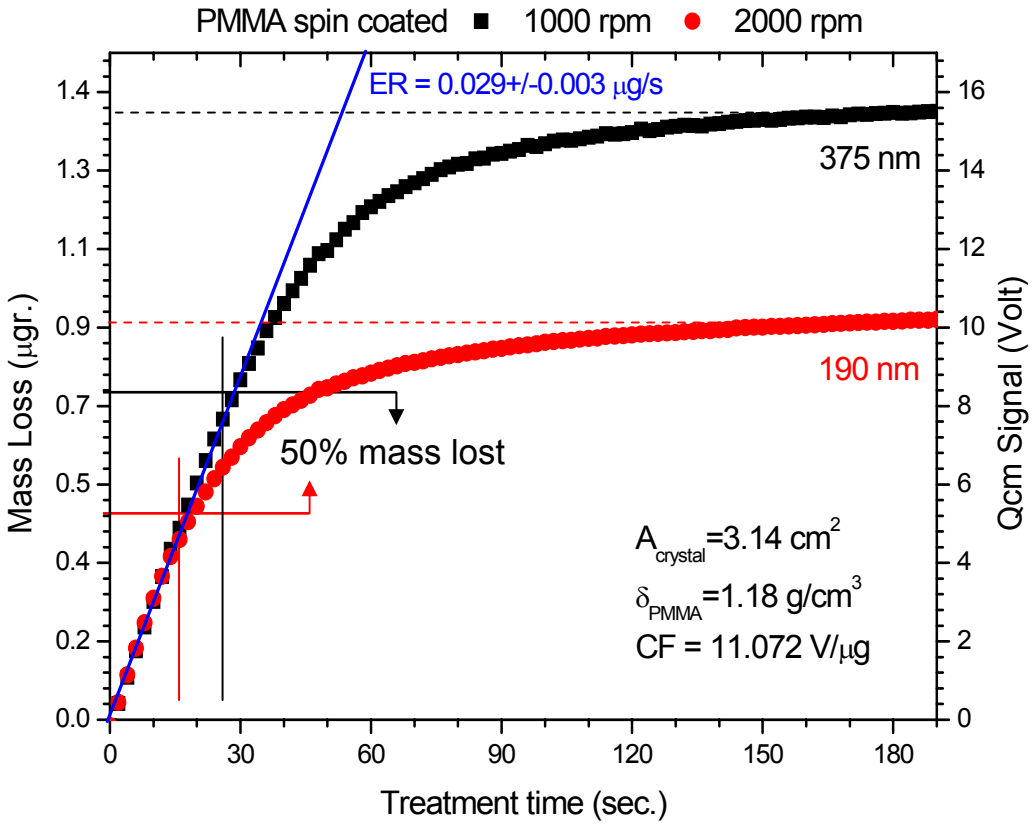

Figure 4.1.9. Test mass-voltage calibration experiments for spin coated PMMA. Plasma treatment parameters are O_2/Ar= 0.27, P = 350 W, p = 10 Pa, Φ_{tot} = 20 sccm.

Depending on the material deposited QCM crystal a calibration procedure for the conversion between frequency shift and mass change (i.e. between QCM monitor voltage

output and mass change in our experiments) have been developed. The procedure for calibration is internal to the experiment and uses the horizontal asymptotic voltage values of the mass loss curves that indicate the end-point mass removed by plasma treatment. By measuring different initial mass deposit conditions and by simple geometric arguments the conversion between mass change and voltage output can be derived, as it is shown in figure 4.1.9 for spin coated PMMA etching experiments. A series of calibration experiments for protein films will be described in chapter 4.2.

References

[1] Kylian O, Rauscher H, Denis B, Ceriotti L and Rossi F 2009 *Plasma Process. Polym*., **6**, pp. 848–54

[2] Buck M 1998 *Quarterly Reviews of Biophysics*, **31**(3), pp. 297-355

[3] Shen X, Ho C M and Wong T S 2010 *J. Phys. Chem. B*, **114**(16), pp. 5269–74.

[4] Heil S, Kudlacek P, Langereis E, Engeln R and Van de Sanden M 2006 W. Kessels, *Appl. Phys. Lett.,* **89**(13), 131505(3).

[5] Rossi F, Kylian O, Rauscher H, Gilliland D and Sirghi L 2008 *Pure Appl. Chem.***, 80**(9), 1939-51.

[6] Fairweather D and Richards R C 1957 *Quartz Crystals as Oscillators and Resonators*; Marconi's Wireless Telegraph Co.: Chelmsford, England..

[7] Frerking, M. E. 1978 *Crystal Oscillator Design and Temperature Compensation*; Van Nostrand Reinhold Co.: New York.

[8] Bechmann R 1956 *Proc. Inst. Radio Eng.*, **44,** pp. 1600-07.

[9] Bechmann, R. 1960 *Proc. Inst. Radio Eng.*, **48**(8), pp. 1494.

4.2 Self limiting etching kinetics

4.2.1 Mass-voltage calibration experiments for protein film

The effect of Ar/O_2 plasma treatment on protein films is shown in figure 4.2.1 for different concentrations of the protein solution. All the discharge parameters (i.e. applied RF power, processing pressure and gas flow) were kept constant for all the treatments and every data series is the average of at least three independent experiments.

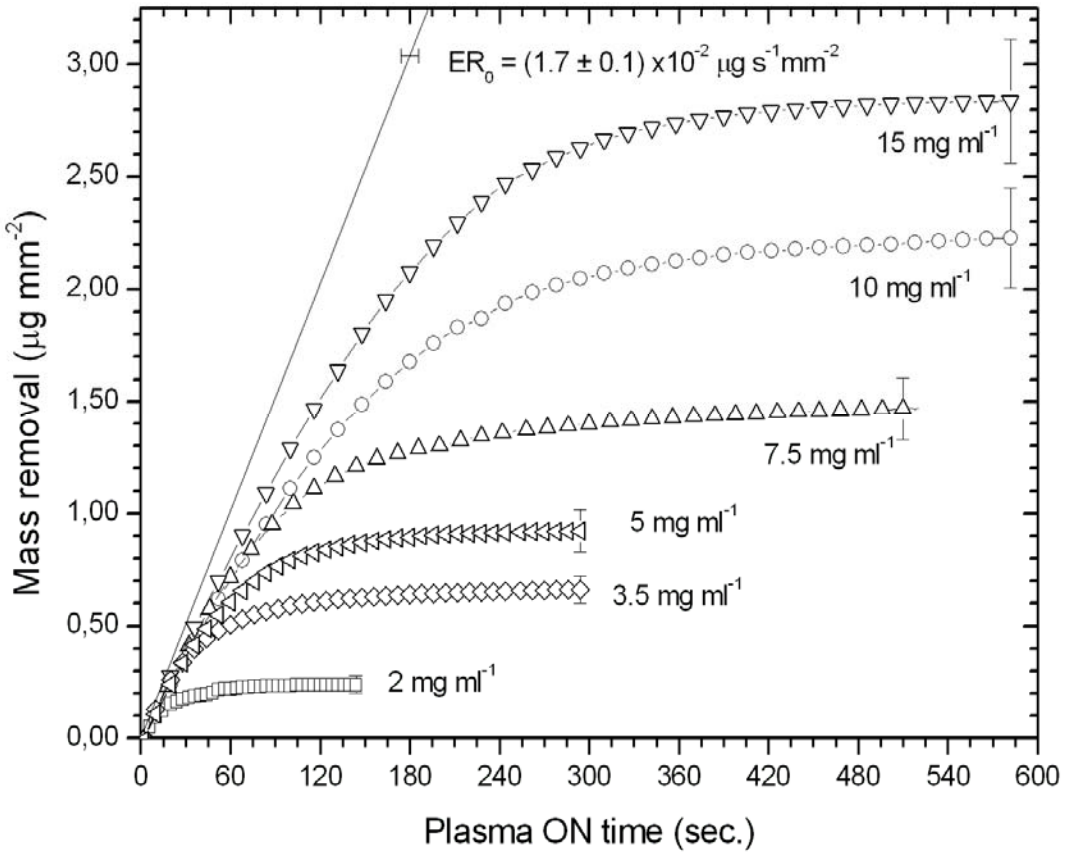

Figure 4.2.1. Mass loss curves as a function of different initial BSA protein solution concentration deposited on the QCM crystal. Plasma treatment parameters are O_2/Ar = 0.27, P = 350 W, p = 10 Pa, Φ_{tot} = 20 sccm.

The mass loss curves show a saturation behavior for long treatment times indicating that the etching process of the protein layer approaches its endpoint, the position of M_{init} is concentration-dependent and shifts to higher values as the amount of deposited material increases, also the characteristic etching time τ shifts to higher values following the same trend. The ratio of these two quantities, ER_0, remains almost constant (with the possible exception of the curve at 2 mg·ml^{-1}), therefore in the initial phase, all the curves show the same removal kinetics indicating that the same plasma-biomaterial interaction mechanism is operating. A summary of the descriptive parameters for this set of curves is given in Table 4.2.1.

Table 4.2.1. Summary of the descriptive parameters for different initial protein concentration set of mass loss curves.

Concentration	**M_{init}**	**τ(s)**	**ER_0**	**t_{trans}**
mg*ml^{-1}	**µg*mm^{-2}**	**s**	**ng*s^{-1}*mm^{-2}**	**s**
2	0.23 ± 0.04	20.0 ± 0.5	11.7 ± 2.2	n.m. [a)]
3,5	0.66 ± 0.06	40.3 ± 2.5	16.5 ± 2.4	n.m. [a)]
5	0.97 ± 0.04	60.2 ± 0.8	16.2 ± 0.8	43 ± 8
7,5	1.54 ± 0.14	92.2 ± 1.5	16.7 ± 1.8	75 ± 5
10	2.63 ± 0.22	152.0 ± 1.6	17.3 ± 1.6	155 ± 13
15	3.06 ± 0.28	181.0 ± 1.7	19.3 ± 1.9	205 ± 14

[a)] not measurable.

From the analysis of the mass loss curves presented, it results that the simple forms of equation (4.1) and (4.2) describes the main features of the mass loss kinetics, but poorly describe the details of the QCM signal evolution. This is evident, for example, from the mass loss rates (plotted in Figure 4.2.2 in a log scale) calculated from the mass loss curves already presented in figure 4.2.1. If equation (4.1.2) strictly holds a linear trend for *ER(t)* would be expected in semi-logarithmic plot against the treatment time. Data in figure 4.1.2 shows instead that the data trends in the range 0.97 to 3.06 µg·mm^{-2} are closely described by equation (4.1.2) when a two-valued characteristic etching time is considered, i.e. the process is described using two different time constants. In these

curves in figure 4.1.2 the kinetic of the mass loss rate at short treatment times is described by time constant value higher than the average characteristic etching time calculated on the complete dataset, while after a certain transition time the time constant describing the exponential decay assumes suddenly a value lower than τ, i.e. the decay of the mass loss rates is slower at short treatment times and is faster at long treatments times. Since the mass loss rate curves (equation 4.2) are described by the same set of parameters of the mass loss curves (equation 4.1) it is possible to derive from the observations described above that at the beginning of the treatment, the protein mass loss due to plasma exposure proceeds with a slower kinetic i.e. the material removal rate deviates slowly from ER_0, while after the transition point a new regime with a faster kinetics is observed, i.e. the instantaneous *ER(t)* drops rapidly to zero.

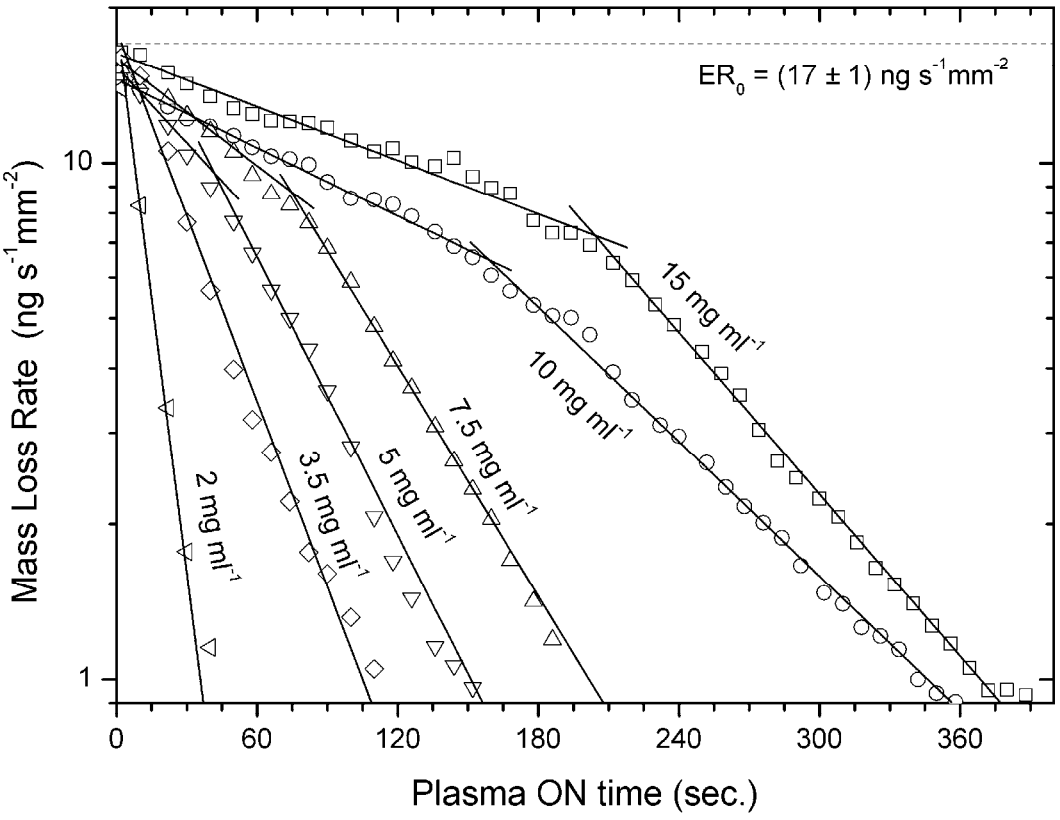

Figure 4.2.2. Kinetics of the time dependent mass loss rate for different initial solution concentration. Rates are calculated from mass loss curve shown in figure 4.2.1.

This sudden jump in the value of the parameter τ at the time t_{trans} is the indication of a modification in the conditions of the removal process. We note also that data points for the low contamination experiments (0.23 -0.66 μg·mm^{-2}) are well approximated by equation 2 and 3 using a single valued time constant.

Some indications about the surface processes related to the phenomenona described above can be derived from XPS and AFM surface analysis described in paragraph 4.2.4.

4.2.2. Influence of applied RF power on etching kinetics.

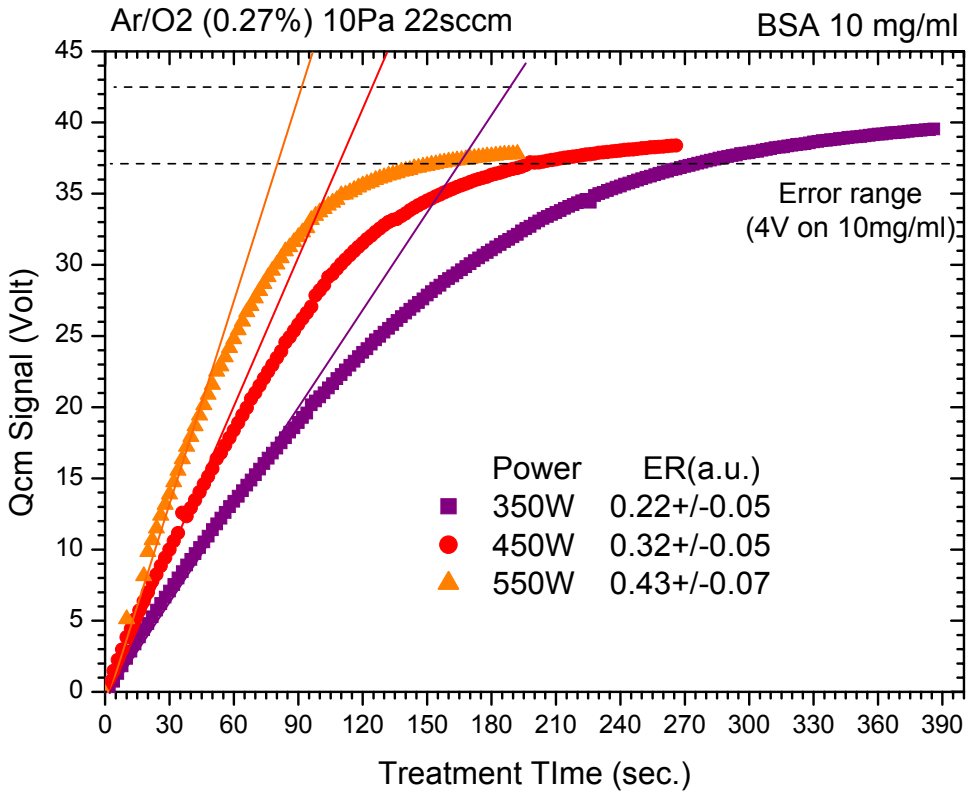

Figure 4.2.3) Mass loss curves as a function of different delivered RF power. Plasma treatment parameters are O_2/Ar= 27%, p= 10 Pa, Φ_{tot}= 20 sccm, BSA initial solution concentration was 10 mg/ml.

Figure 4.2.3 shows the protein film mass loss curves from Ar/O_2 plasma taken at constant pressure (10 Pa) and flow (20 sccm total), RF delivered power was varied between 350 W and 550 W, for our 5 L reactor chamber these values correspond to a power density variation between 0,07 and 0,11 W/cm^3, at this power levels the discharge was observed to be always in the inductive H-mode. The descriptive parameters M_{init}, τ and ER_0 for these curves are summarized in table 4.2.2. At all the power density levels the mass loss curves show approach to saturation region indicating substantial removal of the protein film. Characteristic etching time becomes shorter at higher power density level, changing from 152 s at 0.07 W/cm^3 to 63 s at 0,11 W/cm^3. Since the same BSA solution was used in all these experiments the values of M_{init} are the same within their experimental error (which is caused mostly by the reproducibility of the pipetting procedure), their average value is indicated as reference asymptotic mass loss in figure 4. These data show that increasing the power delivered to the plasma decreased τ while M_{init} was not affected. This means that the initial etching rate increases with RF power. Quantitatively ER_0 varied from 1,26 μg/s to 2,82 μg/s.

Table 4.2.2) Summary of the descriptive parameters for different RF delivered power set of mass loss curves.

RF Power	**δ_{Power}**	**M_{init}**	**τ**	**ER_0**
W	**W/cm^3**	**μg**	**s**	**μg/s**
350	0,07	191 ± 17	152 ± 2	1,26 ± 0,13
450	0,09	183 ± 16	95 ± 2	1,93 ± 0,20
550	0,11	178 ± 14	63 ± 1	2,82 ± 0,27

4.2.3. Influence of positive ions density on etching kinetcs

The experiments described in this section were designed to measure the fluxes of different species in the plasma phase (argon ions, oxygen radicals) and evaluation of their role in the volatilization of a model protein layer (BSA). Particle fluxes have been calculated using data from Langmuir probe and optical emission actinometry measurements. The key role for biomolecules etching of radical – ion combined

mechanism has been suggested by Stapelmann et al. [1] and a pure chemical scheme has been excluded by the results of the beam experiments.[2]

Also the influence of UV and heat on sterilization processes has been reported in literature[3], but in our experiments no significant levels of UV radiation have been recorded for Ar/O_2 discharge in the range 200 - 300 nm, and since the temperature of the quartz crystal as monitored in-situ by infrared pyrometry was kept below 42 °C for the whole treatments duration also the influence of temperature may be ruled out.

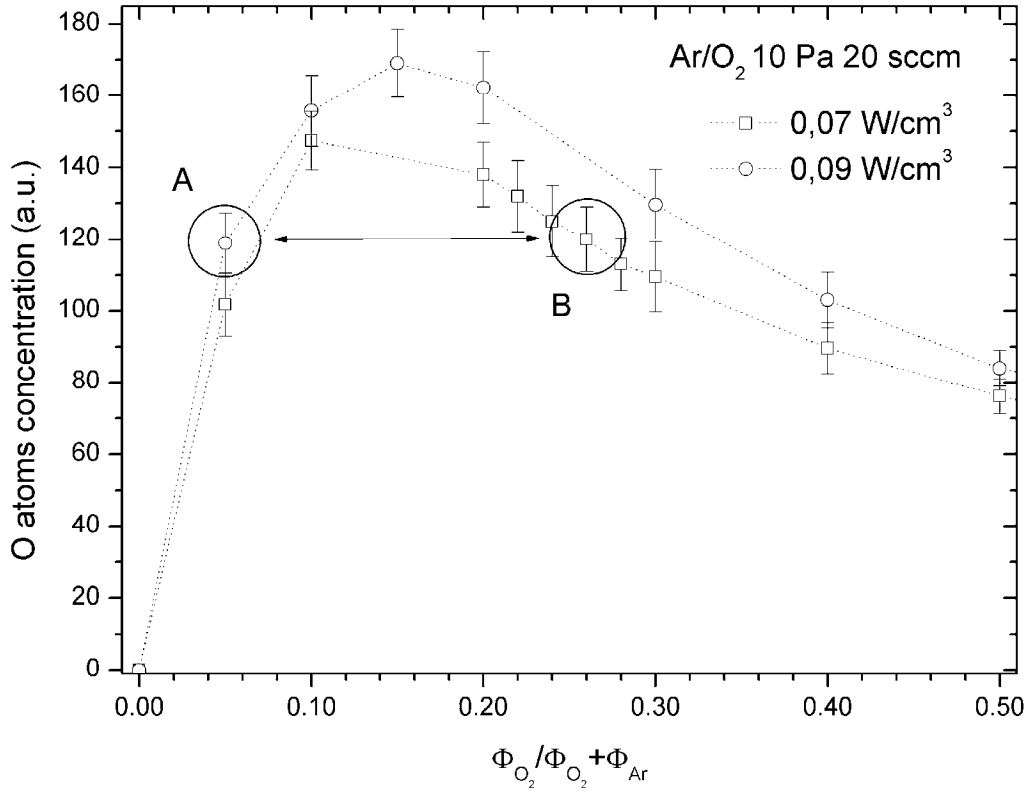

Fig. 4.2.4) Atomic oxygen radicals relative fluxes as a function of molecular oxygen content in the discharge working gas mixture for two different power levels. Optical emission actinometry measurements. Point [A] at $\Phi_{O2} / \Phi_{tot} = 0.05$, P = 350 W and point [B] at $\Phi_{O2} / \Phi_{tot} = 0.27$, P= 450 W show the same relative oxygen atom flux .

Figure 4.2.4 and 4.2.5 shows the variation of argon ions volume density and oxygen atoms relative concentration as a function of the oxygen gas concentration on the working gas mixture for two different power density levels. Changing the composition of

the Ar/O_2 mixture and the power level causes changes both in O atom and positive ion density, therefore to investigate the effect of ions on mass removal curves, two operational reactor parameters sets have been selected (points marked with the tags A and B in figures 4.2.4 and 4.2.5) for protein removal experiments. These two plasma conditions are characterized by the same O atoms density but different ions densities, such conditions can be obtained by simultaneously decreasing the O_2 over Ar flow ratio in the gas mixture and increasing the RF delivered power. Discharge condition B presents an ion density 6.2 times higher than discharge conditions A with the same O atoms density. However, the sheath voltage, measured by Langmuir experiments as $V_{sheath} = V_{plasma}-V_{float}$, was (11,5 ± 0,5) Volts for condition A and (12,3 ± 0,4) Volts for condition B, which means that in both situations nearly the same values of ion bombarding energies.

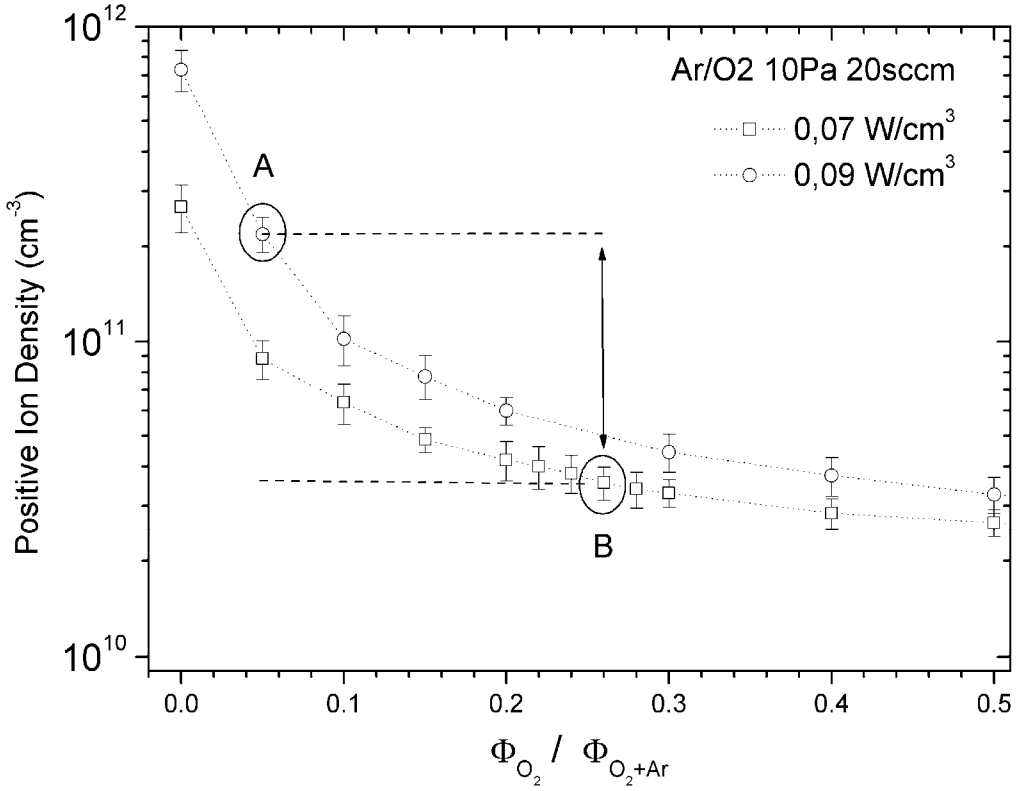

Figure 4.2.5. Argon ions fluxes as a function of molecular oxygen content in the discharge working gas mixture for two different input power levels. Langmuir probe measurements. Point [A] at $\Phi_{O2}/\Phi_{tot} = 0.05$, P = 350 W and point [B] at $\Phi_{O2}/\Phi_{tot} = 0.27$, P= 450 W refers to the same relative oxygen atom flux (see figure 4.2.4).

Figure 4.2.6 shows the experimental data of BSA removal measured by QCM for plasma conditions A and B described in the previous paragraph. The ion density changed from 3.55 x 10^{10} cm^{-3} to 22 x 10^{10} cm^{-3}, while the oxygen density remained constant. The calculated descriptive parameters for the two situations are summarized in table 4.2.3. Both mass loss curves approach the asymptotic mass loss value (which is the same since the same solution concentration was used) indicating an efficient biomaterial removal plasma process. The characteristic etching time τ decreases from 144.5 s to about 77 s if the higher ion density discharge is used, which gives rise in ER0 from 1,29 μg/s to 2,42 μg/s. These data show that the ion density has a substantial effect on the mass removal process when other process internal parameters like ion bombarding energy, oxygen atom density, heat andUV radiation flux are kept constant.

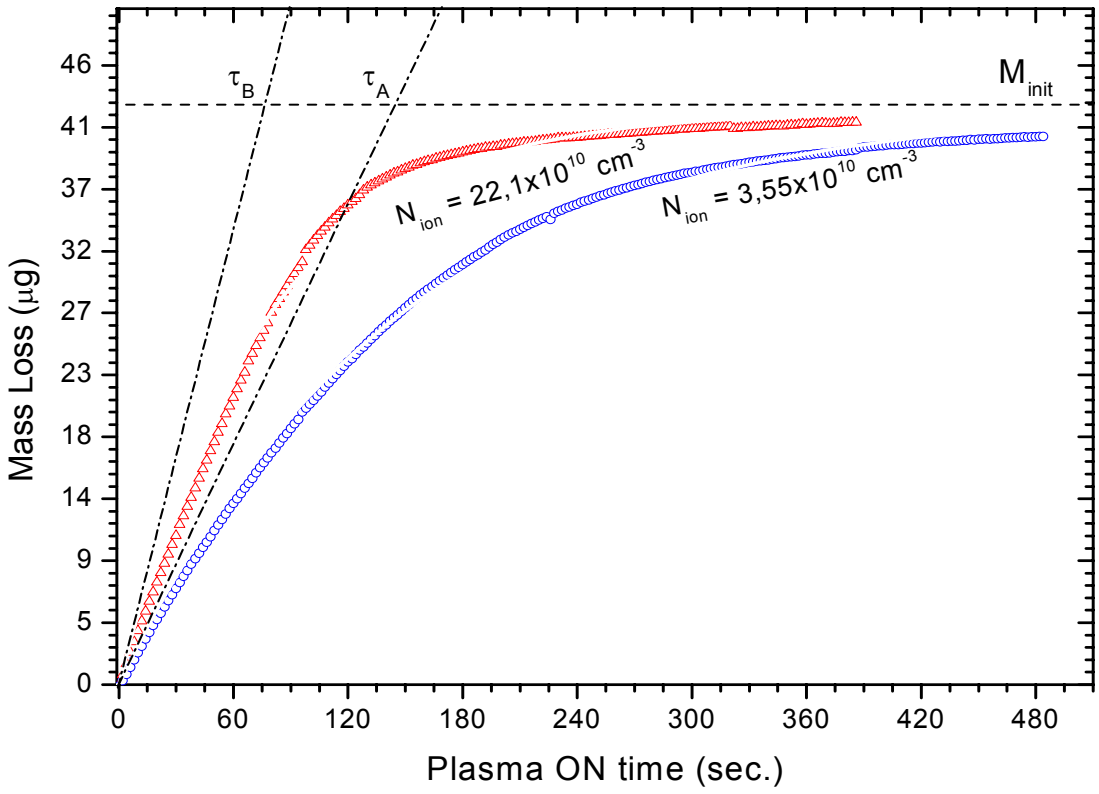

Figure 4.2.6) Mass loss curves as measured by QCM for protein layers deposited from a 10 mg/ml BSA solution. Triangles correspond to a sample treated with an high ion flux plasma discharge (condition [A] from figure 4.2.4 and 4.2.5) while circles correspond to a low ion flux from the plasma discharge (condition [B] from figure 4.2.4 and 4.2.5).

Table 4.2.3] Summary of the descriptive parameters for plasma positive ion density set of mass loss curves.

Name	N_{ion}	M_{init}	τ	ER_0
	cm^{-3}	μg	s	μg/s
B	$3{,}55x10^{10}$	185± 17	144 ± 6	1,29 ± 0,16
A	$22.1x10^{10}$	184 ± 17	77 ± 1	2,42 ± 0,24

4.2.4 Plasma induced chemical and morphological modifications

BSA survey XPS spectra (not shown) recorded for different plasma treatment times generally shows peaks corresponding to oxygen (O, 1s at 532 eV), nitrogen (N, 1s at 400 eV), carbon (C, 1s at about 285 eV), sulphur (S, 2p at about 164 eV) and, for long treatment times, Au (Au, 4f at 84 eV) , i.e. the substrate. Oxygen carbon and nitrogen are the main components of the protein molecular structure while sulphur is attributed to the cysteine present in the BSA. [244] Traces of sodium and calcium together with a substantial peak from fluorine (F 1s, 684 eV) are also detected, probably originated from the protein solution preparation, crystal cleaning protocol or from contamination of the vacuum chamber. XPS data presented in this section are summarized in Table 4.2.2.

Figure 4.2.7 shows in a stack plot the elemental composition of the protein film at different plasma treatment times. The three most important elements present in our samples that do not form volatile compounds after oxygen driven plasma reactions (gold, fluorine and sulphur) are shown. As the treatment time increases, the signals corresponding to gold and fluorine increases: this is due to the plasma etching process which removes the protein layer exposing the substrate (therefore the increase of the Au signal) and increasing the concentration of non-removable species (increase of F, from 5% to 12% after one characteristic etching time). Sulphur signal rises immediately at about three times its initial concentration, and then accounts for about 2% of the total composition, showing no further kinetics. Moreover, strong oxidation of sulphur was observed during the treatment and consequent shift of the XPS peak. The BSA as deposited shows the S2p doublet around 164 eV, which is typical of C-S bonding.[5] On

the other hand, after exposure to the plasma a second peak around 168 eV binding energy that can be attributed to oxidized sulphur starts appearing.[6]

Table 4.2.4. Summary of the XPS data .

Treat. Time	Au	F	S	Au/(C+N)			C/N
	Fig. 6	Fig. 6	Fig. 6	at 7.5 mg*ml^{-1} Fig. 7	at 10 mg*ml^{-1} Fig. 7	at 15 mg*ml^{-1} Fig. 7	Fig. 10
s	%	%	%	%	%	%	%
0	0.000	0.003	0.006	0.000	0.000	0.000	0.246
2	0.000	0.043	0.012	-	0.000	-	0.245
6	0.000	0.047	0.018	-	-	-	-
20	0.001	0.072	0.025	0.029	0.001	-	0.246
40	0.016	0.093	0.025	0.032	0.018	-	0.245
50	-	-	-	-	-	0.030	
60	0.029	0.098	0.019	0.024	0.034	-	0.195
80	0.031	0.120	0.024	0.023	0.038	-	-
100	0.042	0.097	0.032	0.119	0.040	0.059	0.040
150	0.153	0.147	0.022	0.366	0.051	0.038	0.000
200	0.227	0.132	0.017	0.500	0.226	0.063	0.000
250	-	-	-	-	0.464	0.233	-
300	-	-	-	0.510	0.465	0.452	0.000
400	-	-	-	-	-	0.427	-

The total concentration of these three elements raises to (31 ± 5) % in one characteristic etching time (152.0 ± 1.6 seconds) for the specific plasma treatment under investigation, indicating substantial build up of inorganic non-volatile compounds at the surface. This implies the progressive and fast depletion of potential reaction sites for excited atoms and molecules from the surface. This in turn explains the reduction of the mass loss rates as the treatment time progresses. It must be underlined that as soon as the gold substrate signal is observed at a significant concentration (above 3-5%), the BSA protein film has became most likely thinner than 10-12 nm, which is the typical analysis depth of XPS at 90º TOA. [7]

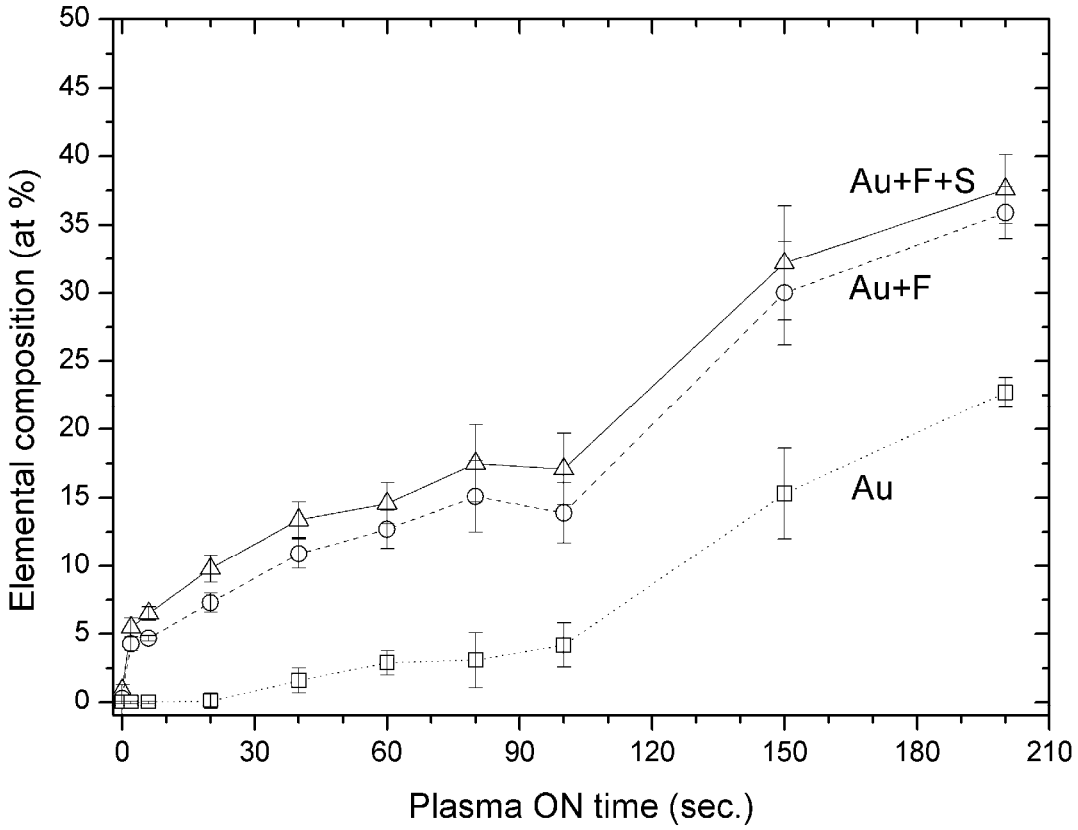

Figure 4.2.7 Surface elemental composition (at %) of Au, Au+F and Au+F+S as a function of plasma treatment time. Data refers to deposits obtained from 10 mg ml^{-1} BSA solution, plasma treatment parameters are O_2/Ar = 0.27, P = 350 W, p = 10 Pa, ϕ_{tot} = 20 sccm. Typical elemental composition measurement error is around ± 10%. All XPS data are summarized in Table 4.2.4.

Figure 4.2.8 shows, as a function of the plasma treatment time, the elemental composition concentration ratios of gold over the sum of nitrogen and carbon, for the three different initial deposit situations. The transition time for the corresponding process is indicated as the shaded area below the data and the width corresponds to the experimental error. The *Au/(N+C)* ratio is zero at the beginning of the treatment, when the crystal surface is still fully covered with the protein layer, and it remains very low for the early stages of the treatment. At treatment times comparable with the transition times points derived from data plotted in Figure 4.2.2, the *Au/(N+C)* ratio shows a fast increase and reaches plateau values around 0.5. This behavior indicates that in the initial stages the plasma interaction

happens with a bulk biological material while later, as soon as this material is removed, the substrate is exposed and the surface covered with proteins is reduced to about half the initial value.

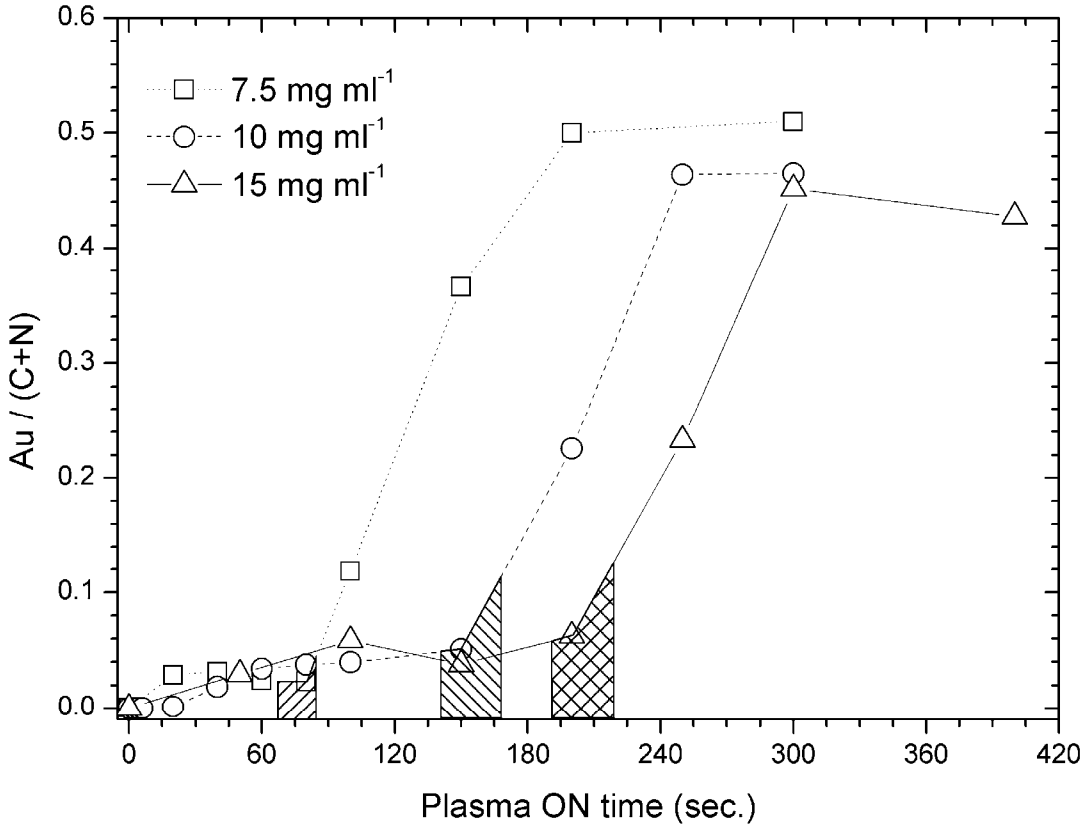

Figure 4.2.8. Elemental composition (at %) ratio of gold over the sum of carbon and nitrogen as a function of the plasma treatment time obtained from XPS analysis recorded at 90° TOA (mean of three independent measurements). The transition time for the corresponding plasma process is indicated as the shaded area below data. Plasma treatment parameters are O_2/Ar = 0.27, P = 350 W, p = 10 Pa, Φ_{tot} = 20 sccm. Typical elemental composition measurement error ± 10%. All the XPS data are summarized in Table 4.2.4.

Evidence of substrate exposure for long treatment times is supported also by AFM measurements of protein layers microscopic RMS roughness (calculated over an area of 1 μm^2) as a function of the treatment time (see Figure 4.2.9). Deposits obtained from three

different initial solution concentrations were investigated. It can be seen that just few seconds of plasma treatment are enough to induce morphological changes on initially smooth surface of BSA. Further plasma treatment leads to the increase of the maximum peak to valley height difference which reaches its maximal value, after the peak a flattening effect is observed. The transition between these two phases happens around the transition time derived from the etching rates curves, which is consistent with interpretation of the XPS data shown in Figure 4.2.8. Measured roughness evolution as shown in Figure 4.2.9 is representative of the different stages of the material removal process [8], for short treatment times the increasing roughness is relate to inhomogeneous etching, where the surface reactions happens at preferential sites: for long treatment times, the average roughness decreases indicating exposure of the flat substrate layer.

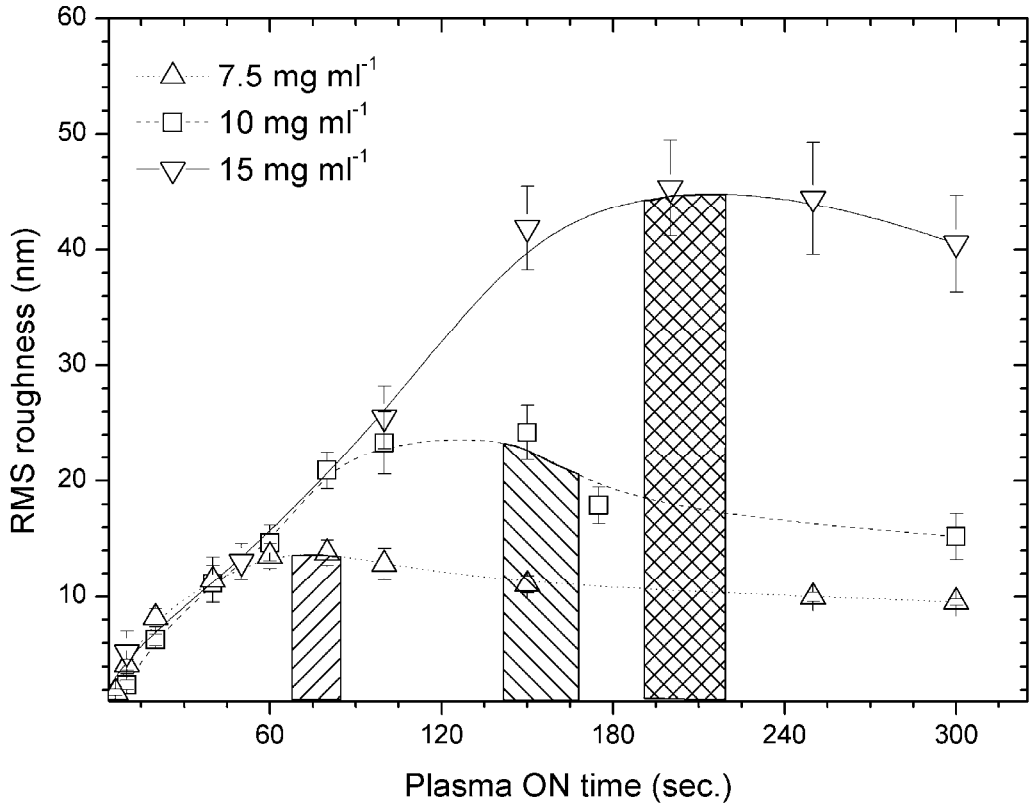

Figure 4.2.9. Microscopic average roughness of the protein surface layer (1μm x 1 μm) as a function of the plasma treatment time as measured by means of AFM. The transition time for the corresponding plasma process is indicated as the shaded area below data. Plasma treatment parameters are O_2/Ar = 0.27, P = 350 W, p = 10 Pa, Φ_{tot} = 20 sccm.

To further explain the slower kinetic of the mass removal rates after the transition time C1s XPS high resolution spectra recorded at 90° TOA at different plasma treatment times have been analyzed. In Figure 4.210 are shown spectra of as-deposited protein, 2 and 20 seconds plasma treated protein (before transition time) and 200 seconds plasma treated protein (after transition time). It is known that BSA C1s peak is the envelope of five components (C0 – C4) which can be attributed respectively to C-C/C-H (ε_{bind} = 285 eV), C-N (ε_{bind} = 285.8 eV), C-O, N-C-O (ε_{bind} = 286.8 eV), C=O, N-C=O (ε_{bind} = 288.4 eV) and COOH/R (ε_{bind} = 289.5 eV). [5]

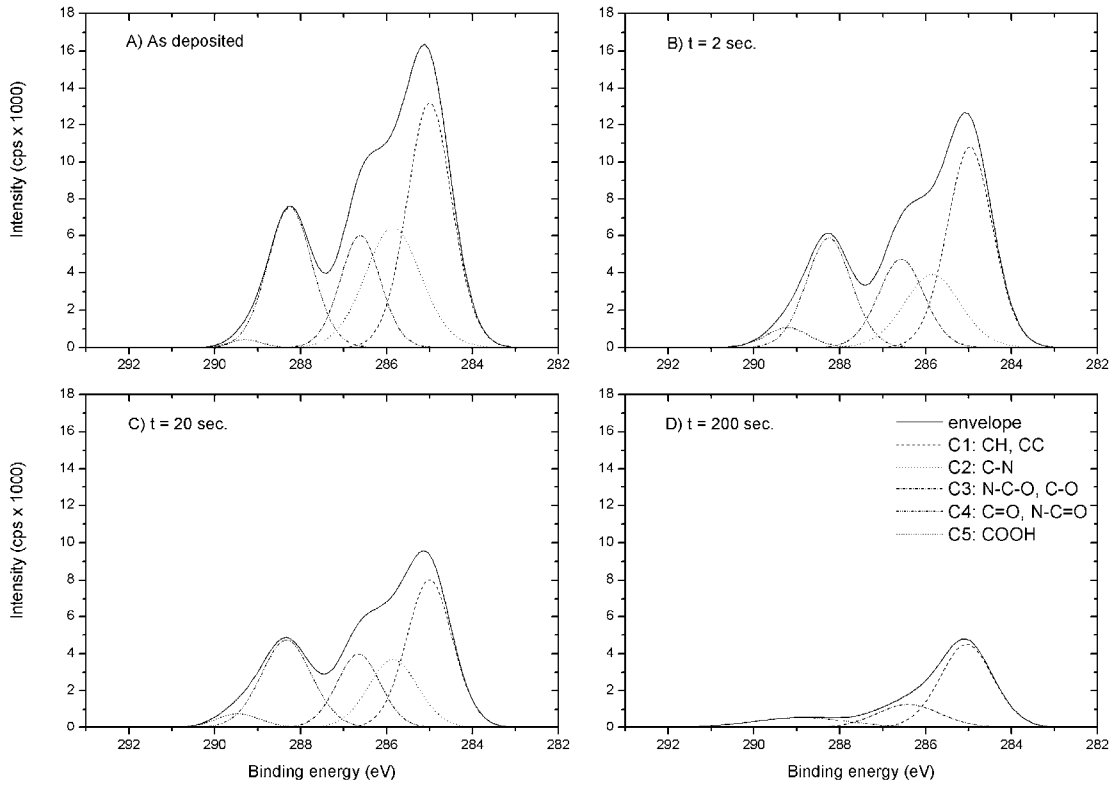

Figure 4.2.10. C1s high resolution XPS spectra recorded at 90° TOA on plasma treated BSA protein films before (A), after 2" (B), after 20" (C) and after 200" (D) Ar/O_2 plasma exposure. Data refers to deposits obtained from 10 mg ml^{-1} BSA solution, plasma treatment parameters are O_2/Ar = 0.27, P = 350 W, p = 10 Pa, Φ_{tot} = 20 sccm.

Comparing the as deposited protein spectrum with the spectra recorded at 2 and 20 seconds treatment time, a general reduction of the intensity in all the components is

observed, with the exception of the high energy edge arising from the contribution of peak C4 which is increasing. This is an indication that the percentage of carbon bonded to oxygen is increasing and support the idea of oxidation processes at the surface. The spectrum recorded at 200 seconds plasma treatment time, well after the transition time for the corresponding mass loss curves (t_{trans} = 155 ± 13 sec.), appears to be dominated by the C0 peak with probably some minor contribution by C-O, C2 peak. Eventual contribution from the C1 (C-N) peak is ruled out by the elemental analysis displayed in Figure 4.2.11 showing that at 200 seconds the nitrogen concentration is zero.

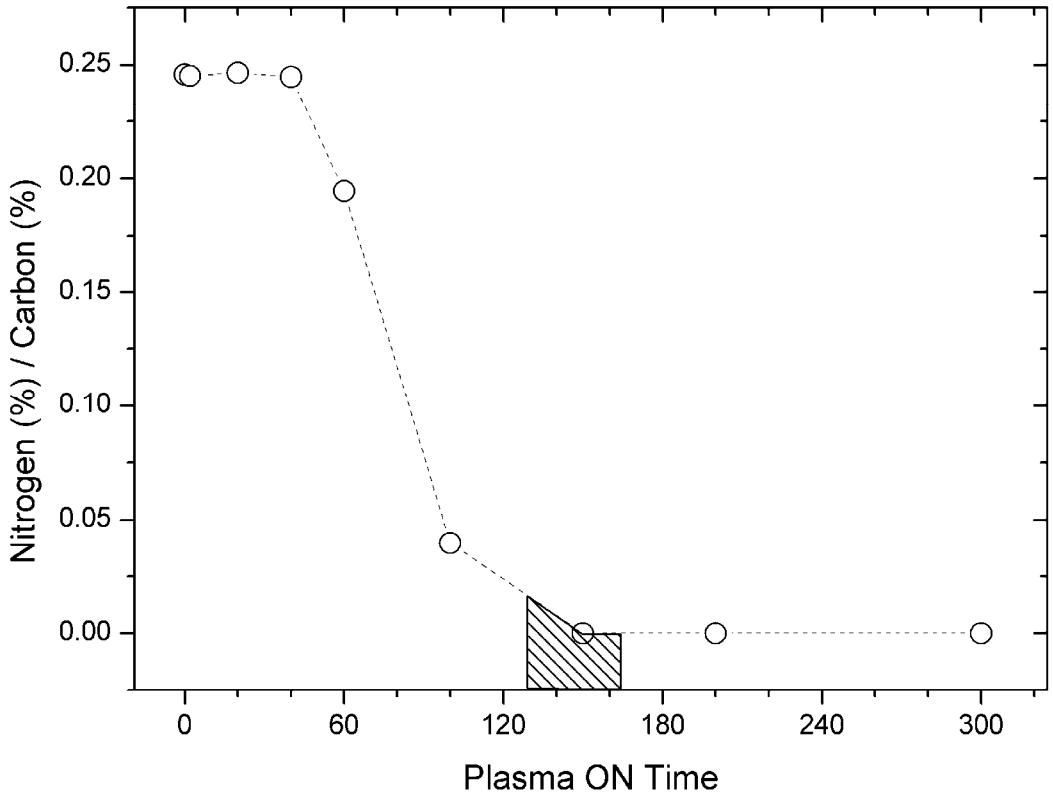

Figure 4.2.11. Elemental composition (at %) ratio of nitrogen over carbon as a function of the plasma treatment time obtained from XPS survey spectra recorded at 90° TOA (mean of three independent measurements). The transition time for the corresponding plasma process is indicated as the shaded area below data. Plasma treatment parameters are O_2/Ar = 0.27, P = 350 W, p = 10 Pa, Φ_{tot} = 20 sccm. Typical elemental composition measurement error ±10 %. All the XPS data are summarized in Table 4.2.4.

These results (Figures 4.2.8 – 4.2.11) show that in the second phase, the residual protein film is localized and composed mainly of amorphous carbon-based deposit, the protein chemical structure being destroyed by the plasma interaction. Films of amorphous carbon show in general slower etch rates under exposure to oxygen-argon plasma. Benedikt et al. [9], using a plasma setup very similar to the one used in this study, measured amorphous hydrogenated carbon film etching rate around 0.3 $nm \cdot s^{-1}$. On the other hand, Kylian et al. [10], always in very similar conditions, measured for bulk BSA etching rates around 20 $nm \cdot s^{-1}$. The substantial modification of the chemical identity of the material and the corresponding reduction in the mass removal rates after the transition point, together with the reduction of the effective area available for plasma interaction (substrate exposure and residuals build up) can explain the slower kinetics of the mass loss curve second regime after the transition.

The ratio *N/C* shown in Figure 4.2.11 is an indicator of the presence of the protein backbone structure. The *N/C* ratio exhibits for short treatment times values around 0.25 compatible with the macromolecular elemental composition of the undamaged BSA protein (2932 *C* and 780 *N* per protein, ratio *N/C* is 0.266), This is considerably changed at long treatment times, namely beyond the transition time, when this ratio falls almost to zero in both cases. This indicates the destruction in the surface layer of the basic building blocks of the proteins primary structure.

Comparison of the data for *N/C* and *Au/(N+C)* ratios shows that the destruction of the last protein units and the substrate exposure are simultaneous events and both happens just around the transition time.

From the overall picture derived from the data shown in Figures 4.2.7 – 4.2.11, it is possible to define the general mechanisms related to the two mass loss curves regimes observed in Figure 4.2.2. The first regime, when the plasma mass removal is faster (higher *ER(t)* values), correspond to the ion enhanced plasma etching of the bulk protein film.[11] Hydrogen, oxygen, carbon and nitrogen in the protein are consumed by surface reactions with oxygen and removed from the surface as volatile by-products. This process initiates at a rate described by the characteristic etching rate ER_0, and slows down because of the increasing surface concentration of inorganic compounds, that corresponds to superficial non-reactive site. When the process approaches the transition time, it is

found that most of the biological material has been removed and the non reactive sites on the surface (either due to exposed substrate or non reactive surface site) determine a slower kinetic of the mass removal, being the plasma etching mechanism less efficient in attacking the residuals left at the end of the processes.

4.2.5 Bi-phasic etching kinetcs

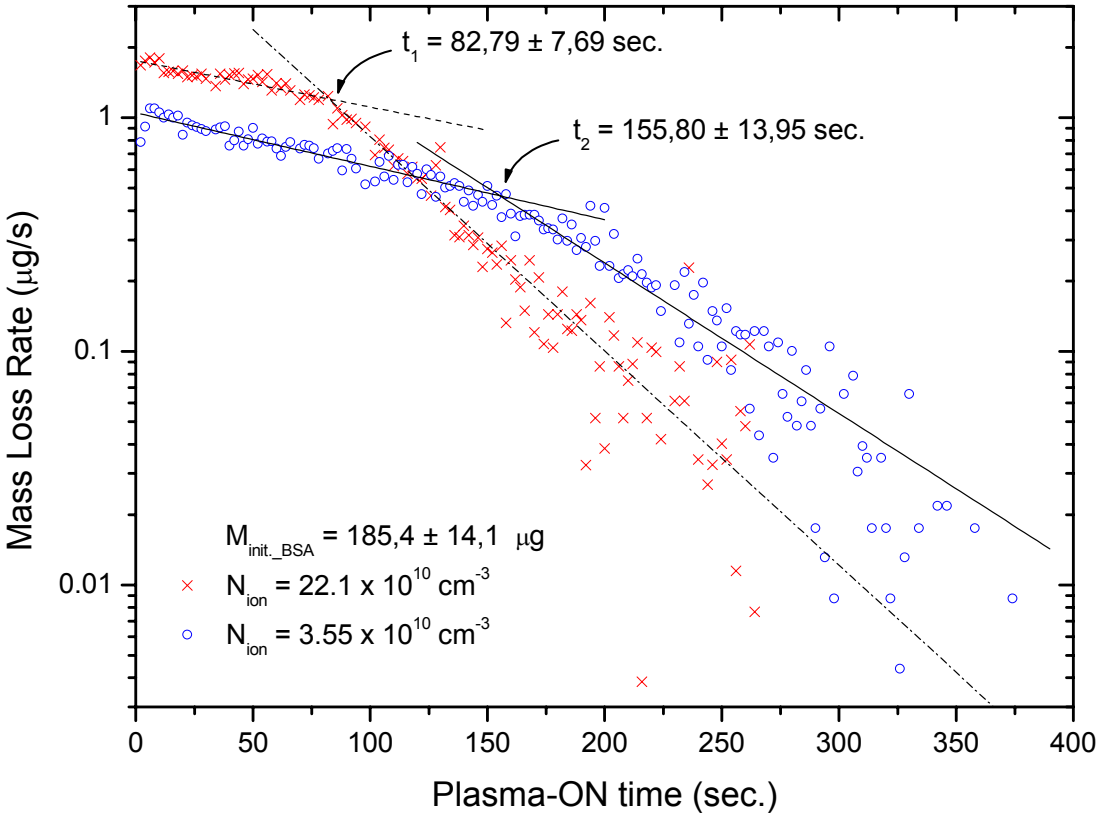

Figure 4.2.12 Bi-phasic kinetics of the time dependent mass loss rate for two plasma conditions, low ion density (circle) and high ion density (cross) with the same atomic oxygen concentration.

XPS surface analysis results allows a deeper interpretation of the mass loss curves kinetics. From the analysis of the mass loss curves presented in paragraph 4.2.1 results that the simple forms of equations (4.1) and (4.2) describes the main features of the mass loss kinetics, but poorly describe the details of the QCM signal evolution. This is evident, for example, from the mass loss rates (re-plotted in figure 4.2.12 in a log scale) calculated

from the mass loss curves already presented in figure 4.2.6. If equation (4.2) strictly holds a linear trend for *ER(t)* would be expected in semi-logarithmic plot against the treatment time.

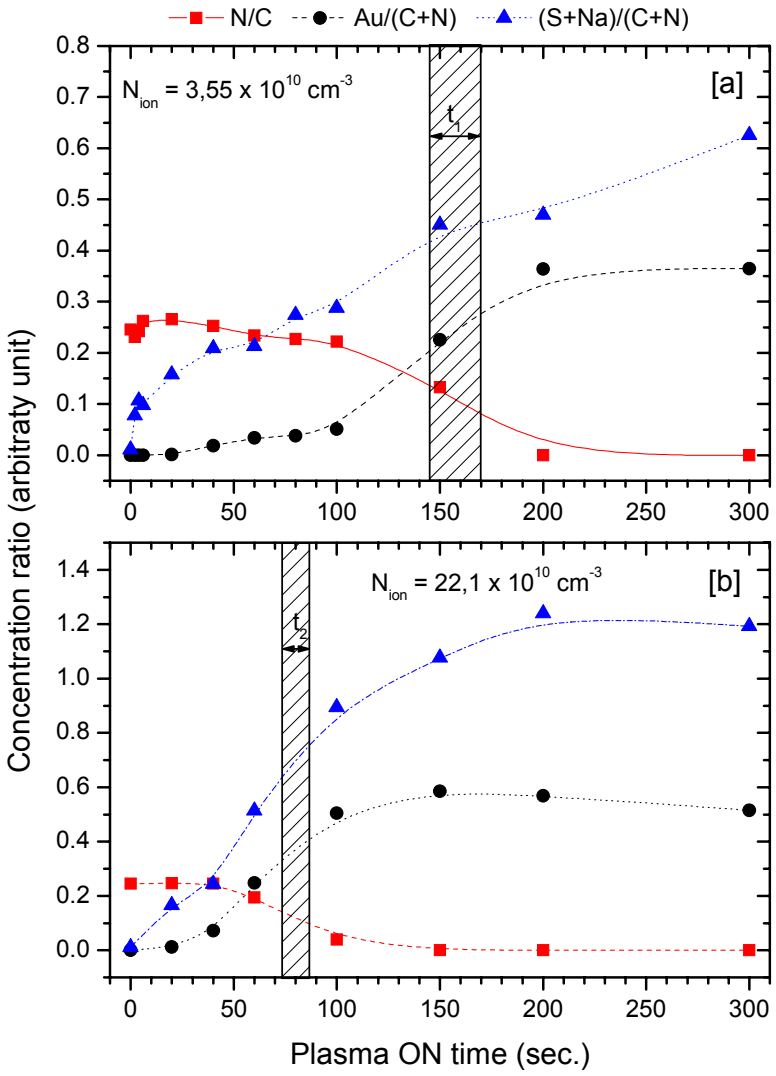

4.2.13) Elemental composition (at %) ratios of the superficial protein layer as a function of the plasma treatment time obtained from XPS survay spectra recorded at 90° TOA (mean of three independent measuraments) for two plasma conditions, low ion density (A) and high ion density (B) with the same atomic oxygen concentration.

Data in figure 4.2.12 shows instead that the data trends are closely described by equation (4.2) when a two-valued characteristic etching time is considered, i.e. the process is

described using two different time constants. In each curve in figure 4.2.12 the kinetic of the mass loss rate at short treatment times is described by higher value of the characteristic etching time, as compared to the average value calculated on the complete dataset, while after a certain transition time the time constant describing the exponential decay assumes suddenly a lower value, i.e. the decay of the mass loss rates is slower at short treatment times and is faster at long treatments times. Since the mass loss rate curves (equation 4.2) are described by the same set of parameters of the mass loss curves (equation 4.1) it is possible to derive from the observations described above that at the beginning of the treatment, the protein mass loss due to plasma exposure proceeds with a slower kinetic i.e. the material removal rate deviates slowly from ER_0, while after the transition point a new regime with a faster kinetics is observed, i.e. the instantaneous *ER(t)* drops rapidly to zero.

This sudden jump in the value of the parameter τ at the time t_{trans} is the indication of a modification in the conditions of the removal process. Some indications about the surface processes related this phenomenon can be derived from XPS and AFM measurements.

Figure 4.2.13a and 4.2.13b shows, as a function of the plasma treatment time, the elemental composition concentration ratios for nitrogen over carbon, gold over the sum of nitrogen and carbon and the sum of sulphur and sodium over the sum of nitrogen and carbon, for the two different plasma conditions described in figures 4.2.6 and 4.2.12. The transition time for the corresponding process is indicated in the graph with its experimental error. These ratios are representative of important characteristics of the surface. The ratio *C/N* is an indicator of the presence of the protein backbone structure, the ratio *Au/(C+N)* represents the relative amount of exposed gold substrate with respect to the protein and *(S+Na)/(C+N)* is an indicator of the accumulation of non-volatile compounds at the surface of the protein layer. The trends of the different elemental concentration ratios (see figure 4.2.13) exhibit behavior compatible with the bi-phasic interpretation of the mass loss curves. The N/C ratio exhibits for short treatment times values around 0,25 compatible with the macromolecular elemental composition of the undamaged BSA protein (2932 *C* and 780 *N* per protein, ratio *N/C* is 26,6), This is considerably changed at long treatment times, namely after the transition time, when this ratio falls almost to zero in both cases. This indicates the destruction of the surface layer

of the basic building blocks of the proteins primary structure. The *Au/(N+C)* ratio is zero at the beginning of the treatment, where the crystal surface is still fully covered with the protein layer, and it remains very low for the early stages of the treatment.At treatment times comparable with the transition time the Au/(N+C) ratio shows a fast increase and reaches a plateau values comprised between 0,35 and 0,5. This behavior indicates that in the initial stages the plasma interaction happens with a bulk biological material while later, as soon as this material is removed, the substrate is exposed and the surface covered with proteins is reduced to about half the initial value. The comparing of the data for *N/C* and *Au/(N+C)* ratios shows that the destruction of the last protein unities and the substrate exposure are simultaneous events and both happens just around the transition time. The last ratio, *(S+Na)/(C+N)*, shows initial values around 0,1. The starting sulphur over C and N concentration ratio in the BSA protein is around 0,01 (39 sulphur atoms per protein), while the rest is the sodium concentration coming form the deposition and cleaning protocol which is difficult to estimate. Moreover sodium concentration exhibited high variability between different experiments. The ratio *(S+Na)/(C+N)* doesn't show a two levels behavior like the former ratios examined, but instead is increasing with the treatment times (with the exception of one point, 300 seconds treatment time for the high ion flux plasma treatment). This behavior indicates that as the plasma treatments proceeds the ion driven etching depletes the material of carbon and nitrogen (and most likely hydrogen as well) by forming volatile reaction by-products like CO_2, NO_2 and H_2O. These elements thus leaves the surface and the concentration of C and N falls, while non reactive compounds remain on the surface and their concentration grows as the mass removal proceeds, therefore the ratio *(S+Na)/(C+N)* raises.

References

[1] Stapelmann K, Kylian O, Denis B and Rossi F 2008 *J. Phys. D: Appl. Phys.*, **41**(19), 192005(6).

[2] Kylian O Benedikt J Sirghi L Reuter R Rauscher H Von Keudell A and Rossi F 2009 *Plasma Processes and Polymers,* **6**(4), pp. 255-61.

[3] Boudam M K and Moisan M 2010 *J. Phys. D: Appl. Phys*., **43**(29), 295202(17).

[4] Friedli G L 1996 Phd Dissertation, *Interaction of Deamidated Soluble Wheat Protein (SWP) With Other Food Proteins and Metals,* University of Surrey, Guildford, England.

[5] Baeamson G, Briggs D, *High resolution XPS of organic polymers: The Scientia 3000 database*, Wiley, Chichester, Sussex, UK, **1992**;

[6] C. Wagner 1979 *Handbook of photoelectron spectroscopy*, Perkin Elmer, Eden Praire, Minnesota, USA.

[7] Dewez J, Berger V, Schneider Y and Rouxhet P 1997 *J. Coll. Int. Sci.*, **191**, pp. 1-10.

[8] Rossi F Kylian O Rauscher H Gilliland D and Sirghi L *Pure and Applied Chemistry* **80**(9) pp. 1939-51.

[9] Benedikt J, Flötgen C, Kussel G, Raballand V and Keudell A 2008 *J. Phys.: Conf. Ser.* **133** 012012(9).

[10] Rossi F Kylian O and Hasiwa M 2006 *Plasma processes and polymers* **3**(6-7) pp. 431-42.

[11] Kylian O Benedikt J Sirghi L Reuter R Rauscher H Von Keudell A and Rossi F 2009 *Plasma Processes and Polymers,* **6**(4), pp. 255-61.

5 Plasma biomaterials interaction.

5.1 Absolute measurements of particles flux.

5.1.1 Langmuir I/V characteristic data analysis

In order to understand the role of the different particles present in the plasma phase during etching processes quantitative measurements of particle fluxes were carried out for species of interest in decontamination processes (oxygen atoms and ions). The diagnostic techniques used to measure fluxes were Langmuir probe and residual gas analysis mass spectrometry.

In order to monitor plasma parameters like ion density and electron temperature a movable RF compensated Langmuir probe was used [1,2,3]. Data acquisition was performed at the centre of the discharge chamber and at a vertical distance of 5.5 cm from the quartz glass facing the antenna. This is the same position of the samples inserted in the reactor via the load lock system.

Since the most performing discharges for decontamination processes were found to be the oxygen containing ones, all the plasmas to be characterized shows a certain degree of electro-negativity.

Because of the presence of negative ions the system routine for plasma parameters calculation performed by the Langmuir probe commercial software was disregarded and a dedicated Mat Lab routine was developed to analyse probe raw data output. The analysis of the characteristics was performed in the framework of the ABR radial motion theory in the case of a thin sheath, modified by the presence of negative ions. Several references for I/V characteristics analysis can be found in literature [4,5,6,7,8]

A typical I/V characteristic and signal analysis are shown in figure 5.1.1, it can be divided in three parts, for sufficiently negative probe voltage the probe collects mainly positive ions, and the corresponding current is called ion saturation current (see equation 5.1), in the transition region close to the floating voltage (when ionic current equals

electronic current, see figure 5.1.2) the probe collects both ions and electrons. For positive voltages the probe collects only electronic current.

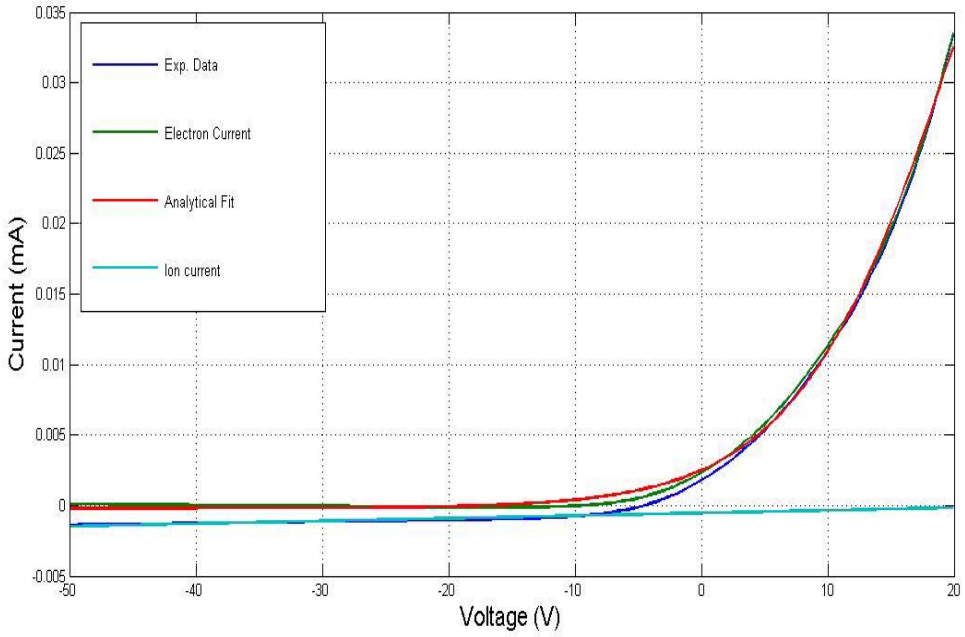

Fig. 5.1.1 Typical Langmuir probe I/V characteristic for pure oxygen plasma discharge. Plasma parameters are P = 500W, p= 10 Pa, Φ_{tot} = 20 sccm. Bleu line is the recorded signal from the discharge, cerulean line is the fitted ion current (using equation 5.1), green line is the calculated electron current and red line is the analytical fit (using equation 5.2) for the electron current.

For plasma parameters estimation the positive ion density n_+ is extracted from the ion saturation current I_+ according to equation (5.1):

$$I_+ = q_+ S n_+ \sqrt{\frac{k_B T_e}{e M_+}} \qquad [5.1]$$

Where I_+ is the positive ion current, S is the probe surface, n_+ is the positive ion density, k_B is the Boltzmann constant, e the electron charge and M_+ the principal positive ion mass.

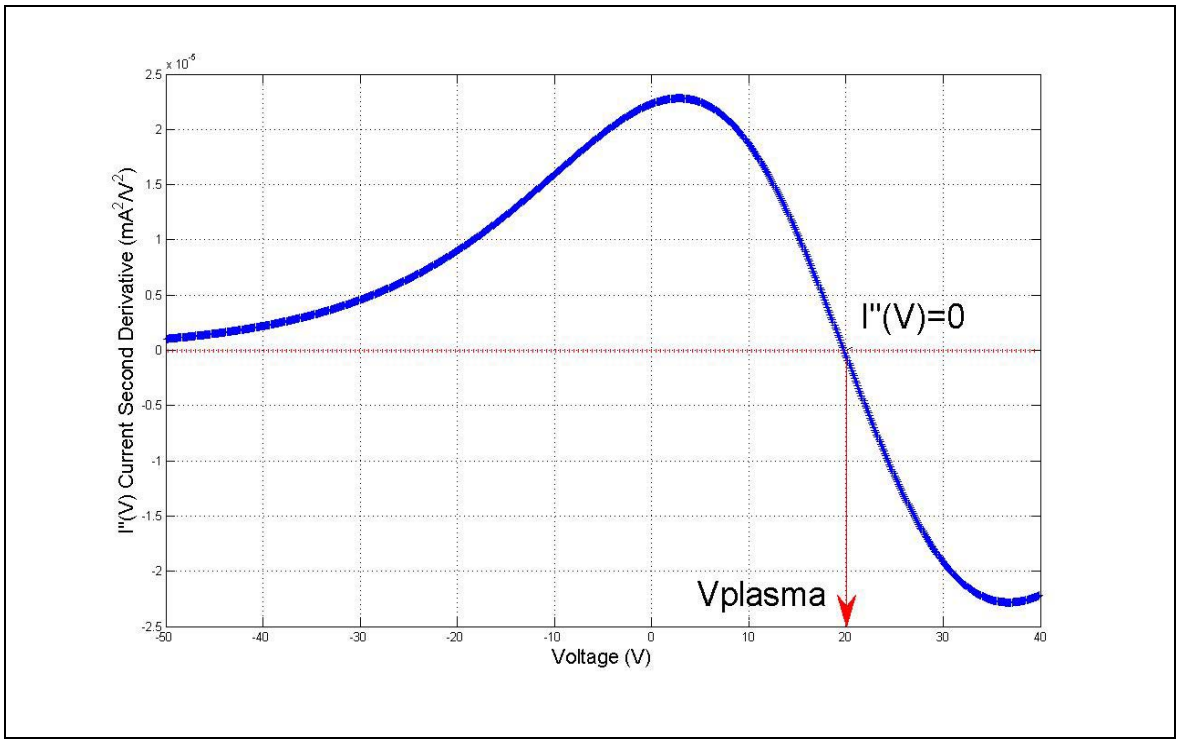

Fig. 5.1.2 Second derivative of the electron current, calculated from the analytical fit. Plasma voltage is measured from the zero current point indicated by the red arrow.

Once that the negative ion current contribution is subtracted from the characteristic the second derivative of the positive carriers current is numerically calculated by smoothing the data [9] with a four parameters function, the form of this equation being the usual form for floating double probes characteristics [10].

$$I_e = a_1 \tanh(a_2 V + a_3) + a_4 \qquad [5.2]$$

The four parameters control the position of the I/V curve with respect to the coordinate system origin (a_3 and a_4), the maximum amplitude of the saturation currents (a_1) and the slope of the transition region (a2).

The plasma potential is taken (Figure 5.1.2) as the voltage coordinate at null voltage second derivative. The electron temperature is calculated from the slope of the I/V characteristic semi-log plot (related to the parameter a_2 in the analytical fit formula for

electron current). Evaluation of the EEDF via the druyvenstein equation was attempted but practical limits to data analysis arose because of the secondary electron emission from the probe tip even at moderately high positive voltages.

Quantities of interest for plasma-biomaterials interaction at the interface are the positive ion flux directed towards the sample and the average energy of the ion population crossing the sheath. Both quantities can be calculated from the Langmuir probe characteristics data analysis

The ion flux J_{ion} expressed in ions/cm^2·s can be calculated from positive ion density and electron energy (for the Bhom velocity of the ions crossing the sheath) via the relation:

$$J_{ion}^{+} = \frac{n_{ion}^{+}\bar{v}_{mean}}{4} = \frac{1}{4} n_{ion}^{+} \sqrt{\frac{k_B T_e}{M_{ion}^{+}}} \qquad [5.3]$$

And the ion bombarding energies ε_{ion} at the plasma-sample interface can be calculated by subtracting the plasma voltage V_{plasma} to the floating voltage $V_{floating}$:

$$\varepsilon_{ion} = V_{sheath} - V_{floating} \qquad [5.4]$$

5.1.2 Ion flux and ion energy measuraments

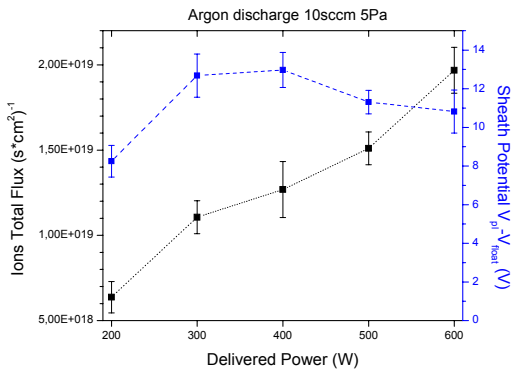

Fig. 5.1.3

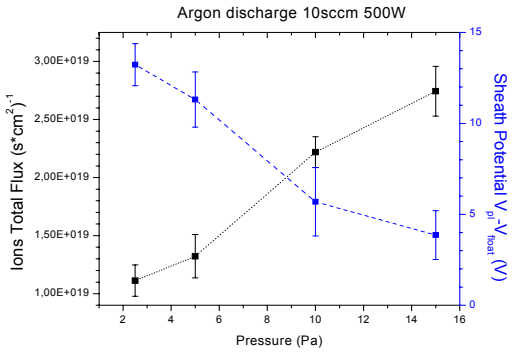

Fig. 5.1.4

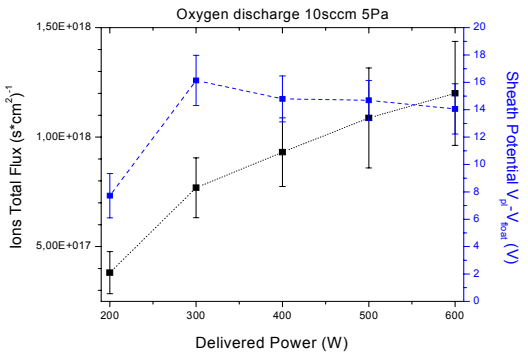

Fig. 5.1.5

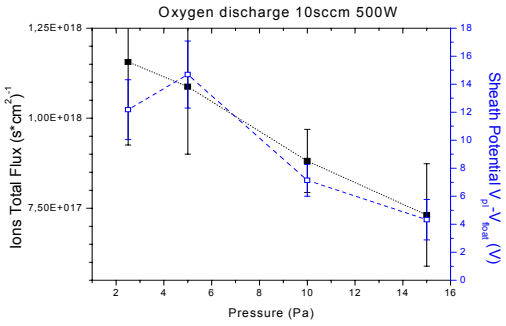

Fig. 5.1.6

Figure 5.1.3 – 5.1.6. Langmuir probe measuraments for ion total flux, left y-axis in black, and ion energy (sheath potential), right y-axis in bleu. Pure Argon discharge paramenters as a function of power (fig. 5.1.3) and pressure (fig. 5.1.4). Pure Oxygen discharge paramenters as a function of power (fig. 5.1.5) and pressure (fig. 5.1.6).

The behaviour of ions flux and energies for both electropositive (Ar) electronegative (O_2) and also for slightly electronegative discharge like pure hydrogen (H_2), varying pressure and RF power, was investigated. Results are shown in Figure 5.1.3 – 5.1.6.

The ion flux in the discharge results to be monotonically increasing with the RF power in the parameters range investigated. This behaviour is well supported by the RF discharge theoretical framework that states the independency at a given operating pressure of the electron temperature from the delivered power and on the other way states that raising the RF power feed delivered into the vacuum chamber more energy is available for ion electron pair creation and thus densities of charged particles raise. From these considerations results of figure 5.1.3 and 5.1.5 are explained by equations 5.3 and 5.4.

The pressure dependencies are more complicated because positive ion densities are proportional to the operating pressure e.g. more molecules that undergo ionizations events are available per unit volume, but the electron temperature drops as the pressure raises because of the effect of the collisions. Always referring to equations 5.3 and 5.4 the overall trends of figures 5.1.4 and 5.1.6 are determined from the extent at which one of the two effects dominate.

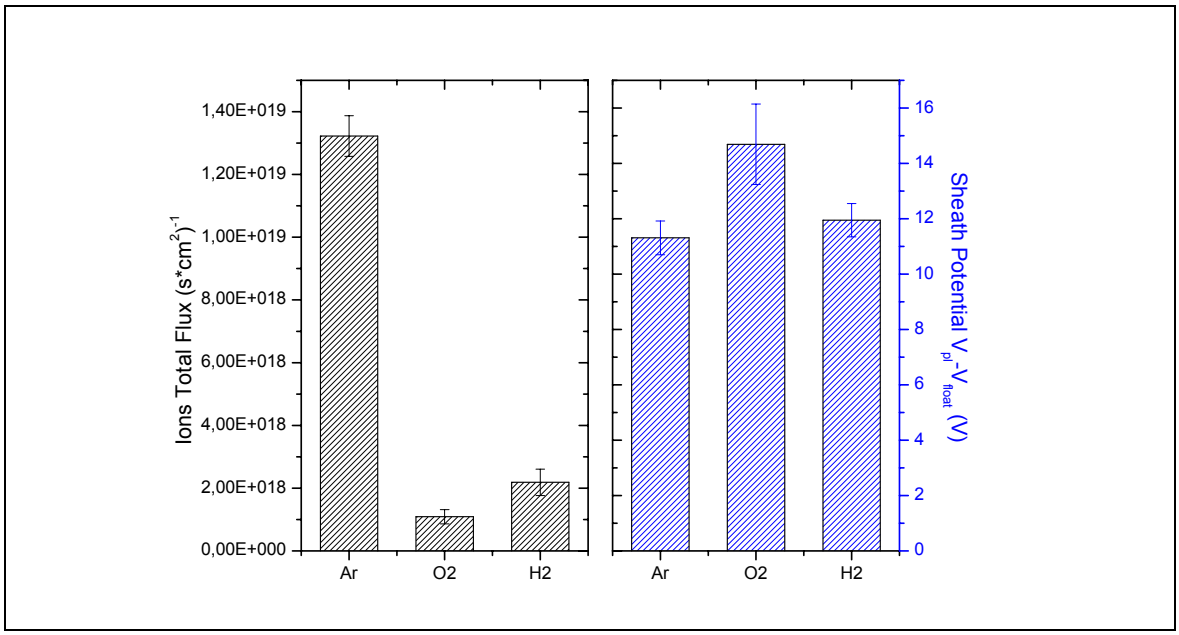

Figure 5.1.7 Langmuir probe measurements for ion total flux, left panel in black, and ion energy (sheath potential), right panel in bleu, for pure Argon, Oxygen and Hydrogen discharges. Common plasma parameters are P = 500W, p= 10 Pa, Φ_{tot} = 20 sccm.

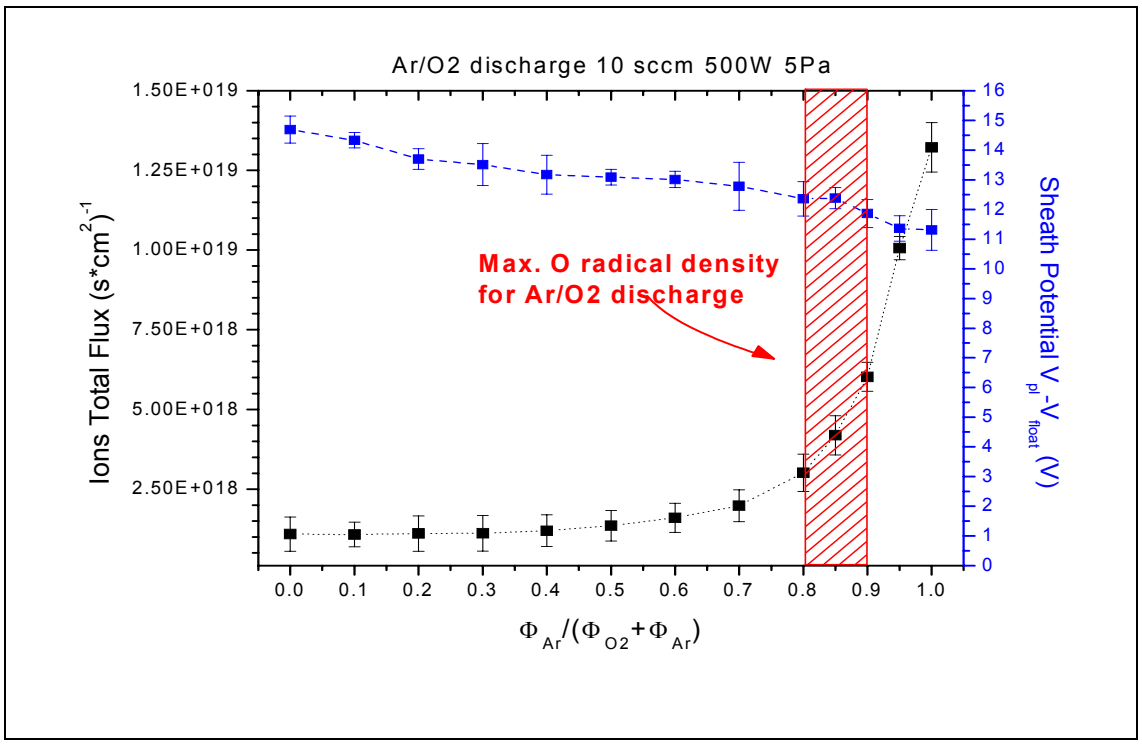

Figure 5.1.8 Langmuir probe measurements for ion total flux, black, and ion energy (sheath potential), bleu, for Argon-Oxygen plasma as a function of the argon fractional flow.

For electropositive discharges the trend is monotonically increasing showing that the density increment is more efficient but for electropositive discharges the electron temperature drop causes the ion flux to decrease as the pressure is raised.

In figure 5.1.7 a summary of the Langmuir measurements concerning pure gases discharges is shown. Plotted data refer to 500 Watts, 10 Pa discharges and serve to illustrate differences between these discharges. In the left panel the ion fluxes are shown and argon plasma have values more than on order of magnitude higher then oxygen and hydrogen, while, on the right panel the sheath potentials are not varying so much and thus ions bombarding energies are comprised between very low values (10-15 eV) for all the discharges.

After determination of pure gases discharges properties their mixtures were also investigated. In Fig. 5.1.8 and 5.1.9 results from Langmuir measurements of ions flux and sheath potentials are shown as a function of the argon content in the working gas mixture for discharges at 500W and 5 Pa.

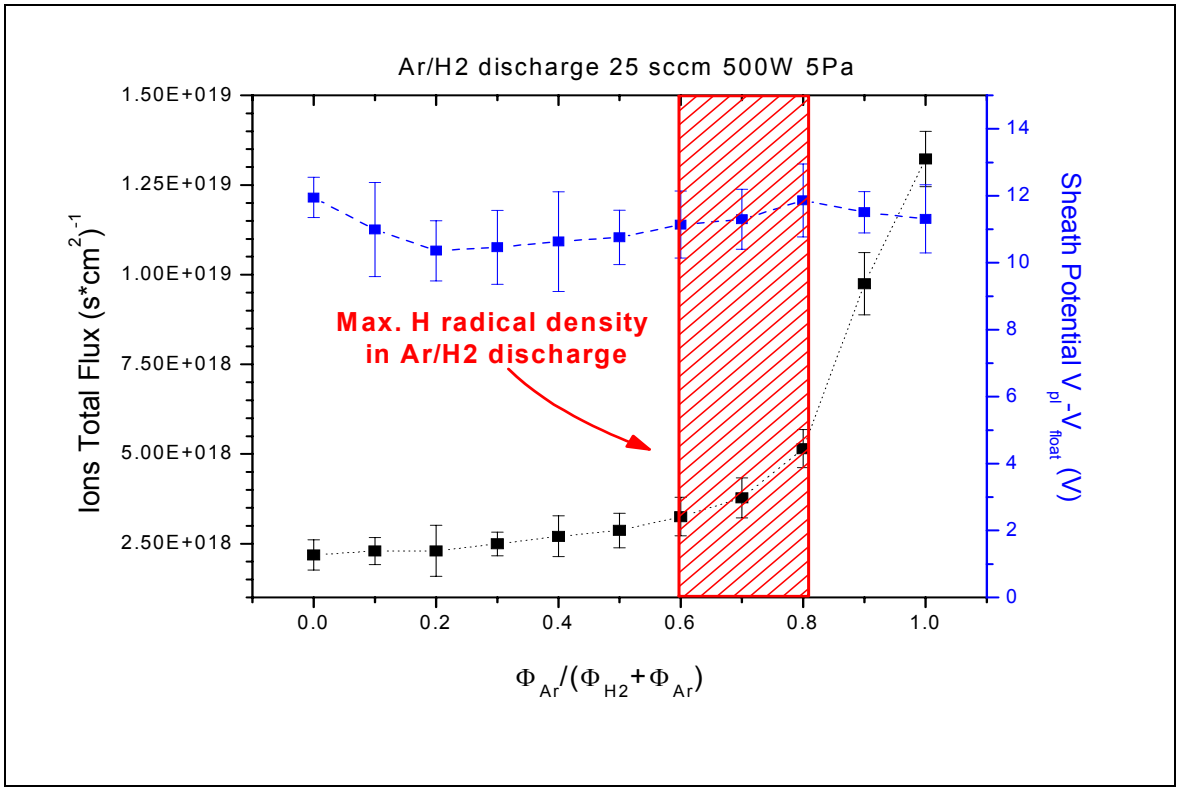

Figure 5.1.8 Langmuir probe measuraments for ion total flux, black, and ion energy (sheath potential), bleu, for Argon-hydrogen plasma as a function of the argon fractional flow.

As example here are shown, among all the possible binary combinations, data concerning Ar/O_2 and Ar/H_2 gas mixtures. A common feature between the two graphs is the sharp raise of the ion fluxes when the argon content in the discharge approaches unity. The trends of sheath potentials instead are more flat and are always comprised between 10 and 15 eV for all the combinations tested. With reference to Figure 5.1.7 showing a summary of results for pure gases discharges it is possible to see how tuning the gas composition by argon addiction to oxygen or hydrogen is possible to vary the ion flux and, at a certain extent, the sheath potentials between the limiting values corresponding to pure argon or pure oxygen/hydrogen.

In figures 5.1.8 and 5.1.9 is also shown, as an area marked in red, the location of maximum production of oxygen or hydrogen radicals, according to independent optical emission spectrometry measurements. The relative concentration of radicals is measured via an actinometric technique (data not shown).

5.1.3 Radicals density mass spectrometric measuraments

In order to evaluate the radicals density in the discharge a mass spectrometric technique was applied. The mass spectroscopy signals of the gas species from a plasma are detected by a residual gas analyzer (Hyden RGA). The RGA is a mass spectrometer consisting of a quadrupole probe and an electronics control unit mounted directly on the probe's flange. The probe consists of three parts: the ionizer, the quadrupole filter and the ion detector. Positive ions are produced in the ionizer by bombarding gas molecules with electrons derived from a heated filament. After filtering by the quadrupole according to z/m ratio, ions are collected on the detector stage where, by means of an electron multiplier a current signal proportional to the ion current is recorded.

In plasmas are present several classes of molecules but only neutral atoms were sampled by RGA mass spectrometry. Ions were removed by adding a suitable electromagnetic field at the sampling orifice. To avoid difficulties arising from plasma chemistry of binary mixtures a discharge composed only by pure oxygen gas was analyzed in the following experiments. In experiments on the BIODECON reactor the signals from

atomic oxygen radicals created by molecular dissociation processes in the plasma phase were very weak over the signal background made up mostly by desorbed species from reactor walls and from carbohydroxy compounds arising from the mechanical pump oil vapour. Moreover the peak at 16 a.m.u. carries the contribution of atomic oxygen sampled from the plasma chamber and dissociations products of oxygen molecules in the ionizing chamber of the mass spectrometers.

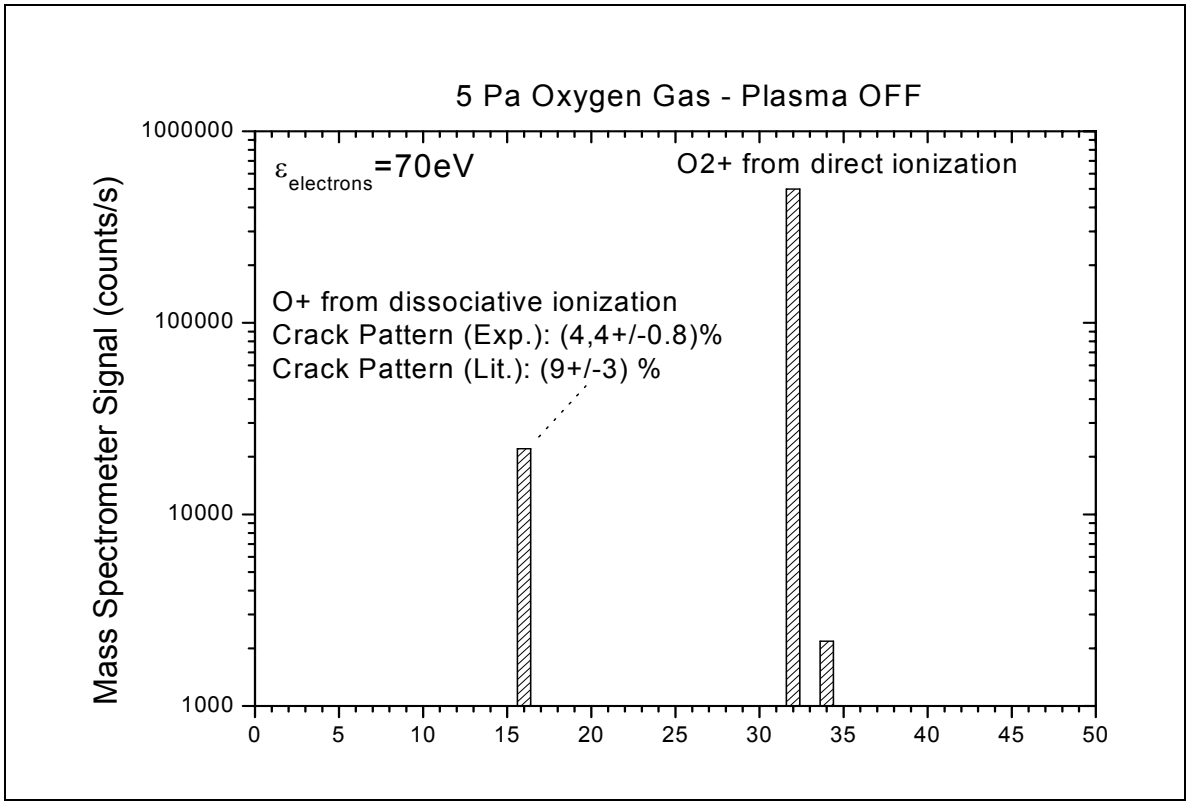

Figure 5.1.9 Oxygen background gas mass spectrum, pressure 5 Pa.

In order to separate these contributions a two step measurement technique for the density of atomic oxygen, shown in Fig. 5.1.9 and Fig. 5.1.10, was used [11,12,13].

As a first step in the evaluation of the contribution of dissociative ionization of molecular oxygen in the ionization chamber, mass spectra of oxygen gas at 5 Pa with the plasma discharge OFF were acquired. After base vacuum background signal subtraction the two most intense peaks left were 32 a.m.u. and 16 a.m.u. In this experiments, since no atomic oxygen was present in the gas inside the chamber, the peak at 16 a.m.u. is representative of the processes of molecular dissociation in the ionizer at a given electron energy (here 70 eV). Peak intensity contributions can be also ascribed to double ionization processes

of the oxygen molecule but at this electron bombarding energies the yield is negligible compared to dissociative ionization.

The intensity of the peak at 16 a.m.u. as measured in these experiments was taken as reference to account for these two processes in measurements of the plasma phase. The value derived by our experiments was 4.4 ± 0.8 % of the intensity of the principal peak (32 a.m.u.) which is not too far from the average of a selection of similar measurements reported in literature, 9 ± 3 %.

Second step of the measurement involves data acquisition in the plasma phase. The discharge was switched on at 5 Pa and 500W and then several replicas of plasma mass spectra were acquired. One example of such a measurement after base vacuum background signal subtraction is shown in Figure 5.1.10. Here again the most prominent peaks in the mass spectra are the ones at 16 and 32 a.m.u., while several new peaks at lower intensities arise most probably due to wall desorption, between them the most interesting are the peaks at 17 and 18 a.m.u. attributed to OH and H_2O molecules.

At this stage to quantify the portion of the signal at 16 a.m.u. arising from O^+ direct ionization of atomic oxygen sampled from the plasma phase, the cracking pattern derived from the plasma OFF measurements shown in Figure 5.1.9 was subtracted to the intensities recorded with the plasma ON. The remnant was attributed to plasma phase atomic oxygen.

For quantification of the mass spectrometer signal expressed in counts/s formula 5 was used.

$$PP_m = S\frac{I_m}{FF_{A\to B}XF_m} \qquad [5.5]$$

This semi-empirical expression relates the partial pressure (PP_m) for the signal on a certain m/z channel to the mass spectrometer intensity signal (I_m) on the same channel. The proportionality factors taken into account are the transmission efficiency of the instrument with respect to mass (S), the fragmentation factor ($FF_{A\to B}$) that takes into account contribution for dissociative ionization processes with respect to a specific reaction pattern and ionization factor (XF_m) that takes into account the ionization

efficiency of the ionization stage of the spectrometer. Proper values for $FF_{A\rightarrow B}$ and XF_m for m=16 and 32 can be found on the instrument manual or in the literature where, to evaluate the transmission efficiency S, the approximation that S was mass-independent was used. Within the limits of this approximation (around 10% variation between the two mass channels as will be shown in Figure 5.1.12) the efficiency value can be calculated from plasma OFF measurement when the partial pressure of molecular oxygen is known.

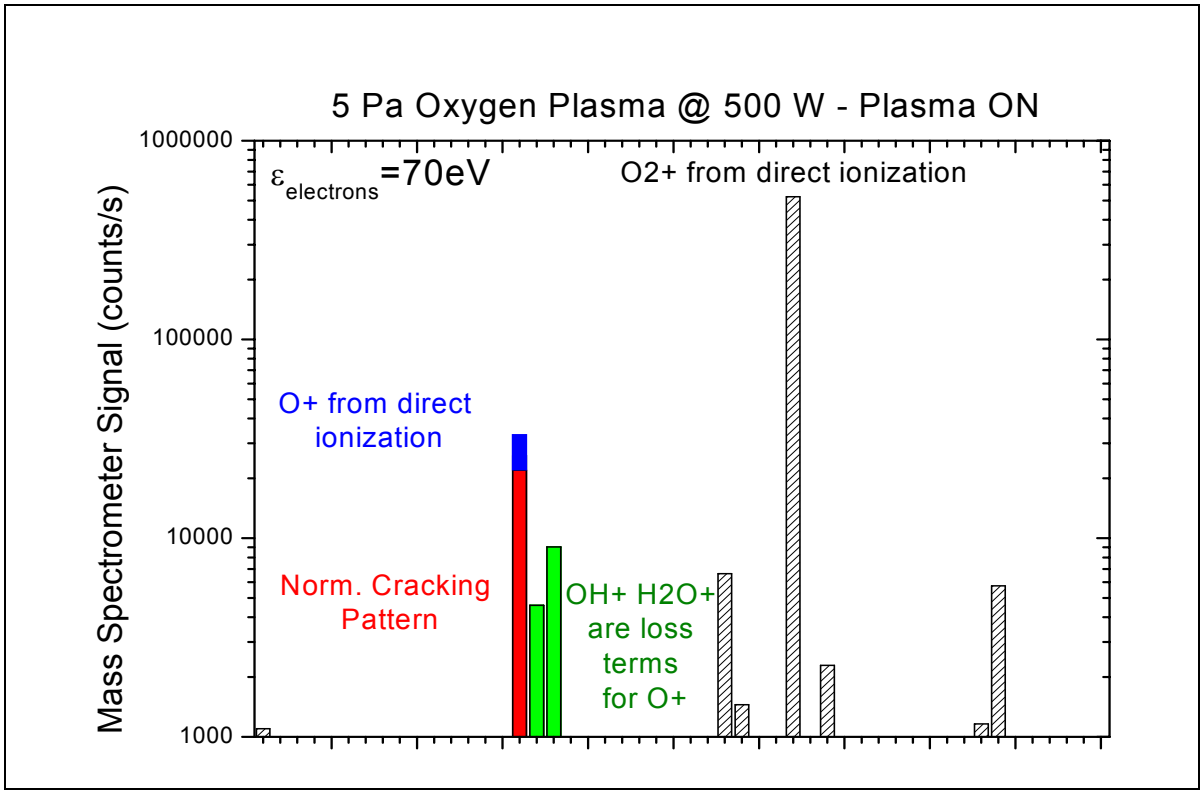

Figure 5.1.10 Oxygen plasma mass spectrum, plasma parameters are P= 500W, p= 5 Pa and Φ= 20 sccm.

Once that the partial pressure of atomic oxygen is calculated from the mass spectra the corresponding neutrals flux can be derived from gas dynamics equations:

$$J_{neut} = \frac{n_{neut}\bar{v}_{thermal}}{4} = \frac{1}{4}\frac{P}{k_B T_{gas}}\left(\frac{8k_B T_{gas}}{\pi M_{neut}}\right) \qquad [5.6]$$

Results of the measurements process described in the previous sections (both ions flux by means of Langmuir probe experiments and neutrals fluxes by mass spectrometry experiments) are summarized in fig. 5.1.11.

On the right panel are shown absolute data corresponding to particles fluxes in an oxygen discharge at 5 Pa as a function of the discharge RF power. On the left panel the data values corresponding to 500 W discharges are normalized to the oxygen molecules flow to show the ratios between ionic, atomic and molecular fluxes. It can be seen from both panels that the atoms flux is about 2 orders of magnitude weaker than the molecules flux while the ions flux is about 5 orders of magnitude weaker than the molecules flow. Within the common approximation of $T_{gas} \sim T_{ion}$ usually valid for plasma discharges in local thermodynamic equilibrium from this data is possible to derive directly the dissociation ratio ($\sim 10^{-2}$) and the ionization ratio ($\sim 10^{-5}$) for the BIODECON reactor, where the precise values depends on the particular discharge parameters (here RF delivered power).

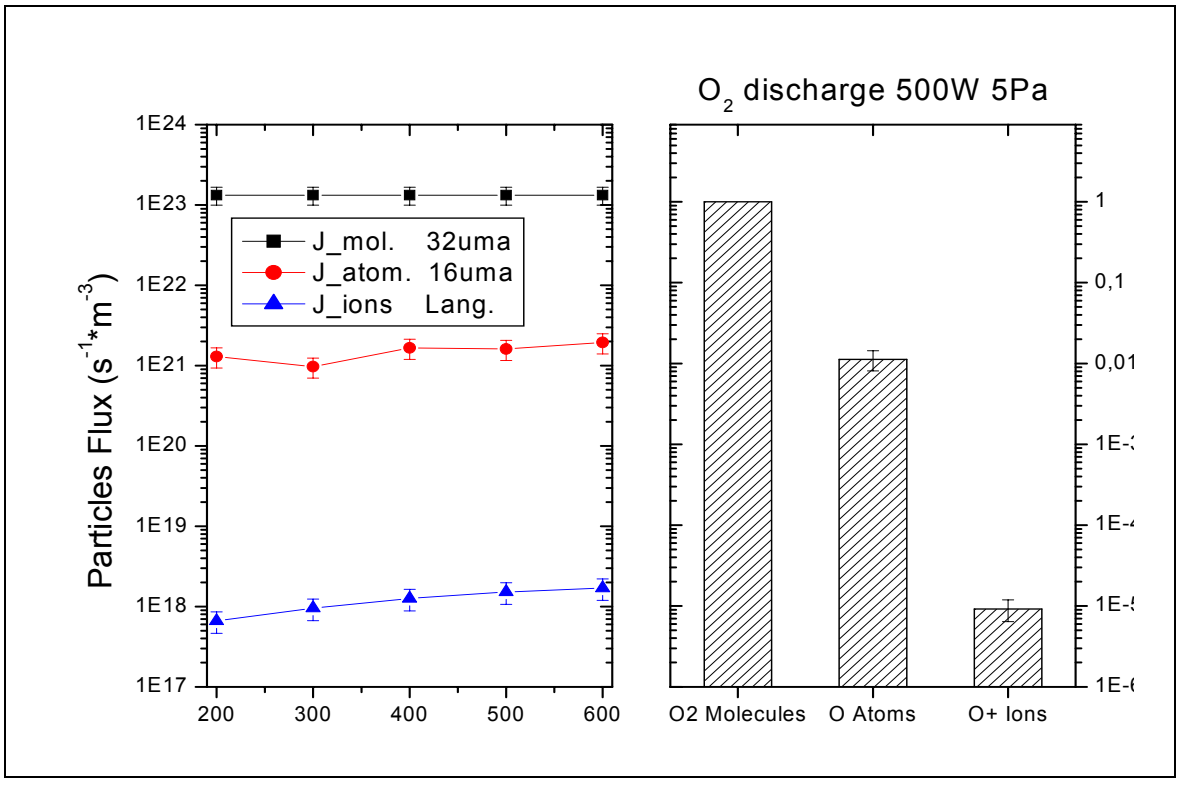

Fig. 5.1.11 Summary of Langmuir probe and mass spectrometric measurements. In the left panel absolute particles fluxes (O_2 molecules, O atoms and positive ions) are shown as a function of RF delivered power. In the right panel, relative fluxes at 500 W are shown.

The second stage of the experiments described in this section involves determination of the densities of oxygen radicals, i.e. the excited states of the oxygen atoms or molecules present in the discharge.

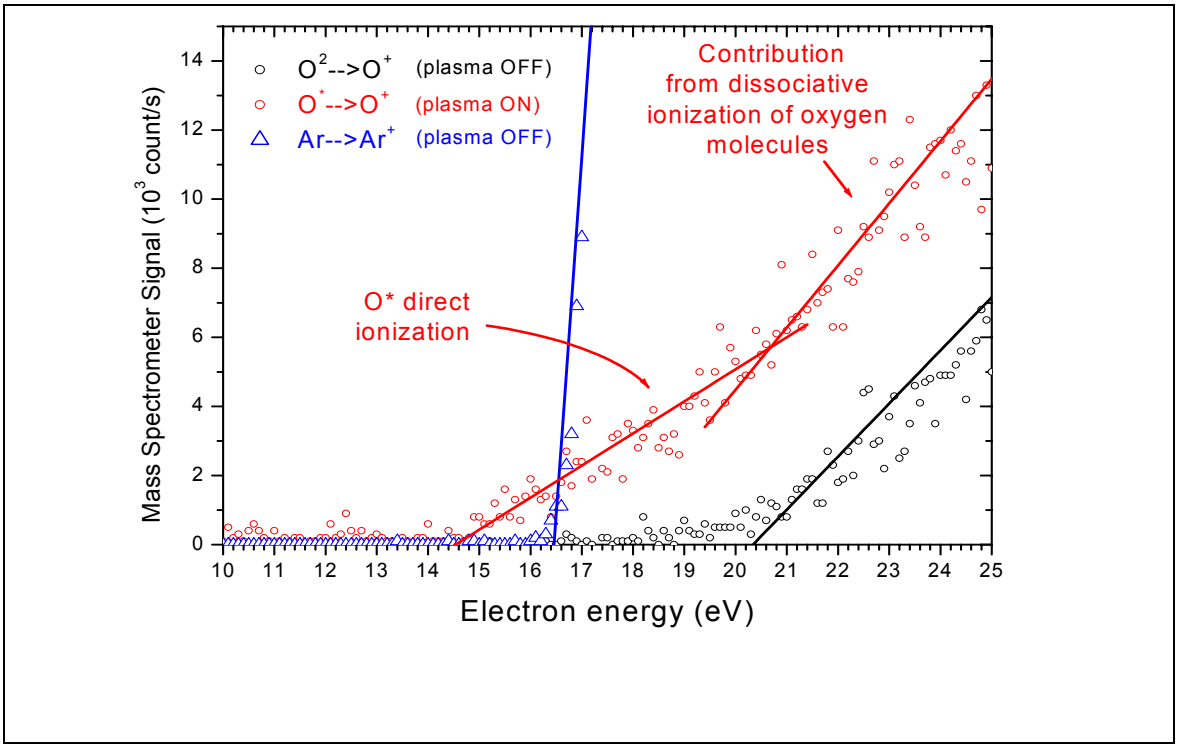

Fig. 5.1.12 Energy resolved mass spectra utilized for a typical TIMS measure. Bleu data refers to argon plasma energy spectra on m/z = 40 mass channel, black data refers to oxygen background gas energy spectra on m/z= 16 mass channel and red data refers to oxygen plasma energy spectra on m/z = 16 mass channel. Common plasma parameters are P= 500W, p= 5 Pa and Φ= 20 sccm.

The technique used for determination of radicals is called TIMS (Threshold Ionization Mass Spectrometry) [14,15,16,17]. The electron energy spectra from detection of neutral species in the mass spectrometer is given by equation (5.7):

$$S = \alpha(m/e) I_e \sigma(\varepsilon) n_{ionizer} \qquad [5.7]$$

where S is the measured signal in counts/s, I_e is the electron current in the ionizer in the mass spectrometer, σ(ε) is the cross section of the ionizing process, $n_{ionizer}$ is the number density of the species sampled by the ionizer, and α(m/e) is a transmission coefficient made up by the product of extraction efficiency of the ions from the ionizer, species mass

to charge transmission efficiency of the quadrupole mass filter and detection coefficient of the channeltron detector.

TIMS technique (see figure 5.1.12) utilizes selective ionization of a oxygen radical (O*) exploiting the energy difference between the ionization threshold of the radical and the dissociation ionization threshold of the parent molecule (O_2). For electron energies comprised between these boundaries the signal measured is due solely to the direct ionization of the radicals. From this signal the number density of the radical of interest can be estimated by considering the ratio between the signal acquired sampling Ar gas at known pressure and the signal to be measured. Using this procedure, in a fashion similar to OES actinometric technique the terms corresponding to different radical signals can be compared.

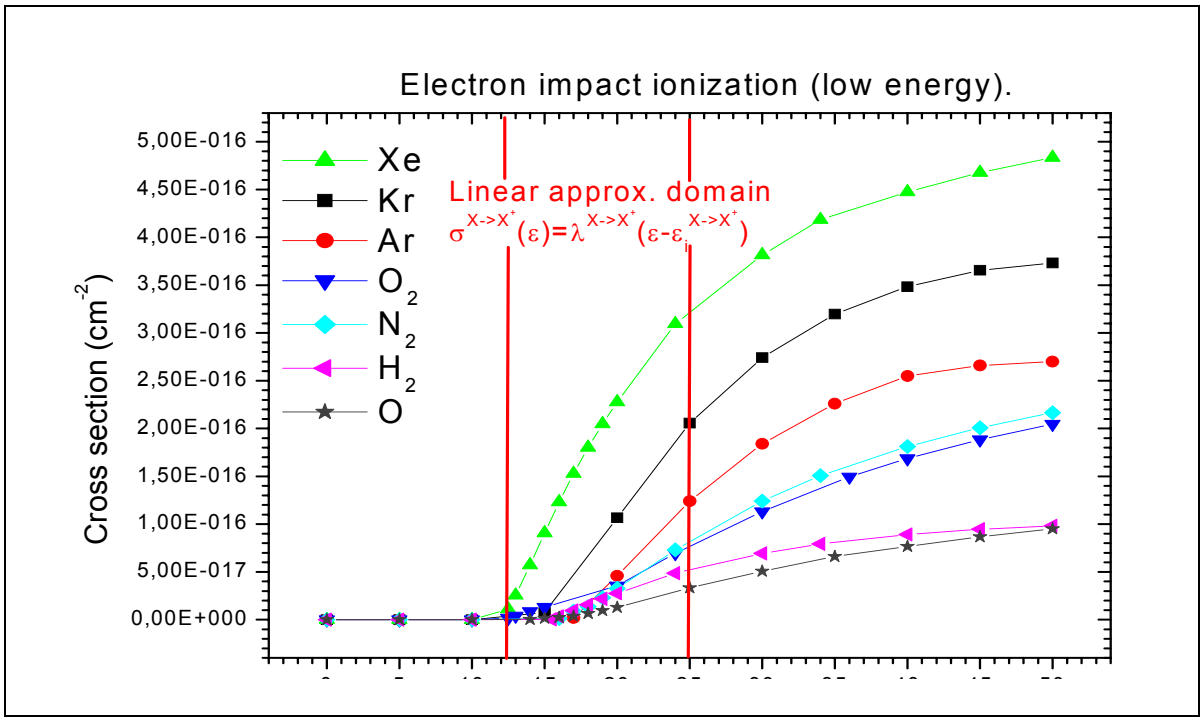

Fig. 5.1.13 Low energy electron impact ionization cross sections data for different gases used in TIMS measuraments and mass spectrometer calibration.

After linearization of the energy dependency of the ionization cross section (an approximation valid near the ionization threshold) and by consequence of the mass spectrometric signal, the functional form of the ratio between argon reference and oxygen radicals signals from the discharge can be written as equation (5.8)

$$\frac{n_X^{On}}{n_{Ar}^{Off}} = \left(\frac{A^{X\to X^+}}{A^{Ar\to Ar^+}}\right)\left(\frac{\lambda^{Ar\to Ar^+}}{\lambda^{X\to X^+}}\right)\left(\frac{\alpha(Ar^+)}{\alpha(X^+)}\right) \qquad [5.8]$$

where A and λ are respectively the slopes of the mass spectrometric signals near and the slope of the ionization cross section near the ionization threshold energy.

Using formula (5.8) the density of the excited states can be evaluated, the slopes of the instrument signals can be directly measured, after interpolation and linear fitting, from the electron energy spectra of argon gas (where the density is calculated by the pressure) and of oxygen plasma. The two missing terms in equation 5.8 are derived as follows.

The ratio between the cross sections slopes near ionization threshold is calculated from the fit of available data in NIST databases (see Figure 5.1.13).

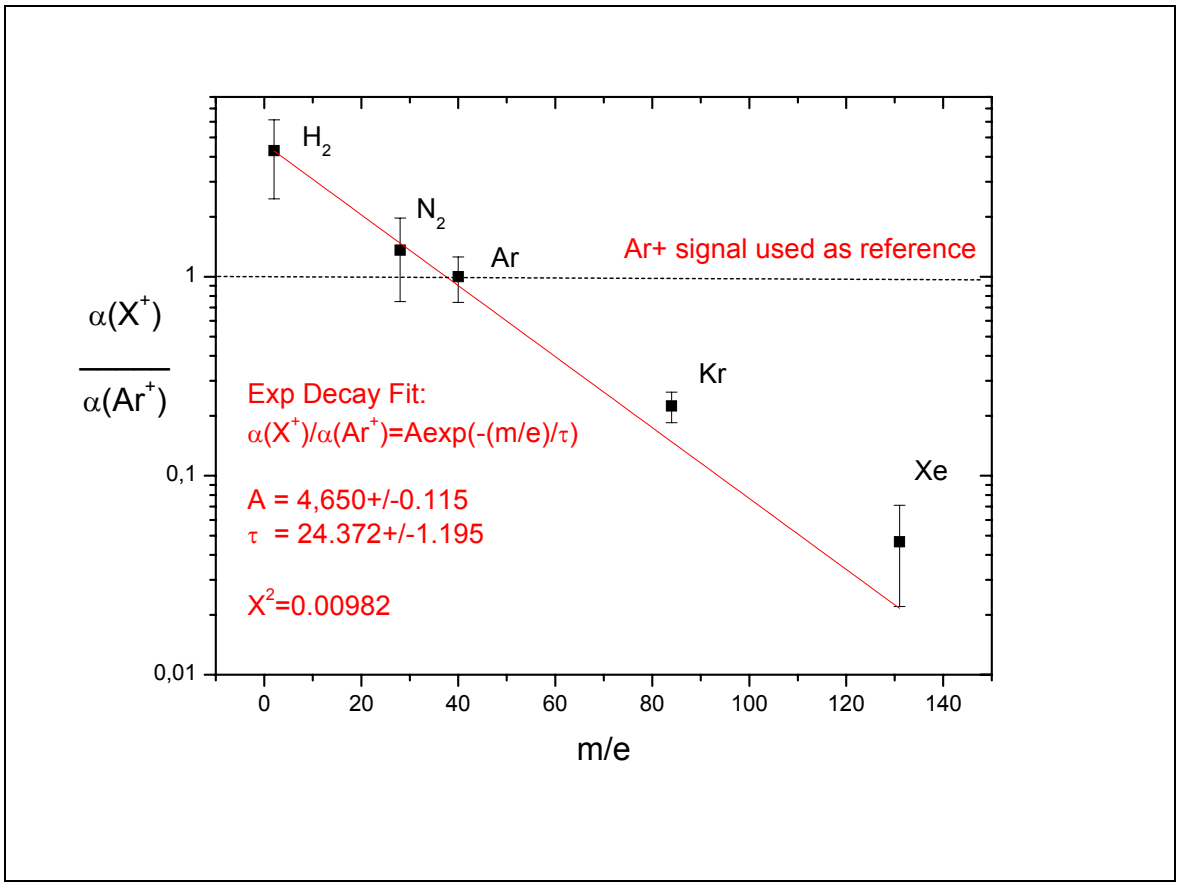

Figure 5.1.14. Calibration curve for the mass to charge ratio dependent trasmission function of quadrupole, ions extraction lenses and channeltron detector.

The ratio between the mass spectrometer transmission coefficients was extrapolated by a calibration procedure described in the following.

Vacuum reactor was filled with a calibration gas mixture (He, N_2, Ar, Kr, Xe, 5 Pa, 20% each) and the gas was sampled on the corresponding mass channels with the plasma off. All the partial pressures were known and the signal slope value of argon was taken as reference. From interpolation and linear fitting of the data the transmission coefficients ratios were calculated and the results as function of the mass to charge ratio are shown in Figure 5.1.14.

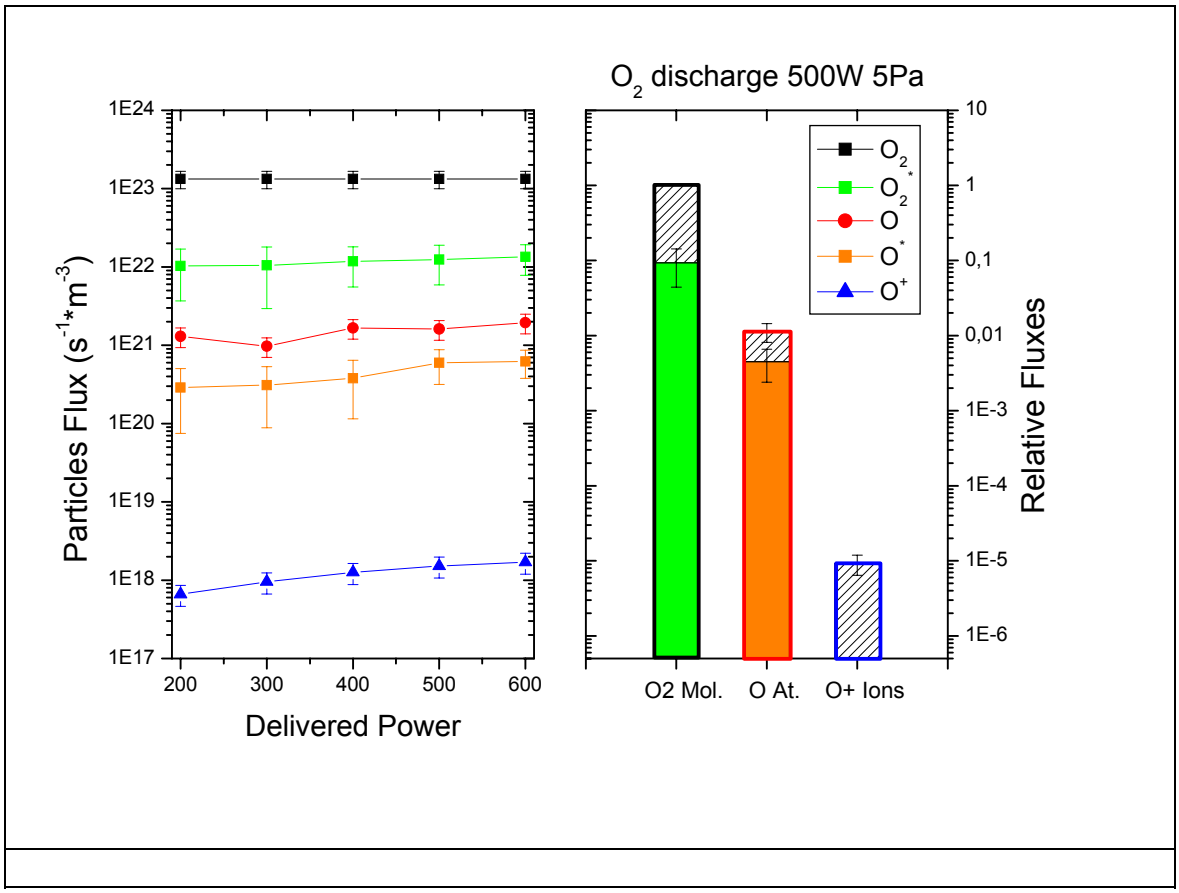

Figure 5.1.15 Summary of Langmuir probe and mass spectrometric meausraments. In the left panel absolute particles fluxes (O_2 molecules, O_2 metastables, O atoms O radicals and positive ions) are shown as a function of RF delivered power. In the right panel, relative fluxes at 500 W are shown.

To obtain the calibration values to evaluate oxygen signals the data from the calibration mixture were fitted with an exponential decay function, the full analytical form of the three factors embedded in α(m/e) was not needed for our experimetns purposes and this approximate expression (see Fig. 5.1.14) was chosen referring to literature. Anyway the chi-squared and the errors and the fitted parameters show good agreement with the data points and the interpolation from the fit was used to derive values for the TIMS.

The procedure described in the previous paragraph was used to measure the densities of oxygen metastables (atoms and molecules) in the plasma phase. On the 32 a.m.u. mass channel signal from the long living (τ=2700s) singlet molecular oxygen state $1\Delta_g$ was detected while on the 16 a.m.u. channel signal from the metastable oxygen atom states $2p^4$ 1D and $2p^4$ 1S were detected.

The TIMS measurements were performed for an oxygen discharge at 5 Pa varying the RF delivered power, results are shown in Figure 5.1.15. In the left panel the trends of metastables states fluxes are shown, as calculated from densities values according to equation 5.6. To grab at once the final picture of the results obteined in this chapter, together with TIMS results are shown fluxes for oxygen positive ions and the total atomic and molecular fluxes as derived from Langmuir probe measurements and mass spectrometric measurements (already shown in Figure 5.1.11).

In the right panel are shown particles fluxes corresponding to an oxygen discharge at 5 Pa and 500 W normalized to the oxygen molecule flux. From these data is possible to evaluate the relative magnitude of metastables states fluxes, oxygen metastables molecules are around (10 ± 3)% of the gas flux while oxygen atoms are around (0,5 ± 0,2)%, there is a factor 20 difference between these two values. Since both species can be accounted for being potentials agents in chemical etching processes and, up to now our attention was focused mostly on atomic oxygen (because of the detection method used, OES actinometry) it will be worthy in the following try to discriminate between the relative importance, for etching processes, of these two particles.

References

[1] Amemlya H, Annaratone B M and Allen J E 1999 *Plasma Sources Sci. Technol.,* **8,** pp. 179-90.

[2] Demidov V, Ratynskaia S and Rypdal K 2002 *Rev. Sci. Instr.*, **73**(10), pp. 3409-39.

[3] Sudit I D and Woods R C 1994 *J. Appl. Phys*., **76**(8), pp. 448-49.

[4] Riccardi C Barni R and Fontanesi M 2001 *Journal of Applied Physics,* **90**(8), pp. 3735-42

[5] Merlino R L 2007 *Am. J. Phys.* **75**(12) pp. 1078-85.

[6] Stoffels E, Stoffels W W, Vender D, Kando M, Kroesen G M W and De Hoog F J 1995 *Physical Review B* **51**(3) pp. 2425-35.

[7] Stranak V, Blazek J, Wrehde S, Adamek P, Hubicka Z, Tichy M, Spatenka P and Hippler R 2008 *Contrib. Plasma Phys.,* **48**(5-7), pp. 503-08.

[8] Stamate E and Ohe K 1998 *Journal of Applied Physics,* **84**(5) pp. 2450-58.

[9] Andrei H, Covlea V, Covlea V V and Barna E 2003 *Rom. Rep. Phys.,* **55**(2), pp. 51-56.

[10] Azooz A A 2004 *Fizika A* **13**(4) pp. 151-60.

[11] Wang Z, Lou Y, Lin K and Lin X 2007 *International Journal of Mass Spectrometry,* **261**, pp. 25-31.

[12] Wang Z, Lou Y, Lin K and Lin X 2008 *Vacuum,* **82**, pp. 84-89.

[13] Wang Y, Van Brunt R J and Olthoff J K 1998 *J. Appl. Phys.,* **83**(2), pp. 703-08.

[14] Pulpytel J, Arefi-Khonsari F and Morscheidt W 2005 *J. Phys. D: Appl. Phys.,* **38**, pp. 1390-95.

[15] Robertson R and Gallagher A 1986 *J. Appl. Phys.* ,**59**(10), pp. 3402-11.

[16] Singh H, Coburn J W and Graves D B 1999 *J. Vac. Sci. Technol. A,* **18**(2), pp. 299-305.

[17] Sugai H and Nakamura K 1995 *J. Vac. Sci. Technol. A,* **19**(3), pp. 887-893.

5.2 Plasma-biomaterial interaction mechanism

5.2.1 Interactions models

In this section will be described how data and measurements regarding absolute values of ions and radicals fluxes presented in section 5.1 have been used to investigate mechanisms for plasma etching of biomaterials.

To analyze surface kinetics, a phenomenological model based on Langmuir-Hinshelwood theory (theory of active sites) was used. The theory assumes that the surface is energetically non uniform and contains active sites, which are able to interact with particles coming from plasma volume gas phase. Therefore, chemical reactions are supported by the absorption of chemical active species at free sites while the sites occupied by reaction products are chemically inert. The basic rules for the analysis of plasma etching processes using this theory can be found in literature. [1,2,3] Later, several reaserchers demonstrated the reliability of this modeling approach both in predictive and quantitative trends. [4,5,6,7,8,9]

In our case the calculations of surface kientics are based on the following assumptions:

(i) only O atoms are effective for surface chemical reactions

(ii) only O^+ ions are effective for sputtering processes

(iii) only O^+ ions can partecipate in ion-stimulated desorption of the reaction products

(iv) etch products in the gas phase do not change plasma parameters

The starting point is the overall picture involving the possible interactions based on ions and radicals occurrence at the surfaces.

The interaction processes taken into account describes the simplest model [10] for oxygen containing plasmas interacting with a substrate X (a generic substrate made up of chemical compounds that support oxidation processes) is described in figure 5.2.1.

The surface (s) made up of a generic chemical compound (X) is described in terms of surface coverage (θ), i.e. fraction of available chemical bonding sites covered with adsorbate. The fluxes impinging the substrate are the incoming fluxes of radicals Γ_{rad} and ions Γ_{ion} that determines adsorption with the probability α_r and α_i respectively. The fluxes leaving the substrate are the oxidised compounds XO describing etching by-products, this

flux of desorbed compounds is divided in two factors: thermal desorption, governed by a temperature dependent constant $K_{thermal}$, while the second term is the ion impact induced desorption of oxidised compounds on the surface, regulated by the yield Y (molecules desorbed per incident ion).

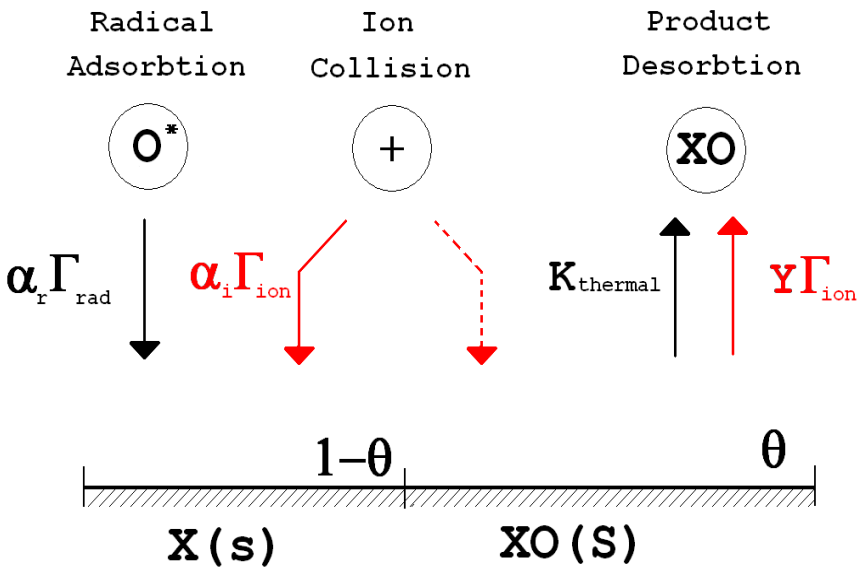

Fig. 5.2.1 Surface etch processes, assuming Langmuir kinetcs, considered for models testing against experiments

In our analysis Langmuir kinetcs for chemisorption of etchant atoms and ion induced or thermal desorption of etch products are assumed. The etch rate is then determined by etchant atom and ion fluxes, temperature and ion bombarding energy at the surface. In figure 5.2.1 the approach for O atom etching of a carbon-based substrate is illustrated.
The set of possible reactions considered here is

(1.a) $O^*(g) + C(s) \rightarrow C : O$ oxygen atom adsorption
(1.b) $O^+ + C(s) \rightarrow C : O$ ion-assisted adsorption
(2.a) $O^+ + C: O \rightarrow CO(g)$ ion assisted desorption
(2.b) $C : O \rightarrow CO(g)$ thermal desorption

Within the framework of the Langmuir kinetic theory for adsorption/desorption of gases from surfaces it is possible to write down equations for etching rates describing the following processes, details of the equation derivation can be found in [11], in all eqautions presented below the rate coefficients and constants are combined into generic coefficient for regression purposes.

A) oxygen atom adsorption (1.a) - thermal desorption (2.b), this process is termed chemical etching. The overall etch rate is determined by oxidation reaction taking place on the surface between the substrate and oxygen atoms flux, adsorption of O atoms as well as the desorption of etch products are considered be comparatively fast steps, the ions play no role in the etching mechanism. then the removal rate is given by equation 5.9:

$$ER = \frac{k_5 \Gamma_O}{1 + k_6 \Gamma_O} \qquad [5.9]$$

B) oxygen atom adsorption (1.a) - ion assisted desorption (2.a), this process is termed ion-assisted chemical etching. this model represents the situation where the ions impinging on the substrate are energetic enough to assist in the desorption of surface bound oxidized species (physisorbed compounds, bound with energies between 0.01 and 0.25 eV), but not energetic enough to promote the forward surface oxidation reactions (chemical bonds energies between 0.4 and 4 eV), it can be seen that it is possible for low energy ions typical of ICP discharges to provide energy for desorption while not providing enough for chemical reactions with higher activation energies, then the removal rate is given by equation 5.10:

$$ER = \frac{k_3 \Gamma_O}{\Gamma_{ion} + k_4 \Gamma_O} \qquad [5.10]$$

C) ion-assisted adsorption (1.b) - ion assisted desorption (2.a): this process is termed ion-assisted chemical etching with ion assisted desorption. In this case the ion flux to the substrate surface both promotes desorption of adsorbed species and provides energy to promote the forward surface oxidation reaction, then the removal rate is given by equation 5.11:

$$ER = \frac{k_1 \Gamma_O \Gamma_{ion}}{\Gamma_{ion} + k_2 \Gamma_O} \qquad [5.11]$$

these equations describes possible processes occurring at the plasma-biomaterials interfaces, that we want to investigate in order to determine which one is occurring in our plasma processes. The selection of the mechanisms to test was done according to the preliminary results obtained in this dissertation and described in paragraphs 3.1, 3.3 and 4.2.

5.2.2 Interaction models statistical analysis

Several plasma treatments were performed on BSA drops spotted on silicon, plasma parameters varied were RF delivered power and discharge pressure.

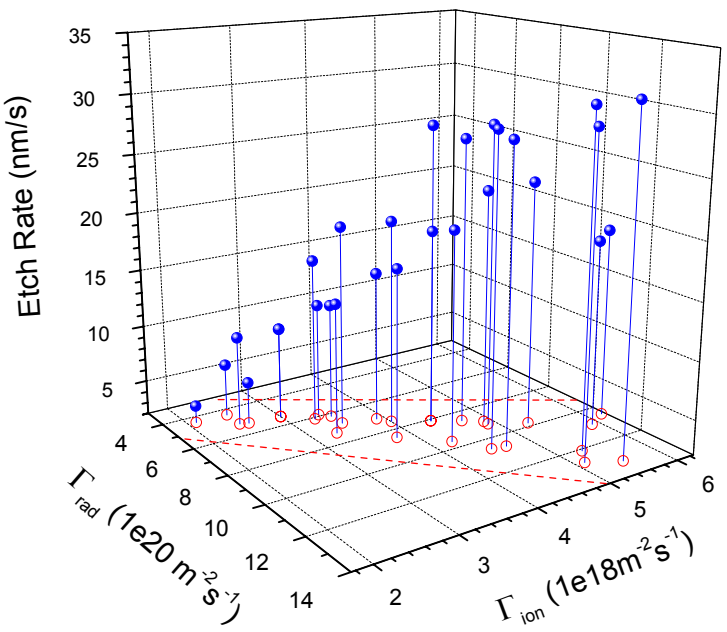

Fig. 5.2.2 BSA etching rates as measured by profilometry as a function of the absolute fluxes of Ar ions and O atoms radicals fluxes.

The values of these external discharge parameters were chosen accordingly to the quantitative characterization described in section 5.1, so in the following paragraphs ER data points will be plotted referring directly to corresponding particles fluxes corresponding to the specific plasma conditions at which plasma treatments were performed (see fig. 5.2.2 and 5.2.4).

The first set of measurements are shown in figure 5.2.2 these treatments were performed at 8 different delivered power levels ranging from 250 to 600 Watts and 3 different pressures from 5 to 15 Pa. Etching rates measurements were performed by means of stylus profilometer, a total amount of three drops were measured 5 times each before and after a treatment of 30 seconds in order to derive the etch rates values. In graph 26 and 29 error bars on data points are not shown for sake of clarity but the average standard deviation on measured etching rates was of the order of 5%.

From the data shown in fig. 5.2.2 is possible to see qualitatively how etch rates values are raising when both ions and radicals flues are increasing, nothing can be said from this data about the trends of an independent increment of ions or the radicals fluxes, the

reason why all the experimental points lie in a narrow region of the Γ_{ion} - Γ_{rad} space is that this two quantities are coupled by the plasma equilibrium and is not possible to vary them in an independent fashion in decontamination experiments in plasma environment. Moreover for our plasma experiments shown in figure 5.2.4 the ion energy in all conditions was always comprised between 10 and 15 eV.

In order to investigate the mechanisms of plasma biomaterials interactions the data from etch rates measurements were compared with calculated etch rates of the three models described before, according to the scheme below: [12,13]

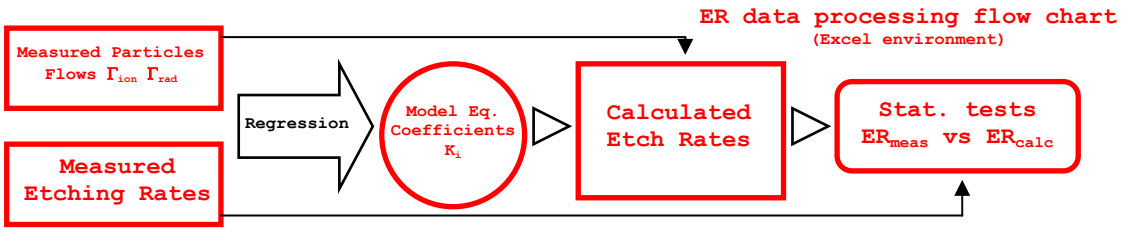

The calculations flow was performed as follows: each group of values (Γ_{ion}, Γ_{rad}) was used to regress linearized forms of equations 5.9, 5.10 and 5.11. After regression routines coefficients $k_1,\ldots,k_6$ were used with the equations 5.9, 5.10 and 5.11 to calculate theoretical etching rates according to the different models proposed. Then calculated ER where compared to measured ER using statistical tools in order to determine the validity of the assumed process mechanism.

The meaning of each test is briefly explained below:

Coefficient of Determination R^2: is a statistic that will give information about the goodness of fit of a model. In regression, the R^2 coefficient of determination is a statistical measure of how well the regression line approximates the real data points. An R^2 of 1.0 indicates that the regression line perfectly fits the data. Adjusted R^2 is a modification of R^2 that adjusts for the number of explanatory terms in a model. Unlike R^2, the adjusted R^2 increases only if the new term improves the model more than would be expected by chance.

Significance F: An F-test is a statistical test in which the test statistic has an F-distribution under the hypothesis of no relationship between measured phenomena. It is

used to compare statistical models that have been fit to a data set, in order to identify the model that best fits the population from which the data were sampled. The significance numerical value, ranging from zero to one, describes the likelihood that the global model describes a random relationship (F=0) between variables.

P-value P: in statistical significance testing, the p-value is the probability of obtaining a test statistic at least as extreme as the one that was actually observed, assuming that there is no relationship between measured phenomena. In other words, it's the probability that test results are a fluke and not representative of physical reality.

Non-parametric tests: In this method, the mean of the predicted values is tested for significant difference from the mean of the data (model ‘‘bias’’). Plots of sample model residuals (the difference between observed and model predicted values of the dependent variable, at a given value of an independent variable) versus each independent variable are examined for slopes that are significantly different from zero. If there is a detectable nonzero slope in one of these plots, then the model is ‘‘skewed’’ (see figure 5.2.3). Then these same plots, as well as a plot of model predicted versus observed dependent variable values, are examined to determine if residuals with positive and negative values are clustered together in only a few ‘‘runs’’ (model ‘‘curvature’’). Curvature is then a descriptive term employed here to describe the effect of autocorrelation in sample model residuals

The results of such statistical procedures are summarized in table 5.1. The first three rows refers to the results of the tests for the three models presented before (eq. 5.9, 5.10 and 5.11), while the fourth and the fifth row show the results of the same procedure for the ion-assisted chemical etching - ion assisted desorption in a radical limited regime and in an ion limited regime respectively. Equations for these two additional regimes are obtained by setting the ion-removed flux of by-products from the surface much higher than the adsorbed radicals on the surface (eq. 5.12) end vice versa (eq. 5.13).

$$\beta y\Gamma_{ion} >> \alpha_r\Gamma_{rad} \quad \longrightarrow \quad ER = \alpha_r\Gamma_{rad} / \beta n \qquad [5.12]$$

$$\beta y\Gamma_{ion} << \alpha_r\Gamma_{rad} \quad \longrightarrow \quad ER = \left[y\left(\sqrt{\varepsilon} - \sqrt{\varepsilon_{th}}\right)\Gamma_{ion}\right] / n \qquad [5.13]$$

According to the different methods of each statistical test the results were marked, in the table, in green when they fulfil the test requirement and in red when the model fails the validation.

Model	Global Tests		Parameters		Local Tests	Non-parametric Tests	
	Corr. R2adj	Signif. (Ftest)	Ki	Kj	P-value (Ttest)	Curv.	Skew.
Ion Etching Ion Desorb.	0.899	0	0.19 ±0.11	0.12 ±0.10	K1:0.077 K2:0.085	1.242	r1:0.682 r2:0.700
Chem. Etching Ion Desorbtion	0.032	0.493	0.02 ±0.03	0.05 ±0.07	K3:0.488 K4:0.493	1.261	r3:0.349
Chem. Etching Therm Desorb.	0.461	0.001	9E-4 ±0.01	0.04 ±0.10	K5:0.946 K6:0.001	1.038	r4:0.682
1.Rad lim.	0.905	0	0.43 ±0.02	n.p.	K7:0	0.923	r5:0.742
1.Ion lim.	0.901	0	0.22 ±0.01	n.p.	K8:0	1.118	r6:0.748

Table 5.1. Summary of the statistical tests results for plasma biomaterials interaction mechanisms (investigated parametric dependencies are ion and oxygen atoms flux)

It can be seen at glance from table 5.1 that models derived from equation 5.2 and 5.3 badly describe the experimental data points while only model built over assumption of mechanism 1 (ion driven adsorption – ion desorption) scores good agreement, but even in this case there is a poor significance of the single terms of the model equation, the P-values for this models tell that significance of the correlation between the individual independent variables (the fluxes) and the dependent variable (the etching rates) is poor. The P value tells how each individual variable has some correlation with the dependent variable. To understand this disagreement models related to equations 5.10 and 5.11 were tested, based on the physical assumption of the disparity of the fluxes orders of magnitude. Both these models in the limited regimes scores good test statistics but they

cannot be both true at the same time, in particular equation 5.12 have to be rejected on the basis of the particle fluxes characterization shown in section 5.1, the inequality underlying this limiting regime being not true in a plasma environment.

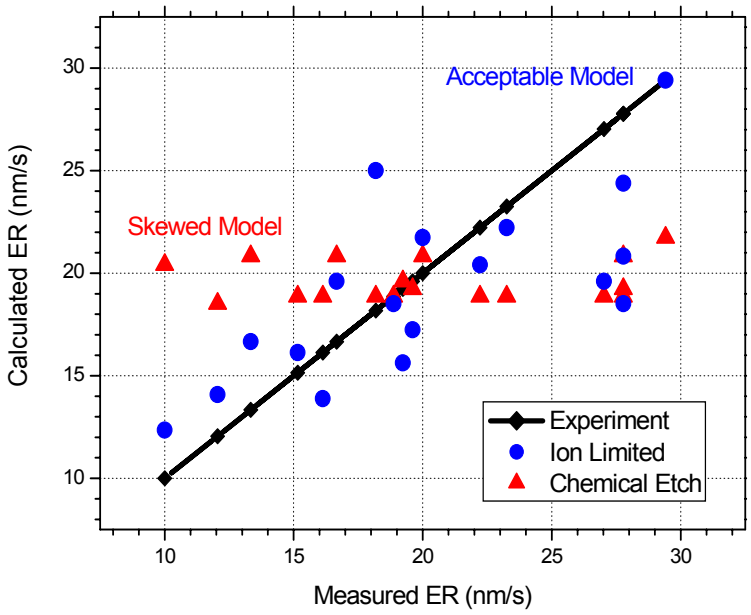

Fig. 5.2.3 Calculated BSA etching rates residuals plotted against measured etching rates. A black line refers to measured etching rates and serves as reference. Red data points refers to chemical etching equation regression and show model skewness, bleu data refers to ion-limited ion-assisted etching equation regression.

In order to further discriminate in between the two hypotheses further experiments were performed in order to extrapolate the ion energy dependence of the ion desorption processes. If the mechanism described from equation 5.9 is true the measured etch rates must show a dependence from ion energy even in the low energy range (< 100 eV) where the effects of pure sputtering are negligible.

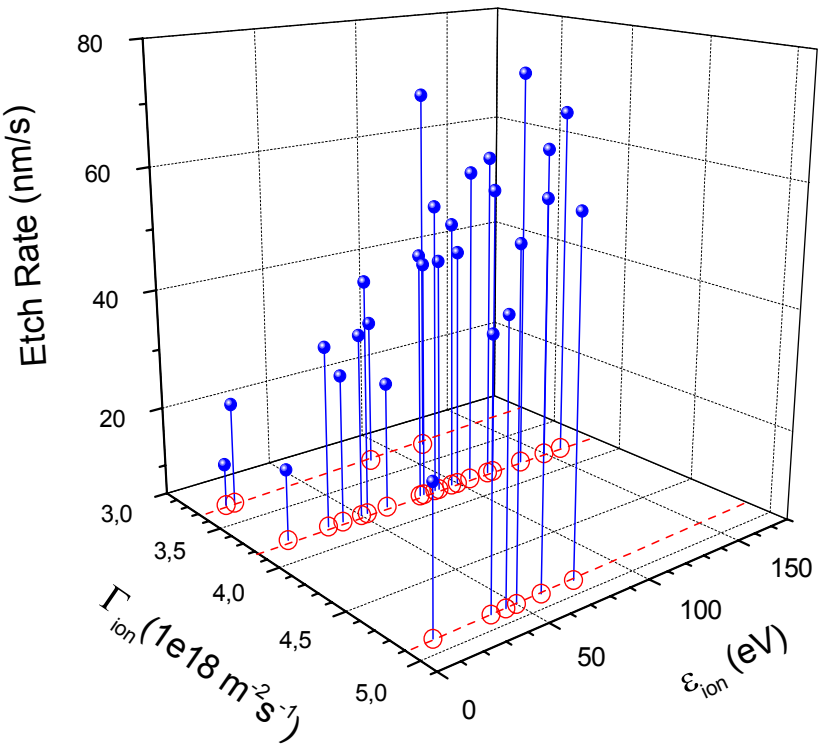

Fig. 5.2.4 BSA etching rates as measured by profilometry as a function of the absolute fluxes of Ar ions flux and ion energy.

In these experiments the same procedure described in the previous paragraph was followed, but now the samples were placed on an active capacitive electrode fed with RF power at 13.56 MHz, with its excitation pulse synchronized with the signal from the main generator feeding the inductive antenna. During these experiments run the DC bias voltage on the capacitive electrode was varied by changing the power of the secondary generator while the values of the ions and radicals fluxes where determined by the plasma conditions set by the inductive antenna power, vacuum chamber pressure and the others operating parameters. BSA etching rates were measured by means of profilometry in the same way described in previous paragraphs. In figure 5.2.4 the raw etching rates data are shown as function of ion energy and fluxes, each point is also determined by an atoms flux which is not shown in figure 5.2.4.

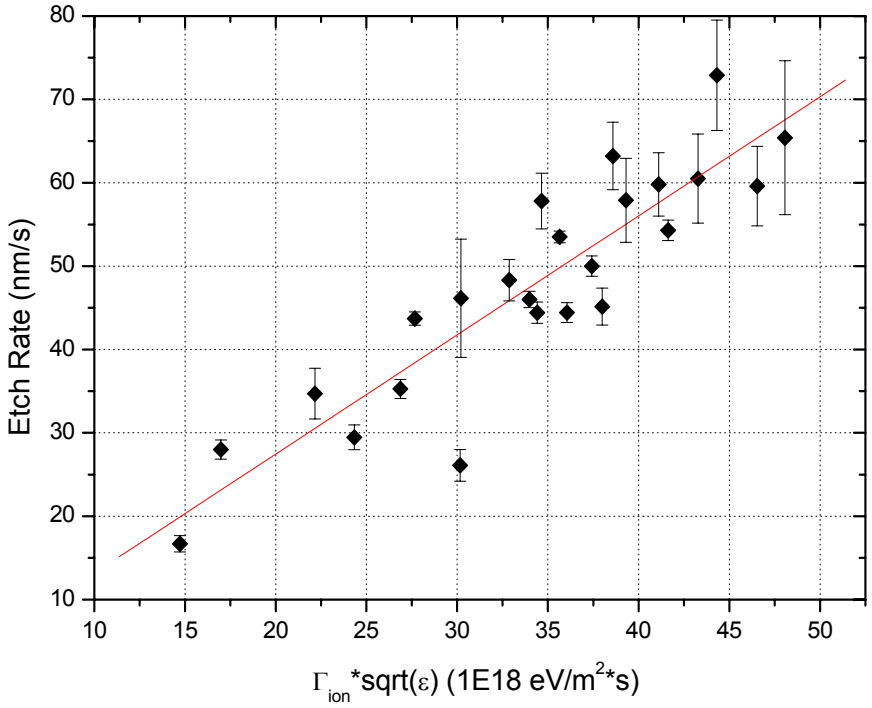

Fig. 5.2.5 Measured etching rates plotted agains Γ_{ion}·sqrt(ε_{ion}). Red line shows data fit using equation 5.13, ion-assisted chemical etching - ion assisted desorption in the ion limited regime.

From the results of fig. 5.2.4 a dependence on ion energy of the etching rates is clearly visible even at very low energy values. To simplify data visualization it is possible to plot the etching rates versus the product of ion flux and the square root of the ion energy (see fig. 5.2.5), as it is suggested by the functional form of equation 5.13, in order to make the dependence on ion energy evident.

The representation of the etching rates data given in fig. 5.2.6 shows already a strong correlation between the rates and the ion enhanced desorption mechanism. In order to have a more rigorous validation of this result the same statistical procedure applied in the previous case was applied to the results shown in figure 5.2.4. The results of the statistical procedure are shown in table 2 and some example of residuals evaluation test are shown in Fig. 5.2.6.

Model	Global Tests		Parameters		Local Tests	Non-Parametric Test	
	Corr. R2adj	Signif. (F-test)	Ki	Kj	P-value (T-test)	Curv.	Skewness
Radical Lim	0.053	0.426	0.34 ±5.49	n.p.	K1:0.787	1.253	r5:-0.441
Ion Lim.	0.796	0	1.42 ±0.14	1.10 ±5.26	K2:0 K3:0.833	1.229	r5:0.900
Ion Lim. No Threshold	0.941	0	1.39 ±0.03	n.p.	K4:0	1.235	r5:0.900

Table 5.2. Summary of the statistical tests results for plasma biomaterials interaction mechanisms (investigated parametric dependencies are ion flux and ion energy)

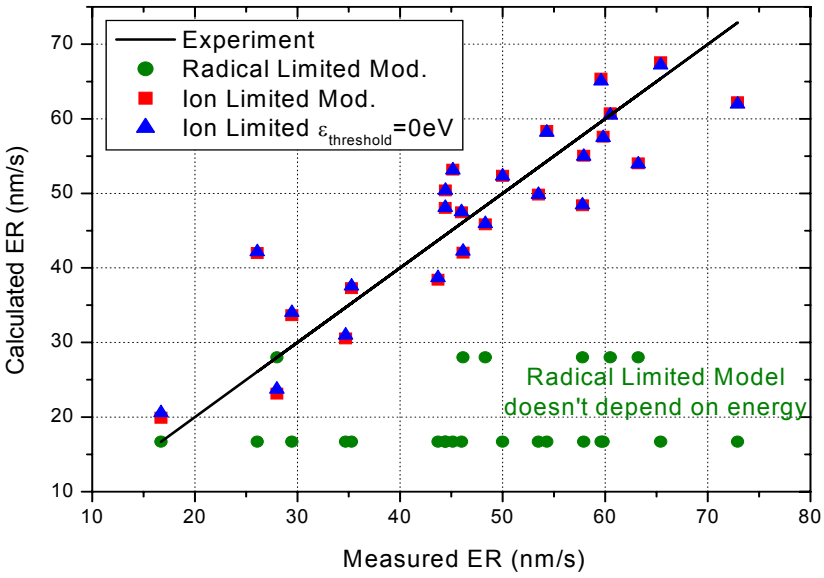

Fig. 5.2.6 Calculated BSA etching rates residuals plotted against measured etching rates. Black line refers to measured etching rates and serves as reference. Red data points refer ion-limited ion-assisted etching equation regression, bleu data refers to same equation regression but with zero energy threshold for ion assisted desorption precesses. Green data refers to radical-limited ion-assisted etching equation regression.

The scores of the radical limited model are in general negative, because this equation has no term to account for the energy dependence (see fig. 30). Even the ion-limited equation shown some negative test, related to the evaluation of the regressor of the constant term in equation 13. This behaviour can be explained considering that the ion energy threshold to trigger the desorption of an oxidised compound from the surface is so low (a chemisorbed molecule can be bounded by a potential well of only 0.5 eV) that the instrumental measurement errors on the etching rates makes impossible the correct determination of this term. If we neglect the energy threshold and this term is set to zero then the agreement becomes positive.

References:

[1] Gerlac-Meyer U 1981 *Surf. Sci.,* **103**, pp. 524-538.

[2] Winters H W and Coburn J W 1992 *Surf. Sci. Rep.,* **14,** pp. 162-200.

[3] Gray D C, Tepermeister I and Sawin H H 1993 *J. Vac. Sci. Technol. A Vac. Surf. Films,* **11, pp.** 1243-57.

[4] Slovetsky D I 1989 *Plasma Chem.,* **15**, pp. 208-250.

[5] Ovchinnikov N L, Svettsov V I and Efremov E M 1999 *Russ. Microelecron*., **28**, pp. 13-17.

[6] Abdallahi-Alibeik S, McVittie J P, Savaswat K C, Shkharev V and Schoenborn 1999 *J. Vac. Sci. Technol. A Vac. Surf. Films,* **17**, pp. 2485-91.

[7] Lee C, Graves D B and Lieberman M A 1996 *Plasma Chem. and plasma Proc.,* **16**, pp. 99-120.

[8] Jin W, Vitale A and Sawin H H 2002 *J. Vac. Sci. Technol. A Vac. Surf. Films,* **20** pp. 2106-14.

[9] Shiozawa M and Nanbu K 2002 *Jpn. J. Appl. Phys.,* **41**, pp. 2213-19.

[10] Lieberman M A 2009 *Plasma Sources Sci. Technol*., **18,** 014002(5).

[11] Bray R P 1997 PhD Thesis, Texas Tech. University.

[12] Bray R P and Rhinehart R R 2001 *Plasma Chem. and Plasma Process*., **21**, pp. 163-174

[13] Bray R P and Rhinehart R R 2001 *Plasma Chem. and Plasma Process*., **21**, pp. 149-161

6 Biological tests

As was described in the previous chapters a variety of plasma processes are capable of destroying both small organic molecules and larger biomolecular structures adhering to, or adsorbed on, a variety of surfaces without causing significant damage to the surfaces themselves, among different works in the literature interesting results can be found in [1,2,3,4]. This has led to a large number of plasma decontamination oriented applications in the research field and in some cases in the medical and electronics industries. However, it would be true to say that, while the technique is capable of very significant reduction of the surface load of organic contamination, the development of methods to quantify the efficacy of particolar treatments lags far behind the development of the plasma processes themselves. The on line QCM diagnostic method proposed in chapter 4 is suitable only for reaserch purposes but has limited applicability for application as a standard quantification method in the medical practice.

The diverse shapes and the different materials used in the manufacture of surgical instruments together with the efficiency of actually employed decontamination methods make measuring protein contaminations on surfaces a non-trivial analytical problem. The cleaning protocols used in surgical instrument reprocessing involve washing procedures that typically reduce the surface residual tissue contamination, of even very heavily contaminated instruments, to levels which cannot be detected by the naked eye. Typically this represents a level of residual protein contamination (averaged over an instrument surface) of about $10\mu g \cdot cm^{-2}$ with localized deposits, the letters rarely exceed a loading of $1\ \mu g \cdot mm^{-2}$ [5,6]. Scanning electron microscopy (SEM), especially when linked to energy dispersive x-ray (EDX) spectroscopic analysis, has proven an efficient tool for the location and analysis of tissue residues on conventionally cleaned instruments [5,7,8,9]. However, SEM-EDX analysis has different limitations: it is non-quantitative, restricted to elemental analysis, applicable only to small objects, time consuming and very expensive.

However, it was demonstrated that plasma treatment can reduce the amount of residual surface contamination to a level where no organic residues are detectable by SEM [8] and

this has led to the development of more sensitive types of analysis. A range of very sensitive spectroscopic techniques can be employed for direct detection of deposits on surfaces at the molecular level, but many of these, like surface plasmon resonance (SPR) [10,11,12], surface-enhanced Raman spectroscopy (SERS) [13,14,15,16] and attenuated total reflection Fourier transform infrared (ATR-FTIR) spectroscopy [17], are limited to specially prepared solid matrices and have more relevance to the development of sensor technology for quantification of materials in solution than for adsorbed species in decontamination applications.

The requirement for a quantitative routine method for analysis of protein molecules bound to surfaces, suitable for measurement of nanogram·mm^{-2} levels, which could be employed, in principle, as a routine method for contamination quantification both before and after plasma decontamination procedures, has led us to test a more general approach. This involves investigation of laboratory protocols for covalent derivatization of surface-bound protein molecules with fluorophores and fluorimetric measuraemnts capable of measuring the resultant fluorescence of labelled proteins bound to the surfaces.

6.1 Fluorescamin staining protocol assessment

6.1.1 Description, calibration and testing

In order to test the temperature monitor and control tools described in paragraph 3.4 and to experiment a realistic decontamination situation it was decided to treat a macroscopic polymeric object, the objects chosen were polystyrene well plates normally used for biological measurements. Well plates were selected in order to couple controlled temperature treatments with the development of a fluorescent technique to monitor the protein removal from such surfaces. The reagent chosen for fluorescence measurements was Fluorescamin, a compound that is not fluorescent itself but reacts with primary amines to form highly fluorescent products, when activated by 365 nm light the protein-dye complex has an emission wavelength of approximately 470 nm. A standard fluorimeter plate reader (Fluostar) was used to carry on measurements. The benefits of choosing Fluorescamin as fluorescent probe are the specificity of the labelling and in

principle the possibility to detect low amount of proteins, in literature sensibility down to 10 pg/well is reported under special conditions [18] but the 1-100 ug/well (about 0.027-2.7 $\mu \cdot mm^{-2}$ of dry deposit) range is a more common area of measurements, drawbacks of the method are the lack of sensitivity in the case of strong blank signals, and the fast signal decay due to high hydrolysis rates at high concentration.

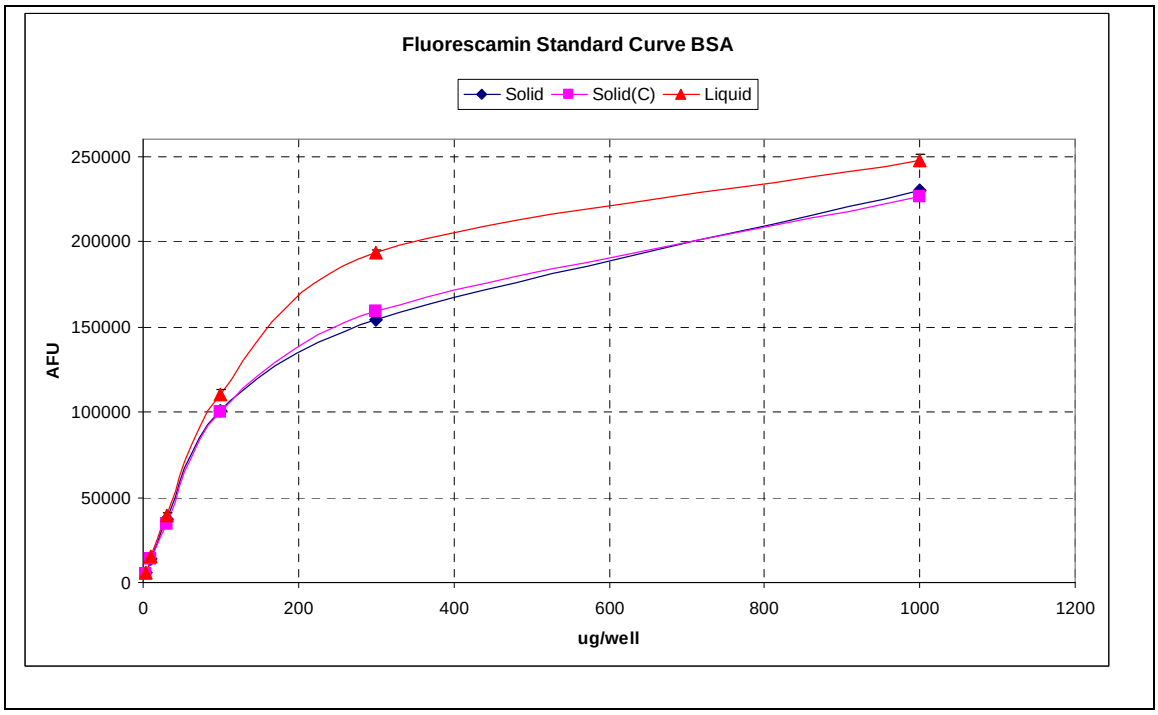

Figure 6.1.1 Set of fluorescamin staining calibration curves in different deposition situations, bleu data correspond to dried BSA deposits, pink data corresponds BSA/solvents solutions obtained from the dried deposits and red data correspond to BSA/solvent solution measurements.

To avoid the first problem (high blank signals) several different well plates were tested analyzing empty wells with the plate reader to identify the less responsive.

To take the time decay of the fluorescent emission into account in our measurements a special protocol described in the following paragraphs was developed.

First a calibration curve for BSA protein spots in the well plate was prepared as follows. For each well in the plate different amount of BSA protein were pipetted and allowed to dry in a flow hood. For each experiment an internal calibration curve and some empty

wells were present as well. After drying of the water the plates were eventually plasma treated and the deposits re-suspended with a die-containing solution. The specifications for Fluorescamin dye solution preparation in the protein mass range 3 – 1000 ug/well are: final volume = 80 uL, 3mg/ml Fluorescamin dye in H_2O + DMSO (1:3) solvent, buffer $NaHCO_3$ 0,1M, pH = 8,3. The mass range per well evaluated in the calibration curve usually ranges from 3 to 1000 ug/well and the signal from the dye-protein complex was measured both in liquid phase and after drying stage and re-suspension.

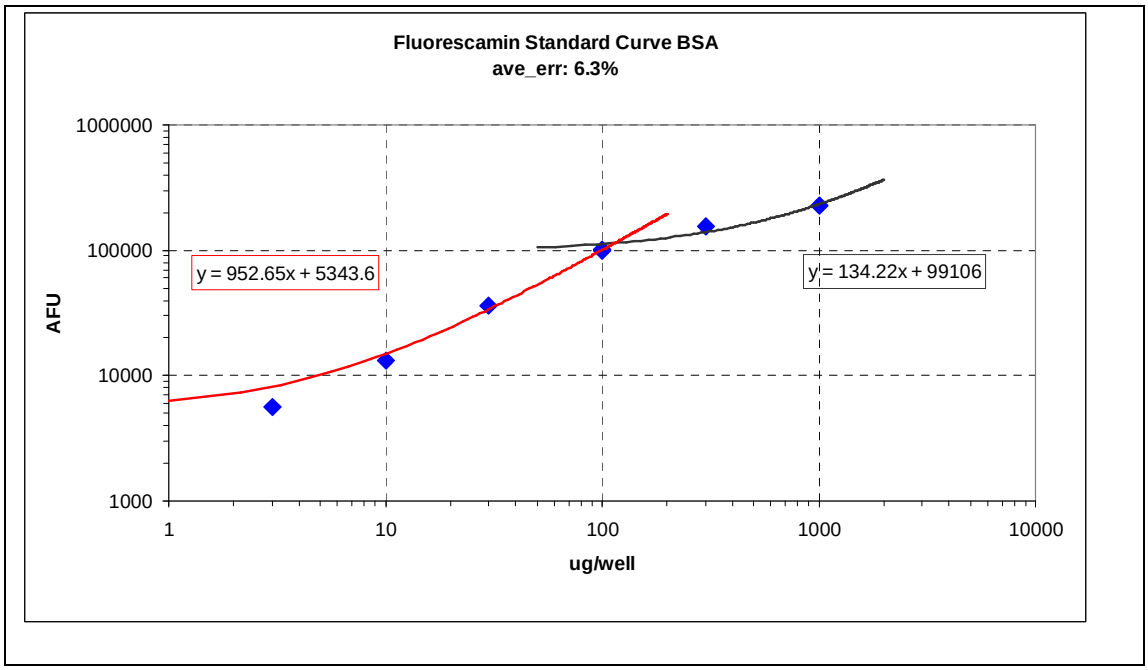

Fig. 6.1.2 Double region linear fits for Fluorescamin staining calibration data.

The first results are shown in figure 6.1.1 where two series corresponding to dried and re-suspended deposits, varying the deposition method, and a series corresponding to liquid phase are displayed. These different deposition methods were investigated because a drying stage after deposition is mandatory to perform plasma treatments on proteins and, on the other hand, the dry deposit is not the standard situation were Fluorescamin staining protocols present in literature applies. In our situation drying of the protein deposit produces lower fluorescent emission intensities with respect to the liquid phase at the same mass per well but the signals are still clearly measurable.

From the results displayed in figure 6.1.1 it can be seen that the useful dynamic range of the Fluorescamin dye is comprised approximately between 3 and 100 ug/well, but after this deposited mass amount, saturation of the signal starts to play a significant role. Another calibration measurements (not shown here) for the mass range 0,1 pg/well to 1 ug well results in a flat fluorimetric signal in the range investigated, this is probably due to the high background of our systems.

The data of the calibration curve for the dried deposit were fitted with two linear functions (see figure 6.1.2), the principal one evaluated from 3 to 100 ug/well and a second one from 100 to 1000 ug/well in order to evaluate signals from the saturation region. Several replicas of the fluorescent measurements at the same deposited mass indicate that the average intensity measurement error for a certain mass per well is about 6,3%.

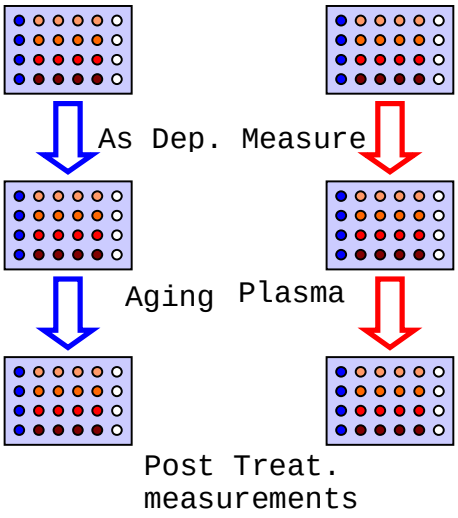

Fig. 6.1.3 Schematics of the sample preparation protocol for fluorescence measurements.

In order to take into account the fluorescence signal decay with time for each experiment two well plates were prepared at the same time with identical BSA spots, both with replicas of experimental points and replicas of calibration points (see figure 6.1.3). Just after preparation a series for calibration and a series for data points were measured and then one of the well plates was plasma treated while the other one was kept under the

flow hood. After plasma treatment the two well plates were again measured and the fluorescence from treated wells, aged wells and aged calibration curve wells were detected. By subtraction and normalization of signals from the treated and aged well plate it is possible to distinguish signal decay due to aging from effect of plasma etching of the protein layer.

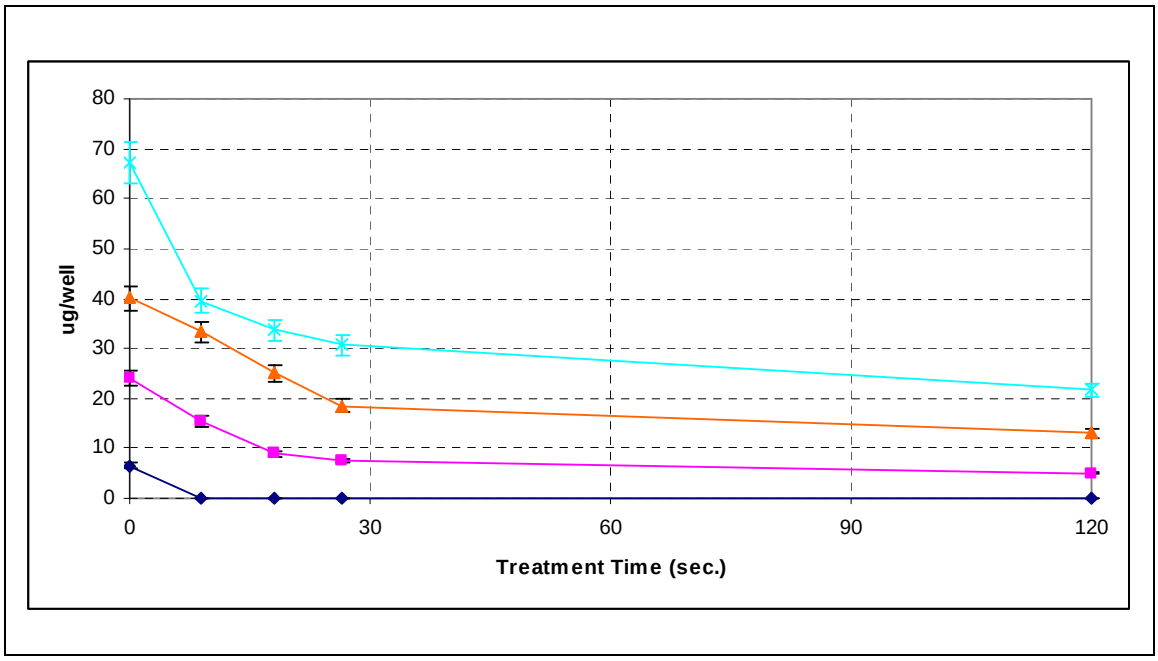

Figure 6.1.4 Quantitative (calibrated) plasma induced protein removal measurements using fluoriscamin protocol. Different curves correspond to different levels of initial contamination.

An example of measurements performed with the method described before for successive plasma treatments is shown in figure 6.1.4. It is important to say that under the conditions of low frequency pulsing of the discharge described in section 1 the well plates used for treatments were not damaged. The plasma treatments parameters set in this case was Ar:O_2 [1:1] gas mixture, power 350 W, pressure 5 Pa, frequency 1 Hz, duty cycle 25%, treatment/cooling time ratio 1:3.

Data shown in Fig. 6.1.4 describes the removal of protein material from the well plates. The curves corresponds to different levels of initial contamination, it can be seen that

after an initial phase of faster removal lasting less than 30 seconds the profiles flatten and the etching is negligible up to 120 seconds of treatments time.

The average etching rate from this data (calculated on the first phase up to 28 seconds treatment time) results to be 0,95 μg/s. The sensitivity of the method applied to Fluorescamin results to be not enough to resolve real low levels of residual contamination (less than 1 $\mu g/mm^2$) mainly because of the influence of the background signals coming from the well plates.

6.1.2 Influence of the rinsing step in plasma induced mass loss measurements.

In the previous paragraph (6.1.1) the temperature controlled treatments protocols described in section 3.4 were successfully applied exposing a real thermo labile object, polystyrene well plates, to plasma conditions normally used for decontamination experiments.

An experimental protocol for testing fluorescent labelling of biomaterials exposed to plasma was developed and tested; the fluorophor used in these experiments was Fluorescamin. An advantage of the method is the lack of a washing step after staining of the fluorophor that may lead to unwanted biomaterial removal other than the plasma action. Rinsing of the sample is a step commonly involved in standard staining protocols; the occurrence of unwanted biomaterial removal during washing makes such protocols not reliable if quantification of plasma induced mass loss is desired. Such an experiment would involve two staining procedures, one to determine the amount of contamination as deposited on the sample and one to measure the residual material after plasma treatment. The mass loss eventually occurring in the initial measurement procedure cannot be distinguished from the mass loss induced by plasma treatment.

In the following an experiment aimed to measure the mass loss induced by rinsing protein deposits with water will be described.

The aim of these experiments is to check the reliability of the Sypro-Ruby staining protocol [19] (chosen as example) of biological material on solid surfaces protocol as a method to determine the proteins residuals. This protocol has been proposed as an

endpoint protein content measurement to evaluate the efficiency of surface sterilization methods. In these experiments we measured the volume of Bovine Serum Albumin (BSA) and of the Brain Homogenate (BrH) deposits on solid samples before and after the staining procedure by means of an ellipsometric technique.

Biological samples have been prepared by means of the microspotter Scenion sciFLEXARRAYER depositing ordered arrays of BSA and BrH spots on polished silicon (100) surfaces; the silicon samples have been cleaned by means of ultra-sound bath in ethanol for 15 minutes, then rinsed using milliQ water for 1 minute and allowed to dry for 1 hour in a common flow hood.

For the stock solutions preparation the BSA (initial fractionation by heat shock, fraction V, minimum 98% for electrophoresis, Sigma) was diluted in TrisHCl buffer 5 mM with a pH of 7.4 at a concentration of 1 mg/ml.

The BrH samples were prepared homogenizing mouse brain in a 10% w/v solution in Phosphate Buffered Saline. The original solution was supplied by the *Institut des Maladies Emergentes et des Therapies Innovantes, Service d'Etude des Prions et des Infections Atypiques*, Fontenay-aux-Roses, France. To allow micro-spotter operation both original solutions has been further diluted down to 0.1% w/v concentration in a TrisHCl buffer 5 mM with a pH of 7.4.

Three replica samples has been prepared by spotting an 2x2 spots array (2 identical spots for each deposited material), every spot was made up by adding 4 drops, distance between spots centers in the array is 800 μm and the typical spot diameter is around 400 μm.

The protein deposits before and after Sypro Ruby fluorescent staining were analyzed by ellipsometric measurements using a variable angle multi-wavelength imaging ellipsometer (model EP3 by Nanofilm Surface Analysis GmbH, Germany). All measurements were performed in air at room temperature at three angles of incidence (65 70 and 75 degrees) and a field of view of 2000 μm × 2000 μm. A monochromatized Xe arc lamp (λ=554.3nm) was used as light source. Conventional PCSA (Polarizer-Compensator- Sample-Analyzer) null-ellipsometric procedure is used to obtain 2D maps of the Δ and Ψ angles.

From the Δ and Ψ data height maps was obtained by fitting the measured data with a two layers (bulk silicon and protein deposit) optical model, the fixed parameters of the model were both refractive index and adsorption coefficients for the two materials. Further evaluation of the height maps was performed using a dedicated MatLab code to extract volumetric values.

Before the staining procedure all the samples were incubated at 37 degrees for 30 minutes then were stained with Sypro Ruby (Invitrogen) for 15 minutes and washed in filtered (0.2-μm membrane) distilled water for 10 minutes. They were allowed to dry for 1 hour in a common flow hood.

In the following figures tridimensional images obtained from ellipsometric measurements of the samples surfaces before (6.1.5) and after (6.1.6) the staining protocol are shown:

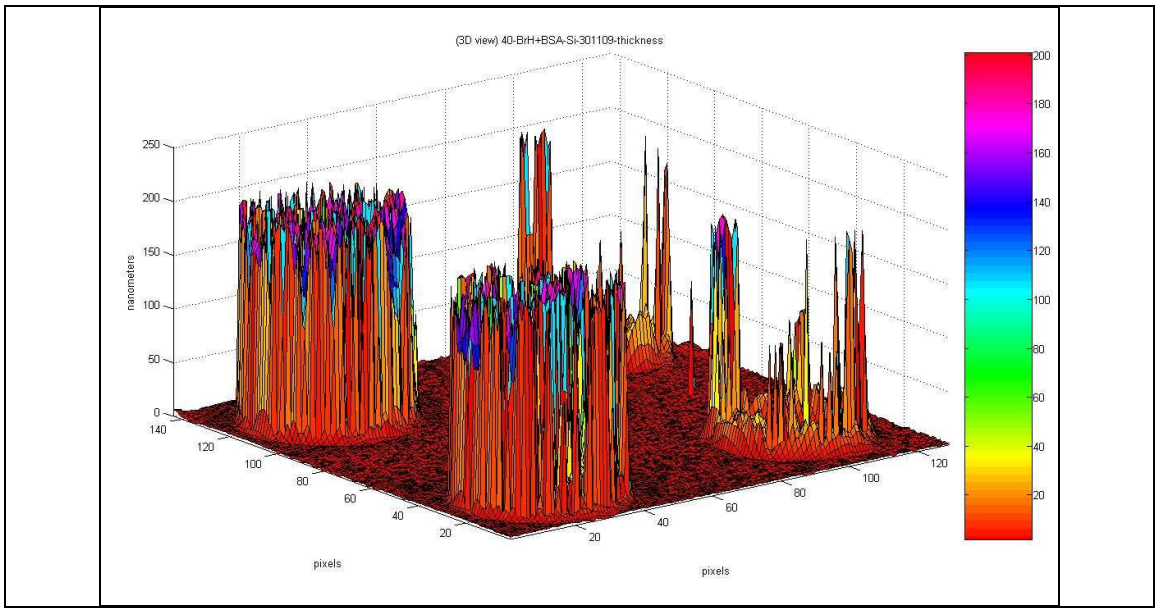

Figure 6.1.5) 3D height maps of the spotted arrays from ellipsometric measurements before the staining protocol, two BSA spots are shown in the left corners and two BrH spots are shown in the right corners.

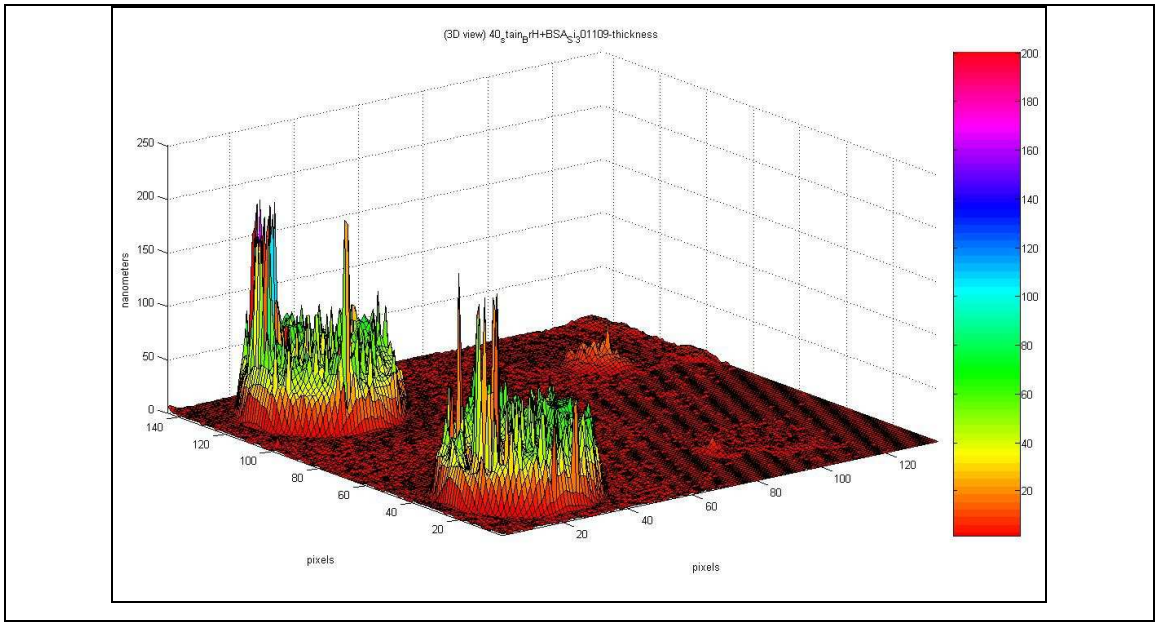

Figure 6.1.6) 3D height maps of the spotted arrays from ellipsometric measurements before the staining protocol, two BSA spots are shown in the left corners and two BrH spots are shown in the right corners

The calculated volume values for each measurement the average of the volumes of the two spots are reported in the table below, absolute average spots volume before and after the staining procedure are compared in figure 6.1.7

Table 6.1) Summary of the experimental data from three different samples.

Spots Volume (μm^3)				
sample	**As Dep.**		**Stain**	
	BSA	**BrH**	**BSA**	**BrH**
35	9689.3	1469.9	5939.4	64.8
37	11894.3	988.4	6667.6	147.55
40	11429.8	1654	5677.4	249.2
Ave.	11004.4	1370.7	6094.8	153.8
St.D.	1162.4	343.7	513.0	92.3

From this data it is possible to deduce that the protocol applied in this experiment for the fluorescent staining of solid samples leads to a removal of the biological material from

the samples itself. From the data shown in the table above (Table 6.1) the calculated relative volume reductions are (44.5±15)% for the BSA and (88.8±31)% for the BrH.

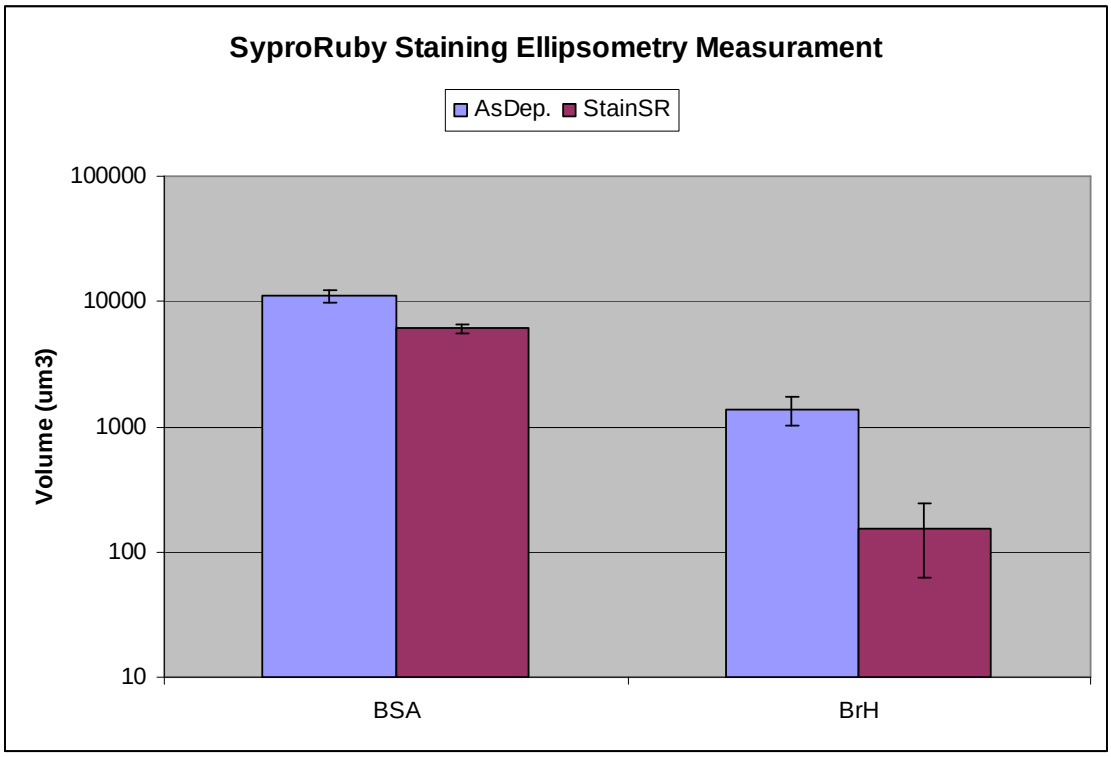

Figure 6.1.7) Absolute volumes, as calculated from ellipsometric images, of spotted BSA and BrH samples before (bleu) and after (violet) the staining procedure.

These measurements shown that the tested fluorescent staining protocol used for the evaluation of the proteinaceous residuals on solid samples treated with plasma discharges cannot be used to evaluate the efficiency of the sterilization processes.

6.2 Immuno-assay experiments

Enzyme-linked immunosorbent assays (ELISAs) are well plate-based assays commonly used in biochemistry. These assays are designed for detecting and quantifying different biomolecules such as peptides, proteins and antibodies. [[20],[21]] In a typical ELISA assay, an antigen is blocked on a solid surface and then combined with an antibody that is linked to an enzyme. Detection is performed by measuring the conjugated enzyme activity by

incubation with a substrate while a measureable byproduct, for example a fluorescent or colorful molecule, is produced via enzymatic reactions in proportion to the concentration of the detected biomolecules.

In this experiment components of a commercially available ELISA test kit were applied (αHu IL-8 Elisa kit SixPak from R&DSystems) to quantify BSA protein deposits used for plasma decontamination experiments. As a chromogen TMB (3,3′,5,5′-tetramethylbenzidine) was utilized that yields blue color when oxidized, typically as a result of oxygen radicals produced by the hydrolysis of hydrogen peroxide by horse-radish peroxidase enzyme. The color of the product changes to yellow after addition of sulfuric acid with maximum absorbance at 450 nm [22]). At the end of the reaction, the absorption of this colorful product was measured by a plate reader (Omega Fluostar).

A known amount of ELISA reagent, (horse-radish peroxidase enzyme, IL-8 antibody conjugate) was diluted in BSA stock solution; all the necessary dilutions for the experiments were prepared using the same stock solution in order to assure the same mass proportion between the protein and the ELISA reagent enzyme, (despite the fact that in the assays kit reagent solution the concentration of IL-8 conjugate antibody is not known). The basic idea behind the experiments described in the next paragraphs is to use the enzyme conjugate to measure the biological activity of a biomolecule under simulated contamination situations, as an alternative indicator compared to the mass of such biological material deposits. In the following we assumed that, even after drying, the enzyme conjugate molecules are homogenously dispersed in the BSA protein matrix. Experiments were carried out using the same sample preparation procedure described in paragraph 6.1.1, i.e. avoiding any sample rinsing step and potential unwanted protein mass loss (see paragraph 6.1.2). A stock solution of 10 $mg \cdot mL^{1}$ BSA was prepared with the following composition: 10 mg of BSA protein, 900 µL of water and 100 µL of enzyme-conjugate solution from the Elisa assay kit. Two times serial dilutions were deposited, each of them in three replicas, with a calibrated pipette in a polystyrene 96-well plate, each well contained 10 µL total solution volume. The solutions deposited in the plates were allowed to dry for 1 h in a flow hood. For control measurements, 10 µL of fresh solution was added to separate wells in three parallels.

The well plates were plasma treated at various treatments times, some wells were covered to protect the deposits from the plasma action, this additional wells were considered as internal calibration control points for activity loss induced by heat effects. The well plates were treated in pure water vapor plasma according to the heat control protocols described in paragraph 3.4. Plasma parameters were: RF delivered power 350 W, operating pressure 10 Pa and total gas flow of 20 sccm, pulsing frequency was 50 mHz at 20% duty cycle. Average polystyrene well plate's temperature during plasma treatment was monitored by means of an IR pyrometer and resulted below 40 °C at all treatment times. After plasma treatment the enzymatic reaction was promoted by addition of 100 μL of [1:1] solution of hydrogen peroxide and a substrate solution included in the assay kit. As a consequence of this step the dried deposits were re-suspended in the liquid phase. The enzymatic reaction was allowed to run for 2 hours and then stopped by addiction of 25 μL of 2N H_2SO_4. Optical density (OD) from each well was measured by means of a plate reader.

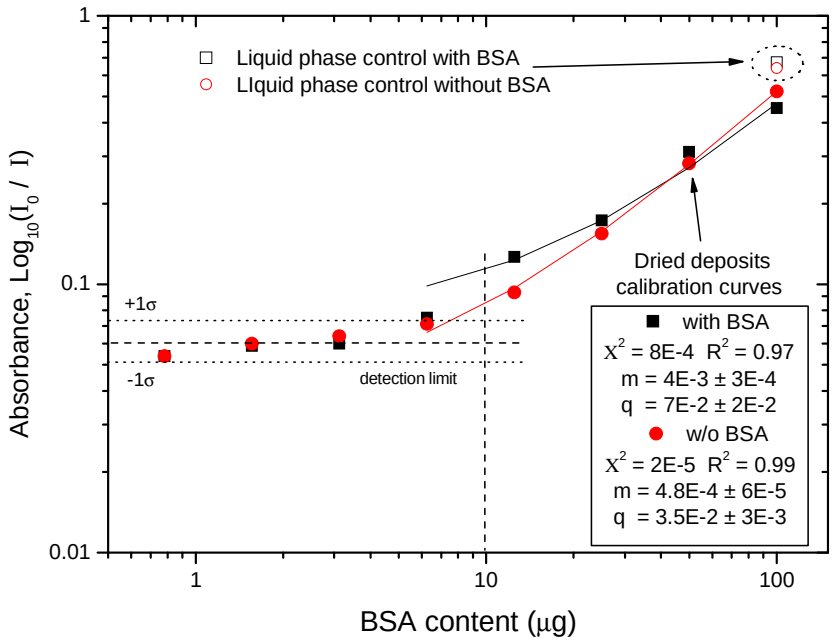

Figure 6.1.8 Set of colorimetric assay calibration curves, resulting from three parallel experiments, in different deposition situations, black data point correspond to BSA and

enzyme-conjugate deposits, red data points correspond to enzyme-conjugate deposits. Fits of the calibration curves linear regions are shown as continuous lines together with the regression parameters.

The calibration curves obtained in the preliminary experiments are shown in figure 6.1.8. Two different calibrations in the range 1 – 100 μg/well (about 0.027-2.7 $\mu g \cdot mm^{-2}$ of dry deposit) were measured for dried spots of enzyme-conjugate deposit only and enzyme-conjugate mixed with BSA, both spots contained the same mass of enzyme-conjugate. Moreover, two control points prepared directly in solution, without drying the samples, were also measured at 100 μg/well. Absorption measurement of the different calibration curves shows that the mixing of the enzyme-conjugate with BSA has a little influence on the enzymatic activity (related to the OD signal). The drying step has an evident effect, and it diminishes the OD signal for a given enzyme mass. This can be seen confronting the signal intensities of the four situations measured at 100 μg/well, dried deposits with and without BSA and measurements in solution with and without BSA. Enzyme spots lose only about 28% of activity after the drying step, while spots of the mixture lose around 48%. The detection limit of the measurement protocol was found around 10 μg/well of protein mixture (corresponding to mass density levels around 0.3 $\mu g \cdot mm^{2}$), taking the signal dispersion in consideration, for lower mass levels the signal from the enzymatic reaction flattens, most probably hidden by the well-plate background signal.
A peroxidase enzyme based assay technique was chosen in order to qualitatively measure the ability of a generic protein to perform a biological activity after exposure to plasma. This is proposed as a new strategy to asses the efficacy of plasma decontamination treatments. At the best of the author knowledge this approach has not yet been reported in the plasma based decontamination literature. The results of the assay were confronted with simultaneous mass loss measurements performed with the QCM technique described in chapter 4. QCM crystals were loaded with the same amount of BSA protein deposited in the wells. Geometrical effect due to different conformation of the well plates and QCM crystals sample holder were not taken into account.
The results of the experiment described above are shown in figure 6.1.9. The time variation of the biological activity of the peroxidase enzyme measured by means of the

cholorimetric assay are shown as black circles, referred to the left y-axis. The initial contamination level was estimated, using the calibration interpolation curve, to be around 1.02 $\mu g \cdot mm^{-2}$. It can be seen that after few seconds of plasma exposure the biological activity of contaminated wells is significantly reduced as compared to untreated samples (e.g. -25% after 30 sec of plasma exposure). The time dependency observed in the biological activity decrease is non-linear; the initial stage of the plasma treatment shows a faster reduction in the enzymatic activity response (linear fit parameter regression estimation of data points between 0 and 40 seconds yields a slope of -8 $ng \cdot mm^{-2} \cdot s^{-1}$) while after 40 seconds of exposure a different, and slower, kinetic is clearly observed (in this case linear regression performed on data points between 40 and 120 seconds yields a slope of -4 $ng \cdot mm^{-2} \cdot s^{-1}$). The observed decrease of the enzymatic activity response stops after 120 seconds of plasma exposure, after this point the detection limit of our method is reached and the measured bioactivity sets at background levels for longer treatment times.

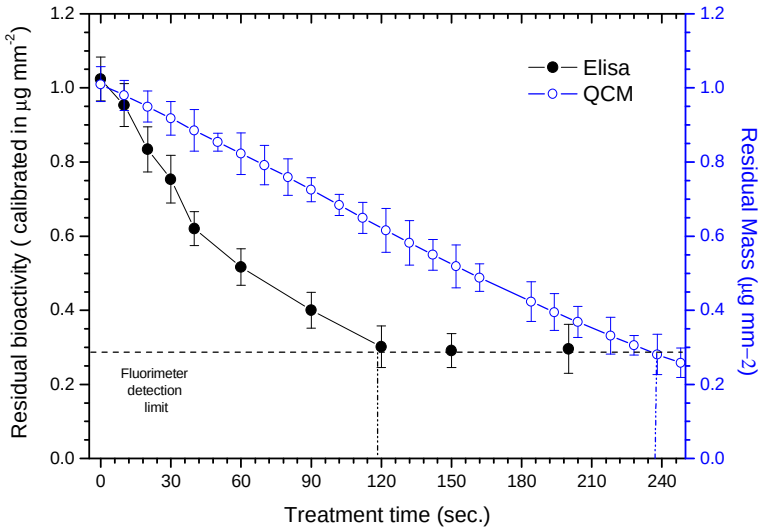

Figure 6.1.9 Residual BSA protein mass, at different plasma treatment points measured with two different methods: in black, calibrated enzyme activity test and in blue in-situ QCM diagnostic.

The time variation of the protein deposit mass as measured by means of quartz crystal microbalance is shown in figure 6.1.9 as blue circles, referred to the right y-axis. QCM voltage signal are transformed into mass density data according to the procedure described in paragraph 4.2. Using this indicator the protein mass in the wells also decreases as soon as the contaminated surfaces are exposed to the plasma but the overall behavior is remarkably different with respect to bioactivity response. In this case the mass loss time variation is linear, within the investigated range, and the calculated mass loss rate is around – 3 $ng \cdot mm^{-2} \cdot s^{-1}$. As evaluated by QCM data the residual protein mass density corresponding to the enzymatic assay detection limit is reached after 240 seconds of plasma exposure.

The differences between the two measured activity and mass loss kinetics (cholorimetric assay and QCM) can be interpreted considering the differences in the measurement techniques; while QCM measure the total mass of the deposit left at different stages of the plasma process, colorful product is formed if the reaction between the substrates and the enzyme happens. This catalytic reaction is possible only if specific biochemical functionalities in the biomolecules are preserved after plasma exposure. In general, mass is removed from the surfaces, according to the mechanisms investigated in paragraph 5.2, by ion collisions with oxidized chemical compounds chemisorbed at the surface, this process is limited, in depth range, by the ion penetration depth which is usually few tenths of nanometers for low ion kinetic energies. In contrary, chemical and structural modification of the biomolecules exposed to plasma discharge can be obtained through a variety of mechanisms: UV induced damage (from UV photons emission by OH molecular A→X bands at 309 nm, see figure 3.2.1) and biomolecule oxidation due to oxygen radicals diffusion within the protein layer can, in principle, suppress certain biological functionalities by chemical modification of the reactive (substrate binding or other functional) sites. Both processes have a longer penetration depth compared to low energy ions. Moreover, chemically active neutral atoms coming from the discharge volume can be involved in exothermic reactions at the surface acting as localized heat sources. [23] This considerations can explain the observed activity and mass loss kinetics difference shown in figure 6.1.9 and the lower rates measured for total biomaterial mass loss compared to biomolecules inactivation.

In conclusion, an alternative approach to plasma decontamination efficacy evaluation is proposed in this proof-of-principle experiment. In contrast with widely employed methods measuring a physical or a morphological quantity of model contamination thin films, the focus is switched on the biological activity inactivation of plasma treated biomolecules which is the ultimate cause of biological hazard on contaminated surfaces.

References

1 Aronsson B O, Lausmaa J and Kasemo B 1997 *J. Biomed. Mater. Res.*, **35**, pp. 49-73.

2 Herrmann F H W, Henins I, Park J and Selwyn G S 1999 *Phys. Plasmas,* **6**, pp. 2285-91

3 Rossi F, Kylian O and Haswa M 2006 *Plasma Process. Polym.*, **3**, pp. 431-42.

4 Moreau M, Orange N and Feuilloley M G J 2008 *Biotechnol. Adv.*, **26**, pp. 610-17.

5 Baxter R L, Baxter H C, Campbell G A, Grant K, Jones A C, Richardson P and Whittaker A G 2006 *J. Hosp. Infect.*, **63,** pp. 439-44.

6 Lipscomb I P, Sihota A K, Botham M, Harris K L and Keevil C W 2006 *J. Hosp. Infect.,* **62**, pp. 141-48.

7 Whittaker A G, Graham E M, Baxter R L, Jones A C, Richardson P R, Meek G, Campbell G A, Aitken A and Baxter H C 2004 *J. Hosp. Infect.*, **56**, pp. 37-41

8 Baxter H C, Campbell G A, Richardson P R, Jones A C, Whittle I R, Casey M, Whittaker A G and Baxter R L 2006 *IEEE Trans. Plasma Sci.*, **34**, pp. 1337-44.

9 Vandervoort K 2009 *Microscopy as an analysis tool for studying plasma applications* (eds. G Brelles-Mariño), New York: Nova Science Publishers.

10 Westphal P and Bommann A 2002 *Sensors Actuators* B, **B84**, pp. 278.

11 Calander N 2006 *Curr. Anal. Chem.*, **2,** pp. 203-11.

12 Phillips K S and Cheng Q 2007 *Anal. Bioanal. Chem.*, **387**, pp. 1831-40.

13 Haynes C L, Yonzon C R, Zhang X and Van Duyne R P 2005 *J. Spectrosc.*, **36**, pp. 471-84.

14 Li T, Guo L and Wang Z 2008 *Biosens. Bioelectron.*, **23**, pp. 1125-30.

15 Scholes F H, Bendavid A, Glenn F L, Critchley M, Davis T J and Sexton B A 2008 *J. Raman Spectrosc.*, **39**, pp. 673-78.

[16] Porter M D, Lipert R J, Siperko L M, Wang G and Narayanan R 2008 *Chem. Soc. Rev.*, **37**, pp. 1001-11.

[17] Rigler P, Ulrich W-P, Hoffmann P, Mayer M and Vogel H 2003 *Chem. Phys. Chem.*, **4**, pp. 268-75.

[18] P. Bohlen 1973 *Arch. Biochem. Biophys.* **155**, pp. 213-220

[19] Lipscomb I P Sihota A K Bothman M Harris K L and Keevil C W 2005 *J. Hosp. Inf.*, **62**, pp. 141-148

[20] Van Weemen B K and Schuurs A H W M 1971 *FEBS Lett*., **15**(3), pp. 232-236.

[21] Lequin R M 2005 *Clin. Chem*., **51**(12) pp. 2415–18.

[22] Josephy P D, Eling T and Mason R P 1982 *J. Biol. Chem*., **257**(7) pp. 3669-75.

[23] Kersten H, Stoffels E, Stoffels W W, Otte M, Csambal C, Deutsch H and Hippler R 2000 *J. Appl. Phys.* **87**(8) pp. 3637-45.

7. Conclusions and summary

The presented work characterizes an ICP reactor for the purpose of surface decontamination and investigates the fundamental sterilization mechanisms of biomolecules such as proteins and biological material matrices. Through the work, particular requirements for low pressure plasma processes applications to the medical field are taken into account (e.g. process compatibility with thermo-labile objects and environmental-friendly, low-cost procedure implementation). Moreover, special attention is devoted to the development of diagnostics and protocols for quantitative measurement of biological residuals on treated surfaces.

Plasma process development. While the use of oxygen-based plasma discharges for biomolecules decontamination has been studied in detail in the past few years, relatively fewer results have been published concerning the removal of proteins and biological matrices from surgical instruments by means of a water vapor discharge. The possibility to eliminate biomolecular contaminations by low-pressure H_2O plasma treatment was addressed in this study. Plasma decontamination of silicon surfaces was achieved using water vapor plasma; model contaminations created either with pure protein or with a biological matrix were effectively reduced by the interaction with the plasma on a reasonable time scale. Mass removal rates for water vapor based discharges are found to be lower then corresponding oxygen-based discharges operated in identical conditions but the absolute values are nevertheless of the same order of magnitude. This result indicates that a water vapor based mixture might be used to implement an efficient cost-effective decontamination device. Water vapor plasma discharges were characterized by means of optical emission spectroscopy and Langmuir probe, and plasma fluxes were measured in several operating parameters conditions ranging from 2 to 20 Pa and 0.03 to 0.09 $W \cdot cm^{-3}$. Plasma fluxes data have been used to predict mass removal rates behavior within the framework of chemical sputtering plasma biomaterial interaction mechanism. Comparison of different interaction schemes indicates that the leading interaction is chemically favored by oxygen atoms reactions on the surface. Anyway, oxygen atoms contribution to mass removal rates cannot alone fully explain the measured data, it is

postulated that hydroxyl molecules plays an auxiliary role both in terms of UV emission and H-abstraction processes.

Plasma-biomaterial interaction mechanisms. Plasma biomaterials interaction analysis in terms of discharge internal parameters (radicals and ions fluxes and energy) presented in this work defines mass removal mechanisms investigations and results on the basis of a known theoretical framework, in real plasma environments and in an ion energy region not investigated by published particle beam experiments. Whitin the framework of Langmuir-Hinshelwood surface reaction theory different plasma-biomaterials interaction models can be derived and tested. Two different radicals-ion synergy schemes and the pure chemical etching scenario have been investigated. Particle fluxes (ions, atoms, molecules) have been measured for several plasma conditions mapping reactor operative parameters to plasma internal parameters. In particular power dependencies of oxygen molecules, atoms and radicals fluxes are derived, as calculated from measured densities values according to gas dynamic equation. Ion fluxes were calculated from Langmuir probe data according to Bohm sheath criterion. Measured fluxes and etch rates were compared with models calculated etch rates using a series of statistical tests.
Plasma discharge characterization and validation of interaction models defined ion assisted chemical etching – ion assisted desorption (in a modified version of the model in order to take into account ion flux limited surface kinetics, chemical bonds breaking energy threshold and bombarding ion energy in the range ε = 10-100 eV) as the most accurate scheme to describe biomaterial mass removal rates in oxygen plasma. Low energy ions number density effect on biomaterial mass removal rates was found to follow a square root energy dependance, with very low (ε_{th} < 1 eV) energy threshold for the ion assisted desorption process. Moreover, in water vapour plasma experimetns, oxygen radicals interaction with biofilm was found to describe etching rates of biomaterials even in presence of hydrogen and hydroxyl active radicals.

Residual contamination in-situ diagnostic. In this study the details of thin protein film removal by means of a low pressure ICP discharge were investigated. For this purpose an in situ diagnostic method, suitable for laboratory studies on model contaminations, based on quartz crystal microbalance was developed and validated. This method allows

quantitative measurements in terms of plasma removed protein mass and detailed investigation of etching rate kinetics. In contrast to commonly empolyed residual contamination evaluation diagnostics, described in plasma decontamination related literature, the proposed approach benefits simultanously of the three following characteristics: is a quantitative measurament, is applicable in-situ during plasma processing without breaking the vaccum and has time resolution down on the seconds scale.

Mass loss curves have been measured and characterized for different model contaminations reproducing the same areal mass density of realistic contamination situations found in medical practice and deposited on substrates (Au coated QCM crystals) with realistic roughness levels, moreover the plasma treatments were performed at temperatures suitable for thermo-labile materials processing. Good sampling frequency of the in-situ QCM technique was exploited to study the details of the etching rate kinetics. Results show that, for thin film contaminations, etching rates are not constant but can be described as a self-limiting process. Descriptive parameters were introduced to account for the kinetics of the removal process and mass loss curves were explained in terms of the modification induced by the plasma - protein interaction. Accumulation of non-reactive compounds and substrate exposure at the interaction interface were identified as the main causes. In particular the time constant of the etching process was found to depend stepwise both on the morphology and the chemical composition thus defining a transition between two regimes of the removal process. In an early regime the kinetic of the mass removal is dominated by non reactive species accumulation while during late stages of the treatment an endpoint regime dominated by reduction of the effective interaction area and substrate exposure was observed. Of importance for the development of a plasma-based decontamination technique, it was found that, in the second etching regime, the basic building blocks of the protein structure (the backbone peptidic chains) have been destroyed by the plasma interaction and the residual structures are composed mainly by amorphous carbon.

Residual contamination ex-situ diagnostics. In the last part of this work a protocol for biological activity measuraments of the residual contamination after plasma treatments was tested. This approach explores a different path with respect to the commonly

reported residual surface contamination assesment methods mainly based on thin films physical properties measuraments. Results show that it is possible to detect low levels (down to 1 $\mu g \cdot mm^{-2}$) of biologically active protein soiling on contaminated surfaces using an immuno asssay test combined woth a spectrophotometeric technique. Moreover a comparison of plasma induced protein films removal rates as measured by quartz crystal microbalance diagnostic and as measured by calibrated immuno assay method shows how mass loss rates and biological activity decrease in plasma treated protein films exhibit different kinetics, the latter being about twice as fast as the former in the investigated range.

Advantages to Common Sterilization Methods. In this work gas mixtures showing sufficient efficacy for decontamination processes are based on combinations of Argon, Oxygen or water vapour. In literature also the use of Nitrogen and Hydrogen is reported. Therefore, the proposed decontamination plasma based process does not involve the presence of either hazardous oxidizing agents or toxic ingredients, as is the case of ethilene oxide or hydrogen peroxide based sterilizers. The characteristic and total treatment times are in the time scale of minutes, while common sterilization processes may take from a few hours up to days to complete. The process have been tested against thermo-labile materials and thermo compatible process conditions (below 40 ºC) are possible, polymeric materials that will be damaged by high temperature autoclave processing can be treated by a plasma-based device.

8. Publications and Conferences

Major parts of this thesis are published or submitted for publication:

1) Fumagalli F, Kylian O, Hanus J and Rossi F, *Plasma Process. Polym.* 2011, "In-situ quartz crystal microbalance measuraments of thin film plasma removal", Accepted. *Preprint* DOI: 10.1002/ppap.201100098.

2) Fumagalli F, Kylian O, Amato L and Rossi F, Journal of Physics D: Applied Physics, 2011, "Low pressure water vapour plasma treatment of surfaces for biomolecules decontamination", Submitted.

Other publications not included in the dissertation:

1) Siliprandi, R Zanini S, Grimoldi E, Fumagalli F, Barni R, Riccardi C, 2011 *Plasma Chemistry and Plasma Processing*, "Atmospheric Pressure Plasma Discharge for Polysiloxane Thin Films Deposition and Comparison with Low Pressure Process" 31(2), pp. 353-372(20).

Part of this work was presented at the following conferences:

1) NATO Advanced Research Workshop, "Plasma for bio-decontamination, medicine and food security", Jasná, Slovakia, March 15-18, 2011. Poster session: "Biomaterials etching in low pressure inductively coupled discharge", Fumagalli F and Rossi F.

2) XX National Congress Italian Vacuum Association: " Energy and materials: technologies and perspectives" Padova, Italy, May 17-19 2011. Oral presentation: "Bio-decontamination of surfaces by low pressure plasma discharges" Fumagalli F and Rossi F.